UNIVERSITY OF SOUTHAMPTON

FACULTY OF PHYSICAL SCIENCES AND ENGINEERING

School of Electronics and Computer Science

Human-Powered Inertial Energy Harvesters: The Effect of Orientation, Location and Activity on the Obtainable Electrical Power

by

Hui Huang

Thesis for the degree of Doctor of Philosophy

March 2014

UNIVERSITY OF SOUTHAMPTON

ABSTRACT

FACULTY OF PHYSICAL SCIENCES AND ENGINEERING
ELECTRONICS AND COMPUTER SCIENCE

Doctor of Philosophy

HUMAN-POWERED INERTIAL ENERGY HARVESTERS: THE EFFECT OF ORIENTATION, LOCATION AND ACTIVITY ON THE OBTAINABLE ELECTRICAL POWER

by Hui Huang

Human-powered inertial energy harvesting is an emerging technology that can power electronic devices using electrical energy scavenged from human motion. Traditional energy harvesters generate energy only from a single axis, and are referred to one degree-of-freedom (1-DOF) energy harvesters. In this thesis, a two degree-of-freedom (2-DOF) energy harvester consisting of two orthogonal 1-DOF energy harvesters is studied. This research theoretically and experimentally investigates the effect of orientation, location and activity on the obtainable power from 2-DOF human-powered inertial energy harvesters.

An on-body measurement study has been conducted to collect acceleration data from five key locations on the body during both walking and running. The collected data have been analyzed to evaluate the harvestable power along different orientations of both 1-DOF and 2-DOF inertial energy harvesters. The results show that the orientation of 1-DOF generators on the body greatly affects the output power. 2-DOF generators can maintain a more constant power output with rotation, thus are more reliable than 1-DOF generators. For 1-DOF generators, and for each location and activity, only 6% of the tested orientations harvest over 90% of the maximum power. For 2-DOF generators, this is increased to 32%, showing a considerable improvement.

To validate the analytical results, 1-DOF mechanical- and magnetic-spring electromagnetic generators have been designed and prototyped. A novel design has been proposed to linearise magnetic springs for low frequency use. Experimental validation shows that the design exhibits a linearity of 2% across a ±25 mm displacement range, presenting a significant improvement over the state-of-the-art. A 2-DOF inertial generator that consists of two orthogonal 1-DOF mechanical-spring generators has been tested at three locations around the knee while running. At each location, the 2-DOF generator has been rotated to four different angles. The results show that 2-DOF generators can generate over 81% of the maximum power in all orientations. For 1-DOF generators, it is only 35%.

Contents

List of Figures

List of Tables

DECLARATION OF AUTHORSHIP

I, Hui Huang declare that the thesis entitled 'Human-Powered Inertial Energy Harvesters: The Effect of Orientation, Location and Activity on the Obtainable Electrical Power' and the work presented in the thesis are both my own, and have been generated by me as the result of my own original research. I confirm that:

- this work was done wholly or mainly while in candidature for a research degree at this University;
- where any part of this thesis has previously been submitted for a degree or any other qualification at this University or any other institution, this has been clearly stated;
- where I have consulted the published work of others, this is always clearly attributed;
- where I have quoted from the work of others, the source is always given. With the exception of such quotations, this thesis is entirely my own work;
- I have acknowledged all main sources of help;
- where the thesis is based on work done by myself jointly with others, I have made clear exactly what was done by others and what I have contributed myself;
- parts of this work have been published as listed in section 1.4 of this thesis.

Signed: ……..

Date:…….

Acknowledgments

I would like to express my sincere appreciation and gratitude to my supervisors Dr Geoff Merrett and Professor Neil White for their technical supervision and guidance throughout my PhD.

I wish to thank Dr Dibin Zhu and Dr Cheryl D Metcalf for their kind help in this research. I am thankful for the research facilities and support provided by the School of Electronics and Computer Science (ECS), the Institute of Sound and Vibration Research and the Human Performance Laboratory. I am also grateful to the people taking in part in the on-body acceleration measurement and the on-body experimental validation. I also wish to thank the people in the Electronics and Electrical Engineering Laboratory for making my stay in Southampton memorable.

In addition, I wish to thank my family and friends for their support. Special thanks must go to my parents and grandparents for giving me strength and support over the past four years. Finally, I would like to thank my wife, Lijun Yao, for her love, understanding and encouragement. This thesis is dedicated to my wife, parents, and grandparents, without whom none of this would have been possible.

Nomenclature

α	Angular tolerance [degrees]
β	Angle about XY plane [degrees]
$\Delta\beta$	Angle difference of β [degrees]
$\emptyset$	Angle about Y axis [degrees]
$\Delta\emptyset$	Angle difference of $\emptyset$ [degrees]
Φ	Magnetic flux [Wb]
σ_{max}	Maximum deviation [m]
δ	Independent linearity [%]
θ	Rotation angle [degrees]
$\Delta\theta$	Angle difference of θ [degrees]
φ	Angle of interception [degrees]
τ	Rotate ability [%]
γ, γ'	Factor used in the angular tolerance calculation
ξ_e	Electric damping ratio
ξ_p	Parasitic damping ratio or mechanical damping ratio
ξ_T	Total damping ratio
μ	Coefficient of kinetic friction
ω	Vibration frequency [rad s^{-1}]
ω_n	Natural frequency [rad s^{-1}]
ω_0	Resonant frequency [rad s^{-1}]
ε	Dielectric constant [F m^{-1}]
$\boldsymbol{a}$	Acceleration vector [m s^{-2}]
$\boldsymbol{a_p}$	Acceleration vector projected onto a plane [m s^{-2}]
$\boldsymbol{a'}$	Acceleration vector projected onto a direction [m s^{-2}]
A	Peak acceleration of external vibration [m s^{-2}]
$A_{1,2}$	Acceleration magnitude of the projected vibrations [m s^{-2}]
A_b	Maximum acceleration in frequency bands [m s^{-2}]
A_c	Cross-sectional area of a coil [m^2]
A_{in}	Peak amplitude of external vibration [m s^{-2}]
A_{out}	Peak amplitude of acceleration along generators [m s^{-2}]
A_0	Plate area of a capacitor [m^2]
A_{exc}	Acceleration magnitude of the external vibration [m s^{-2}]

b Damping coefficient [N s m^{-1}]

B Flux density [T]

B_r Remanent flux density [T]

C Capacitance [F]

d Wire diameter [m]

d_0 Distance between two parallel plates of a capacitor [m]

D Mean diameter of spring coil [m]

emf Electromotive Force [V]

E Electric energy [J]

E_0 Young's modulus [Pa]

Δf Bandwidth [Hz]

f Vibration frequency [Hz]

f_0 Resonant frequency [Hz]

f_n Natural frequency [Hz]

f_b Frequency corresponding to A_b [Hz]

f_{beam} Resonant frequency of a cantilever [Hz]

f_c Frequency of voltage signal across coils [Hz]

f_s Sampling frequency [Hz]

f_x, f_y Resonant frequencies along two axes of 2-DOF generators [Hz]

F Electric reaction force [N]

F_f Friction [N]

F_n Normal force [N]

F_s Extended or compressed force on a spring [N]

'g' Gravity of earth = 9.81m s^{-2}

G Modulus of rigidity [Pa]

h Thickness of the cross section of a cantilever [m]

I Moment of inertia [kg m^2]

I_s Spring index

k Spring stiffness [N m^{-1}]

k_{eq} Equivalent spring stiffness of a cantilever [N m^{-1}]

l Length of a coil [m]

L Cantilever length [m]

L_c Coil inductance [H]

m Seismic mass [kg]

m_{eq}	Equivalent mass of a cantilever [kg]
m_0	Mass of a cantilever [kg]
M	End mass of a cantilever [kg]
N	Turns number of a coil
N_a	Number of active coils
$\widehat{\boldsymbol{P}}$	Unit vector of generator orientations
P_d	Power dissipated in the damper [W]
P_e	Power extracted by energy transduction mechanisms [W]
P_L	Power dissipated in a load [W]
$P_{\max}$	Maximum relative or normalised power [W/kg or %]
P_{peak}	Peak power from a resonant system [W]
P_n	Normalised power [%]
P_{opt}	Power on optimum load resistance [W]
P_r	Relative power [W/kg]
Q	Q-factor
Q1	25^{th} percentiles quartile
Q3	75^{th} percentiles quartile
Q_0	Electric charge [C]
$\hat{\boldsymbol{r}}, \hat{\boldsymbol{r}}_{\boldsymbol{0}}$	Unit vectors for rotation
$\boldsymbol{R}_\theta$	Rotation matrix
R_c	Coil resistance [Ω]
R_L	Resistive load [Ω]
R_{opt}	Optimum load resistance [Ω]
t	Time [s]
V	Electric potential [V]
V_s	Relative moving speed of a conductor [m s^{-1}]
V_t	Measured voltage across optimum load resistance [V]
w	Width of the cross section of a cantilever [m]
x_q	Quiescent position [m]
x	Relative displacement of seismic mass with respect to outer frame [m]
X	Peak displacement of seismic mass with respect to outer frame [m]
X_L	Inductive reactance [Ω]
X_s	Displacement of a spring [m]
$\hat{\boldsymbol{x}}, \hat{\boldsymbol{y}}, \hat{\boldsymbol{z}}$	Unit vectors aligned with the three accelerometer axes

y Displacement of outer frame [m]

y_{pp} Full scale region of best-fitting straight line [m]

Y Peak displacement of external vibration [m]

Abbreviations

1-DOF	One Degree-Of-Freedom
2-DOF	Two Degree-Of-Freedom
FEA	Finite Element Analysis
FFT	Fast Fourier Transform
IQR	Interquartile range
MEMS	Micro-Electro-Mechanical Systems
PVDF	Polyvinylideneflouride
PZT	Lead Ziroconate Titanate
rms	root mean square
RFID	Radio-Frequency Identification
STD	Standard Deviation

Chapter 1
Introduction

Applications of body sensor networks are continually increasing in popularity over the last decade [1], for example, monitoring of the electrical activity of the heart, from a simple heart rate to a full electrocardiogram (ECG) [2, 3]; fall detection systems for the elderly [4, 5]; sport training [6]. Body sensors usually require inconvenient or cumbersome battery replacement or recharging. Ideally, prolonged or even indefinite operation without intervention is desired from such devices. A promising way of addressing this is to make use of energy harvesting technology [7], which can convert ambient energy, such as light, temperature gradients and vibrations, into useful electrical energy to power electronic devices. A tremendous energy source for energy harvesting is the human body [8, 9]. For example, Jo *et al.* [10] developed a flexible thermoelectric generator which can convert body heat into electrical power. The generator was attached to the human body, and the output power was 2.1 μW when the temperature difference between the human body and ambient air was 19 K. Li *et al.* [11] designed a knee-mounted energy harvester that harvests energy from the angular displacement at the joints during human walking. It was designed to efficiently convert the mechanical power into electricity during the end of swing extension with little extra user effort. The output power was 4.8 W at a walking speed of 5.40 km h^{-1}. A backpack instrumented with piezoelectric shoulder straps has been developed by Granstrom *et al.* [12]. The electrical energy is generated from the strain generated in the straps of the backpack due to walking. When the backpack was worn on the body with 220 N load, an average power of 45.6 mW was generated at a walking speed of 3.24-4.68 km h^{-1}. Shoe-mounted energy harvesters that use the impact of the foot on the ground while walking and running have been proposed by the researchers at the MIT Media Laboratory [13]. One reported shoe-mounted rotary magnetic generator was able to generate 250 mW during walking at a pace of two steps per second.

The power obtainable from human motion energy harvesting depends greatly on the dominant frequency and acceleration of human motion, and varies at different locations on the body for different activities of daily living. For example, in an on-body acceleration measurement reported in [14], a 76 kg subject was wearing standard running shoes and walking at 5 km/h, and acceleration data were measured from the ankle, wrist, chest, upper arm, and head. It was found that the ankle gives the maximum acceleration of over 100 m s^{-2} (peak, in the direction of walking) at 1.2 Hz. The peak acceleration in the vertical direction was much smaller (20 m s^{-2}). At all other locations, the frequency remained constant, and the peak acceleration in the vertical

and walking axes were less than 7 m s^{-2}.

Human motion energy harvesting devices can be classified into direct-force harvesters and inertial harvesters [8]. For direct-force harvesters, the exciting force is directly applied to the proof mass of the harvester (Figure 1.1.a). For example, researchers at MIT developed a piezoelectric shoe-mounted insert to generate electrical power from the force of the impact of the foot on the ground [15]. For inertial harvesters, on the other hand, the exciting force is applied to the housing and the resulting inertial force excites the proof mass (Figure 1.1.b). In one paper [16], a suspended-load backpack has been developed to convert mechanical energy from the vertical movement of carried load to electricity during normal walking. From Figure 1.1, it should be noted that direct-force harvesters require two mechanical attachments to make the relative displacement between the proof mass and the housing (for example, between the foot and the shoe/floor), but only one mechanical attachment is needed for inertial harvesters (for example, between the backpack and the human body).

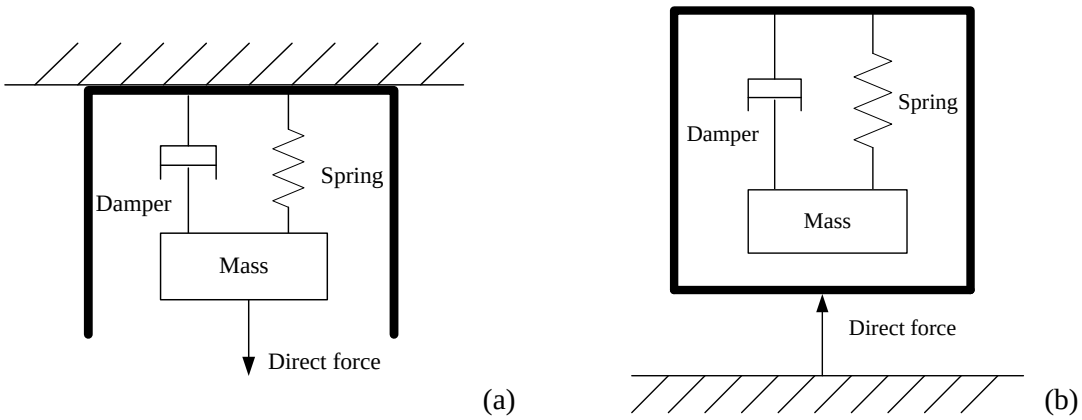

Figure 1.1 Generic models of (a) direct-force harvesters and (b) inertial harvesters.

Human motion is characterized by acceleration of low frequency and high amplitude. For example, Figure 1.2 shows the frequency spectra of measured acceleration waveforms at wrist, elbow and knee along three orthogonal axes while walking on a treadmill at 4 km h^{-1} [17]. The results show that the dominant frequencies are all below 10 Hz, and the peak amplitude is close to 4 m s^{-2}. Comparatively, some vibration sources, such as bridges, window frames, and combination boilers, all have dominant frequencies over 100 Hz and below 1 m s^{-2} [18].

Owing to the low frequencies of human motion (<10 Hz), the generated electrical power from inertial energy harvesters is typically in the range of a few μW [17, 19, 20], which is not enough to power most body sensors. The average power consumption of most wireless sensor nodes is in the range of 100 μW-100 mW [21]. Table 1.1 shows the average power consumption of a selection of consumer mobile devices and wearable body sensors. For example, if the output

power from energy harvesters is up to 50 μW, it can power RFID tags and the Seiko AGS quartz watch; however, this is not enough for other devices, such as a heart rate monitor, triple axis accelerometer or humidity sensor.

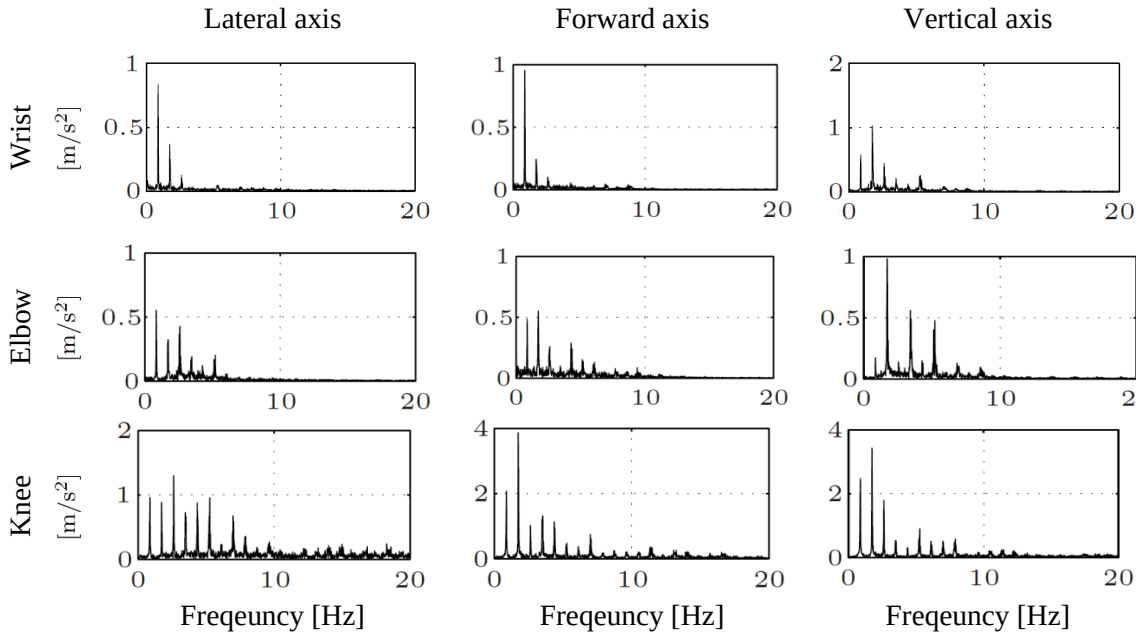

Figure 1.2 Frequency spectra of measured acceleration waveforms during walking at 4 km h^{-1} at wrist, elbow and knee along lateral axis, forward and vertical axes. (Reproduced from [17]).

Table 1.1 Average power consumption of some consumer mobile devices and wearable health sensors [8, 15, 22, 23].

Mobile devices and wearable health sensors	**Average power consumption**
Seiko AGS quartz watch	0.7 μW
RFID tags	10 μW
Hearing aids	100 μW
Temperature sensor-ADT7320	0.693 mW
Humidity sensor-HIH 3610 series	1 mW
Triple axis accelerometer-ADXL335	1.05 mW
Heart rate monitor	2.178 mW
RF receiver-TDA 5200	24 mW
Small portable FM radio	30 mW
GPS receiver-Fastrax IT500	75 mW

Based on the number of axes in which energy can be harvested, some energy harvesters can be classified as one degree-of-freedom (1-DOF) or two degree-of-freedom (2-DOF). For a 1-DOF inertial energy harvester, the proof mass of the generator oscillates along a single axis. For example, a flashlight powered by shaking by hand [15] or the general inertial harvester shown

in Figure 1.1b. If the proof mass oscillates along two axes, the generator is referred to as a 2-DOF energy harvester. Some reported 2-DOF energy harvesters are reviewed in Section 2.3.1.

1.1 Research Justification

To understand the movement of the human body in daily life and investigate the attainable energy from human motion, existing studies have investigated the motions at different key locations on the body for various activities of daily living: for example, Yun *et al.* [24] and Büren *et al.* [25]. The corresponding acceleration data have been measured using triple axis accelerometers. The harvestable power was estimated by assuming a 1-DOF inertial energy harvester would be located at the test locations and that the oscillation of the generator would be aligned with one of the axes of the accelerometer. Therefore, all existing studies investigated only the three orthogonal axes at each tested location, and the harvestable power has been evaluated only exactly along the three axes. Subsequently, the effect of orientation on the output power has not fully investigated.

The orientation of 1-DOF inertial energy harvesters is an important factor that affects the harvestable output power from human motion. As 1-DOF inertial energy harvesters are able to oscillate only in a single direction, the component of human motion that is orthogonal to this axis cannot be used for energy harvesting. In the worst case, if the axis of oscillation is perpendicular to the direction of motion, none of the available kinetic energy from the motion can be harvested. Therefore, optimal energy harvesting requires that the oscillation of 1-DOF energy harvester is aligned with the direction of maximum acceleration motion. However, proper alignment is hard to achieve. One reason for that is the lack of knowledge about the characteristics of the motion under consideration. The other reason is that such motion varies with activity and between individuals, and the direction of human motion may demonstrate unexpected shifts from its dominant direction in practice.

One way to overcome the restrictions of 1-DOF inertial energy harvesters is to use structures capable of oscillating in two orthogonal directions, and thus capable of harvesting from two components of the vibration source. This can be achieved by combining two separate orthogonal 1-DOF energy harvesters. Therefore, 2-DOF energy harvesters have the potential to harvest more energy from human motion, and also have a greater tolerance to rotation. However, existing studies have not investigated these benefits of 2-DOF energy harvesters, which will be explained in details in Section 2.4.

1.2 Research Aims

The aims of this research are:

1) To understand on-body energy harvesting from human motion and identify what factors affect the harvested energy;

2) To explore how power output is affected by orientation of on-body energy harvesters;

3) To explore whether or not 2-DOF inertial energy harvesters can provide significant improvement in output power and tolerance to rotation over 1-DOF inertial energy harvesters;

4) To experimentally validate the analytical results of aims 2 and 3.

1.3 Research Contributions

The major contributions of this research are:

1) An in-depth study into the effect of rotation on harvested energy from on-body energy harvesters. How the orientation of energy harvesters affects the output power from human motion has been fully studied. At the ankle during walking, a rotation of 20° from the optimum direction reduces the available output power by 10%. This variability is demonstrated for many different locations on the body in activities of daily living.

2) A comparison of the performance of 1-DOF and 2-DOF inertial energy harvesters. In this thesis, a 2-DOF inertial energy harvester that consists of two orthogonal 1-DOF inertial energy harvesters is investigated. The analytical results show that 2-DOF inertial energy harvesters are, while not harvesting significantly more power, able to significantly increase the tolerance to rotation. At each location on the body and activity, the output power is increased only by 18% (average), but the tolerance to rotation increases significantly by 73%.

3) In the development of electromagnetic energy harvesters to validate the analytical results, a novel linearised magnetic spring has been designed for low-frequency use. Simulation results indicate that, compared to the state-of-the-art, this design exhibits improved linearity (2%) across a wider displacement range (±25mm). Two prototypes have been fabricated, and the simulation results have been experimentally validated.

1.4 Published Papers

The following papers have been published as a result of the research shown in the thesis:

1) H. Huang, G. Merrett, and N. White, "Human-powered inertial energy harvesters: the effect of orientation, location and activity on obtainable power," in *Proc. Eurosensors XXV, 4th-7th September 2011*, Athens, Greece, 2011, 4pp.

2) H. Huang, G. Merrett, and N. White, "Design of a linearized magnetic spring for body-worn inertial energy harvesters," in *Proc. Int. Workshop Algorithms and Concepts for Networked Sensing Systems Powered by Energy Harvesters (EnHaNSS'12),11th-14th June 2012*, Antwerp, Belgium, 2012, 4pp.

1.5 Thesis Structure

The structure of the remainder of this thesis is as follows:

Chapter 2 provides a review of existing literature on human motion energy harvesting, to identify the work undertaken in areas relevant to this thesis. This highlights the fact that the motion of the body at various locations during different activities needs to be investigated, in order to evaluate the effect of orientation on harvestable power from 1-DOF and 2-DOF inertial energy harvesters.

Chapter 3 presents the design of an on-body measurement study to collect acceleration data from the human body, and the analytical procedure for evaluating the harvestable power from 1-DOF and 2-DOF inertial energy harvesters. The effect of orientation on harvestable power from 1-DOF and 2-DOF inertial energy harvesters is also investigated, shown in Chapter 4.

To validate the analytical results presented above, a 2-DOF inertial energy harvester, consisting of two orthogonal 1-DOF inertial energy harvesters, has been designed, modelled, and fabricated, as shown in Chapter 5. The aim of the design of the 2-DOF inertial energy harvester is to validate the effect of orientation on harvestable power, but not to achieve a harvester with best performance of output power. Hence, the harvester is not optimised in terms of output power. The prototype 1-DOF inertial energy harvesters have been tested and characterized on a controlled vibration source, and the prototype 2-DOF inertial energy harvester has been tested on the human body to validate the analytical results. These experimental validations are presented in Chapter 6.

Chapter 7 concludes the thesis, and outlines areas of future work.

Chapter 2
Human-Powered Inertial Energy Harvesting

One aim of this research is to understand on-body energy harvesting from human motion and identify what factors affect the harvested energy. To provide an overview of energy harvesting, Section 2.1 presents the basic transduction mechanisms for converting kinetic energy to electronic energy, followed by the introduction and analysis of existing human-powered inertial energy harvesting devices. Human motion is a combination of low frequency (<10 Hz) vibrations. A review of existing techniques of harvesting full amount of kinetic energy from human motion and methods of harvesting energy from low frequencies is presented in Section 2.3. To identify what factors affect the harvested energy from human motion, the existing studies on the effect of location and activity on harvestable power are reviewed in Section 2.4.

2.1 Transduction Mechanisms for Converting Kinetic Energy to Electrical Energy

This section describes the generic model of kinetic energy transduction, which is then followed by the introduction to, and analysis of, three kinetic energy transduction mechanisms: piezoelectric, electrostatic and electromagnetic transductions.

2.1.1 General Model of Inertial Energy Harvesters

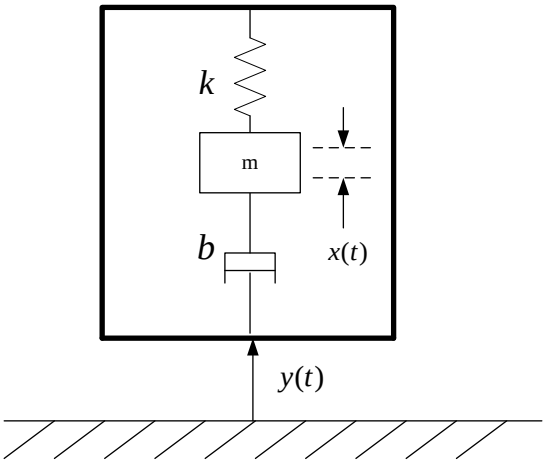

Figure 2.1 A second-order spring-mass system.

Inertial energy harvesting devices can be modelled as a second-order spring-mass system composed of an outer frame, a seismic mass m [kg], a spring of stiffness k [N m^{-1}] and a

damper of damping coefficient b [N s m^{-1}] (Figure 2.1). This inertial energy harvester model has been shown and investigated in the literature [26-30]

Assuming that the outer frame is excited by an external vibration source, the position of the outer frame relative to the equilibrium position is written as $y(t)$ [m], and the position of the seismic mass movements relative to the outer frame is notated as $x(t)$ [m]. The external vibration source, for ease of analysis, is assumed to be a sinusoidal signal, which is written as:

$$y(t) = Ysin(\omega t) \tag{2.1}$$

where Y [m] is the peak displacement of the external vibration, ω [rad s^{-1}] is the vibration frequency and t [s] is time. The equilibrium of the forces applied to the seismic mass can be described as Equation (2.2) under two assumptions: one is that the mass of the external vibration source is much bigger than the proof mass and the other is that the vibration source is an infinite source of power [31]. These two assumptions guarantee that the external vibration cannot be affected by the motion of the generator.

$$m\ddot{x}(t) + b\dot{x}(t) + kx(t) = -m\ddot{y}(t) \tag{2.2}$$

Considering the sinusoidal excitation, the steady-state solution for $x(t)$ in Equation (2.2) is written as:

$$x(t) = \frac{\omega^2}{\sqrt{\left(\frac{k}{m} - \omega^2\right)^2 + \left(\frac{b\omega}{m}\right)^2}} Ysin(\omega t) \tag{2.3}$$

The generated power from the energy harvesting device can be considered as the dissipated power in the damper of the spring-mass system. The total dissipated power in the damper can be expressed as:

$$P_d = \frac{m\xi_T Y^2 \left(\frac{\omega}{\omega_n}\right)^3 \omega^3}{\left[1 - \left(\frac{\omega}{\omega_n}\right)^2\right]^2 + \left[2\xi_T(\frac{\omega}{\omega_n})\right]^2} \tag{2.4}$$

where ξ_T is the total damping ratio, written as:

$$\xi_T = \frac{b}{2m\omega_n} \tag{2.5}$$

where ω_n [rad/s] is the natural frequency of the spring-mass system.

The natural frequency ω_n is defined as:

$$\omega_n = 2\pi f_n = \sqrt{\frac{k}{m}} \tag{2.6}$$

where f_n [Hz] is the natural frequency.

The resonant frequency ω_0 [rad/s], defined as the frequency for which the amplitude of the response $x(t)$ has its maximum, is expressed as [32]:

$$\omega_0 = 2\pi f_0 = \omega_n\sqrt{1 - 2\xi_T^2} \tag{2.7}$$

where f_0 [Hz] is the resonant frequency. When the damping ratio is small, the difference between the resonant frequency and the natural frequency is small.

If an inertial energy harvester is placed in the direction of gravity, the quiescent position x_q [m] of the seismic mass m due to the gravity 'g' (where 'g': gravity of earth, 1'g' = 9.81 m s^{-2}) is written as:

$$x_q = \frac{m\text{`}g\text{'}}{k} \tag{2.8}$$

Considering Equation (2.6), the quiescent position can be rewritten as:

$$x_q = \frac{\text{`}g\text{'}}{(2\pi f_n)^2} \tag{2.9}$$

Then, the quiescent position is inversely proportional to the square of the natural frequency. The quiescent position is an important consideration in designing inertial energy harvesters.

In Equation (2.4), maximum power occurs when the vibration frequency is equal to the natural frequency, i.e. $\omega = \omega_n$. The maximum power is expressed as:

$$P_d(\omega_n) = \frac{mY^2\omega_n^3}{4\xi_T} \tag{2.10}$$

The peak displacement Y can be replaced by the peak acceleration A [m s^{-2}] using $Y = A/\omega^2$. Then, Equation (2.10) is rewritten as:

$$P_d(\omega_n) = \frac{mA^2}{4\omega_n\xi_T} \tag{2.11}$$

In Equation (2.11), the output power at resonance is inversely proportional to the damping ratio. It appears that infinitely large output power would be achieved as the damping ratio approaches zero, but in practice, this is not possible. The total damping ratio can be expressed as:

$$\xi_T = \frac{Y}{2X} \tag{2.12}$$

where X [m] is the peak displacement of the seismic mass with respect to the outer frame.

A damping ratio that approaches zero will lead to an infinitely large displacement of the proof mass if the external vibration is fixed. In practice, the maximum displacement of the proof mass is limited by the physical dimensions and geometry of the energy harvester.

The total damping ratio ζ_T is the sum of the electric damping ratio ξ_e and the parasitic damping ratio (also referred to as the mechanical damping ratio) ξ_p, i.e. $\zeta_T = \xi_e + \xi_p$. The electric damping ratio ξ_e presents the energy transduction from the kinetic energy to electrical power. The parasitic damping ratio ξ_p presents the wasted energy during the energy transduction, for example, the energy dissipated in air resistance or mechanical friction. The maximum power extracted by the energy transduction mechanism is given by:

$$P_e = \frac{mA^2\xi_e}{4\omega_n\left(\xi_e + \xi_p\right)^2} \tag{2.13}$$

P_e [W] is maximized when the electrical damping ratio equals the parasitic damping ratio, i.e. $\xi_e = \xi_p$. In this case, P_e is given as:

$$P_e(max) = \frac{mA^2}{16\omega_n\xi_e} \tag{2.14}$$

One important parameter of resonant damped systems is the Q-factor, which is defined by:

$$\mathrm{Q} = \frac{1}{2\xi_T} \tag{2.15}$$

The Q-factor describes how under-damped a resonant system is, and is inversely proportional to the damping ratio.

The Q-factor can be expressed as the ratio of the resonant frequency f_0 to frequency bandwidth Δf, as shown in Equation (2.16). Bandwidth Δf is the frequency range with power over half of the maximum power ($P_{peak}/2$) and illustrated in Figure 2.2.

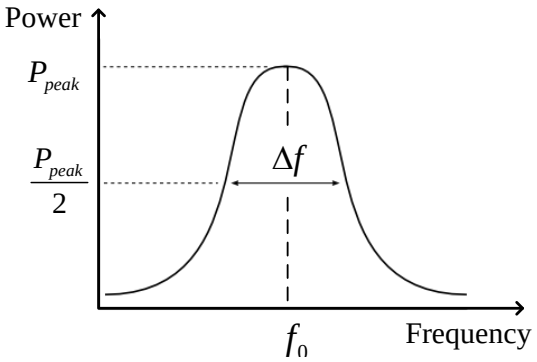

Figure 2.2 Bandwidth of a resonant system [33].

$$\mathrm{Q} = \frac{f_0}{\Delta f} \tag{2.16}$$

To illustrate the effect of the Q-factor on the bandwidth and output power of energy harvesters, Figure 2.3 shows the power output against frequency for a range of Q-factors. In this plot, the natural frequency ω_n in Equation (2.4) is fixed at 1 Hz, and the Q-factor is ranged from 50 to 500 (ξ_T: 10^{-2}-10^{-3}). Hence, the resonant frequency is very close to the natural frequency. The power output is normalised to the power at resonance with a Q-factor of 500. From Figure 2.3, it is found that the bandwidth of the system is increased as the Q-factor is reduced. In addition, the higher the Q-factor, the more sensitive the power output is to the deviation from the natural frequency. In the case of human motion, it is a combination of low frequency vibrations. Therefore, for the energy harvesting from human motion, the Q-factor should be designed to allow the energy harvester to extract energy from a wide frequency band.

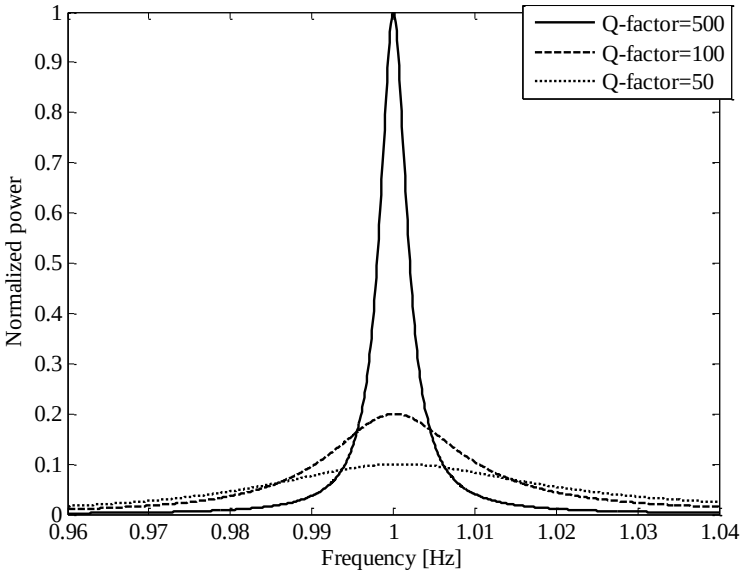

Figure 2.3 Normalised power against frequency. The natural frequency is set to 1 Hz, and the power output normalised to the power at resonance with a Q-factor of 500.

To evaluate the power obtainable from different locations on the body and other common vibration sources, this research analysed the acceleration dataset from the Energy Harvesting Network Data Repository [18]. Table 2.1 shows the peak acceleration A and the corresponding frequencies f [Hz] ($f = \omega/(2\pi)$) of various vibration sources at different locations on the body. The acceleration dataset were acquired for an 82 kg man, wearing ordinary running shoes, jogging at 6.5 km h^{-1} on a treadmill. Some common vibration sources are also listed for comparison, such as a microwave, the driver's seat in a car, a bridge, a washing machine, and a window frame approximately 8 m from a road.

Table 2.1 Potential power from human body and other common vibration sources.

	Vibration sources	A [m s^{-2}]	f [Hz]	X [mm]	$P_d(\omega_n)$ [mW]
Participant Jogging (6.5 km/h) on a treadmill	Front of chest	8.56	2.66	154	549
	Side of head	6.35	2.59	120	309
	Just above hip	8.11	2.69	142	486
	Outside of ankle	9.78	1.31	719	1450
	Outside of wrist	11.0	2.69	193	897
Other common vibration sources	Microwave	3.21	100	0.0406	2.04
	Driver seat in a car [a]	2.16	33.0	0.251	2.80
	Middle of the bridge [b]	0.0598	292	0.0000874	0.000236
	Washing machine	2.33	11.0	2.44	9.84
	Side of window [c]	0.149	192	0.000506	0.00224

[a] Logger is positioned on the cushion seat with driver sitting directly on top.
[b] Logger is positioned on the metal railing separating the road from the pedestrian walk.
[c] The side of window is approximately 8m from road.
Acceleration data from Energy Harvesting Network Data Repository [18].

In Table 2.1, the output power is estimated from the generic model of inertial energy harvesters presented in this section. The natural frequency is assumed to be the same as the vibration frequency, i.e. $\omega = \omega_n$. The proof mass and the damping ratio are set to 50 g and 0.1, respectively. Hence, based on Equation (2.11), the power obtainable from the body and different vibration sources is estimated.

In addition to the output power, the maximum displacement of proof mass, X, is evaluated. Substituting $Y = A/\omega^2$ in Equation (2.12) gives

$$X = \frac{A}{2\xi_T \omega^2} \tag{2.17}$$

Based on Equation (2.17), the peak displacement X can be calculated.

Replacing the peak acceleration A in Equation (2.11) using Equation (2.17), the maximum power is rewritten as

$$P_d(\omega_n) = mX^2\xi_T\omega_n^3 \tag{2.18}$$

Then, with a given maximum displacement of proof mass, increasing frequency would improve the output power from inertial energy harvesters.

The results of the output power and the maximum displacement of proof mass are shown in Table 2.1. It is found that the frequencies on the body (<3 Hz) are lower than those for the common vibration sources, but the peak acceleration values (>6 m s^{-2}) are greater. Consequently, the output power available from the body is much greater than that from the common vibration sources. In addition, the required maximum displacement of the proof mass for the vibration sources on the body is far greater. At the ankle, it is up to 719 mm, which is unrealistic for body-worn energy harvesters. Therefore, the human body is a promising energy source for energy harvesting, but, the large required displacement of proof mass highlights the difficulty of designing inertial energy harvesters for human motion.

2.1.2 Piezoelectric Transduction

Piezoelectric materials generate an electric field when a mechanical strain is applied, and conversely an electric field can cause the materials to undergo a mechanical strain. This property presents an attractive solution for mechanical-to-electrical energy transduction in kinetic energy harvesting devices [28, 34, 35], for example, energy harvesting from a backpack instrumented with piezoelectric shoulder straps [12]. Commonly used piezoelectric materials for inertial energy harvesting are lead ziroconate titanate (PZT) and polyvinylideneflouride (PVDF) [36-38]. PZT is a polycrystalline ceramic. It has a higher stiffness coefficient and better performance in electro-mechanical coupling efficiency when compared to the polymeric material PVDF, but PVDF has higher tensile strength and lower stiffness.

The commonly used operation modes are the mode 33 and the mode 31, as shown in Figure 2.4. The *x*, *y*, and *z* axes are labelled 1, 2, and 3. Piezoelectric material is polarized along the thickness (the 3 direction). If piezoelectric material is used in the 33 mode, it means both the voltage and the mechanical stress act in the 3 direction (Figure 2.4a); if piezoelectric material is operated in the 31 mode, it means the voltage acts in the 3 direction and the stress acts in the 1 direction (Figure 2.4b). Table 2.2 lists some reported piezoelectric generators with their main characteristics.

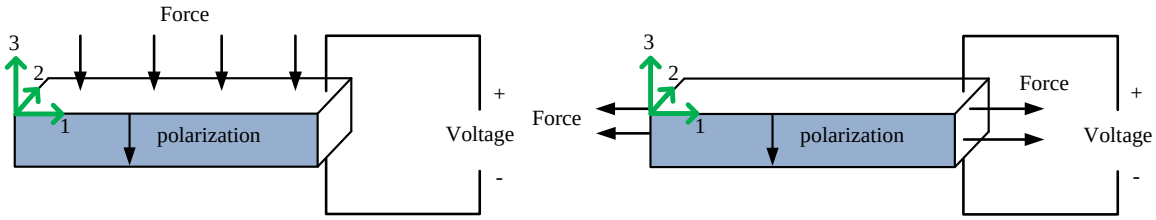

(a) (b)

Figure 2.4 Illustration of two operation modes of piezoelectric transduction. (a) Compression 33 mode caused by pressure; (b) transverse 31 mode caused by stretching.

Table 2.2 Summary of piezoelectric generators.

Reference	Frequency (Hz)	Acceleration (m s^{-2})	Mass (g)	Volume (mm^3)	Power (μW)	Power density (μW mm^{-3})	Material
Roundy *et al.* (2003) [28]	120	2.5	9.2	1,000	250	0.25	PZT
Jeon *et al.* (2005) [39]	13,900	-	-	-	1	-	PZT
Jeong *et al.* (2008) [40]	120	0.98	-	-	500	22	PMNZT
Kok *et al.* (2008) [41]	230	12.25	-	-	0.298	-	PZT
Shen *et al.* (2009) [42]	183	7.35	-	0.769	0.32	0.416	PZT
Berdy *et al.* (2012) [43]	49	1.96	4.4	4,036	118	0.0292	PZT

2.1.3 Electrostatic Transduction

The change in voltage or charge on parallel plate capacitors can be extracted to generate electrical energy using electrostatic energy harvesters. The capacitance of a parallel plate capacitor can be defined as:

$$C = \varepsilon \frac{A_0}{d_0} = \frac{Q_0}{V} \tag{2.19}$$

where C [F] is the capacitance, ε [F m^{-1}] is the dielectric constant of the insulating material between the parallel plates, A_0 [m^2] is the plate area, d_0 [m] is the separation between two plates, Q_0 [C] is the charge stored on the plates and V [V] is the electric potential between the plates.

The electric energy stored in the capacitor, E [J], is linearly proportional to the charge Q_0 and electric potential V, as shown in Equation (2.20).

$$E = \frac{1}{2} Q_0 V \tag{2.20}$$

If the charge Q_0 is held constant, then combining Equation (2.19) and (2.20), the energy becomes

$$E = \frac{{Q_0}^2 d_0}{2\varepsilon A_0} \tag{2.21}$$

while if the voltage $V$is held constant, the energy becomes

$$E = \frac{\varepsilon A_0 V^2}{2d_0} \tag{2.22}$$

Changing the physical configuration of a parallel plate capacitor, including changing the gap between plates or the overlap area of plates, is able to cause a reaction force F [N]. The reaction force depends on whether the gap or the overlap area of the capacitor is varied and on whether the voltage or the charge is constrained. If the charge on the plates is constrained, the perpendicular force between the plates is written as

$$F = \frac{{Q_0}^2}{2\varepsilon A_0} \tag{2.23}$$

If the voltage between the plates is constrained, the perpendicular force between the plates is written as

$$F = \frac{\varepsilon A_0 V^2}{2{d_0}^2} \tag{2.24}$$

The external work done against the reaction force F leads to a change in the charge stored on the plates or a change in the voltage between the plates, and therefore energy can be harvested from the changes of these electric parameters.

Electrostatic generators can be classified into three types [44]: ‘In-plane overlap’, in which the overlap area between interdigitated fingers varies; ‘in-plane gap closing’, in which the gap between interdigitated fingers varies; ‘out-of-plane gap closing’, in which the gap between two parallel plates varies. Table 2.3 lists some reported electrostatic generators with their main characteristics.

Table 2.3 Summary of electrostatic generators.

Reference	Frequency (Hz)	Acceleration (m s^{-2})	Mass (g)	Volume (mm^3)	Power (μW)	Power density (μW mm^{-3})
Peano *et al.* (2005) [45]	911	164	-	-	5	-
Lo *et al.* (2008) [46]	50	576	54	5,000	17.98	0.000359
Daniel *et al.* (2009) [47]	1,300-1,500	127	-	-	3.5	-
Suzuki *et al.* (2010) [48]	63	19.6	-	-	1	-
Guilllemet *et al.* (2013) [49]	150	9.8	-	-	2.2	-

2.1.4 Electromagnetic Transduction

Faraday's law of electromagnetic induction states that an electric current will be induced in any closed circuit when the magnetic flux through a surface bounded by the conductor changes. This applies whether the field itself changes in strength or the conductor is moved through it. The induced voltage, also known as electromotive force (emf [V]), can be written as:

$$\text{emf} = -\frac{d\Phi}{dt} \tag{2.25}$$

where Φ [Wb] is the magnetic flux. The direction of the emf is given by Lenz's law.

In electromagnetic generators, permanent magnets are used to produce a magnetic field and coils are used as the conductor. In the simple case of a coil with N turns and length l [m] moving through a perpendicular magnetic field of constant strength, the emf across the coil is given by:

$$\text{emf} = -NlBV_s \tag{2.26}$$

where B [T] is the flux density going through the coil and V_s [m s^{-1}] is the velocity of the relative motion. It is seen that the emf is proportional to the moving velocity when the coil is moving through the magnetic field. In addition, increasing the length and the number of turns increases the emf, but increases the coil resistance. Thus more power will be wasted through the coil.

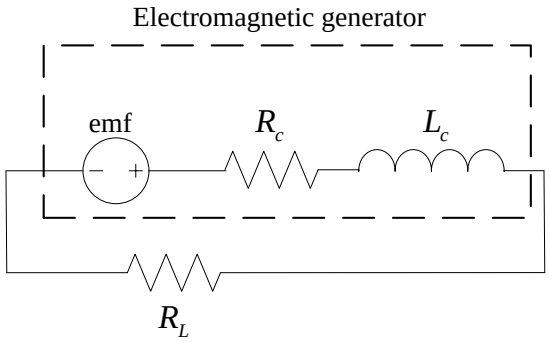

Figure 2.5 Circuit representation of an electromagnetic generator with a resistive load. (Reproduced from [50])

The circuit representation of an electromagnetic generator with a resistive load R_L is shown in Figure 2.5. The relationship between the current through the load and the induced emf is given by

$$\text{emf} + i \cdot (R_L + R_c) + L_c \frac{di}{dt} = 0 \tag{2.27}$$

where R_c [Ω] and L_c [H] are the resistance and inductance of the coil, respectively. Table 2.4lists some reported electromagnetic generators with their main characteristics.

Table 2.4 Summary of electromagnetic generators.

Reference	Frequency (Hz)	Acceleration (m s^{-2})	Mass (g)	Volume (mm^3)	Power (μW)	Power density (μW mm^{-3})
Beeby *et al.* (2007) [51]	52	0.589	0.66	150	46	0.307
Sari *et al.* (2007) [52]	3,300-3,600	430-512	-	1,400	0.5	0.000357
Yang *et al.* (2009) [53]	369	7.45	-	-	1.16	-
Zorlu *et al.* (2013) [54]	10	5.88	-	458	1.2	0.00262
Zhang *et al.* (2013) [55]	82	110	90	26,010	158,000	6.07

2.1.5 Comparison of Transduction Mechanisms

The comparison is carried out in the following aspects:

1) Separated voltage sources

Electrostatic generators can be divided into two categories: electret-free electrostatic generators

and electret-based electrostatic generators. Electret-free electrostatic generators need separate voltage sources to charge up the capacitor to an initial voltage level for the energy transduction to start. This is not an issue if the generator is used to charge a battery or other type of secondary storage components, because the necessary inertial excitation level will be available. Another solution to this issue is using electrets. Electret-based electrostatic generators use electrets to provide the initial charge, and electrets with good stability are capable of storing charge for many years. Piezoelectric and electromagnetic generators require no external voltage sources to charge up before energy harvesting.

2) Scaling down to micro scale

Piezoelectric generators are compatible with the Micro-Electro-Mechanical-System (MEMS) fabrication process; hence they can be fabricated in small volume. For example, Lee *et al.* [56] developed piezoelectric MEMS generators fabricated with PZT thin films. The device is 3000 μm × 1500 μm by 750 μm thick, and the maximum output power is 2.76 μW with 1.79 peak-to-peak output voltage at 256 Hz and 24.5 m s^{-2} acceleration.

As electrostatic generator have variable capacitor structures that are commonly used in MEMS devices, it is easy to integrate electrostatic generators with MEMS fabrication process. For example, Mitcheson *et al.* [57] and Miao *et al.* [58] designed a MEMS inertial electrostatic generator that operates in applications in which the amplitude of the external motion is larger than the maximum inertial displacement of the proof mass of the generator. The device is 20 mm × 25 mm by 1.5 mm thick. The predicted output power is 80 μW at 30 Hz and 10 m s^{-2} acceleration.

Due to the use of discrete permanent magnets, it is difficult to integrate electromagnetic energy harvesters with MEMS fabrication process, but it is able to develop electromagnetic generators in micro scale. For example, a micro electromagnetic generator has been developed in [51, 59]. The proposed 150 mm^3 electromagnetic generator is able to produce an average power of 46 μW at 0.589 m s^{-2} acceleration at a frequency of 52 Hz, and the practical peak open-circuit voltage is 1.14 V. It has been proven that electromagnetic generators perform better in macro scale than in micro scale in terms of power density (output power normalised for physical volume), since it is difficult in achieving sufficient electromagnetic coupling as electromagnetic generators reduce in size [60]. Moreover, micromachined electromagnetic generators with electroplated coils and magnets may not be able to deliver practical voltage and power levels because of the relatively poor properties of planar magnets, the restrictions on the number of planar coil turns, and the too-small vibration amplitudes.

3) Output voltage and current

Piezoelectric generators have the simplest structure among the three transducers. The transduction efficiency is strongly linked to piezoelectric properties of chosen materials. Because of the capacitive nature of piezoelectric generators, they are able to produce relatively high output voltage but at low output currents. The output impedance of piezoelectric generator is typically very high (>100 kΩ). To maximum the output power, the optimum load needs to match the high output impedance. In addition, piezoelectric materials need to be strained to generate power; hence their mechanical properties limit their overall performance and lifetime of the generators.

Electrostatic generators are characterized by a high output voltage that may reach some hundreds of volts and a low output current (some 100 nA). Hence, it is impossible to power any electronic device with such a power supply (generally <100 μW). Consequently, power management circuits are used to turn output power from electrostatic generators into viable supply sources for electronic devices. High output impedance is often obtained from electrostatic generators. In addition, electrostatic generators suffer from parasitic capacitances within the devices. The parasitic capacitances can sometimes lead to poor generator efficiencies. Moreover, the output power from electrostatic generators is tightly linked to variations of capacitance, which needs to be maximized to maximize the output power. Hence, the air gap between plates must be controlled precisely and minimized to reach high capacitances, and mechanical constraints are often needed to prevent pull-in and electrical breakdown problems.

Due to the inductive property of electromagnetic generators, relatively high output current levels are achievable at the expense of low voltage (typically <1 V). Voltage multiplier may be a suitable solution to increase the voltage level.

2.2 Human-Powered Inertial Energy Harvesting Devices

Human-powered energy harvesters can be classified into active human-powered generators and passive human-powered generators. If users are required to perform specific activities purely to excite the generator, this can be referred to as an ‘active’ human-powered generator. Examples include the flashlight powered by shaking with a hand [15], the wind-up radio powered by turning a hand crank on the case [61], and the mobile phone charged by a pedal-driven generator [62]. If power is harvested indirectly from the user’s everyday actions, and not consciously generated by the user, this can be classified as a ‘passive’ human-powered generator. Active human-powered generators are not covered in this literature review, because

inertial energy harvesters should not affect the behaviour or cause inconvenience to the user in their daily life. Furthermore, in the following paragraphs, only wearable human-powered inertial energy harvesters are discussed, while other kinds, such as implantable energy harvesters [8] and energy harvesters not located on the body, are not discussed.

The harvestable power from human motion has been simulated and evaluated in past work. For example, the available power output from walking activity was estimated by Amirtharajah and Chandrakasan [63]. Walking motion was simulated as random signals with a predominant frequency of 2 Hz, with the amplitude limited to within 2 cm. An inertial electromagnetic energy harvester with a resonant frequency of 2 Hz was simulated. The results show that the attainable average power from the energy harvester is 400 μW. Since the mechanical damping was not considered in the calculation, the output power in practice should be less than 400 μW. In this simulation, the resonant frequency of the generator matched the predominant frequency of walking. However, the maximum displacement of the proof mass was not considered in the calculation. The huge displacement corresponding to the low frequency of walking would make it not appropriable for on-body use.

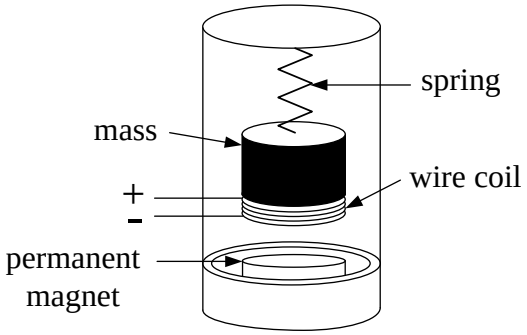

Figure 2.6 The simulated inertial electromagnetic generator. (Reproduced from [63])

A review on human-generated power by Starner and Paradiso [64] gave an overview of the energy potentially attainable from the human body. They not only included human motion, but also body heat, respiration and blood pressure. The ideal attainable power from human motion is listed in Table 2.5, showing that footfalls have the potential to generate the most power, compared to other human motion. The results highlight that human motion is a tremendous energy source for energy harvesting. However, due to the low conversion efficiency only a small fraction of the energy from human motion can be harvested.

Table 2.5 The attainable power from human motion [64].

Type of motions	Possible power
Finger motion during typing keyboards	0.76-2.1 mW
Arm motion during hand waving	0.33 W
Chest movement during breathing	0.42 W
Footfalls during walking	5.0-8.3 W

Electrostatic energy harvesters have been used for harvesting energy from human motion. For example, Naruse *et al.* [65] designed a small electrostatic energy harvester with a volume of 5cm^3 for low frequency vibrations. Power is generated while the external vibration changes the overlap area between the two parallel plates of the electrostatic energy harvester. An external vibration of 3.92 m s^{-2}, at 2 Hz, was assumed as the vibration of walking motion at the waist. As reported, the measured average power across the optimum load is 40 μW. This is less than 4% of the theoretical maximum power output mainly due to considerably mechanical damping caused by end-stop collisions. This result highlights the challenge of designing such small energy harvesters powered by human motion, as a requirement for a large proof mass displacement makes it difficult to scale the generator down in size.

Piezoelectric energy harvesters have also been used for harvesting energy from human motion. For example, Renaud *et al.* [66] demonstrated a piezoelectric energy harvester with a volume of 25 cm^3 and a weight of 60 g, as shown in Figure 2.7. The energy harvester is designed for capturing energy from limb motion in daily living. It consists of two opposing piezoelectric benders, an internal case composed of processing electronics and the application to be powered, and an object that can freely move along a guiding channel. The electrical energy is extracted through the impacts of the moving object on the piezoelectric benders. The obtainable power is 47 μW when the device is rotated by 180 °each second. Although this device is able to generate more power than the device designed by Naruse *et al.* [65], it is difficult to achieve the 47 μW power output in daily living, because providing a rotation of the device by 180 °at 1 Hz is hard to implement. In addition, the sliding direction is limited along one axis, but the direction of the limb motion is not fixed in one direction. Thus, the resulting collisions between the moving mass and the guiding channel could result in significant mechanical damping when strenuous limb movements occur.

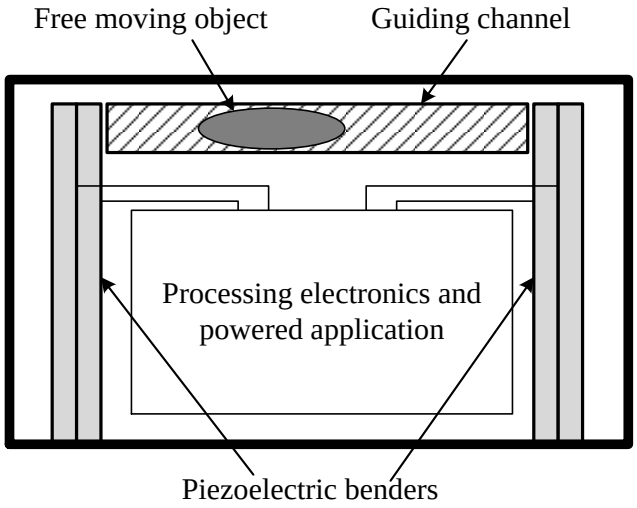

Figure 2.7 The limb motions-based piezoelectric energy harvester. (Reproduced from [66])

Electromagnetic energy harvesters have also been used for harvesting energy from human motion. For example, the first Seiko automatic generating system (AGS) was introduced in 1988, which utilizes the natural rotary motion at the wrist to power a quartz watch through an electromagnetic generator. It is reported that the AGS can produce 5 μW on average when the watch is worn, and up to 1 mW when the watch is forcibly shaken [15].

An inertial electromagnetic generators designed by Morais *et al.* [67] can be embedded in a hip prosthesis as shown in Figure 2.8. It has a volume of 4 cm^3 and weight 15 g. The device is composed of a Teflon tube, four magnets embedded in the Teflon tube and two coils wound outside the tube. The material of Teflon was chosen to reduce friction. In the experimental test, the prototype was attached to the side of a leg at hip height during walking. The generated average power across an optimum load is 1.53 mW. In this system, a small magnet works as a magnetic stop-end to prevent physical collision between the moving magnets and the Teflon tube.

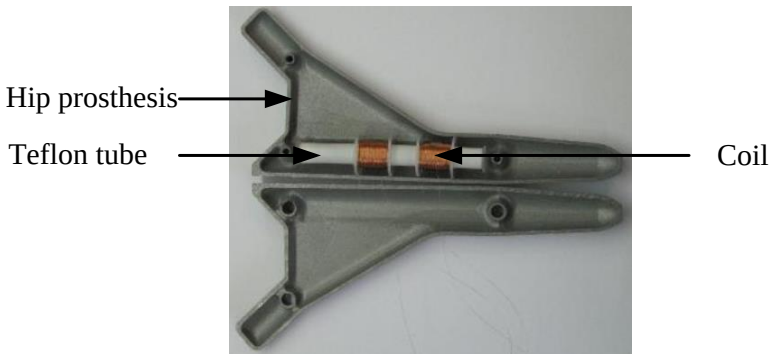

Figure 2.8 The hip motion-based electromagnetic energy harvester. (Reproduced from [67])

Büren *et al.* [17] designed a human motion-based inertial electromagnetic energy harvester with a resonant frequency of 18.5 Hz, volume 30 cm^3, and mass 43 g. Figure 2.9 shows the basic structure of the energy harvester. The translator consists of several axially magnetized disc-shaped magnets separated by soft-magnetic spacers. This device uses four flexible notch hinges to decrease spring stiffness of the cantilevers, and thus decrease the resonant frequency of the energy harvester. The generator was tested at different locations on the body while walking on a treadmill at 4 km h^{-1}. As reported, the energy harvesting device provides 5 μW if the harvester is mounted on the upper arm, while if the harvester is mounted below the knee, the output power is around four times greater, i.e. 22 μW. This device highlights a novel way to achieve compactness and low resonant frequency at the same time.

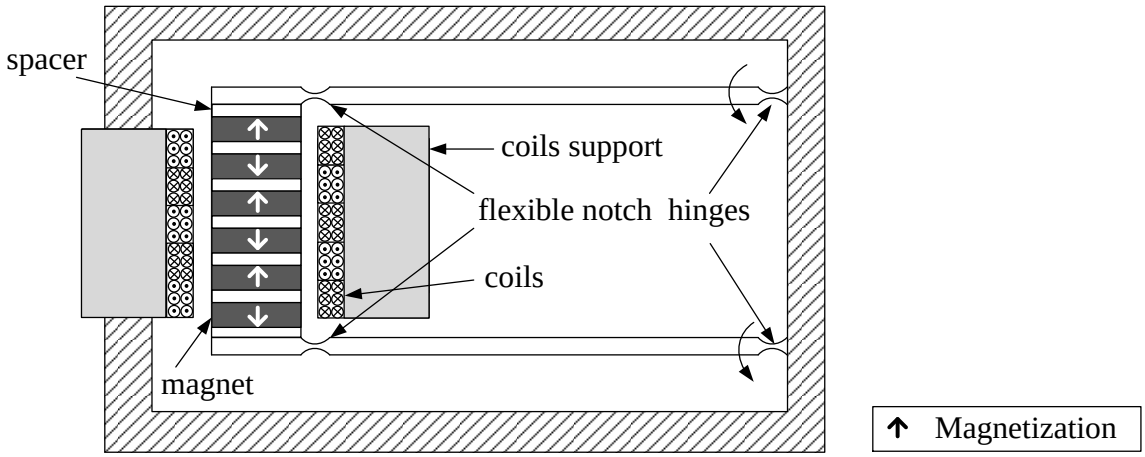

Figure 2.9 The electromagnetic generator using notch hinges to decrease the resonant frequency. (Reproduced from [17])

Bedekar *et al.* [19] reported an inertial electromagnetic energy harvesting device with a volume of 9 cm^3 integrated inside a pen, as shown in Figure 2.10. The transduction mechanical structure of this pen-harvester is based on a coil, with a moving magnet inside it. All of the components are integrated inside a pen. As reported, the pen-harvester can be used to power pulse rate sensors by locating it in the pocket near to the heart. The output power is 4 μW for walking normally, or up to 460 μW for jumping at 2 Hz. For jogging at around 3 Hz, the output power is 660 μW.

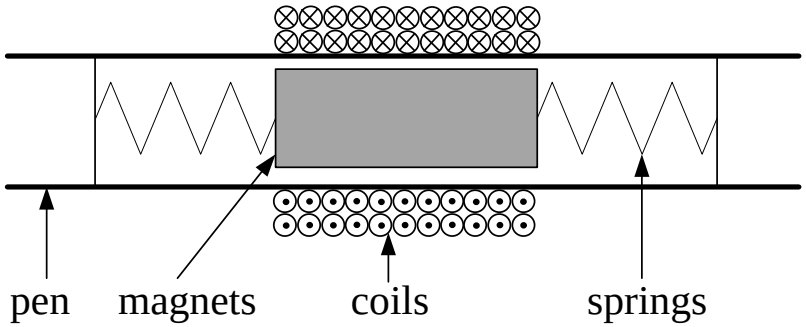

Figure 2.10 The inertial electromagnetic generator capsulated in a pen. (Reproduced from [19])

Rome *et al.* [16] made use of a DC brushless motor to work as an energy generator in a backpack. Electrical energy is extracted from the vertical motion of the load during normal walking by a DC brushless motor, as described in Figure 2.11. Experimental results demonstrated that when a participant walked at a speed of 6.4 km h^{-1} and carried a 38 kg load in the 5.6 kg backpack, the average electric power generated from the vertical movement of backpack was up to 7.4 W. A downside of this type of harvester is that extra metabolic energy is required during the electricity generation. It has been found that the motion of the pack increased the energy expended by 19.1 W or about a 3.2% increase over the energy expelled without the harvesting device [68]. In addition, the heavier the load and the faster the walking speed, the greater the energy generated from the backpack energy harvesting device will be. Hence, this kind of vibration-based energy harvesting devices is not suitable for users in daily life. Nevertheless, it is an appealing possibility for energy harvesting for hikers and soldiers during outdoor activities, since the average weight of soldiers' load is 40 kg during summer months [69].

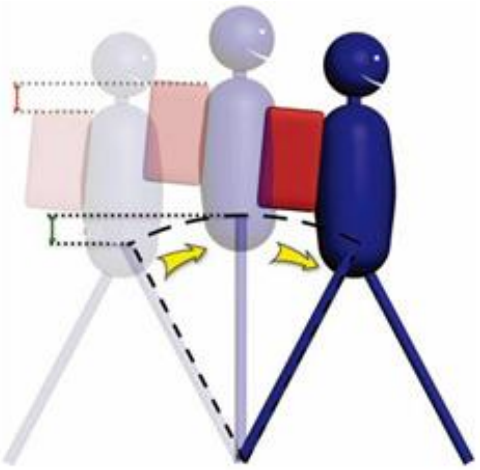

Figure 2.11 An electromagnetic energy harvester in a backpack. (Reproduced from [16]).

Table 2.6 Comparison on energy harvesting devices.
(PZ: piezoelectric; ES: electrostatic; EM: electromagnetic)

Type	Reference	Locations	Weight [g]	Volume [cm^3]	Excitation	Output Power [μW]
ES	Naruse *et al.* [65]	Waist	-- [a]	5	3.92 m s^{-2} at 2 Hz [b]	40
PZ	Renaud *et al.* [66]	Limbs	60	25	1 Hz shaking	47
EM	Seiko AGS watch [15]	Wrist	150	18	Natural movements	5
EM	Morais *et al.* [67]	Hip	15	4	Normally walking	1,530
EM	Büren *et al.* [17]	Knee	43	30	Walking at 4 km/h	22
EM	Bedekar *et al.* [19]	Chest	100 [c]	9	Normally walking	4
EM	Rome *et al.* [16]	Back	44,000	backpack	6.4 km h^{-1} Walking	7,400,000

[a] Not given in the reference.
[b] Generated by a shaker.
[c] Extrapolated from data in the reference.

Based on the review of body-worn inertial energy harvesters, it is evident that a small and lightweight device is desirable to reduce inconvenience to users during energy harvesting. Table 2.6 shows a summary of the specifications of the human-powered inertial energy harvesters described above, all of which are less than 30cm^3 in volume and 150g in weight, except for the backpack energy harvester. In addition, the magnets and coils in the mechanical structure of electromagnetic energy harvesting devices are essential and difficult to fabricate into a miniature volume. Furthermore, the proof mass of all above generators, except the Seiko AGS watch, is moving only along one axis, i.e. they are all 1-DOF generators. The vibration of human motion can be resolved as components along three orthogonal axes and each axis has a comparative acceleration magnitude (shown in Figure 1.2). Therefore, 1-DOF generators, which are efficient along one axis, cannot harvest all kinetic energy from human motion. Moreover, if the motion of the proof mass is not along the oscillation of the generator, physical collisions will occur, and thus unwanted mechanical damping will be introduced. This is evident from Büren *et al.* [17] discussing the mechanical damping caused by unwanted lateral motion of the translator (shown in Figure 2.9).

Human motion is characterized by large displacements (several mm or cm) and low frequencies. In the design of body-worn inertial energy harvesters, a major challenge is the large displacement of the proof mass when excited by human motion, which is highlighted by the energy harvesters reviewed above. In Naruse *et al.*'s structure [65], the large displacement of the proof mass at the waist during walking results in the collision between the moving mass and the housing, introducing mechanical damping. Seiko's AGS watches make use of the rotating movement of the proof mass to overcome the problem of large displacement [15]. Instead of avoiding the collision, Renaud *et al.* made use of it to generate energy using piezoelectric

materials [66]. Another way to avoid such collisions is adding magnetic stop-ends in electromagnetic generators; the repelling magnetic force between the end-stop magnet and the moving magnet can be used to prevent the physical collision, as shown in the work done by Morais *et al.* [67].

The large displacement of the proof mass in human-powered inertial generators results in an increase in physical volume and weight of the generators. The maximum potential volume and weight greatly depend on the mounting locations on the body. The mounting location should be where people are willing to wear such a device, and the designed body-worn energy harvester should not affect the way people do their activities of daily living. For example, in Yun *et al.* [24], 2 g/4.2 cm, 36 g/10 cm, and 100 g/20 cm (the poof mass / the maximum displacement of the proof mass) were considered to be suitable for body-worn energy harvesters incorporated into a wristwatch on the wrist, a cell phone on the hip, and a shoe, respectively. For some locations on the body, for example the knee, the allowed volume and weight can be comparatively big and heavy. For example, a knee-joint piezoelectric generator with 226 cm^3 volume and approximate 235 g weight was designed by Pozzi *et al.* [70]. The generator relies on the plucking technique to achieve frequency up-conversion. Donelan *et al.* [71] designed a human-powered energy harvester which is mounted on a customized orthopaedic knee brace, and the total mass of the device is 1.6 kg. The generator selectively harvests energy at the end of the swing phase during walking, thus assisting deceleration of the joint which minimises the extra user effort during energy harvesting.

None of the energy harvesters described above match the low frequency of human motion (<10 Hz). This is because the manufacturing of energy harvesters with low resonant frequencies is very hard. For example, the quiescent position of the seismic mass limits the design of the inertial energy harvester. The smaller the resonant frequency, the larger the quiescent position will be (shown in Equation (2.9)), and thus the larger physical size of the generator that is required potentially. This is made evident by Morais *et al.* [67] discussing the difficulty in manufacturing a low-frequency spring suitable for body-worn energy harvesters.

2.3 Design Considerations for Human-Powered Energy Harvesting

Designing energy harvesters for low frequencies and extracting the full amount of energy from human motion is a problem, as discussed in previous sections. Most existing devices harvest energy from high frequencies and only along a single axis. In this section, methods to address some of these challenges are reviewed, including energy harvesting using 2-DOF devices and

techniques for obtaining energy from low frequencies.

2.3.1 Energy Harvesting using 2-DOF Devices

2-DOF energy harvesters are able to harvest energy from two different axes. However, in some existing studies, energy harvesters that comprise two freely moving parts, but have both aligned in the same axis are also considered as 2-DOF devices [72, 73]. For example, a piezoelectric energy harvester that consists of a proof mass and two cantilevers has been proposed by Kim *et al.* [72]. Two piezoelectric sheets are attached to each cantilever and the proof mass is connected to the ends of the two cantilevers, as shown in Figure 2.12. To guarantee rotational compliance, two ball bearings are placed between the proof mass and the cantilevers. In addition, Wu *et al.* [73] designed a piezoelectric energy harvester that comprises one main cantilever beam and one secondary cantilever beam cut out within the main beam, as shown in Figure 2.13. These structures are efficient only along one axis, and not able to harvest the full amount of energy from human motion. In this thesis, only 2-DOF energy harvesters that vibrate along two orthogonal axes are studied, as shown in Figure 2.14. They can be modelled as two orthogonal 1-DOF energy harvesters.

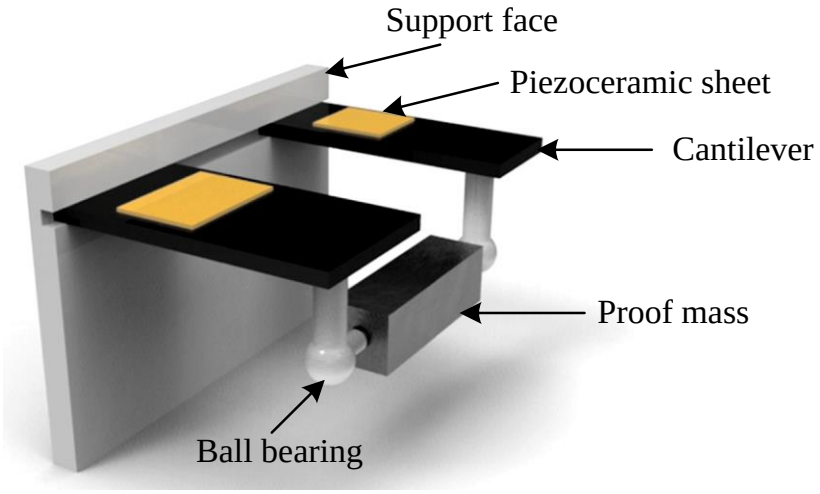

Figure 2.12 Simplified mechanical model of a piezoelectric energy harvester that consists of two cantilevers and one proof mass. (Reproduced from [72])

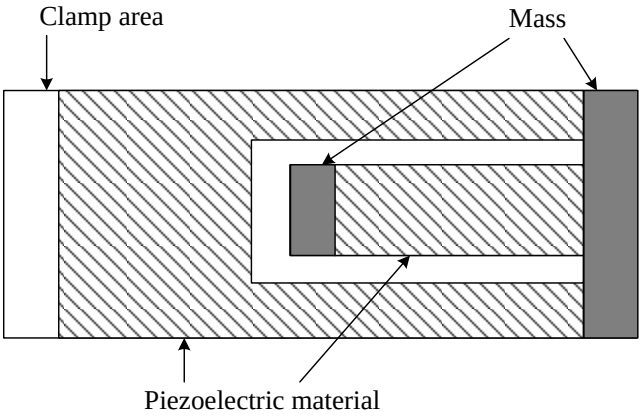

Figure 2.13 Schematic of a piezoelectric energy harvester that vibrates along one axis with two freely moving masses. (Reproduced from [73])

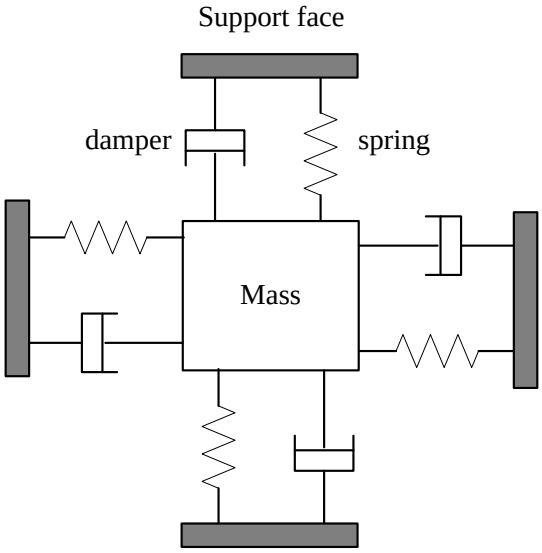

Figure 2.14 Schematic of a 2-DOF energy harvester that vibrates along two orthogonal axes.

To illustrate the benefits of 2-DOF energy harvesters over 1-DOF energy harvesters, the output power from 1-DOF and 2-DOF energy harvesters excited by vibrations with random direction in a plane has been studied. In this study, two identical 1-DOF energy harvesters are orthogonally oriented in a plane. If the oscillation direction of a 1-DOF energy harvester and the external source of vibration intercept an angle φ [degrees], only the projection of the external vibration onto the oscillation direction will excite the harvester. Therefore, the projected vibrations along the oscillation directions of the two 1-DOF energy harvesters are expressed as

$$A_1 = A_{exc}\cos(\varphi) \tag{2.28}$$

$$A_2 = A_{exc}\sin(\varphi) \tag{2.29}$$

where A_{exc} [m s^{-2}] is the magnitude of the acceleration of the external vibration and $A_{1,2}$ [m s^{-2}] is the magnitude of the acceleration of the projected vibrations.

Substituting Equation (2.28) and (2.29) in Equation (2.11) gives

$$P_{d_1} = \frac{mA_{exc}^2 \cos(\varphi)^2}{4\omega_n \xi_T} \tag{2.30}$$

$$P_{d_2} = \frac{mA_{exc}^2 \sin(\varphi)^2}{4\omega_n \xi_T} \tag{2.31}$$

where $P_{d_{1,2}}$ is the output power from the two 1-DOF energy harvesters.

In the case where the external vibration source acts in random directions, the harvested energy has to be averaged over the relevant directions. As shown in Equation (2.32) and (2.33), $\cos(\varphi)^2$ and $\sin(\varphi)^2$ both average to 1/2, therefore, 1-DOF energy harvester generates half of the energy per cycle that it would have generated if it were able to always follow the excitation direction.

$$\overline{P_{d_1}} = \frac{1}{2\pi}\int_0^{2\pi} \frac{mA_{exc}^2 \cos(\varphi)^2}{4\omega_n \xi_T} = \frac{1}{2} \cdot \frac{mA_{exc}^2}{4\omega_n \xi_T} \tag{2.32}$$

$$\overline{P_{d_2}} = \frac{1}{2\pi}\int_0^{2\pi} \frac{mA_{exc}^2 \sin(\varphi)^2}{4\omega_n \xi_T} = \frac{1}{2} \cdot \frac{mA_{exc}^2}{4\omega_n \xi_T} \tag{2.33}$$

where $\overline{P_{d_{1,2}}}$ is the average output power from the two 1-DOF energy harvesters.

The two orthogonal 1-DOF energy harvesters are considered as a 2-DOF energy harvester. Therefore, the output power from the 2-DOF energy harvester is the sum of the output power from the two 1-DOF energy harvesters. Consequently, the 2-DOF energy harvester generates twice as much average power as the 1-DOF energy harvester, when both are excited by external vibrations with random directions in a plane. The output power in Equation (2.30) and (2.31) is normalised to the maximum power. The results of normalised power at different angles φ are illustrated in Figure 2.15. The normalised powers for P_{d_1} and P_{d_2} are shown in green and blue lines, respectively. The black line shows the normalised output power from the 2-DOF energy harvester.

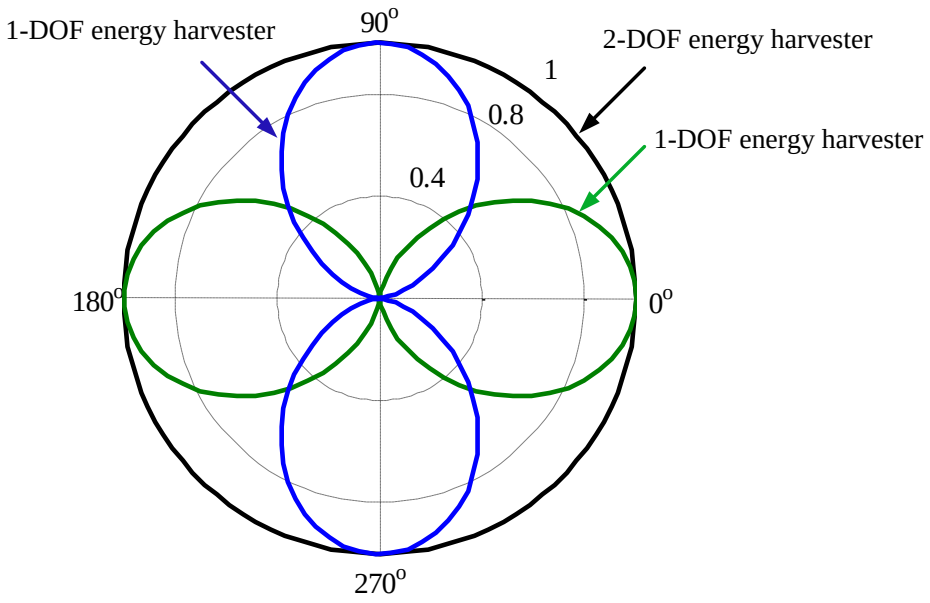

Figure 2.15 Normalised output power from the 1-DOF and 2-DOF energy harvesters.

Bartsch *et al.* [74] reported a 2-DOF in-plane resonator for kinetic energy harvesting, as shown in Figure 2.16. The disk-shaped resonator has a resonant frequency of close to 370 Hz. The physical dimensions of this 2-DOF resonator (diameter: 4 mm, height: 525 μm) are suitable for on-body use, but the resonant frequency is too high for harvesting energy from human motion.

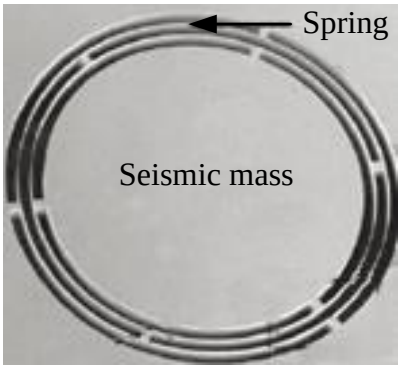

Figure 2.16 Micrograph of the fabricated 2-DOF resonator. (Adapted from [74])

2-DOF energy harvesters have been developed. For example, Zhu *et al.* [75] designed a 2-DOF energy harvester with square-shaped proof mass, as shown in Figure 2.17. In this structure, the four frames on the sides of the central mass consist of narrow electrostatic gaps. Ultrasonic sources induced an in-plane vibration. The ultrasonic transducer was actuated by 10 V_{pp}, 38 kHz ac voltage. This vibration was converted into electrical energy through the four electrostatic frames. The 2-DOF energy harvester can extract ultrasonic energy from all directions in the plane, broadening the bandwidth of the operational frequency. The MEMS technique was used to fabricate the generator. The physical dimension of this 2-DOF resonator (length: 1 mm, width:

1 mm, thickness: 25 μm) is suitable for on-body use, but the resonant frequencies along the two orthogonal axes (both 38 kHz) are both much higher than the frequencies of human motion. If the ultrasonic transducer is 0.5 cm away from the generator, 21 nW energy can be generated. In addition, Andò *et al.* [76] proposed a 2-DOF piezoelectric energy harvester with two orthogonal cantilevers, as shown in Figure 2.18. One cantilever is on the XZ plane and the other is on the XY plane. A maximum power of 3.2 μW (rms) has been detected for each beam with optimal load of 330 kΩ at an external vibration of 9 '*g*' (rms). The reported energy harvester is able to extract energy from ambient vibrations with arbitrary directions.

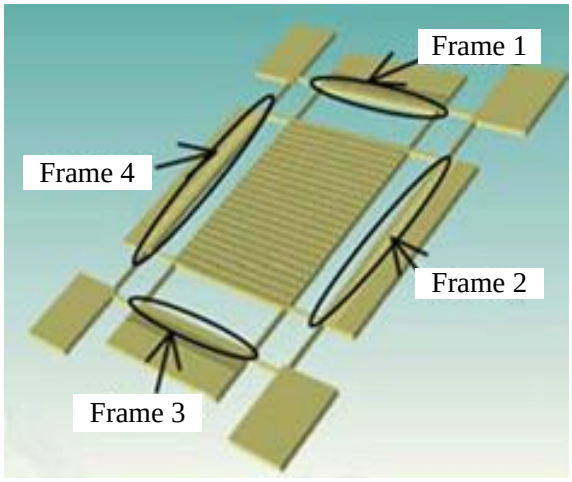

Figure 2.17 Schematic of the 2-DOF energy harvester with four electrostatic frames on the sides. (Adapted from [75])

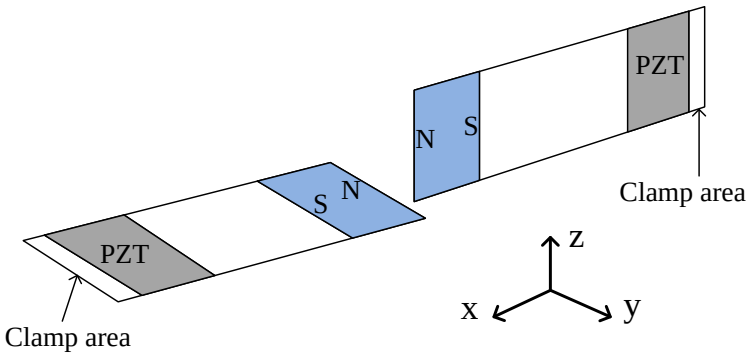

Figure 2.18 Schematic of the 2-DOF energy harvester with two orthogonal cantilevers. (Adapted from [76])

2.3.2 Technique to Obtain Energy from Low Frequencies

To improve the harvested power from human motion, specific methods have been developed to harvest energy from low frequencies. In this section, these methods are reviewed.

1) Frequency Up-Conversion

With a given maximum displacement of proof mass, increasing the vibration frequency would improve the output voltage from inertial energy harvesters (shown in Equation (2.18)). To increase the power output under low frequency vibrations, frequency up-conversion mechanisms have been developed. Ashraf *et al.* overviewed the frequency up-conversion techniques in [77]. An energy harvester with a high resonant frequency is excited by low frequency vibrations through, for example, magnetic force [78] or mechanical impact [79-81]. In one example, Sari *et al.* [78] proposed an electromagnetic generator to convert low frequency environmental vibrations to a higher frequency by using the frequency up-conversion technique. It is composed of a magnetic diaphragm with a low resonant frequency of 113 Hz and 20 serially connected resonating cantilevers with a high resonant frequency of 2 kHz, as shown in Figure 2.19. When the magnetic diaphragm is excited and moving up and down, at a certain point of its movement, it catches the cantilever and pulls the cantilever up. After the cantilever is released, it resonates at its relatively high natural frequency. In this device, the diaphragm beams still needs to be resonated at low frequencies.

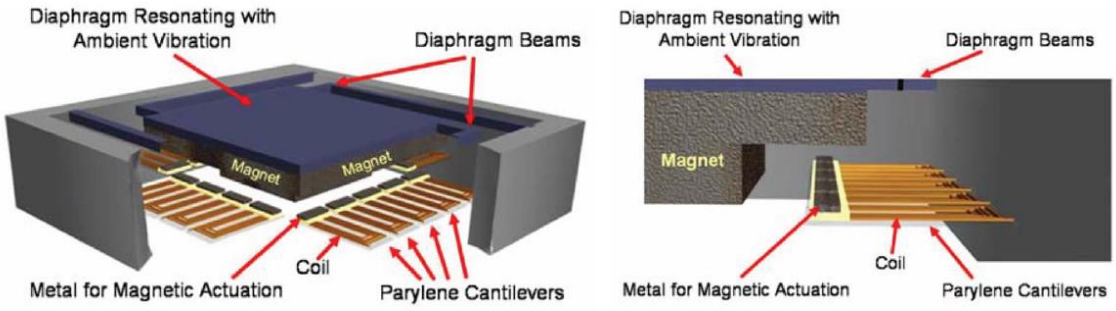

Figure 2.19 Illustration of the frequency up-conversion system. (Reproduced from [78]).

Pozzi *et al.* [79] recently reported a knee joint piezoelectric energy harvester which up-converts the low frequency of the knee's motion to a higher frequency. As shown in Figure 2.20, the stator (red) and the rotor (green) are fixed on the knee joint. In bending or extending, the knee rotates the rotor, and then the plectra on the inner ring pluck the piezoelectric (PZT) bimorphs. In this way, the low frequency of knee's movement is converted to the high frequency of vibration of the bimorph. It is noticed that four bimorphs are excited by the plectra simultaneously to maximize the output power. It is reported that if the plucking actions occur every 5 ms to 10 ms, average power ranging from 5 mW to 7 mW can be achieved. This device uses the direct force from the knee to excite the PZT bimorphs. In terms of the output power, the knee-mounted electromagnetic device developed by Donelan *et al.* [71] is able to generate much greater power of 4.8 W in the generative-braking mode during walking on a treadmill at

1.5 m s^{-1}. Donelan *et al.*'s device is designed to generate electricity during the braking phase of walking with minimal user effort. The weight of Donelan *et al.*'s device is 1.6 kg, which is 6.8 times heavier than Pozzi *et al.*'s device (235 g) [79].

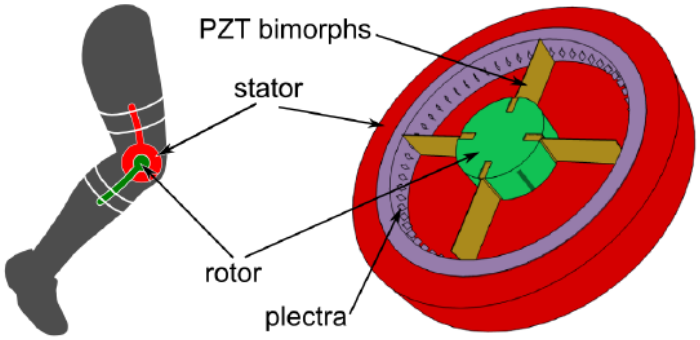

Figure 2.20 Schematic of the knee joint piezoelectric harvester. The stator (red) and the rotor (green) are fixed on the knee joint. Electrical energy is generated from the PZT bimorphs (yellow). (Reproduced from [79]).

Zorlu *et al.* [80] proposed a mechanical frequency up-conversion mechanism for harvesting energy from external low frequency vibrations. The structure consists of two cantilevers whose tips are overlapping. A low frequency cantilever actuates the high frequency cantilever through the barrier arm of the low frequency cantilever. A magnet placed on the low frequency cantilever as proof mass, and a coil placed on the high frequency cantilever. Electrical energy is harvested by relative motion of the coil and the magnet. Gu *et al.* [81] designed a piezoelectric energy harvester based on impact driven frequency up-conversion mechanism. Frequency up-concretion has been achieved by mechanical impact of a proof mass placed on a low frequency cantilever with a high frequency piezoelectric cantilever. A comparison of frequency up-conversion based energy harvesters has been shown in Table 2.7.

Table 2.7 Comparison of frequency up-conversion based energy harvesters.

Reference	Dimension	Frequency	Acceleration	Power
Sari *et al.* (2010) [78]	148 mm^3	95 Hz	-	5.0 nW (max)
Pozzi *et al.* (2011) [79]	238,000 mm^3	100 Hz plucking	-	7.0 mW (average)
Zorlu *et al.* (2009) [80]	2.96 cm^3	10 Hz	-	69 μW (rms)
Gu *et al.* (2011) [81]	-	8.2 Hz	0.4 '*g*'	0.43 mW (average)

The frequency up-conversion technique appears to be a promising way to increase the power output from low frequency vibrations. The output power is generated from energy harvesters resonated at high frequencies. However, this thesis is studying the factors affecting the harvested power from human motion. Only energy from inertial energy harvesters resonated at

low frequencies of human motion is studied in this thesis.

2) Decreasing Resonant Frequencies

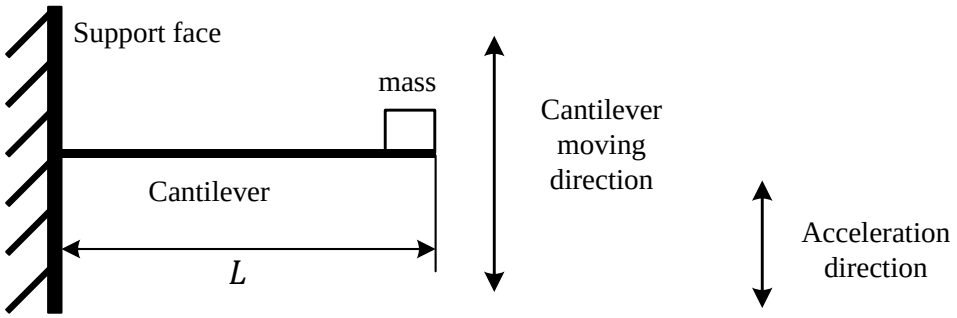

Figure 2.21 A straight cantilever with a mass at the free end.

Maximum output power from inertial energy harvesters can be achieved when the resonant frequency of the generator matches the low-frequency vibration of human motion. Based on Equation (2.6), decreasing the spring stiffness and increasing the proof mass will reduce the resonant frequency of inertial energy harvesters. In the case of cantilever structures, shown in Figure 2.21, one side of the cantilever is fixed and the other side is attached with an end load, the equivalent mass of the cantilever, m_{eq} [kg], is defined as [82]:

$$m_{eq} = M + 0.23m_0 \tag{2.34}$$

where M [kg] is the end mass and m_0 [kg] is the mass of the cantilever. The equivalent spring stiffness of the cantilever is defined as [82]:

$$k_{eq} = \frac{3E_0 I}{L^3} \tag{2.35}$$

where E_0 [Pa] is Young's modulus, I [kg·m^2] is the moment of inertia of the cross section of the cantilever, and L [m] is the length of the cantilever. The moment of inertia of the cross section can be expressed as

$$I = \frac{wh^3}{12} \tag{2.36}$$

where w [m] and h [m] are the width and the thickness of the cross section of the cantilever, respectively. Hence, the moment of inertia of the cross section is proportional to h^3. From Equation (2.35), the stiffness of the cantilever decreases with scaling down of the thickness.

Based on Equation (2.6), the resonant frequency of the cantilever, f_{beam} [Hz], is expressed as:

$$f_{beam} = \frac{1}{2\pi} \cdot \sqrt{\frac{3E_0 I}{(M + 0.23m_0)L^3}} \tag{2.37}$$

It is notable that the resonant frequency of the cantilever is inversely proportional to $\sqrt{L^3}$. Therefore, increasing the cantilever's length can decrease the resonant frequency of cantilever.

To increase the length of a cantilever in a limited physical volume, spiral-shaped cantilevers are a possibility. Choi *et al.* [83] proposed a spiral shape of piezoelectric beam to achieve compactness and low resonant frequency at the same time (Figure 2.22). The spiral cantilever is made of piezoelectric material and the electrical energy is scavenged through the vertical motion of the central mass to the plane of the spiral-shaped beam. Similar structures have been reported by Hu *et al.* [84] and Niu *et al.* [85].

Figure 2.22 Schematic diagram of a spiral-shaped piezoelectric beam. (Reproduced from [83]).

Magnetic springs can be used for low-frequency energy harvesting applications. Typically, a magnetic spring consists of a tube, two magnets at the end of the tube, and a magnet suspended in the middle due by the magnetic repelling force between the middle magnet and the end magnets, as shown in Figure 2.23. Saha *et al*. [86] designed a magnetic spring that is able to provide linear operation for a body-worn energy harvester with a low resonant frequency. The device, which had a resonant frequency of 8 Hz, was designed to harvest energy during walking and slow running. However, the frequency of walking and running is within 1-3 Hz [17, 87], so clearly, there is a mismatch between the resonant frequency of the magnetic-spring energy harvester and the low frequency of human motion. As reported, the 'almost linear' operation of this magnetic spring is 8mm from the quiescent position. However, this range of the linear operation needs to be increased for harvesting energy from human motion, because the maximum displacements of the proof mass are generally over 8mm if the generator is on the body (shown in Table 2.1).

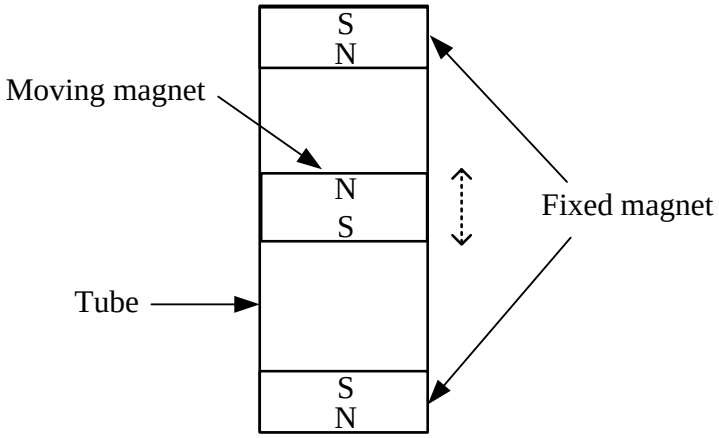

Figure 2.23 Structure of a magnetic spring.

2.4 The Effect of Location and Activity on Harvested Power

To understand what factors will affect the harvestable energy from human motion, this section reviews the existing studies investigating the harvestable energy at different locations on the body and for different activities. The results from the existing studies give an indication of the effect of location and activity on the harvestable energy.

The majority of the studies are based on the analysis of real data through experimenting on the human body [20, 24, 25, 87-90]. Some of the studies measured the triple axis acceleration data [24, 25, 88-90], while others measured the actual power output from body-worn energy harvesters [20, 87]. In some of the studies, participants were performing walking or running on a treadmill [25, 87]; in others, measurements were taken while participants were performing their normal daily routine [24, 89, 90]; finally, in some, participants were doing specific activities of daily living, such as walking, jumping and cycling [20, 88]. Additionally, some of the studies investigated body motion for a short period of time, such as 60s [25], 35s [20] and 5s [87], while others considered ranges of several hours [89] or even days [24, 90]. Some of the studies took the measurement from single individual [20, 87, 88], while others did this from several participants [24, 25] or even 40 participants [89, 90]. The parameters used by different on-body studies are shown in Table 2.8. The test locations on the body are illustrated in Figure 2.24.

Table 2.8 The parameters used by different on-body studies.

Reference	Measured data	Sample No.	Duration	Activities	Locations No.[a]
Yun *et al.* [24]	Triple axis acceleration	8	3 days	Normal daily routine	6
Büren *et al.* [25]	Triple axis acceleration	8	60 s	Walking on a treadmill at 4 km/h	9
Yew *et al.* [88]	Triple axis acceleration	1	10 s	Normal walking	4
Yarkony *et al.* [89]	Triple axis acceleration	40	8 hours	Normal daily routine	1
Olivares *et al.* [20]	Output power	1	35 s	9 activities of daily living	4
Romero *et al.* [87]	Output power	1	5 s	Walking and running on a treadmill at a set of speeds	6

[a] Number of the test locations on the body.

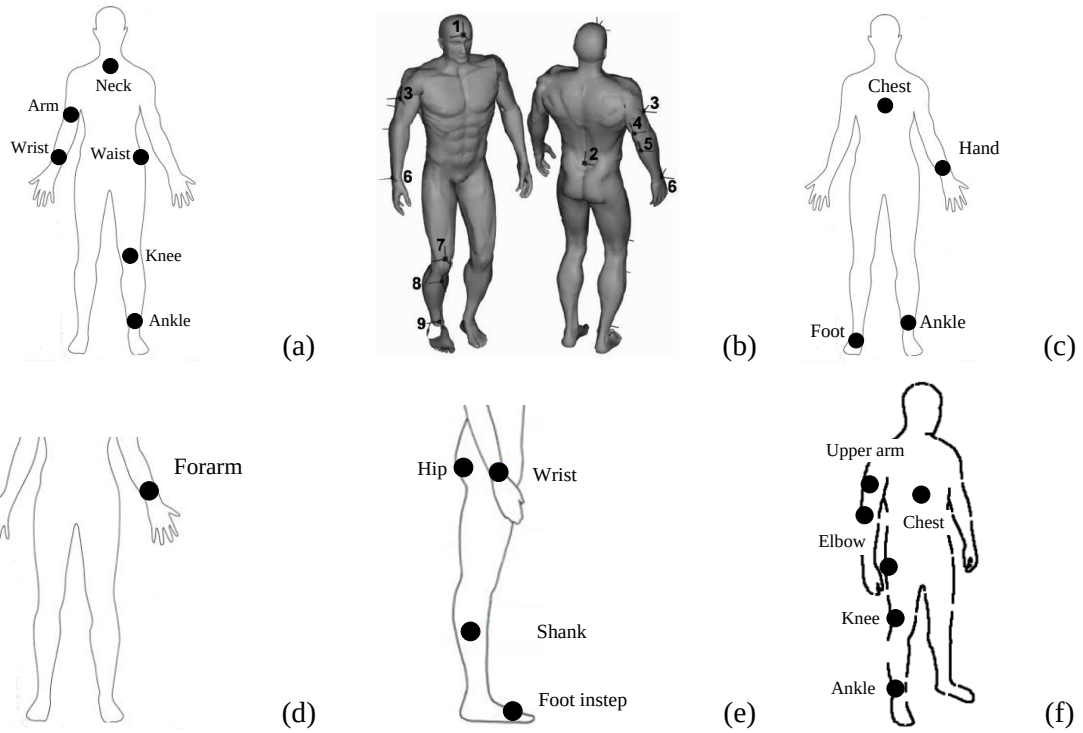

Figure 2.24 Illustration of test locations on the body. (a) Yun *et al.* [24]; (b) Büren *et al.* [25]; (c) Yew *et al.* [88]; (d) Yarkony *et al.* [89]; (e) Olivares *et al.* [20]; (f) Romero *et al.* [87].

In some of the studies, the acceleration on the body was measured, and the acceleration data were fed into the generic model of inertial energy harvesters to calculate the theoretical power in the three orthogonal Cartesian axes of the accelerometer at each test location [24, 25]. Before the power calculation, some of the studies make assumptions regarding the proof mass and the maximum displacement of the proof mass based on possible applications. For example, in Yun *et al.* [24], energy harvesters were assumed to be incorporated into electronic devices. A

wristwatch, a cell phone and a shoe-mounted device were chosen. Appropriate values were then assumed for the proof mass and the maximum displacement of the proof mass for energy harvesters inside the chosen items for evaluating the output power. The electronic devices were considered positional at various locations on the body, for example, the cell phone was expected to be suspended on a necklace around the neck, inside an arm band, or in a waist holster. Some of the studies make assumptions for comparison purposes. For example, in Büren *et al.* [25], a set of proof masses and the maximum displacements of the proof mass have been assumed before estimating the power output. The mass was set from 0.1 g to 2 g and the maximum displacement was set from 0.05 mm to 20 mm. The results of the estimated power based on the different configurations gave an indication of generator scaling effects.

Based on the estimated and measured output power from energy harvesters, conclusions on the effect of location and activity on the output power have been derived. The results show that the predominant frequency of normal daily routine and walking is approximately 1 Hz or 2 Hz [24, 25, 87-89]. Additionally, the locations on the lower body, such as the knee, ankle, and foot instep, were shown to be able to generate more power than those on the upper body, such as the waist, elbow, and wrist [20, 25, 87]. For example, in Yun *et al.* [24], the generator integrated in a shoe on the ankle was estimated to be able to generate 4.9 mW average power, while the generator integrated in a watch on the wrist just generated 29 μW average power.

In terms of activities, running and walking activities were shown to be able to generate more power over a day than the other activities, such as driving, shopping or dressing, for the generator integrated in a watch on the wrist, in a phone on the arm or in a shoe on the ankle [24]. In addition, the results from Olivares *et al.* [20] show that if the body-worn generator is mounted on the same position, during different activities, the output power can be quite different. For example, the foot instep, the intense activity running can produce 28.4 μW average power, while the less intense activity of walking produces less average power in comparison (11.5 μW). The results of power measurements from an on-body energy harvester concluded that the hip is the optimal point to place the device for human-powered energy harvesting, and that at the hip, fast running and jumping generate more energy than other activities. However, in practice, people do not spend much time fast running or jumping in daily life. In Romero *et al.*'s study [87], it was found that power output from the on-body energy harvester increases with the increase of the walking or running speed.

In Olivares *et al.* [20], the results show that the movement frequency, amplitude and impact are the factors that influence the generated power and among these three factors, the impact is the most important factor to the output power. The measured output power shows that activities

featuring impacts, such as walking, running, and jumping, are able to produce more power than activities with no impacts having the same frequency and similar amplitude, such as cycling and arm swinging.

Another key factor that affects the power output is the orientation of the piezoelectric generator. This is made evident by Olivares *et al.* [20], who discusses the mismatch between the orientation of a piezoelectric beam harvester and the predominant direction of human motion. In the worst case, if the direction of motion is parallel to the piezoelectric beam, only a small fraction of the kinetic energy from human motion can be used, which highlights the disadvantage of 1-DOF generators when used to harvest energy from human motion. In this case, 2-DOF generators are promising replacements for 1-DOF generators.

Moreover, the existing studies solely investigated the harvestable power from a single axis [20] or from the three Cartesian axes of accelerometers [24, 25, 89] at each test location. Based on these power values, the effect of the harvester's orientation on the power output has not been fully examined in the existing studies. In this thesis, the output power generated along different orientations in three-dimensional space at each test location is estimated to investigate the effect of orientation on the output power.

2.5 Conclusions

This literature review has reviewed the transduction mechanisms for converting kinetic energy to electrical energy. It has been found the human body is a promising energy source for energy harvesting, but, due to the low frequency and high amplitude of human motion, the large required displacement of proof mass makes it difficult to design inertial energy harvesters for human motion. Existing human-powered inertial energy harvesters have also been reviewed. The review has shown that all of the reviewed on-body energy harvesters are 1-DOF; hence they are not able to harvest the full amount of the kinetic energy from human motion. Moreover, none of the energy harvesters match the low frequencies of human motion, which limit the performance of the on-body inertial energy harvesters in terms of the output power.

Based on the literature around existing 2-DOF energy harvesters, it has been found that 2-DOF energy harvesters are a promising replacement for 1-DOF energy harvesters in harvesting energy from human motion. This is because a 2-DOF energy harvester is able to generate twice as much average power as a 1-DOF energy harvester, when both are excited by external vibrations with random directions in a plane. However, none of the existing 2-DOF energy harvesters have been designed for harvesting energy from human motion. For 2-DOF energy

harvesters being used to harvest energy from human motion, the benefits in terms of output power and tolerance to rotation have not been investigated in the existing studies.

In addition, the technique used to obtain energy from low frequencies has been reviewed. It has been found that the frequency up-conversion technique is a promising way to increase the output power from energy harvesters under low-frequency ambient vibrations. However, increasing the output power from human-powered energy harvesters is not an aim of this research. Energy only from inertial energy harvesters resonated at low frequencies of human motion is studied in this thesis. Therefore, the methods to decrease resonant frequencies of inertial energy harvesters have been reviewed. Using spiral-shaped beams is a promising way to increase the length of cantilever beams within a volume-limited device, and to hence decrease the resonant frequency. In addition, magnetic springs have been reviewed as a method to make a low-frequency generator. The resonant frequencies of magnetic-spring generators should match the frequency of human motion, and the range of the linear operation should be large enough for harvesting energy from human motion.

To understand what factors will affect the harvestable energy from human motion, existing studies on investigating the harvestable energy at different locations on the body and for different activities have been reviewed. The results show that the predominant frequency of normal daily routine and walking is approximately 1 Hz or 2 Hz. Locations on the lower body were shown to be able to generate more power than those on the upper body. In addition, running and walking activities were shown to be able to generate more power over a day than other activities, such as driving, shopping or dressing, for the generator integrated in a watch on the wrist, in a phone on the arm or in a shoe on the ankle. Intense activities are able to generate relatively large power output. However, existing studies only investigated the power output from a single axis or the three Cartesian axes of accelerometers. The effect of the harvester's orientation has not been fully examined in the existing studies. Olivares *et al.* [20] have highlighted the importance of orientation of their piezoelectric cantilever energy harvester on the output power. Mismatch between the orientation of the harvester and the predominant direction of human motion will decrease the output power. Therefore, it is worth investigating the effect of orientation on the output power from human-powered energy harvesters. The next chapter will evaluate harvestable power from human motion.

Chapter 3
Evaluating Harvestable Power from Human Motion

From the literature review, the existing studies on energy harvesting have considered the effects of location and activity on the output power from energy harvesters. They have not investigated the effect of orientation (i.e. the direction of oscillation of the seismic mass of the inertial energy harvester) on the output power. Additionally, all of the reported on-body energy harvesters are 1-DOF. As a promising replacement of 1-DOF energy harvesters, 2-DOF energy harvesters have the potential to harvest more energy from human motion and have a greater tolerance to rotation. However, no 2-DOF energy harvesters have as yet been developed for human motion, and the benefits of 2-DOF energy harvesters have not been investigated in the existing studies.

Therefore, this chapter presents acceleration measurements collected on the body during typical activities of daily living. This data are used to evaluate power availability from 1-DOF and 2-DOF inertial energy harvesters. Numerical methods for the power evaluation are subsequently presented. The analysis of the evaluated power including the investigation of the benefits of 2-DOF inertial energy harvesters is presented in the next chapter.

3.1 Experimental Design

In this study, acceleration on the human body was measured in order to understand the movement of human motion, after which harvestable power from the human body was evaluated. A set of representative activities and locations were selected for the study. Walking and running exercises on a treadmill were chosen, as the speed of the two activities can be well controlled and monitored. Five locations (the elbow, wrist, waist, knee and ankle) were chosen based on the reported on-body acceleration measurements in Section 2.4. Acceleration at the various locations was measured using a triple axis accelerometer from G-link [91]. Figure 3.1 shows the five data collection locations and the triple axis accelerometers used. The X, Y and Z arrows show the directions of the accelerometers' axes. The accelerometer's measurement range is ± 39.2 m s^{-2}, i.e. ± 4'g' [m s^{-2}] with an accuracy of 0.01'g' [m s^{-2}]. The accelerometer is $58 \times 43 \times 21$ mm^3 with a weight of 40g. In the study, participants reported that the accelerometers did not significantly affect the way they walked and ran. Ethical approval for the study was obtained from the University's Electronics and Computer Science ethics committee under application N/10/10/002.

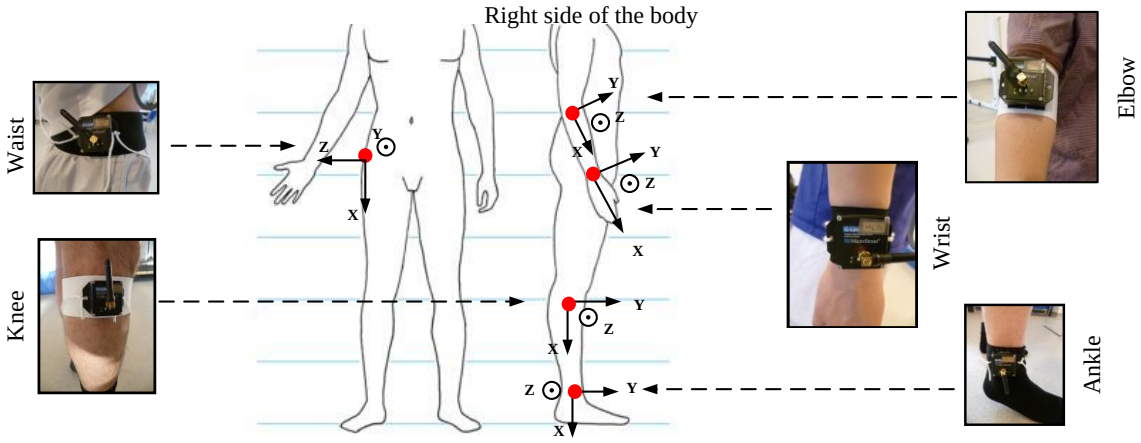

Figure 3.1 Five data collection locations, showing the directions of the accelerometers' axes.

For the measurements, the five data collection locations are (indicating precise locations for repeatability between subjects):

1) Elbow: on the lateral aspect of lower arm and slightly below the elbow, ideally located along the length of the ulna and radius toward the location of the elbow;

2) Wrist: on the dorsal surface of the wrist, where a wristwatch is usually worn;

3) Knee: on the lateral aspect of lower leg and slightly below the knee, ideally above the top of the tibia;

4) Ankle: on the lateral aspect of lower leg and above the ankle;

5) Waist: on hip, ideally located above the top of femur.

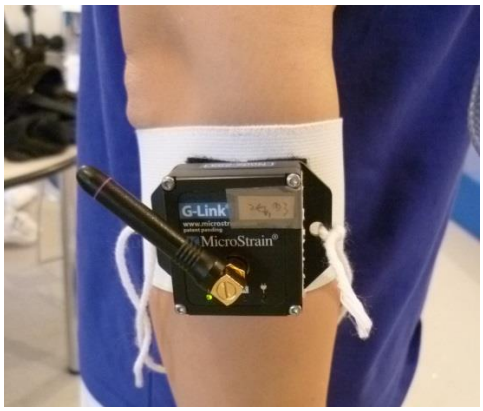

Figure 3.2 The accelerometer G-link mounted on the elbow using an elastic band.

In this study, participants were asked to wear 'instrumented bands' which comprise a band of elastic with a triple axis accelerometer held on by Velcro, as shown in Figure 3.2. The elastic bands were tightly fastened to body using Velcro ends to ensure that the accelerometer closely

follows motions of the body. A piece of ribbon was used to loosely fasten the accelerometer to the body to prevent it from causing damage in case the Velcro fails during the measurements.

Data were collected from 23 participants (17 male and six female, age: 26 ± 2.8 years, height: 173 ± 8.9 cm (mean ± standard deviation (STD)) wearing triple axis accelerometers sampling at 128 Hz. Participants were wearing socks without shoes during the measurements. As natural walking and running speeds vary among different participants, a fixed walking or running speed was not pre-set on the treadmill. Instead, in the study, at first, each participant set the treadmill to run at a speed he/she felt comfortable walking and running at, and this speed was recorded. After that, the participant was asked to maintain this speed during the test with the aid of a metronome. During the measurements, participants were asked to walk and run for 30 seconds while the acceleration data were locally saved in the G-link memory (Figure 3.3). When the participant finished all exercises, the acceleration data were wirelessly downloaded from the G-link and saved on a computer with the aid of a G-link USB base station. In total, 230 acceleration waveforms of 30 seconds length were recorded.

Figure 3.3 A participant walking on a treadmill, with accelerometers mounted on the knee and ankle.

To explore whether or not there are correlations between the human physical parameters and the walking or running frequency, the lengths of limbs and legs including upper arms, forearms, upper legs and lower legs were measured for each participant. The step rate (how many steps

the participants took per minute) was recorded to calculate the step frequency of walking and running. The resonant frequency of on-body energy harvesters should match the frequency of ambient vibration to achieve the maximum power output. Hence, the step frequency of walking and running are an important indicator in the design of the resonant frequency. If such correlations between the human physical parameters and the step frequency exist, the human physical parameters will affect the design of the energy harvesters.

The values of the age, gender, height, arm length, leg length, speed and step-frequency of the participants were listed in Table 3.1. The step frequencies of walking and running were 1.8 ± 0.16 Hz (mean ± STD) and 2.7 ± 0.22 Hz, respectively, which highlights the low frequencies of human motion. The small STD (both below 10% of the mean) indicate that the participants have similar step frequencies while doing the same activity.

The expected correlations would be between the human physical measured parameters and the step frequency. However, from Table 3.1, it is found that there is little correlation between them. For example, Figure 3.4a shows the step frequency against the height during walking and running. Running speed generally has a relatively higher step frequency, compared to walking speed, as shown in Figure 3.4b. Speed is a representative parameter of walking and running. Therefore, this correlation between the speed and the step frequency highlights the necessity to analysis the human-powered energy harvesters for walking and running, separately.

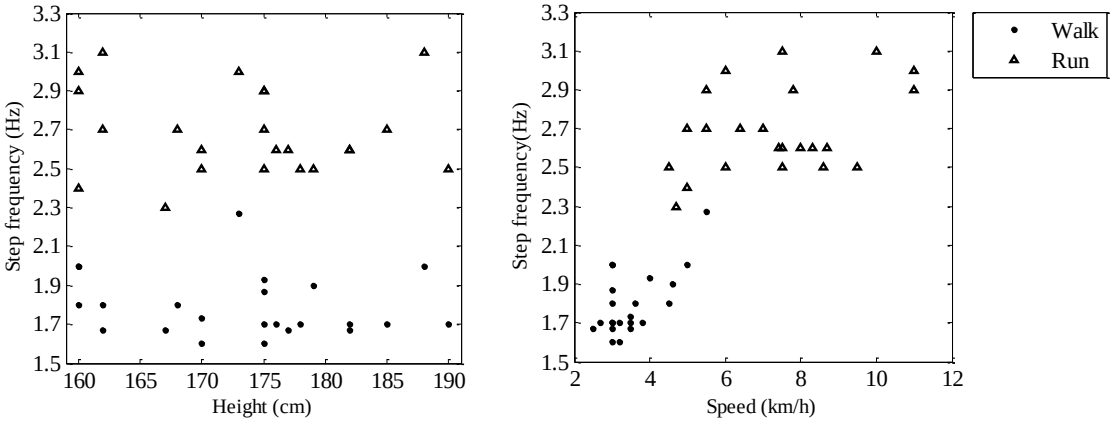

(a) (b)

Figure 3.4 (a) Step frequency vs. hight and (b) step frequency vs. speed while walking and running.

Table 3.1 Participant details recorded in the on-body acceleration measurement.

ID	Age [years]	Gender	Height [cm]	Length [cm]				Speed [km/h]		Step frequency [Hz]	
				Upper arm	Forearm	Upper leg	Lower leg	Walk	Run	Walk	Run
1	31	M	177	28	28	51	45	3.5	7.5	1.7	2.6
2	30	M	182	27	27	51	43	3.0	8.3	1.7	2.6
3	27	M	170	27	25	48	39	3.0	8.7	1.6	2.6
4	26	F	160	25	24	46	38	3.0	5.0	1.8	2.4
5	25	M	175	27	26	48	40	3.0	5.0	1.9	2.7
6	25	M	175	28	26	50	42	4.0	11	1.9	2.9
7	21	M	162	26	25	46	38	3.6	10	1.8	3.1
8	28	M	170	26	25	49	40	3.5	9.5	1.7	2.5
9	27	M	175	27	26	51	42	3.2	7.8	1.6	2.9
10	27	M	173	25	24	48	40	5.5	11	2.3	3.0
11	25	F	160	24	23	46	37	3.0	6.0	2.0	3.0
12	24	F	162	23	22	45	39	2.5	5.5	1.7	2.7
13	25	F	167	26	24	48	39	2.5	4.7	1.7	2.3
14	28	M	179	29	28	50	43	4.6	8.6	1.9	2.5
15	24	M	175	27	25	47	41	3.5	6.0	1.7	2.5
16	28	M	182	27	27	51	43	3.2	7.4	1.7	2.6
17	33	M	185	30	29	53	46	3.0	6.4	1.7	2.7
18	24	M	176	28	27	47	42	3.8	8.0	1.7	2.6
19	24	M	190	31	30	55	46	2.7	4.5	1.7	2.5
20	23	F	160	25	24	45	36	3.0	5.5	2.0	2.9
21	24	F	168	28	25	48	39	4.5	7.0	1.8	2.7
22	25	M	178	30	28	50	43	3.0	7.5	1.7	2.5
23	24	M	188	30	30	50	44	5.0	7.5	2.0	3.1
Mean	26		173	27	26	49	41	3.5	7.3	1.8	2.7
STD	2.8		8.9	2.0	2.2	2.6	2.8	0.79	1.92	0.16	0.22

3.2 Processing Methods to Evaluate Harvestable Power

In this research, acceleration data processing methods for evaluating power availability from 1-DOF and 2-DOF inertial energy harvesters were designed. The flowchart in Figure 3.5 shows the power estimation procedure. The harvestable power is calculated using the measured acceleration dataset from each participant at each location during each activity. After that, statistical analysis is carried out to investigate the power distribution among all participants at each location during each activity.

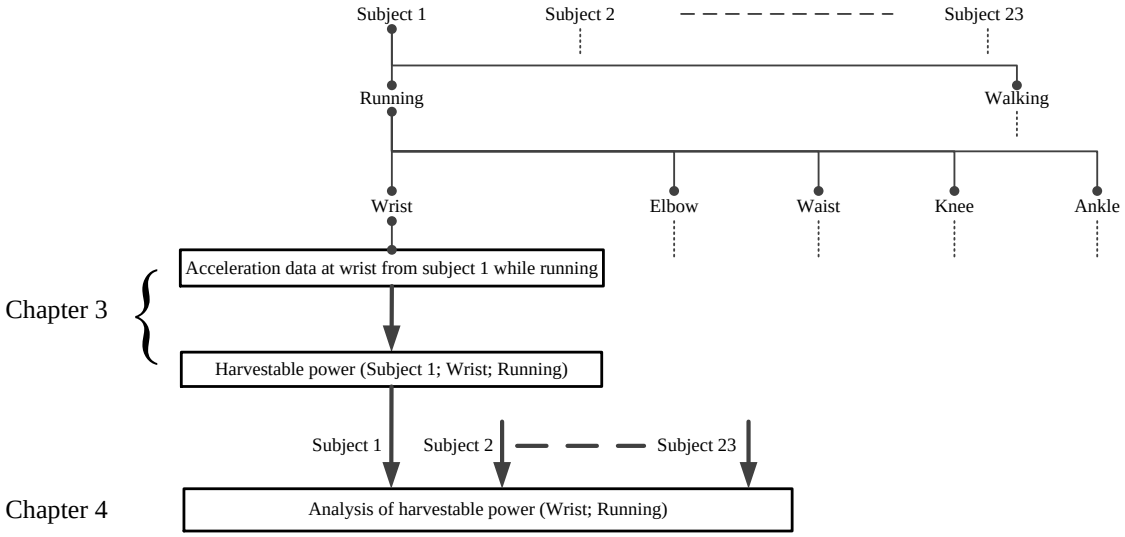

Figure 3.5 The harvestable power calculation based on collected acceleration dataset.

In performing this power estimation procedure, the following assumptions are made:

1) The general second-order spring-mass system is considered as the model of body-worn energy harvesters; the fundamental equations for available power are then used in this data analysis;

2) A 1-DOF generator is considered to harvest energy from only motion along a single axis;

3) A 2-DOF generator is considered to be formed from two orthogonally-mounted 1-DOF generators;

4) The modelled on-body generator is modelled as a point mass without considering the physical size, shape and structure of the generator.

The acceleration data analysis for the power estimation is carried out for both 1-DOF and 2-DOF inertial energy harvesters, as presented in Section 3.2.1 and 3.2.2, respectively.

3.2.1 1-DOF Analysis

Initially, the acceleration on vector $\boldsymbol{a}(t)$ [m s^{-2}] is formed from the output of the triple axis accelerometer as shown in Equation (3.1), where $\hat{\boldsymbol{x}}$, $\hat{\boldsymbol{y}}$ and $\hat{\boldsymbol{z}}$ are unit vectors aligned with the three Cartesian accelerometer axes.

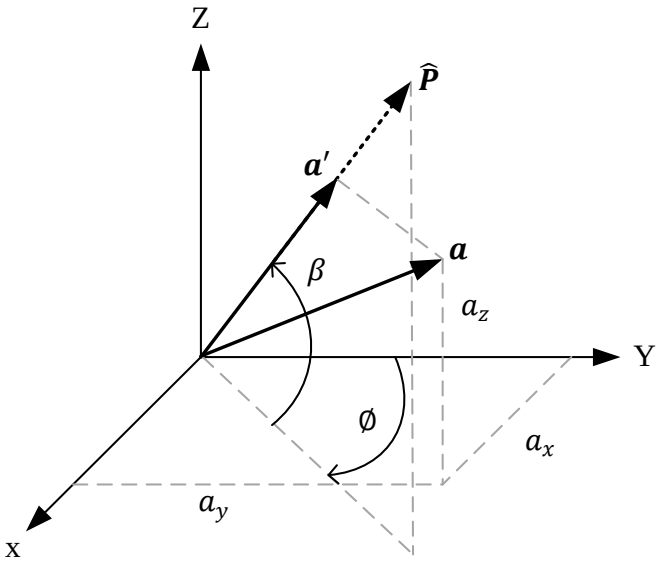

Figure 3.6 The projection of the acceleration vector $\boldsymbol{a}$ onto the direction of unit vector $\widehat{\boldsymbol{P}}$ and the unit vector $\widehat{\boldsymbol{P}}$ is defined by angles β and $\emptyset$.

$$\boldsymbol{a}(t) = (a_x(t)\hat{\boldsymbol{x}}, a_y(t)\hat{\boldsymbol{y}}, a_z(t)\hat{\boldsymbol{z}}) \tag{3.1}$$

To evaluate different generator orientations, a unit vector $\widehat{\boldsymbol{P}}$ is defined as:

$$\widehat{\boldsymbol{P}}(\beta, \emptyset) = (\cos\beta \sin\emptyset\, \hat{\boldsymbol{x}}, \cos\beta \cos\emptyset\, \hat{\boldsymbol{y}}, \sin\beta\, \hat{\boldsymbol{z}}) \tag{3.2}$$

This vector represents the direction along which energy is harvested by a 1-DOF generator (its 'sensitive' direction), as illustrated by Figure 3.6. The unit vector $\widehat{\boldsymbol{P}}$ is defined by angles β and $\emptyset$ [degrees], defined by Equation (3.3) and (3.4). The angle β is ranged from $0°$ to $90°$ at a resolution of $5°$ and the angle $\emptyset$ is ranged from $0°$ to $360°$ at a resolution of $10°$. Correspondingly, a half sphere shaped by 649 of unit vectors $\widehat{\boldsymbol{P}}$ is built to model possible generator orientations in three-dimensional space.

$$\beta \in 5 \cdot \mathbb{N}_0 \quad , \quad \beta \leq 90 \tag{3.3}$$

$$\emptyset \in 10 \cdot \mathbb{N}_0 \quad , \quad \emptyset < 360 \tag{3.4}$$

By taking the scalar product of Equation (3.1) and (3.2), the acceleration vector $\boldsymbol{a}$ is projected onto the direction of $\widehat{\boldsymbol{P}}$, as shown in Equation (3.5)**.**

$$a'(t, \beta, \emptyset) = \boldsymbol{a}(t) \cdot \widehat{\boldsymbol{P}}(\beta, \emptyset) \tag{3.5}$$

This provides a measure of magnitude of the acceleration in the sensitive axis of the generator, where $a' = \|\boldsymbol{a}'\|$.

Next, the acceleration data a' is converted from the time domain to the frequency domain using the Discrete Fourier Transform function in MATLAB, following which the frequency axis is split into discrete 'bands' to investigate the effect of the frequency of human motion on the output power. 16 discrete bands are defined as {[0.5, 1), [1, 1.5), [1.5, 2), [2, 2.5), [2.5, 3), [3, 4), [4, 5), [5, 10), [10, 15), [15, 20), [20, 25), [25, 30), [30, 35), [35, 40), [40, 45), [45, 50)} Hz. Considering the feature of low frequencies of human motion, the low frequency bands are set to relatively small ranges. Acceleration data with frequencies lower than 0.5 Hz are discarded to remove DC components, and ensure that all recorded acceleration results from human motion, as opposed to gravity.

The output power from human-powered energy harvesters within the frequency bands is evaluated. For each band in the range of [0.5, 5) Hz, the maximum amplitude A_b [m s^{-2}] and its corresponding frequency f_b [Hz] is extracted, and these values are used to calculate the obtainable power based on Equation (2.11). In this work, 'relative power' P_r [W/kg] is used for ease of comparison, and is defined with m/ξ_T set to unity, as shown in Equation (3.6).

$$P_r = \frac{{A_b}^2}{8\pi f_b} \tag{3.6}$$

The obtainable power is affected by both acceleration and frequency, and the maximum acceleration in each frequency band does not always relate to the maximum power level. To make an accurate power calculation, the frequencies above 5 Hz, which are in a band of 5 Hz, are treated as dimensions of 1 Hz. For each band in the range of [5, 50) Hz, the relative power for each 1 Hz frequency range is calculated firstly and then the maximum of the five relative power values is sorted out as the relative power in the band. For example, the relative power in the band of [5, 10) Hz is defined as Equation (3.7).

$$P_r(\text{5-10 Hz}) = \max\left(P_r(\text{5-6 Hz}), P_r(\text{6-7 Hz}), P_r(\text{7-8 Hz}), P_r(\text{8-9 Hz}), P_r(\text{9-10 Hz})\right) \tag{3.7}$$

For any one dataset obtained (for example, 30 seconds of acceleration data from a single participant's ankle while running), a direction, max($\widehat{\boldsymbol{P}}$), will be identifiable in which maximum relative power, max(P_r), is generated. Both of these values will vary between participants; for example, an individual who has more pronounced movements would expect to give comparatively larger acceleration magnitudes. To permit effective comparison of generator orientation between participants, a concept of 'normalised' power is introduced as:

$$P_n = \frac{P_r}{\max(P_r)} \times 100\% \tag{3.8}$$

Therefore, for each dataset, the normalised power shows how much power an individual is generating with respect to the maximum that they are capable of.

3.2.2 2-DOF Analysis

The analysis method shown in Section 3.2.1 allows for easy interpretation of the effect of orientation on a 1-DOF generator. The two angles β and $\emptyset$ intuitively map to the generator's sensitive direction $\widehat{\boldsymbol{P}}$. However, to fully evaluate the effect of rotation on a 2-DOF generator, consideration of an additional rotation is necessary. Therefore, an extended analysis method is used.

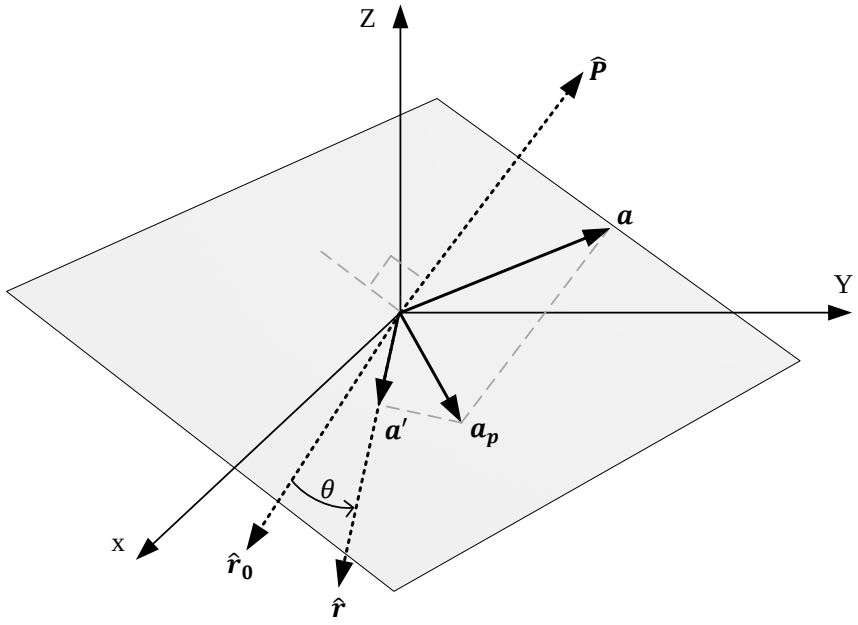

Figure 3.7 The projection $\boldsymbol{a_p}$ of the acceleration vector $\boldsymbol{a}$ onto a plane defined by the origin and the normal unit vector $\widehat{\boldsymbol{P}}$, and the acceleration magnitude of a' resulting from the subsequent rotation of $\boldsymbol{a_p}$ on this plane by an angle θ.

As with the previous method, the output of the triple axis accelerometer is mapped to an acceleration vector $\boldsymbol{a}$, and angles β and $\emptyset$ define a unit vector $\widehat{\boldsymbol{P}}$. However, the acceleration vector $\boldsymbol{a}$ is now projected onto the plane perpendicular to the unit vector $\widehat{\boldsymbol{P}}$ as $\boldsymbol{a_p}$ [m s^{-2}] (Equation (3.9)). In this case, the origin and the normal vector $\widehat{\boldsymbol{P}}$ are used together to define the planes for the generator rotation**.**

$$\boldsymbol{a_p}\,(t,\beta,\emptyset)\;=\;\widehat{\boldsymbol{P}}(\beta,\emptyset)\times\left(\boldsymbol{a}(t)\times\widehat{\boldsymbol{P}}(\beta,\emptyset)\right) \tag{3.9}$$

Next, a unit vector $\boldsymbol{r_0}$ (representing the sensitive direction of the harvester) is defined on this plane (Equation (3.10) and (3.11)), where $\hat{\boldsymbol{y}}$ is the unit vector along the y-axis and P_z is the component of the unit vector $\widehat{\boldsymbol{P}}$ in the z-axis.

$$\boldsymbol{r_0}\,(\beta,\emptyset)\;=\;\hat{\boldsymbol{y}}\times\widehat{\boldsymbol{P}}(\beta,\emptyset) \tag{3.10}$$

$$\hat{\boldsymbol{r}}_{\boldsymbol{0}}\,(\beta,\emptyset)\;=\;\frac{\boldsymbol{r_0}\,(\beta,\emptyset)}{\|\boldsymbol{r_0}\,(\beta,\emptyset)\|} \tag{3.11}$$

The unit vector $\hat{\boldsymbol{r}}_{\boldsymbol{0}}$ is subsequently rotated about the normal vector $\widehat{\boldsymbol{P}}$ by an angle θ [degrees] such that:

$$\hat{\boldsymbol{r}}(\beta,\emptyset,\theta)\;=\;\boldsymbol{R}_\theta\,\hat{\boldsymbol{r}}_{\boldsymbol{0}}\,(\beta,\emptyset) \tag{3.12}$$

where $\boldsymbol{R}_\theta$ is a rotation matrix used to rotate counter-clockwise about the vector $\hat{\boldsymbol{r}}_{\boldsymbol{0}}$ by an angle of θ. The rotation matrix $\boldsymbol{R}_\theta$ can be derived through:

$$\boldsymbol{R}_\theta=\begin{cases}\hat{\boldsymbol{r}}\cdot\hat{\boldsymbol{r}}_{\boldsymbol{0}}=\cos(\theta)\\ \hat{\boldsymbol{r}}_{\boldsymbol{0}}\times\hat{\boldsymbol{r}}=\sin(\theta)\widehat{\boldsymbol{P}}\\ \|\hat{\boldsymbol{r}}\|=1\end{cases} \tag{3.13}$$

The projected acceleration vector $\boldsymbol{a_p}$ is subsequently projected onto $\hat{\boldsymbol{r}}$ using Equation (3.14).

$$a'(t,\beta,\emptyset,\theta)\;=\;\boldsymbol{a_p}\,(t,\beta,\emptyset)\cdot\hat{\boldsymbol{r}}(\beta,\emptyset,\theta) \tag{3.14}$$

This provides a measure of the magnitude of the acceleration in the sensitive axis of the generator. From this, the data is transformed into the frequency domain and analysed in discrete frequency bands as described by Equation (3.6) and (3.7) in Section 3.2.1.

In the case of a 2-DOF generator, it is assumed that the two sensitive axes are perpendicular to each other. Therefore, the obtainable power is calculated assuming that the second sensitive axis is offset by a rotation of 90˚ on the plane. The rotation angle θ is ranged from 0 ° to 90 ° (Equation (3.15)). The relative power obtainable from the 2-DOF generator, P_r, is the sum of powers available from each of the projected accelerations $a_1{}'$ and $a_2{}'$.

$$\theta\in 10\cdot\mathbb{N}\quad,\quad\theta<90 \tag{3.15}$$

$$a_1'(t,\beta,\emptyset,\theta) = a'(t,\beta,\emptyset,\theta)$$
$$a_2'(t,\beta,\emptyset,\theta) = a'\left(t,\beta,\emptyset,\theta+\frac{\pi}{2}\right) \quad (3.16)$$

For ease of direct comparison between the 1-DOF and 2-DOF generator in terms of output power, the rotation of 1-DOF generators can be evaluated using this data processing method as well. In the case of a 1-DOF generator, the rotation angle θ ranges from 0 ° to 180 ° (Equation (3.17)) to fully evaluate the rotation effect on the plane.

$$\theta \in 10 \cdot \mathbb{N}_0 \quad , \quad \theta < 180 \quad (3.17)$$

In this data processing method, six discrete frequency bands are defined as {[0.5, 1), [1, 1.5), [1.5, 2), [2, 3), [3, 4), [4, 5)} Hz. The frequency components greater than 5 Hz are not considered in this data processing. The reason is if all the 16 frequency bands were used, the additional processing requirement involved in the 2-DOF analysis would make the simulation time become prohibitive, especially considering that the frequency above 5 Hz has been found not be particularly relevant to human motion in the literature (shown in Table 2.1 and Section 2.4).

3.3 Conclusions

This chapter describes the acceleration data collection process from the human body during walking and running. The methods of acceleration data analysis for evaluating power output from 1-DOF and 2-DOF inertial energy harvesters have been presented. The flowcharts in Figure 3.8 and Figure 3.9 illustrate the power estimation procedures for 1-DOF and 2-DOF inertial energy harvesters presented in this chapter, respectively. First, 30 seconds of acceleration data from one participant at one location during walking or running are projected onto different orientations. For 1-DOF generators, the orientation is along one axis defined by two angles; for 2-DOF generators, the orientation consists of two mutually perpendicular axes defined by three angles. Then, the projected acceleration data is converted from the time domain to the frequency domain using the discrete Fourier Transform computed with a Fast Fourier Transform (FFT) algorithm. 16 (1-DOF generators) and six (2-DOF generators) discrete frequency bands have been defined and investigated. The maximum amplitude of the acceleration data in each frequency band is found in order to calculate the relative power, after which the maximum relative power among all evaluated orientations is found, so as to calculate the normalised power along each orientation.

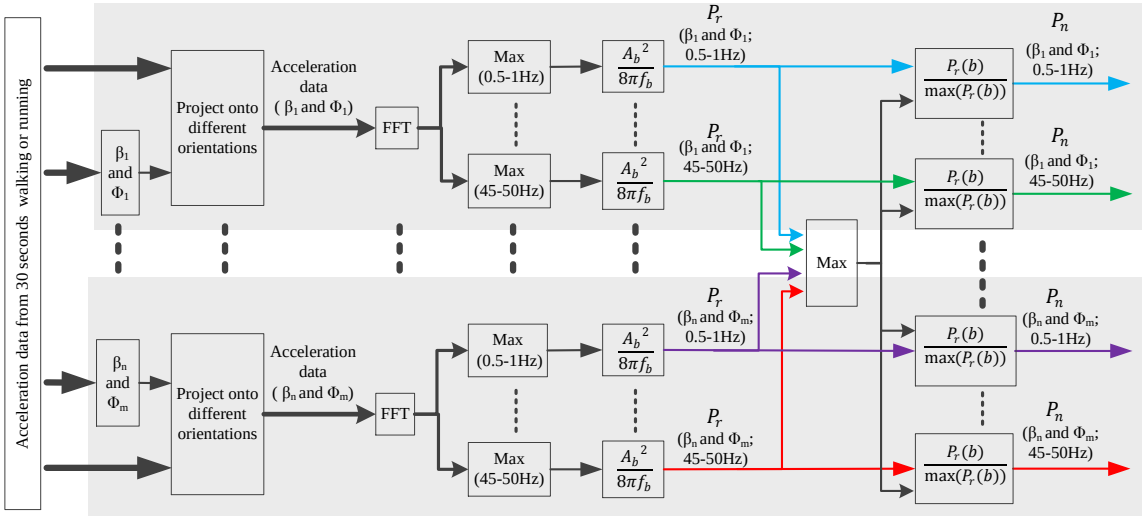

Figure 3.8 The method of acceleration data analysis for 1-DOF inertial energy harvesters based on one dataset obtained from a single participant at one location.

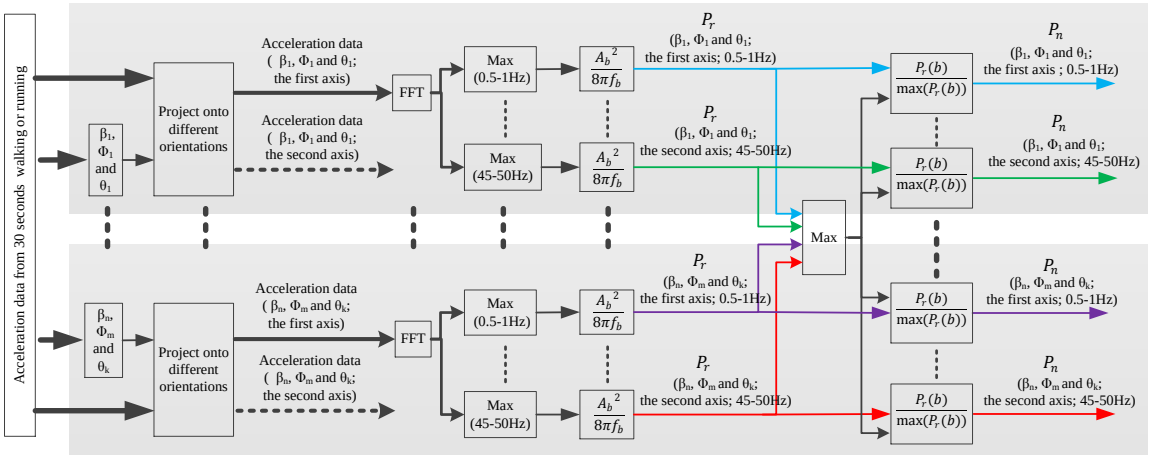

Figure 3.9 The method of acceleration data analysis for 2-DOF inertial energy harvesters based on one dataset obtained from a single participant at one location.

The data processing method for 1-DOF generators allows for easy interpretation of the data in different orientations, because the evaluated power is directly corresponding to different orientations. However, it is not suitable for directly comparing the relative performance of both a 1-DOF and 2-DOF generator, because the methods for analysing 1-DOF and 2-DOF generators use different parameters and it is not easy to compare them side by side in a graph. In contrast, the results from the method of 2-DOF generators are not intuitively interpretable, because the evaluated power is corresponding to different planes for the generator rotation. However, the method is suitable to be used for the comparison, because the methods for 2-DOF generators can also be used to evaluate the output power from 1-DOF generators, and the comparison can be taken under the same parameters.

This chapter presents the methods for evaluating the harvestable energy from human motion. Based on the evaluated output power from 1-DOF and 2-DOF energy harvesters, the effect of orientation, location and activity on the output power is investigated. The investigation results are shown in next chapter.

Chapter 4
Analysing the Effect of Orientation, Location and Activity on Harvested Power

In the previous chapter, a study was presented which considered on-body acceleration measurements at five key locations on the body during two common activities. Methods for evaluating the output power from 1-DOF and 2-DOF energy harvesters were developed. This chapter discusses the effects of orientation, location and activity on the evaluated power from energy harvesters. Section 4.1 presents the analytical results for 1-DOF energy harvesters, and Section 4.2 presents the results for 2-DOF energy harvesters. In each section, the effects of orientation and predominant frequency of human motion on the output power is explored. Section 4.3 compares 1-DOF and 2-DOF energy harvesters to investigate the benefits of 2-DOF energy harvesters in terms of output power and tolerance to rotation. In this chapter, the ankle location is used to illustrate the analysis.

4.1 Results of 1-DOF Analysis

In Section 4.1.1, the probability distribution of the harvestable power across all participants is studied in order to decide on a suitable statistical method to present the results of output power. After that, the harvestable power along different orientations is plotted and analysed to investigate the tolerance to rotation. The tolerance to rotation is an important metric used to investigate the effect of orientation on output power. Based on the harvestable power and the tolerance to rotation, the optimum orientations for 1-DOF generator at different locations on the body are identified for different activities. Then, the power and the tolerance to rotation along the identified optimum orientations are compared for different locations and activities to explore the combined effects of orientation, location and activity on the power output. In Section 4.1.2, the predominant frequencies of the two test activities at each location on the body are identified.

4.1.1 Effect of Orientation on Harvested Power

1) Statistic Distribution among Participants

To analysis data using statistical techniques, such as mean and STD, it should be verified that the data set is normally distributed. Figure 4.1 shows the probability distribution function of the obtainable power at ankle. It is found that the obtainable power is not normally distributed, and

this is true for all locations. This might be because of the small sample size of 23. Therefore, the mean and STD cannot be used. Instead of these, the median and interquartile range (IQR) are used to represent the results of analysis; these metrics are commonly adopted when data are not normally distributed. In Figure 4.1, the obtainable power plotted is the maximum relative power that each participant can achieve on the ankle. In this work, the relative power P_r is calculated by defining m/ξ_T to unity (Equation (3.6)); hence the influence of the damping ratio is not considered. The power difference among the participants is due to the kinematics of gait, such as different speeds or different step frequencies.

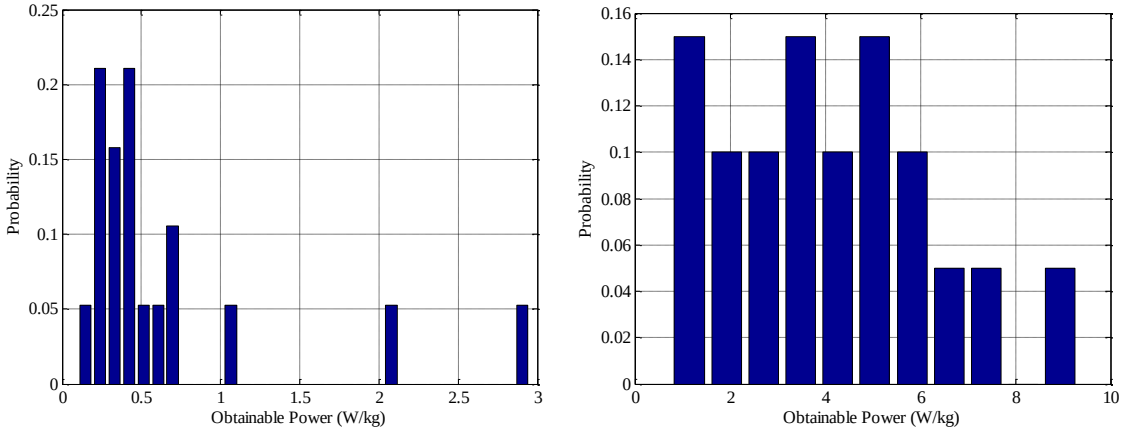

(a) (b)

Figure 4.1 Probability distribution function of obtainable power from a 1-DOF generator among all participants on the ankle during (a) walking and (b) running.

2) Power Output along Different Orientations

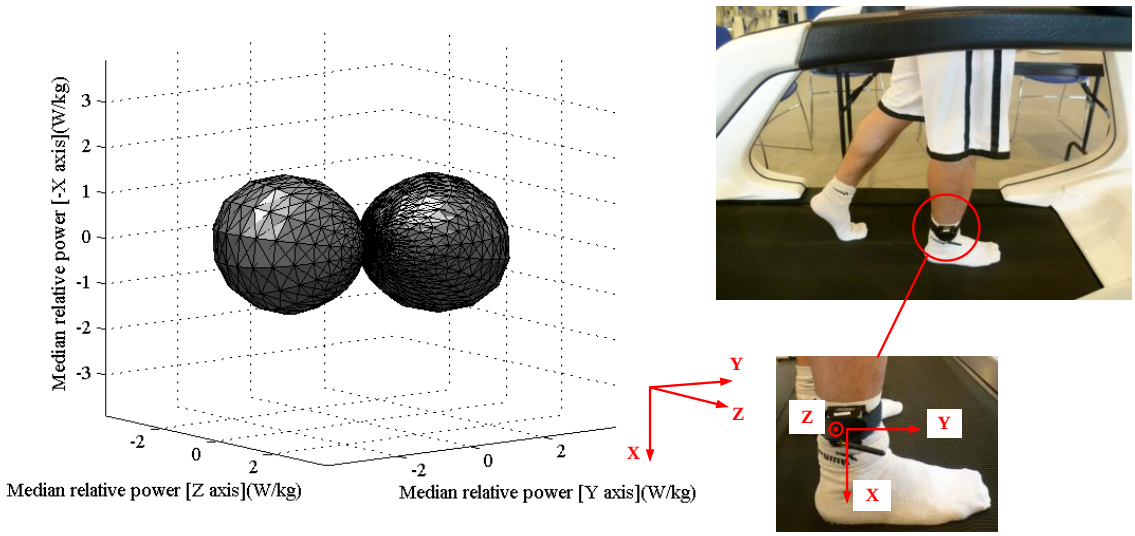

Figure 4.2 Median of relative power from a 1-DOF generator across all participants, for various orientations on the ankle during running.

Figure 4.2 shows the median of the relative power across all participants, for various orientations during running. It is found that the predominant direction of running is along the direction of overall travel. When the orientation of generators is perpendicular to this, only a small fraction of the kinetic energy is harvested. This plot illustrates the great influence of orientation on the output power from 1-DOF energy harvesters. Therefore, it is worth identifying optimum orientations for 1-DOF energy harvesters to improve the generated power output. In addition, although the impact of orientation on the output power can be noticed easy from Figure 4.2, it is not easy to quantify the impact from the plot. Therefore, numerical analysis of the effect of orientation on output power is made.

To identify the optimum orientation of 1-DOF energy harvesters, for example, on the ankle while running, the power obtainable from different individuals along a range of orientations is investigated. For illustration, Figure 4.3a overlays the relative power for each participant through the X-Y plane. The power vectors for different participants exhibit a wide range of magnitudes, but similar directions. Figure 4.3b shows the median of relative powers across participants in circles and the values of the 75^{th} percentiles quartile (Q3) and the 25^{th} percentiles quartile (Q1) at the ends of the solid lines on X-Y plane. IQR is the difference between Q3 and Q1. In Figure 4.3b, significant variation can be observed, which could be attributed to a poor correlation between participants, hence limiting the identification of the optimum orientation. Therefore, normalised power is studied to decrease the variation among participants.

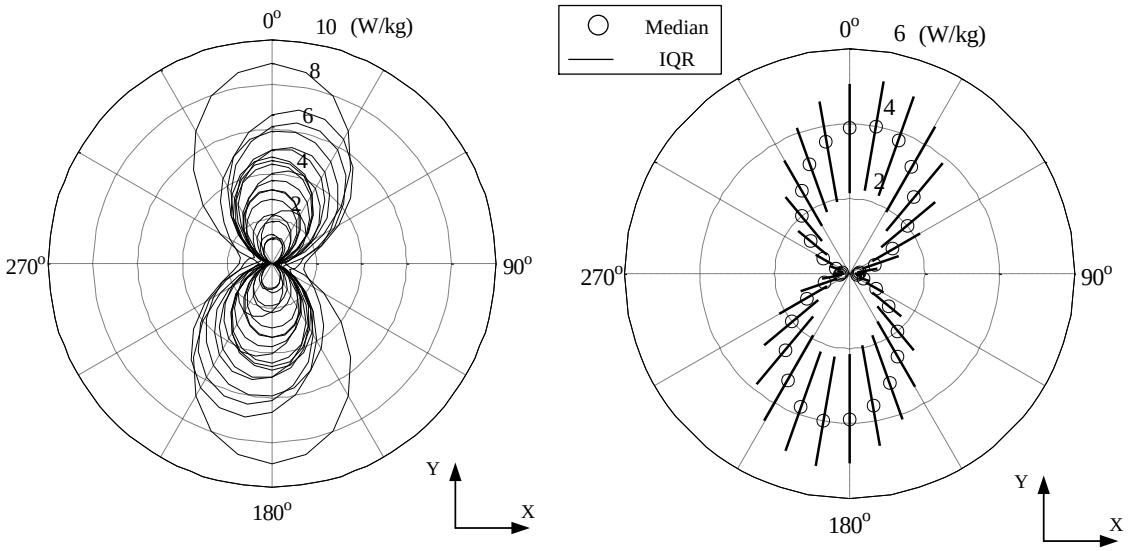

(a) (b)

Figure 4.3 Relative power from a 1-DOF generator on the ankle during running in X-Y plane. (a) Overlay of relative powers obtainable from each participant. (b) Median and IQR of relative powers across all participants.

The poor correlation of relative power between participants makes it difficult to identify the optimum orientation. To identify the optimum orientation, relative powers at different orientations are normalised to each participant's maximum defined by Equation (3.8). Figure 4.4 shows the median and IQR of the normalised power in X-Y plane. The reduction in the IQR is clear, compared to Figure 4.3b. This reduction means there is smaller amount of variation around the median. Therefore, by normalizing the power, it is found that there is a common direction along which the most power generates, but the magnitude of the power depends on each person. Taking ankle and running for example, in X-Y plane, the orientation with $\emptyset$ of 0 °, i.e. along the running direction Y, has the maximum normalised power of 97%. The small value of IQR (6%) in that orientation means most participants can achieve the maximum normalised power.

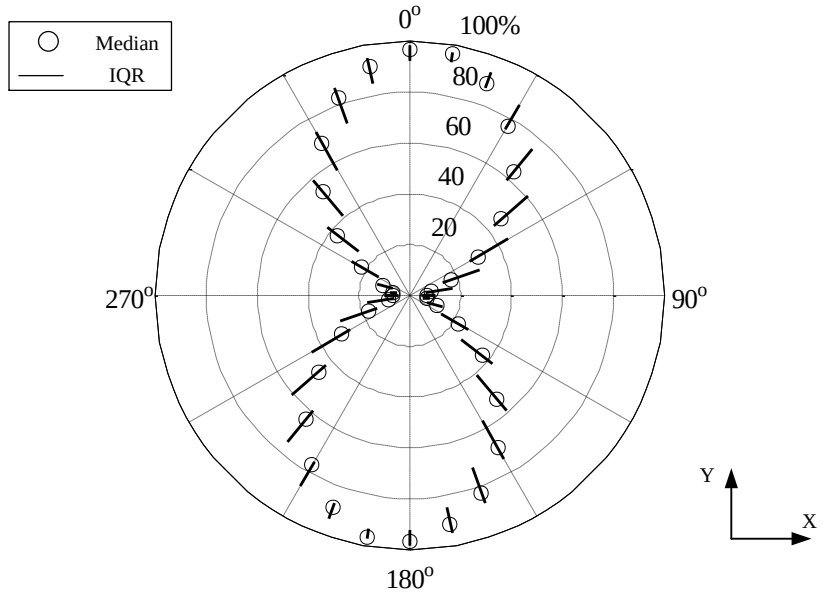

Figure 4.4 Median and IQR of normalised powers from a 1-DOF generator on the ankle during running in X-Y plane.

Extending the normalised power on the X-Y plane to three-dimensional space (X, Y and Z) gives the values of power over all evaluated orientations. Figure 4.5 shows contour plots of the normalised power over orientations that are defined by the angles β and $\emptyset$ during running. These contour plots give an intuitive view of the power distribution against orientation. The angle about the X-Y plane, β, is extended to 360 ° and the angle about Y axis, $\emptyset$, is shown from 0 ° to 360 ° for easy analysis, hence there is repetition in the plot. The orientation (β, $\emptyset$), the orientation (β+180 °, $\emptyset$) and the orientation (180 °-β, $\emptyset$+180 °) present the same orientation. The maximum normalised power is 97% for running in the orientation (β:0 °, $\emptyset$:0 °).

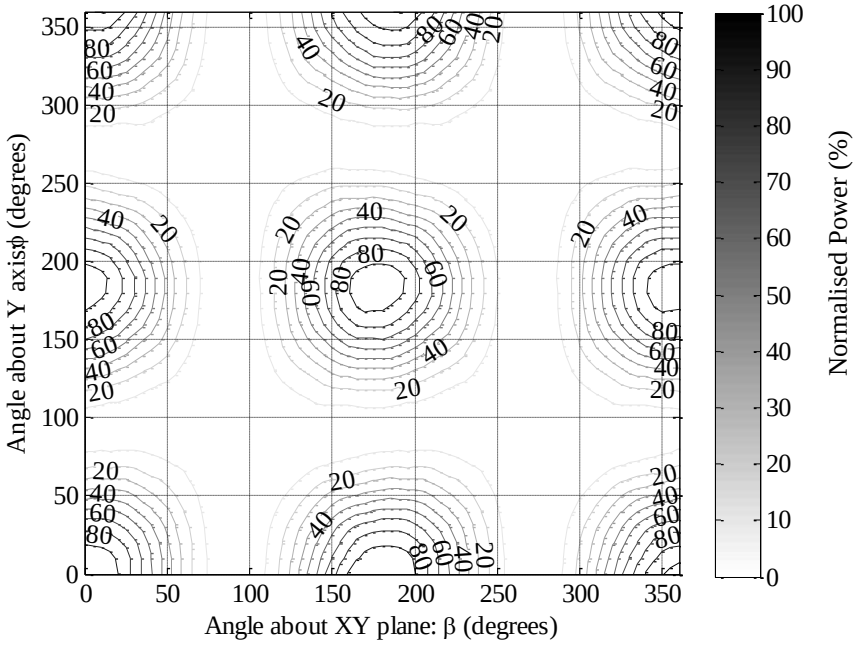

Figure 4.5 Contour plots showing the normalised power from a 1-DOF generator over orientations defined by the angles β and $\emptyset$ on the ankle during running.

3) Calculating Angular Tolerance

The output power along the orientations is not the only important parameter for identifying the optimum orientations of generators. In fact, the orientations having the maximum power varies among individuals. Additionally, in practice, the orientation of an on-body generator cannot always be along the designed optimum axis due to human motion. A shift in the orientation could greatly reduce the output power. Therefore, the sensitivity of the output power to the deviation of the orientation from each evaluated orientation should be studied. The term 'angular tolerance', α [degrees], is proposed for that purpose in this thesis.

The angular tolerance α can be calculated through the power distribution among the orientations shown in Figure 4.5. Assuming an orientation defined by β_0 and $\emptyset_0$ giving a power P_{n_0} [W/kg or %], the angular tolerance α is defined as the largest value of factor γ [degrees] for which the points in the range, as shown in Equation (4.1), have power higher than or equal to 90% of the power P_{n_0}. Figure 4.6 illustrates the range that is extended by γ from the centre (β_0, $\emptyset_0$).

$$\beta_0 - \gamma \leq \beta \leq \beta_0 + \gamma \quad \text{and} \quad \emptyset_0 - \gamma \leq \emptyset \leq \emptyset_0 + \gamma \tag{4.1}$$

For example, on the ankle during running in Figure 4.5, the angular tolerance α at the orientation (β:0 °, $\emptyset$:0 °) having the maximum normalised power is calculated to be 20 °.

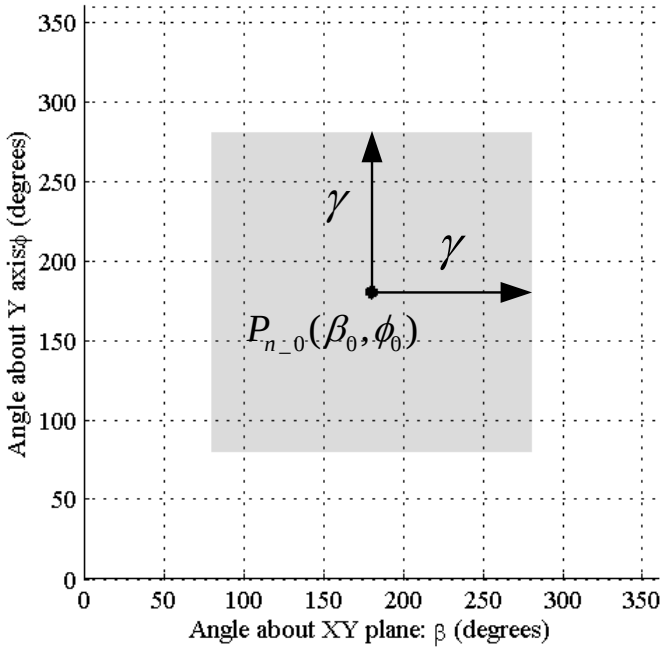

Figure 4.6 Illustration of the range that is extended by γ from the centre (β_0, $\emptyset_0$).

4) Identifying Optimum Orientations

Orientations in Figure 4.5 have different combinations of the parameters (the power and the angular tolerance). Thus, there might be one having high output power but small angular tolerance; or there might be one having low output power but large angular tolerance. The orientation having the maximum relative or normalised power might not have the biggest angular tolerance. Therefore, a cost function is needed to evaluate the output power and the angular tolerance to identify the optimum orientation. The two parameters are considered in conjunction to identify the optimum orientation.

The cost function used in this data analysis is that:

1) Firstly, the orientations having power greater than or equal to 95% of the maximum power $P_{\max}$ [W/kg or %] are selected.

2) Secondly, for these selected orientations, the product of the power value and the angular tolerance is taken, as a high power output and a large angular tolerance are desired simultaneously.

3) Finally, the orientation with the maximum of the products is identified as the optimum orientation.

The process of identifying the optimum orientation is expressed as

$$\max\left(P_1 \cdot \alpha_1,\ P_2 \cdot \alpha_2, \cdots, P_n \cdot \alpha_n\right), \qquad n \in \mathbb{N}_0 \tag{4.2}$$

where $P_{1,\,2,\,\ldots,\,n} \geq (95\% \cdot P_{\max})$.

5) Discussion on Power and Angular Tolerance along Optimum Orientations

Table 4.1 lists the obtainable power and the angular tolerance along a number of optimum orientations. The corresponding frequencies are also shown. The angular tolerance is related to the optimum orientation. Hence, an orientation that shifts away from the optimum orientation within the angular tolerance has power over 86% (86%=95%×90%) of the maximum power, because the optimum orientation has over 95% of the maximum power and the angular tolerance guarantee the power will not decrease by more than 10%.

Table 4.1 Obtainable power and angular tolerance along optimum orientations for a 1-DOF generator at the five locations during walking and running.

			β	$\emptyset$	Power	α	IQR	Frequency	IQR
Unit:			[Degrees]		[% or W/kg]	[Degrees]	[% or W/kg]	[Hz]	
P_n [%]	ankle	walk	5	200	93	15	6	0.938	0.281
		run	0	0	97	20	6	1.34	0.172
	knee	walk	20	320	95	20	10	0.875	0.156
		run	25	310	95	20	14	1.31	0.188
	waist	walk	0	60	79	10	48	1.75	0.188
		run	5	270	98	15	7	2.61	0.281
	elbow	walk	0	70	78	20	23	1.38	0.875
		run	10	320	85	15	30	2.66	0.367
	wrist	walk	40	330	86	20	31	0.875	0.109
		run	10	330	92	15	19	2.64	0.359
P_r [W/kg]	ankle	walk	5	210	0.362	20	0.333	1.00	0.805
		run	5	180	3.96	15	2.66	1.34	0.172
	knee	walk	10	320	0.471	20	0.419	0.875	0.125
		run	25	310	2.57	10	1.86	1.31	0.188
	waist	walk	20	50	0.033	10	0.0321	1.75	0.875
		run	0	90	1.28	15	1.01	2.61	0.281
	elbow	walk	5	230	0.0688	10	0.076	1.59	0.875
		run	15	310	2.15	10	1.35	2.66	0.367
	wrist	walk	45	340	0.127	15	0.102	0.875	0.109
		run	5	330	2.32	20	1.66	2.64	0.359

- **Optimum Orientation**

While searching for the optimum orientation, it is noticed that at the same location, the optimum orientations for walking and running are different. To explore whether or not it is possible to design a generator for both activities with high output power, the difference of the optimum orientations for both activities is investigated. From Figure 3.6, an orientation of $(\beta, \emptyset)$ is the same as orientations of $(\beta+180°, \emptyset)$ and $(180°-\beta, \emptyset+180°)$. Then, the smallest values of the differences of the optimum orientations ($\Delta\beta$ [degrees] and $\Delta\emptyset$ [degrees]) between walking and running are found. The results are shown in Table 4.2. If the angular tolerance is greater than the difference of the optimum orientations, a generator can be designed for both activities with over 86% of the maximum power, as discussed above. Therefore, the knee is the only location where generators can achieve over 86% of the maximum power (both normalised and relative power) along the same orientation for both activities.

In addition, at the elbow, $\Delta\emptyset$ between walking and running (the shaded numbers in Table 4.2) is close to 90°. This is because the participants were keeping their arms straight in a relaxed manner during walking, while they raised their forearms to keep their balance during running, reducing the angle between the forearm and the upper arm. Therefore, the oscillation of a 1-DOF generator on the elbow for these two activities should have around 90° difference; hence, 1-DOF generators are not appropriate in this case.

Table 4.2 Differences between the optimum orientations of a 1-DOF generator for walking and running.

	P_n [%]					P_r [W/kg]				
[degrees]	Ankle	Knee	Waist	Elbow	Wrist	Ankle	Knee	Waist	Elbow	Wrist
$(\Delta\beta, \Delta\emptyset)$	(5, 20)	(5, 10)	(5, 30)	(10, 70)	(30, 0)	(0, 30)	(15, 10)	(20, 40)	(10, 80)	(40, 10)

- **Angular Tolerance**

For the angular tolerance, it is found that the angular tolerances are less than or equal to 20°, which means the rotation of 20° from the optimum direction drops the available output power by at least 10%. Therefore, the orientation of 1-DOF energy harvesters is an important factor that affects the output power.

- **Best Locations to Place Generators during Walking and Running**

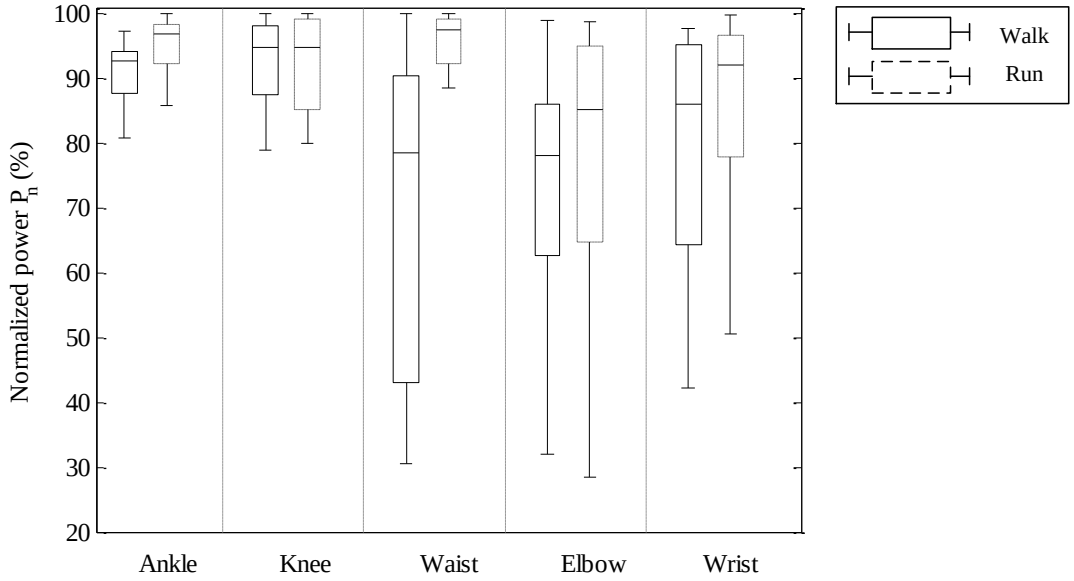

Figure 4.7 Normalised power along optimum orientations from a 1-DOF generator at the five locations during walking and running.

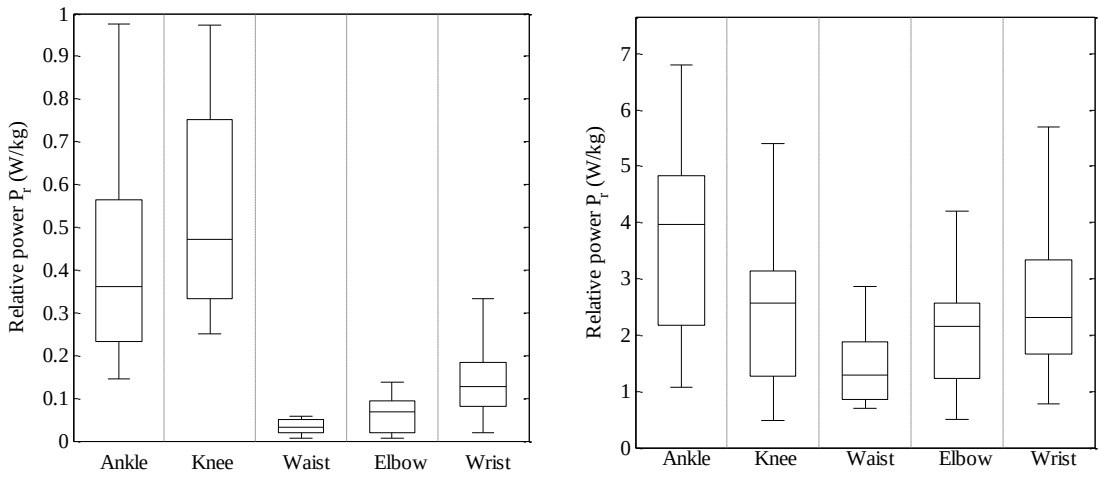

(a) (b)

Figure 4.8 Relative power along optimum orientations from a 1-DOF generator at the five locations during (a) walking and (b) running.

From the evaluated power in Table 4.1, it is found that for walking, the maximum normalised or relative power is found at the knee (the green cells in Table 4.1); for running, the maximum normalised power can be harvested at the waist and the maximum relative power is found at the ankle (the blue cells in Table 4.1). Hence, for running, the optimum locations to place generators are not the same for the normalised and relative power.

Normalised power shows how much power an individual is generating with respect to the maximum that they are capable of, while relative power shows the obtainable power from each person. Because of these different definitions, the optimum orientations for normalised and relative power are not always the same in the case of the same location and activity, which is noticed in Table 4.1. Some locations may have a high normalised power but a low relative power; some locations may have a low normalised power but a high relative power. Either of the situations is not wanted during energy harvesting from human body. For example, during running, the waist has the maximum normalised power but minimum relative power. The optimum placement of generators should provide a high relative power and a high normalised power simultaneously. Therefore, the normalised power and relative power are considered in conjunction to identify the optimum placement of generators.

To identify the optimum placement of generators, the power obtainable from different locations is illustrated. Figure 4.7 shows the normalised power along optimum orientations at the five locations; the results of the relative power are shown in Figure 4.8. In this thesis, the central mark of a box plot is median, the edges of the box are Q1 and Q3 and the ends of the whisker are the lowest datum still within 1.5 IQR of the lower quartile Q1 and the highest datum still within 1.5 IQR of the upper quartile Q3. The data outside this range are considered as outliers and are not drawn.

From Figure 4.7 and Figure 4.8, it is found that the knee has the maximum normalised power, and the maximum relative power for walking, and that the ankle has both the second-highest normalised power and the maximum relative power for running. Therefore, the knee and the ankle are the optimum locations for walking and running, respectively.

- **Obtainable Power at the Different Locations**

In Figure 4.7, significant variation in normalised power along the optimum orientations can be observed on the upper body (waist, elbow and wrist), which could be attributed to a poor correlation between participants. This variation means some people might have the ability to generate large output power along the optimum orientation, while others might just generate a little power. Therefore, the upper body is not appropriate to place generators for harvesting energy from walking and running.

In addition, in Figure 4.8, it is found that the lower body (ankle and knee) can generate much more relative power than the upper body during walking. The median of the relative power on the lower body is 0.033-0.127 W/kg, while it is 0.362-0.471 W/kg on the upper body, representing a large increase in the power output. For running, the relative power at the five

locations has a significant improvement and the median of the relative power is increased to 1.28-3.96 W/kg; the lower body does not get significantly more power than the upper body, because the increased movement of the upper body during higher activity exercises such as running. Therefore, for walking, there are great benefits of lower body in power output, however, for running, the difference between the power output on the upper and lower body is less significant.

4.1.2 Influence of Predominant Frequency of Human Motion on Harvested Power

To explore the effect of predominant frequencies of human motion on the output power, the frequencies used in the calculation of the power obtainable in the optimum orientations are shown in Table 4.1. Figure 4.9 illustrates the distribution of the predominant frequencies across participants. For walking, the medians of the predominant frequencies are in the range of 0.875-1.75 Hz. For running, they are 1.31-1.34 Hz on the lower body and 2.61-2.66 Hz on the upper body. These results agree well with the existing studies shown in Section 2.4.

It is noticed that during running, the medians of the predominant frequencies on the upper body are approximately two times bigger than the values on the lower body. This is because the impact between ground and foot was much stronger when the participants were running instead of walking. The foot-ground impact produces an instant vibration signal that is transmitted through the human body. There are two legs per body and one leg has only one frequency, hence the upper body has twice it. However, the magnitude of the vibration signal on the upper body is smaller than that on the lower body.

Moreover, in Figure 4.9, significant variation of predominant frequencies for each location and each activity can be observed, such as at the elbow during walking, which could be attributed to a poor correlation between participants. This variation means, taking the elbow during walking for example, some people might have a predominant frequency of 1 Hz, while others might have a predominant frequency of 2.5 Hz. However, typically, there is only one resonant frequency for an inertial energy harvester, and the maximum output power is generated when the resonant frequency matches the frequency of external vibrations. Therefore, it is worth investigating the effect of predominant frequency on the output power within a narrow frequency band.

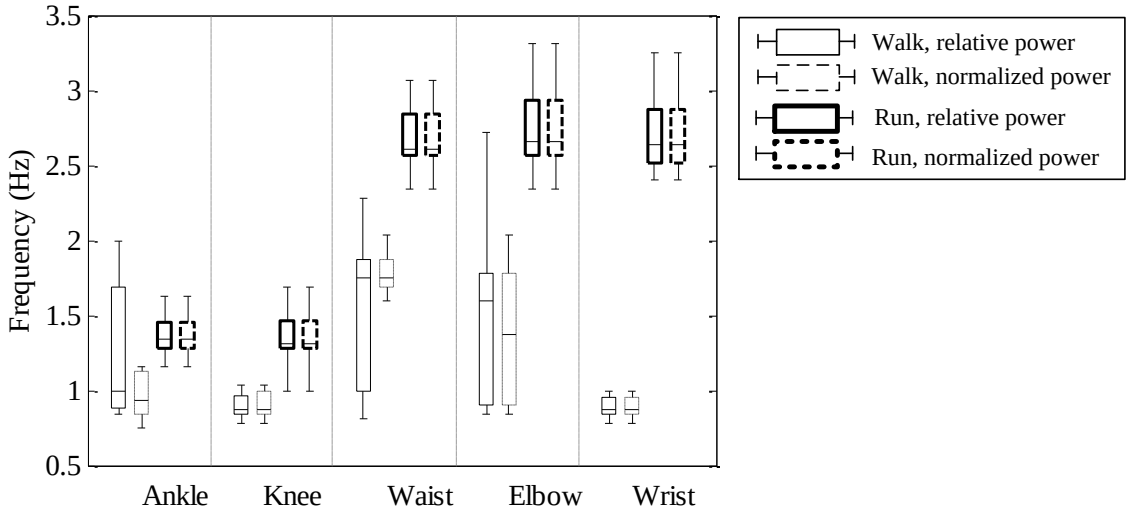

Figure 4.9 Frequencies corresponding to the power obtainable in the optimum orientations.

Significant variation in predominant frequencies of walking and running has been observed from Figure 4.9. Therefore, to explore the influence of predominant frequency of human motion on harvested power, the output power within the discrete frequency bands is investigated. Figure 4.10 shows the relative power in different frequency bands during walking and running. All frequency components in the range $[5, 50)$ Hz are grouped into a single band for clarity, especially considering that the predominant frequencies at the five locations during walking and running are all below 3.5 Hz (shown in Figure 4.9).

From Figure 4.10, frequency bands that make a great contribution to the output power are identified. Some locations, such as ankle during running, have only one predominant frequency band. Some locations, such as knee during running, have two predominant frequency bands. The ankle while walking has several predominant frequency bands. Therefore, during the design of generator's bandwidth, the predominant frequency bands should be considered to harvest energy from all predominant frequency bands and then increase the output power. The predominant frequency bands are shown in Table 4.3. It is found that for walking, the predominant frequency bands are all below 2.5 Hz at all locations, while, for running, the higher frequency band of 2.5-3 Hz is introduced to provide high output power. In addition, the ankle during walking has a relatively wide predominant frequency band compared to other locations; therefore, energy harvesters should be designed with a relatively wide bandwidth (2.5 Hz) to harvest energy from the ankle during walking. In contrast, energy harvesters used for harvesting energy from the ankle during running or the waist during running should have a relatively narrow bandwidth (0.5 Hz), because only one frequency band makes a significant contribution to the output power.

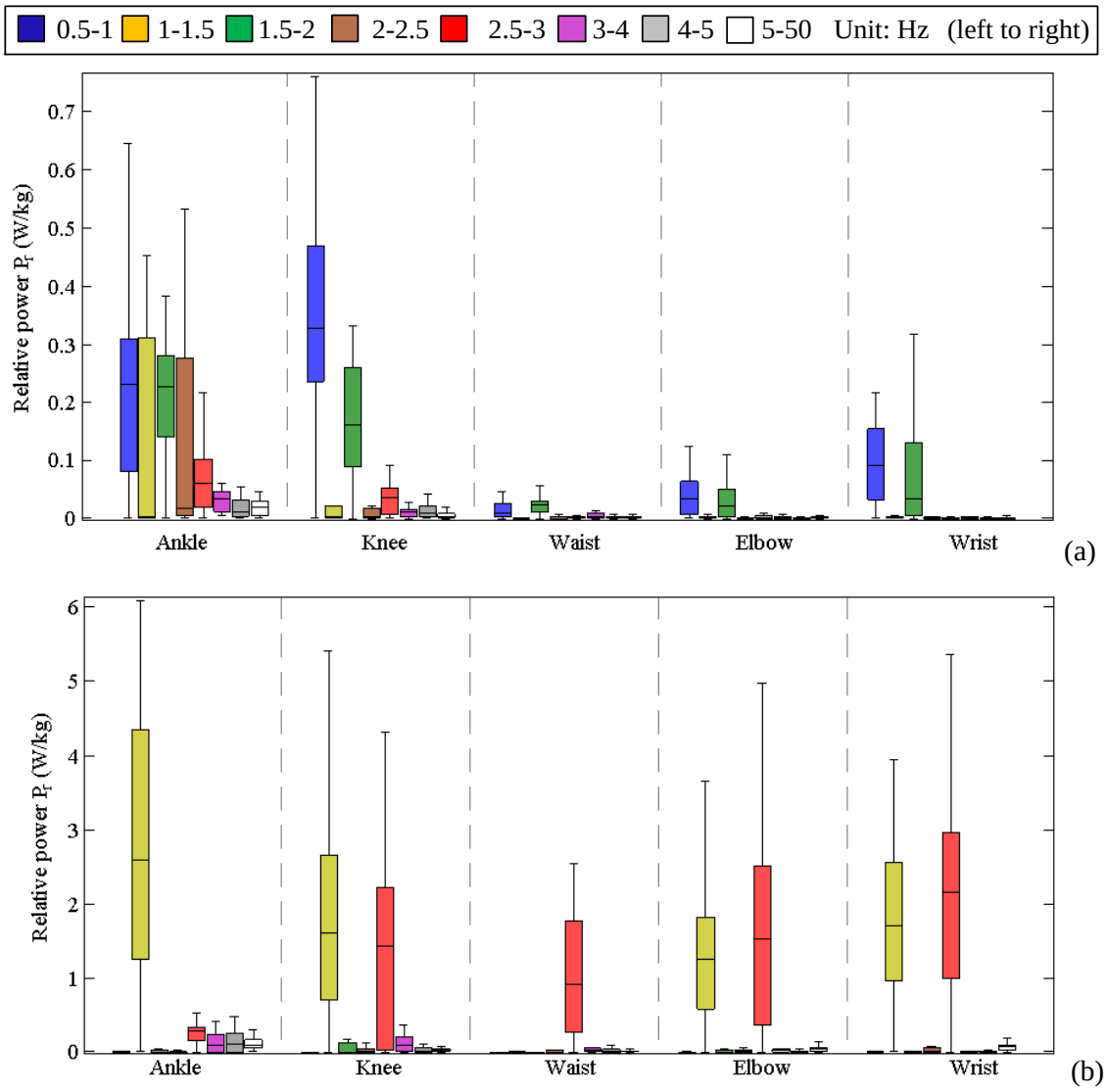

Figure 4.10 Relative power from a 1-DOF generator across different frequency bands for (a) walking and (b) running.

Table 4.3 Predominant frequency bands of the relative power from a 1-DOF generator.

	Ankle	Knee	Waist	Elbow	Wrist
Walk [Hz]	0.5-2.5	0.5-1, 1.5-2	0.5-1, 1.5-2	0.5-1, 1.5-2	0.5-1, 1.5-2
Run [Hz]	1-1.5	1-1.5, 2.5-3	2.5-3	1-1.5, 2.5-3	1-1.5, 2.5-3

4.2 Results of 2-DOF Analysis

In Section 4.2.1, the harvestable power from 2-DOF generators along different orientations is plotted and analysed to investigate the tolerance to rotation. Based on the harvestable power and the tolerance to rotation, the optimum orientations at different locations on the body while doing different activities are identified. Then, the power and the tolerance to rotation along the

identified optimum orientations are compared between different locations and activities to investigate the effect of orientation, location and activity on the power output. In Section 4.2.2, the predominant frequencies of the two test activities at the locations on the body are identified.

4.2.1 Effect of Orientation on Harvested Power

1) Power Output along Different Orientations

As with 1-DOF energy harvesters, the probability distribution function of the obtainable power from 2-DOF energy harvesters is not a normal distribution, probably because of the small sample size. Therefore, the median and IQR are used to represent the results of 2-DOF analysis.

In this thesis, a 2-DOF inertial energy harvester is assumed to consist of two orthogonal 1-DOF energy harvesters. In this section, the situation in which the two resonant frequencies of the two 1-DOF energy harvesters are different is studied, as is the situation in which the two are the same.

As with 1-DOF energy harvesters, there is significant variation in the relative power across participants due to the poor correlation between participants. To identify the optimum orientation, normalised power is studied, to decrease the variation among participants. Figure 4.11 shows the median and IQR of the normalised power in all evaluated orientations at the ankle during running. The three angles, i.e. β, $\emptyset$ and θ (defined in Section 3.2.2), represent one orientation. The colour of points is relative to the amount of power. The darker the colour, the more power there is. The rotation angle θ is extended to 180 ° for easy analysis, hence there is repetition in the plot. The orientation (β, $\emptyset$, θ) and the orientation (β, $\emptyset$, θ+90 °) represent the same orientation.

In Figure 4.11, the points with large normalised power generally have small IQR. For example, the points (β: 90 °, $\emptyset$: 0 °, θ: 0 °-180 °) all have 91% normalised power (median value) with IQR of 13-28%, indicating a small amount of variation around the median. Such points with high median and small IQR represent those at which most participants can generate a large amount of output power along these orientations. Furthermore, this plot illustrates the influence of orientation on the output power. Some orientations have high median of the normalised power (presented by dark area), while some have low median (presented by light area). For example, the points (β: 0 °, $\emptyset$: 0 °, θ: 0 °-180 °) (all have 6% normalised power) represent the orientations on a plane that is vertical to the running direction Y, as illustrated by the green plane in Figure 4.12, while the points (β: 90 °, $\emptyset$: 0 °, θ: 0 °-180 °) represent the orientations on a plane that is parallel to the running direction Y, as shown by the blue plane in Figure 4.12. From Figure 4.11,

it is found that the normalised power generated in the vertical plane is much smaller than parallel plane, which highlights the effect of orientation on the output power. In addition, the orientations on the parallel plane are always able to generate 91% normalised power, which shows a great tolerance to rotation. Therefore, it is worth identifying the optimum orientations for 2-DOF energy harvesters.

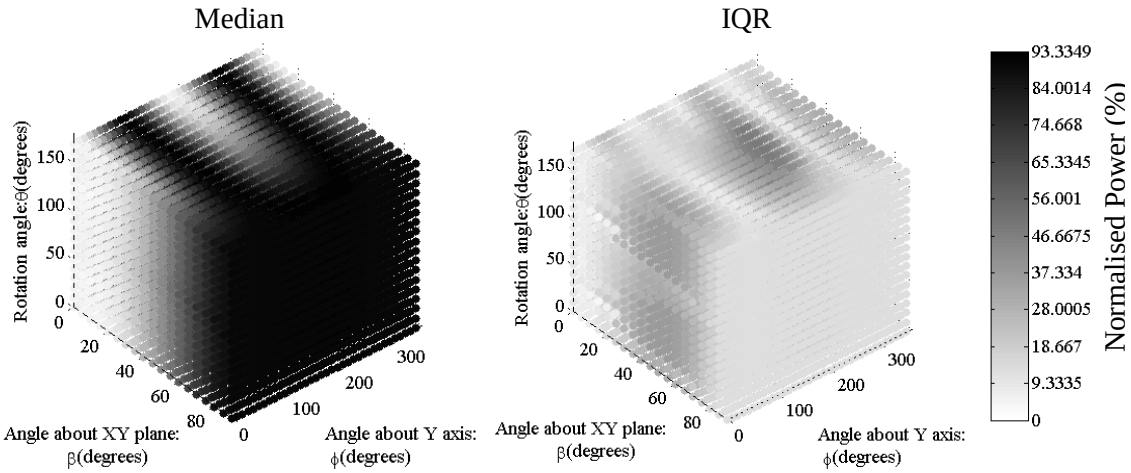

Figure 4.11 Median and IQR of normalised power for a 2-DOF generator on the ankle during running. The three angles define the orientations and the colour of the points is relative to the amount of the normalised power, where a darker point represents more power.

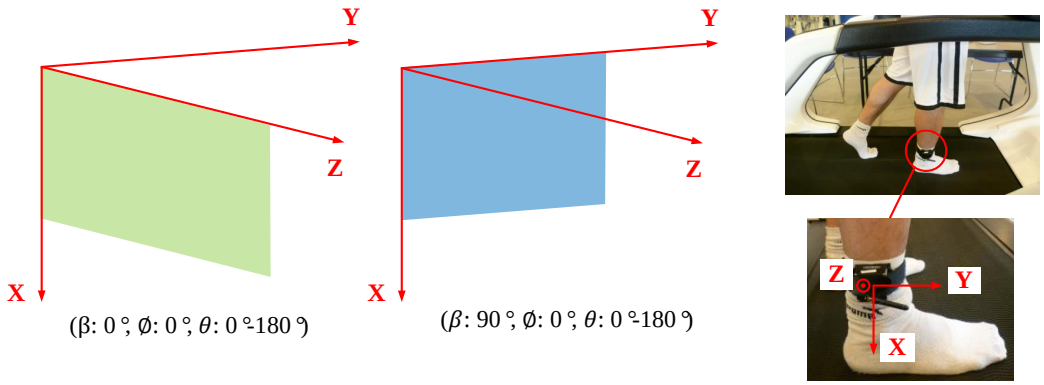

Figure 4.12 Illustration of two planes for the generator roation. The green and blue planes are vertical and parallel to the running direction Y, respectively.

2) Calculating Angular Tolerance

Similarly to the 1-DOF energy harvesters previously, angular tolerance is calculated to identify the optimum orientations. The angular tolerance α for a 2-DOF energy harvesters is calculated by investigating the median of power output among orientations shown in Figure 4.13. The angular tolerance calculations are very similar to the procedure for 1-DOF generators. The only

difference is that the calculation for 2-DOF energy harvesters is based on three angles rather than two angles for 1-DOF energy harvesters.

Assuming an orientation defined by β_0, $\emptyset_0$ and θ_0 giving a power P_{n_0}, the angular tolerance α is defined as the largest value of factor γ' [degrees] for which the points in the range, as shown in Equation (4.3), have power higher than or equal to 90% of the power P_{n_0}. Figure 4.13 illustrates the range that is extended by γ' from the centre (β_0, $\emptyset_0$, θ_0).

$$\beta_0 - \gamma' \le \beta \le \beta_0 + \gamma' \quad \text{and} \quad \emptyset_0 - \gamma' \le \emptyset \le \emptyset_0 + \gamma' \quad \text{and} \quad \theta_0 - \gamma' \le \theta \le \theta_0 + \gamma' \qquad (4.3)$$

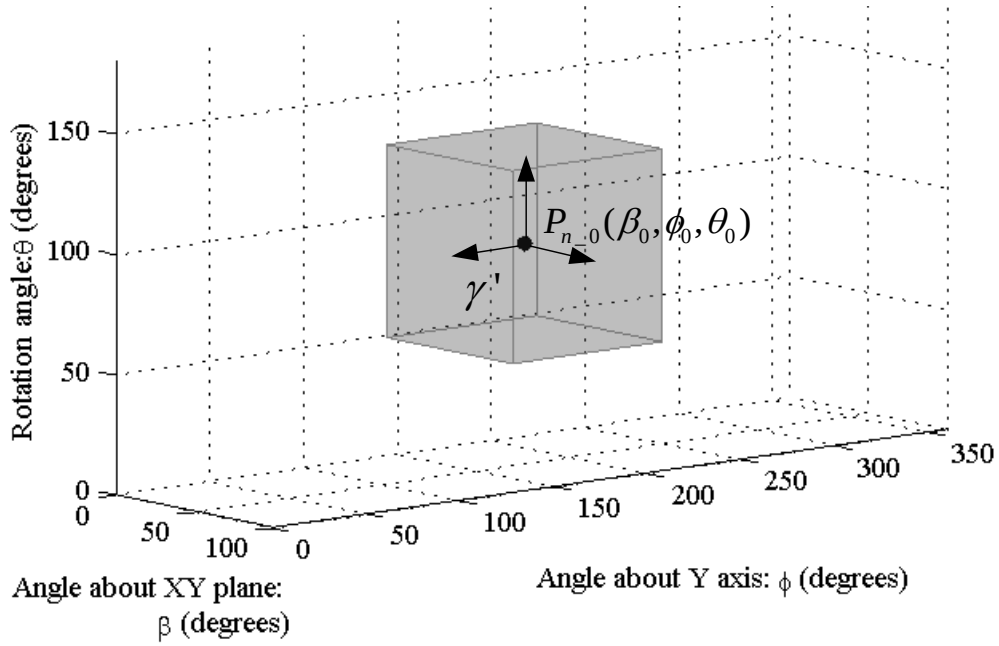

Figure 4.13 Illustration of the range that is extended by γ' from the centre (β_0, $\emptyset_0$, θ_0).

The identification of the optimum orientation followed the same procedure as for the 1-DOF generators, through processing the power and the angular tolerance.

3) Discussion on Power and Angular Tolerance along Optimum Orientations

Table 4.4 lists the obtainable power and the angular tolerance along optimum orientations. The corresponding frequencies along the two axes of 2-DOF generators are also shown, which are denoted as f_x and f_y.

Table 4.4 Obtainable power and angular tolerance along optimum orientations for a 2-DOF generator at the five locations during walking and running.

			β	$\emptyset$	θ	Power	α	IQR	f_x	IQR	f_y	IQR
Unit:			[Degrees]			[% or W/kg]	[Degrees]	[% or W/kg]	[Hz]		[Hz]	
P_n [%]	ankle	walk	75	310	20	94	20	62	1.75	0.242	0.875	0.0625
		run	45	100	60	92	20	9	1.33	0.141	1.33	0.141
	knee	walk	55	210	30	86	10	13	1.75	0.125	0.875	0.0625
		run	70	180	60	94	15	5	2.59	0.375	1.31	0.188
	waist	walk	80	80	0	81	15	45	1.75	0.0938	1.75	0.188
		run	60	180	0	96	30	4	2.61	0.281	2.61	0.188
	elbow	walk	25	320	0	82	10	72	0.875	0.0859	0.875	0.0625
		run	60	220	30	90	10	18	1.31	0.188	2.66	0.344
	wrist	walk	40	180	10	82	10	22	1.75	0.203	0.875	0.0781
		run	75	180	30	96	20	13	1.33	0.156	2.64	0.359
P_r [W/kg]	ankle	walk	80	340	20	0.404	10	0.261	1.75	0.242	0.875	0.0625
		run	35	100	0	2.88	20	3.20	1.31	0.109	1.34	0.156
	knee	walk	0	60	0	0.375	10	0.244	1.75	0.219	0.875	0.0625
		run	65	180	60	2.96	20	3.18	2.59	0.375	1.31	0.188
	waist	walk	10	120	70	0.047	10	0.031	1.75	0.0938	0.875	0.0313
		run	80	150	20	1.14	20	1.16	2.61	0.281	2.61	0.188
	elbow	walk	20	320	10	0.0528	15	0.0622	0.875	0.0859	1.78	0.0938
		run	75	180	40	3.35	10	2.85	1.31	0.188	2.66	0.344
	wrist	walk	35	200	80	0.127	10	0.256	0.875	0.0781	1.75	0.156
		run	75	180	20	3.73	15	2.95	1.33	0.156	2.63	0.359

- **Optimum Orientation**

While searching for the optimum orientation, it is noticed that at the same location, the optimum orientations for walking and running are different. To explore whether or not it is possible to design a 2-DOF generator for both activities with high output power, the difference of the optimum orientations for both activities is investigated. From Figure 3.7, an orientation of (β, $\emptyset$, θ) is the same as orientations of (β+180 °, $\emptyset$, θ) and (180 °-β, $\emptyset$+180 °, θ). Then, the smallest values of the differences of the optimum orientations ($\Delta\beta$, $\Delta\emptyset$ and $\Delta\theta$ [degrees]) between walking and running are found. The results are shown in Table 4.5. If the angular tolerance is greater than the difference of the optimum orientations, a generator can be designed for both activities with over 86% of the maximum power. The results show that the differences of the optimum orientations are all bigger than the angular tolerance at the five locations, hence none of the locations is able to get over 86% of the maximum power (either normalised or relative power) along the same orientation for both activities.

Table 4.5 Differences between the optimum orientations of a 2-DOF generator for walking and running.

	P_n [%]				
[degrees] ($\Delta\beta$, $\Delta\emptyset$, $\Delta\theta$)	Ankle (30, 210,40)	Knee (15, 30, 30)	Waist (20, 100, 0)	Elbow (25, 100, 30)	Wrist (25, 0, 20)
	P_r [W/kg]				
[degrees] ($\Delta\beta$, $\Delta\emptyset$, $\Delta\theta$)	Ankle (45, 240, 20)	Knee (65, 60, 60)	Waist (70, 30, 50)	Elbow (55, 140, 30)	Wrist (40, 20, 60)

- **Best Locations to Place Generators during Walking and Running**

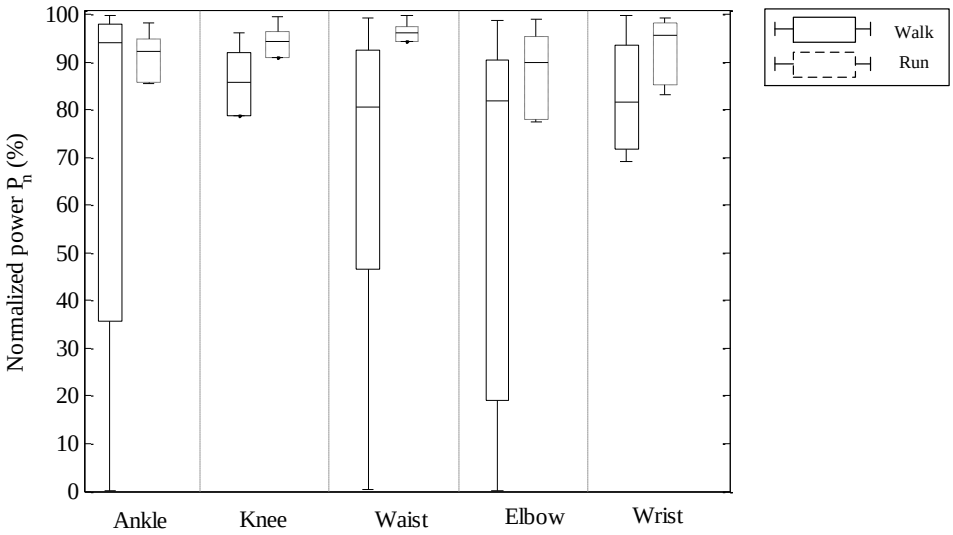

Figure 4.14 Normalised power along optimum orientations from a 2-DOF generator at the five locations during walking and running.

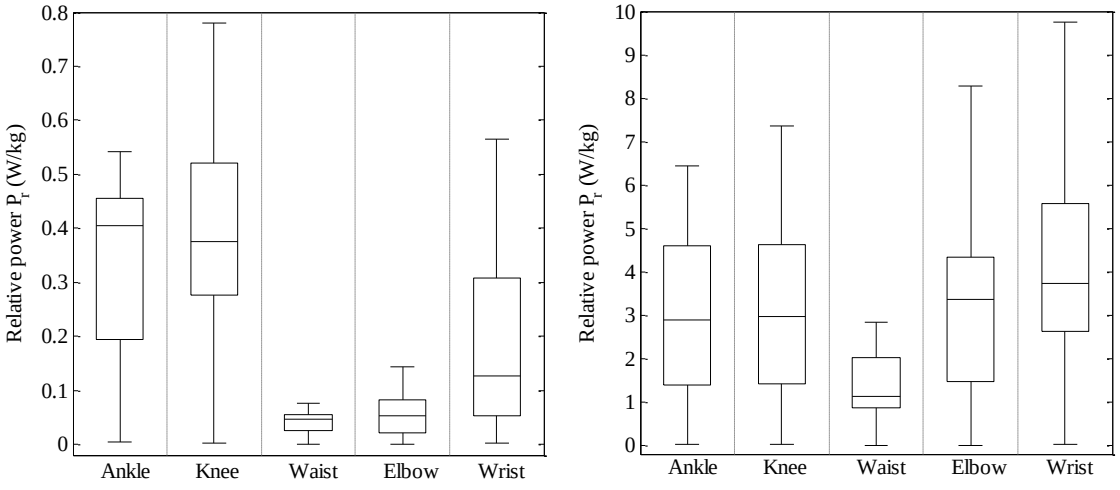

(a) (b)

Figure 4.15 Relative power along optimum orientations from a 2-DOF generator at the five locations during (a) walking and (b) running.

From the evaluated power in Table 4.4, it is found that for walking, the maximum normalised or relative power is available at the ankle (the green cells in Table 4.4); for running, the maximum normalised power is found at the waist and wrist (both 96%) and the maximum relative power is developed at the wrist (the blue cells in Table 4.4). Similar to 1-DOF analysis, the normalised and relative power are considered in conjunction to identify the optimum placement of generators; considered thusly, the ankle and the wrist are found to be the optimum locations for walking and running, respectively.

- **Obtainable Power at the Different Locations**

To illustrate the power obtainable from different locations, Figure 4.14 shows the normalised power along optimum orientations at the five locations, and the results of the relative power are shown in Figure 4.15. In Figure 4.14, significant variation of normalised power along the optimum orientations can be observed at the ankle, waist and elbow. They are greater than in the 1-DOF case (Figure 4.7). One explanation for that is poor correlation between participants. The other reason is probably that the power is contributed by two 1-DOF generators. The additional 1-DOF generator might introduce an additional variable component to the device. If the two resonant frequencies of the two 1-DOF generators are limited in the same frequency bands, the variation of the normalised power might be reduced. This will be validated in the next section.

In addition, in Figure 4.15, it is found that the lower body can generate much more relative power than the upper body during walking. The median of the relative power on the upper body is 0.047-0.127 W/kg, while it is 0.375-0.404 W/kg on the lower body, showing a big increase in the power output. For running, the relative power at the five locations is significantly improved and the median of the relative power is increased to 1.14-3.73 W/kg; the lower body does not generate more power than the upper body, and the medians of relative power at the elbow and wrist are more than those at the ankle and knee. However, for running, the variation of the relative power at the elbow and wrist is bigger than the ankle and knee, which indicates that the correlation of output power among participants at the wrist and elbow is worse than the lower body. Therefore, for walking, there are great benefits for the lower body in terms of power output; while running, the elbow and wrist have the advantage in power output, but the correlation of output power among participants is not as good as for the lower body.

4.2.2 Influence of Predominant Frequency of Human Motion on Harvested Power

Similar to the 1-DOF, the effect of predominant frequency of human motion on harvested power is investigated within the discrete frequency bands. Figure 4.16 shows the relative power in

different frequency bands during walking and running. The predominant frequency bands are identified and listed in Table 4.6. It is found that the predominant frequency bands are wider than or equal to those of 1-DOF energy harvesters. This is probably because in 2-DOF analysis, the two frequency bands of 2-2.5 Hz and 2.5-3 Hz are grouped into a single band 2-3 Hz. Considering that, the results in Figure 4.16 show the same influence of predominant frequency on the output power from 2-DOF generators as 1-DOF generators.

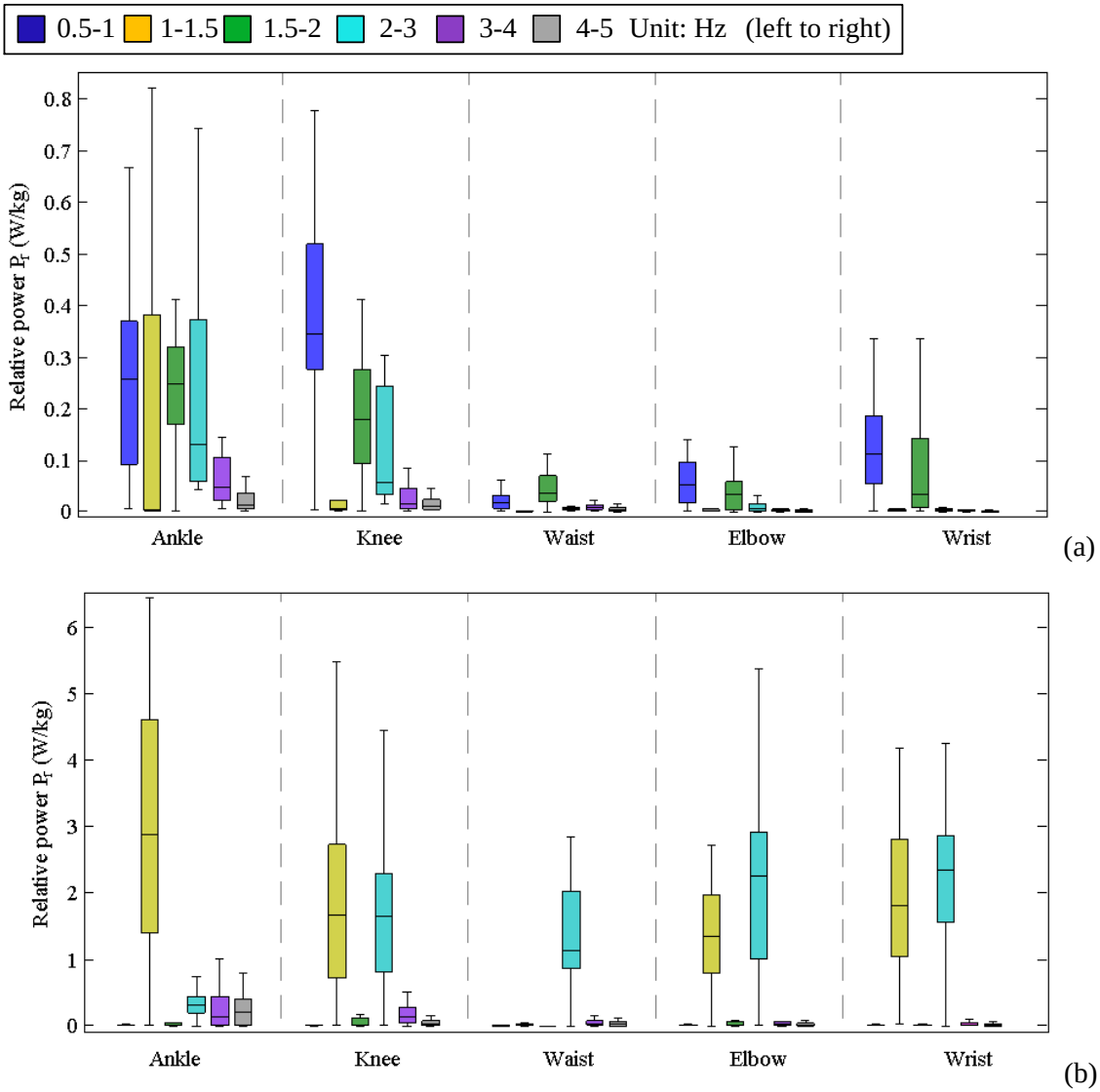

Figure 4.16 Relative power from a 2-DOF generator across different frequency bands for (a) walking and (b) running.

Table 4.6 Predominant frequency bands of the relative power from a 2-DOF generator.

	Ankle	Knee	Waist	Elbow	Wrist
Walk [Hz]	0.5-3	0.5-1, 1.5-3	0.5-1, 1.5-2	0.5-1, 1.5-2	0.5-1, 1.5-2
Run [Hz]	1-1.5	1-1.5, 2-3	2-3	1-1.5, 2-3	1-1.5, 2-3

Figure 4.17 shows the normalised power in the predominant frequency bands during walking. It is found that the variation of the normalised power is significantly reduced, compared to Figure 4.14. This reduction shows that limiting the two resonant frequencies of 2-DOF generators to be in the same frequency band helps to reduce the variation.

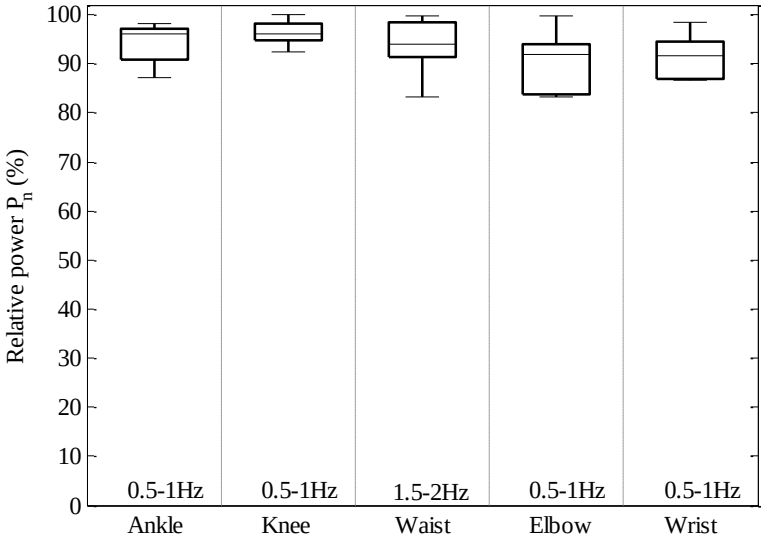

Figure 4.17 Normalised power from a 2-DOF generator in the predominant frequency bands during walking.

4.3 Comparison between 1-DOF and 2-DOF Inertial Energy Harvesters

As described in Section 3.2.2, the 2-DOF analysis method can be used to analyse 1-DOF generators. While the results are not intuitive, they allow for direct comparison of performance with 2-DOF. In this section, the benefits of 2-DOF energy harvesters when harvesting energy from human motion are investigated. The comparison between 1-DOF and 2-DOF inertial energy harvesters in terms of output power and the angular tolerance is made.

For comparison, 1-DOF and 2-DOF generators are assumed to work in the same predominant frequency band, and the two resonant frequencies of 2-DOF energy harvesters are assumed to be in the same frequency band. In Figure 4.10 and Figure 4.16, the frequency band that provides the maximum median of relative power at each location is identified, as shown in Table 4.7. The predominant frequency bands of 2-DOF energy harvesters are wider than or equal to the bands of 1-DOF energy harvesters and 2-DOF analysis method is used for comparison, therefore, the predominant frequency bands of 2-DOF energy harvesters are used in this section.

Table 4.7 Frequency bands that provides the maximum median of relative power.

		Ankle	Knee	Waist	Elbow	Wrist
1-DOF generators	Walk [Hz]	0.5-1	0.5-1	1.5-2	0.5-1	0.5-1
	Run [Hz]	1-1.5	1-1.5	2.5-3	2.5-3	2.5-3
2-DOF generators	Walk [Hz]	0.5-1	0.5-1	1.5-2	0.5-1	0.5-1
	Run [Hz]	1-1.5	1-1.5	2-3	2-3	2-3

1) Ability to Maintain Power at Rotation

As presented in Section 3.2, for 1-DOF generators, the orientation is along one axis defined by two angles; for 2-DOF generators, the orientation consists of two mutually perpendicular axes defined by three angles. The data processing method for 1-DOF generators allows for easy interpretation of the data in different orientations, because the evaluated power is directly corresponding to different orientations. However, it is not suitable for directly comparing the relative performance of both a 1-DOF and 2-DOF generator, because the methods for analysing 1-DOF and 2-DOF generators use different parameters and it is not easy to compare them side by side in a graph. In contrast, the results from the method of 2-DOF generators are not intuitively interpretable, because the evaluated power is corresponding to different planes for the generator rotation. However, the method is suitable to be used for the comparison, because the methods for 2-DOF generators can also be used to evaluate the output power from 1-DOF generators, and the comparison can be taken under the same parameters.

In this section, the 2-DOF analysis method is used to evaluate the output power from 1-DOF energy harvesters for comparison. Figure 4.18 shows the median of relative power among all participants from 1-DOF and 2-DOF generators in different orientations at the ankle during running (frequency band of 1-1.5 Hz). The results show that for 2-DOF energy harvesters, there are more orientations having large relative power than for 1-DOF energy harvesters. It is intuitive to find that 2-DOF generators have greater angular tolerance than 1-DOF generators. For example, if a 2-DOF and a 1-DOF generator are each rotating on the plane (β: 90°, Ø: 0°), the 2-DOF generator is able to generate high output power in all orientations, while the 1-DOF generator is only able to generate high output power in a limited range of orientations.

To investigate the consistency of output power under rotation, the percentage of the orientations with high output power is studied. In Figure 4.18, the ratio of the number of orientations having power greater than or equal to 90% of the maximum median of the relative power to the total number of the orientations is calculated. The term ‘rotate ability’, τ [%], is proposed to represent this ratio. It represents the ability of generators to maintain output power after rotation. For example, in Figure 4.18, the maximum median of the relative power from 1-DOF generators

is 2.60 W/kg, there are 1,300 orientations having power greater than or equal to 2.34 W/kg (90%×2.60 W/kg), and the total number of the orientations is 12,312. Hence the rotate ability τ is 10.6% (1,300/12,312). The rotate ability τ of 1-DOF and 2-DOF generators is calculated independently. The results of the rotate ability τ are shown in Figure 4.19. For 1-DOF generators, and for each location and activity, only 6% (average) of the tested orientations harvest over 90% of the maximum power. For 2-DOF generators, this is increased to 32% (average), showing a considerable improvement. The numbers beside the bars show how much greater the 2-DOF case is than the 1-DOF case, i.e. $\tau_{2\text{-DOF}}/\tau_{1\text{-DOF}}$. The results show that the rotate ability τ of 2-DOF generators is 5.7 times (average) greater than that of 1-DOF generators, indicating a significant increase of the rotate ability τ. For example, it is 9.5 times bigger at the elbow during running. It means that in this case, among all evaluated orientations, 2-DOF generators have 9.5 times greater potential to generate over 90% of the maximum power. Furthermore, the benefit of 2-DOF generator in the rotate ability τ is also found in the normalised power. The results show that the rotate ability τ of 2-DOF generators is 5.2 times (average) greater.

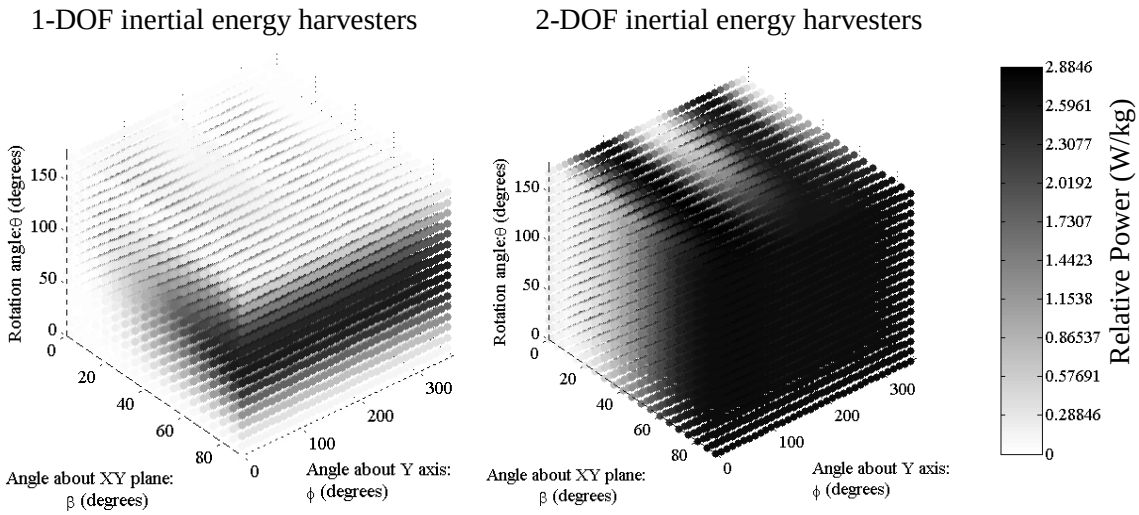

Figure 4.18 Median of relative power from 1-DOF and 2-DOF generators in different orientations on the ankle during running (frequency band of 1-1.5 Hz).

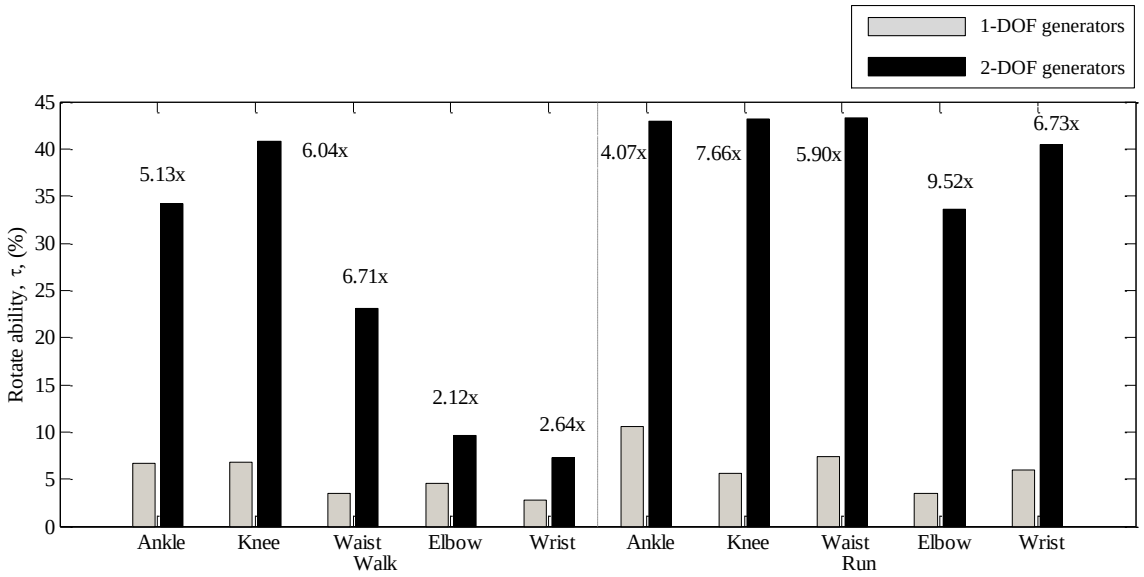

Figure 4.19 Rotate ability τ of 1-DOF and 2-DOF generators at the five locations. The numbers beside the bars show how much greater the 2-DOF case is than the 1-DOF case, i.e. $\tau_{\text{2-DOF}}/\tau_{\text{1-DOF}}$.

2) Output Power

To compare the output power from 1-DOF and 2-DOF generators, the normalised and relative power in the predominant frequency bands are investigated. The results show that if a 2-DOF and a 1-DOF generator are placed along the same orientation, the 2-DOF generator is able to harvest more power than the 1-DOF generator. Along each orientation (shown in Figure 4.18), the increase in power output is calculated. It is found that the normalised power from 2-DOF generators is 1.42-2.14 times (the median of the increase across all orientations at each location during each activity) greater than that from 1-DOF generators, or 2.10-2.67 times greater for the relative power.

The results show that the optimum orientations of 1-DOF and 2-DOF generators are not the same for the same location and activity. For example, in Figure 4.18, the optimum orientation is ($\Delta\beta$: 80 °, $\Delta\emptyset$:160 °, $\Delta\theta$: 90 °) for 1-DOF generators, while it is ($\Delta\beta$: 35 °, $\Delta\emptyset$:100 °, $\Delta\theta$: 0 °) for 2-DOF generators. If a 2-DOF and 1-DOF generator is along their optimum orientations, the 2-DOF generator does not get significantly more power than the 1-DOF generator. During walking and running, 2-DOF generators produce 18% (average) more in the median of the relative power than 1-DOF generators along the optimum orientations, or just 6% for the normalised power. The results of the relative power along the optimum orientations during running are shown in Figure 4.20. The increases are only 11%, 4%, 6%, 7% and 6% at the ankle, knee, waist, elbow and wrist, respectively.

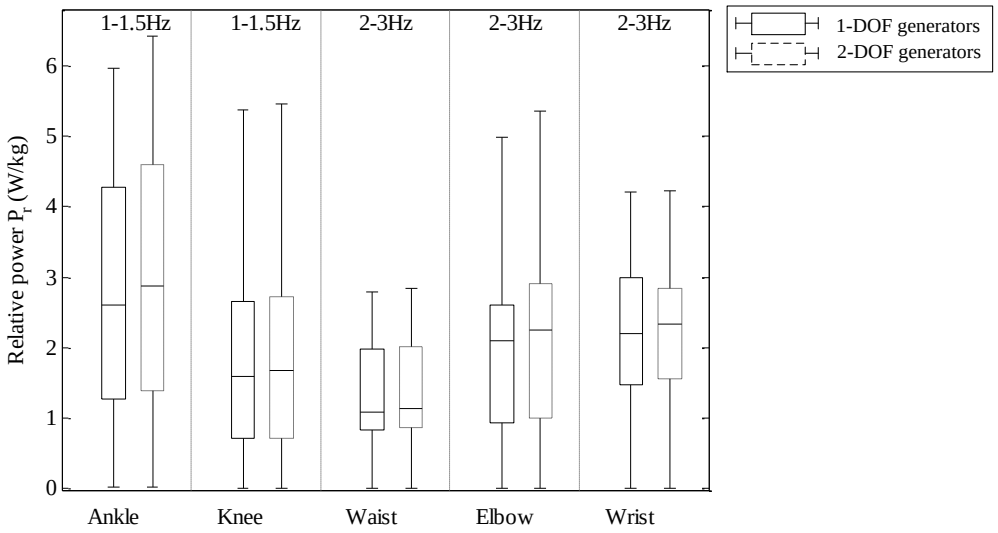

Figure 4.20 Comparison of relative power from 1-DOF and 2-DOF generators along the optimum orientations in the predominant frequency bands during running.

3) Angular Tolerance

For comparison, the angular tolerance α of the optimum orientations for 1-DOF and 2-DOF energy harvesters is studied. The angular tolerance α for the relative power is shown in Figure 4.21. The numbers beside the bars are the values of the 2-DOF generator's angular tolerance over the 1-DOF generator's angular tolerance, showing how much greater the 2-DOF case is than the 1-DOF case. The results show the angular tolerances of 2-DOF generators are greater than or equal to those of 1-DOF generators. It is up to three times greater at the ankle while walking. The average increase of the angular tolerance for the relative power is 73%. Furthermore, the benefit of 2-DOF generators in the angular tolerance is also found in the normalised power. The average increase is 38%. Therefore, 2-DOF energy harvesters are able to significantly increase the tolerance to rotation if the two kinds of generators are both along the optimum orientations.

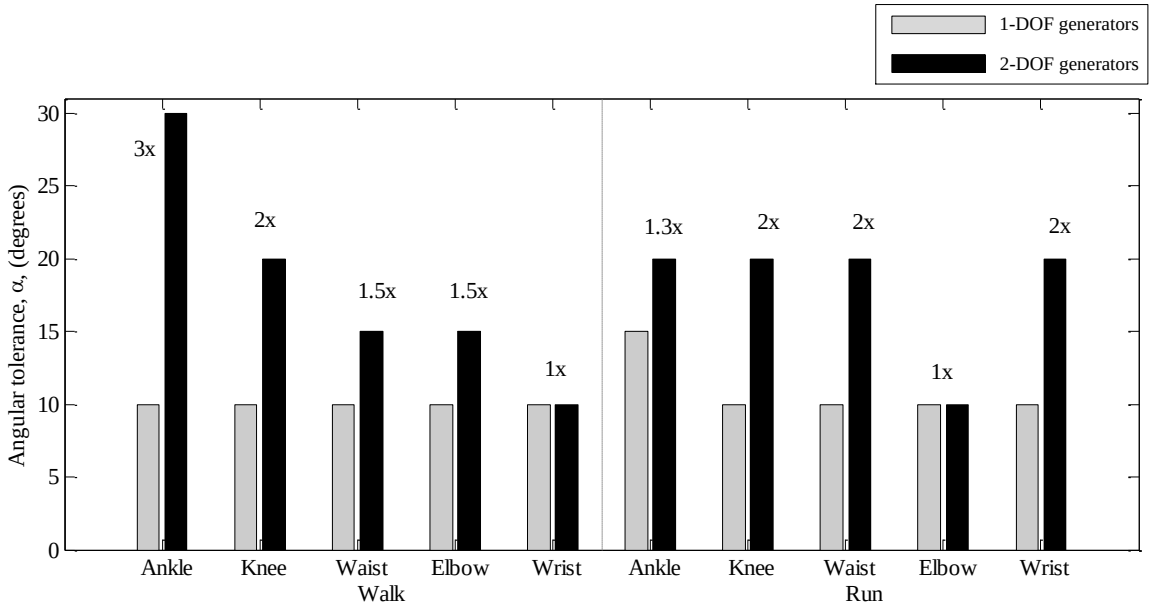

Figure 4.21 The angular tolerance of the optimum orientations for 1-DOF and 2-DOF generators on the relative power. The numbers beside the bars show how much greater the 2-DOF case is than the 1-DOF case, i.e. $\alpha_{\text{2-DOF}}/\alpha_{\text{1-DOF}}$.

4) Different 2-DOF Arrangements

The effect of 2-DOF arrangements that employ different angles between the two 1-DOF generators on the output power has been evaluated. The angle is increased from 0° to 90° in steps of 10°. Table 4.8 shows the relative power, the angular tolerance along the optimum orientations, and the rotate ability of different 2-DOF arrangements. Comparing the relative power at 0° and 90° angles, the output relative power from two parallel 1-DOF generators is 1.72 times (average) larger than that from two orthogonal 1-DOF generators when both 2-DOF generators are along their own optimum orientations. Hence, arranging two separate 1-DOF generators in orthogonal directions decreases the power density (power normalised for mass) generated along the optimum orientations. In addition, from Table 4.8, the output relative power is decreasing with the increase of the angle, which highlights that the arrangement of two orthogonal 1-DOF generators does not have benefits in terms of power output generated. However, the arrangement of two orthogonal 1-DOF generators offers the advantage of improving the angular tolerance and the rotate ability. It has a relative great angular tolerance at the five locations during walking and running, and its average angular tolerance is 18°. The average angular tolerance is 11°, 11°, 11°, 11°, 16°, 17°, 17°, 17°, and 19° for 0°-80°, respectively. Moreover, the arrangement of two orthogonal 1-DOF generators is able to significantly improve the rotate ability. Its rotate ability is 33.5% (average), which is 5.83, 5.81, 5.77, 5.57, 5.40, 4.79, 4.51, 3.96, and 2.89 times greater than that at 0°-80°, respectively. To

validate the benefits of 2-DOF generators that consist of two orthogonal 1-DOF generators in terms of angular tolerance and rotate ability, two orthogonal 1-DOF generators have been designed, fabricated and tested on the human body. This work is presented in Chapter 5 and 6.

Table 4.8 Output relative power, angular tolerance along the optimum orientations, and rotate ability of different 2-DOF arrangements in the predominant frequency bands.

	ankle						**knee**					
	walk			run			walk			run		
Angle	P_r	α	τ	P_r	α	τ	P_r	α	τ	P_r	α	τ
0	0.458	10	6.65	5.20	15	10.6	0.678	10	6.76	3.20	10	5.63
10	0.468	10	5.86	5.18	15	11.1	0.669	10	6.83	3.15	10	5.81
20	0.454	10	6.71	5.07	15	10.6	0.653	10	6.90	3.09	10	5.71
30	0.441	10	5.92	4.85	20	11.3	0.630	10	6.94	2.96	10	6.08
40	0.416	10	6.99	4.67	15	10.6	0.596	20	7.29	2.81	20	6.25
50	0.391	10	6.94	4.33	20	11.5	0.559	20	7.56	2.64	25	7.10
60	0.360	10	7.76	4.00	20	11.6	0.512	20	8.54	2.40	20	7.88
70	0.327	10	9.49	3.63	20	12.0	0.460	20	9.50	2.17	20	9.33
80	0.290	30	12.5	3.26	20	13.2	0.404	20	12.8	1.86	20	12.8
90	0.257	30	34.2	2.88	20	43.0	0.345	20	40.8	1.67	20	43.1
	waist						**elbow**					
	walk			run			walk			run		
Angle	P_r	α	τ	P_r	α	τ	P_r	α	τ	P_r	α	τ
0	0.0498	10	3.44	2.16	10	7.33	0.0718	10	4.56	4.20	10	3.53
10	0.0495	10	3.78	2.16	10	8.26	0.0716	10	4.79	4.02	10	3.46
20	0.0494	15	3.64	2.11	10	7.68	0.0707	10	4.57	4.09	10	3.44
30	0.0460	10	4.24	2.04	10	8.52	0.0671	10	4.26	3.81	10	3.50
40	0.0463	20	4.85	1.93	10	8.79	0.0649	10	3.80	3.72	20	3.27
50	0.0443	20	6.89	1.81	10	9.65	0.0632	10	3.67	3.74	20	4.17
60	0.0431	20	7.65	1.66	10	10.1	0.0658	10	1.37	3.15	20	4.49
70	0.0406	20	8.44	1.50	10	10.9	0.0681	20	1.31	2.88	20	6.13
80	0.0413	10	15.5	1.31	20	14.4	0.0596	20	2.01	2.49	15	9.97
90	0.0379	15	23.1	1.14	20	43.3	0.0533	15	9.67	2.25	10	33.6
	wrist											
	walk			run								
Angle	P_r	α	τ	P_r	α	τ						
0	0.179	10	2.77	4.40	10	6.00						
10	0.182	10	2.74	4.41	10	5.15						
20	0.178	10	2.77	4.28	10	5.93						
30	0.171	10	2.74	4.20	10	5.80						
40	0.166	10	2.82	3.93	15	6.03						
50	0.163	15	2.65	3.74	15	7.07						
60	0.145	10	2.73	3.46	20	7.26						
70	0.140	10	2.49	3.11	20	8.97						
80	0.129	15	2.84	2.70	20	11.6						
90	0.113	10	7.31	2.34	20	40.4						

Unit: Angle [degrees], P_r: [W/kg], α [degrees], τ [%].

4.4 Conclusions

This chapter presented the investigation of the effect of orientation, location and activity on generated power from 1-DOF and 2-DOF inertial energy harvesters. The results show that the output power is affected by the orientation of both 1-DOF and 2-DOF energy harvesters. A rotation of $20°$ from the optimum direction reduces the available output power from 1-DOF generators by at least 10%. For 2-DOF generators, this tolerance is increased to $30°$.

The normalised and relative power are considered in conjunction to identify the optimum locations to place 1-DOF generators. It has been found that the knee and ankle are the optimum locations for walking and running, respectively. The optimum locations for 2-DOF generators during different activities have also been identified. The ankle and wrist are the best places for 2-DOF generators for walking and running, respectively.

In addition, the results of 1-DOF generators show that the lower body can generate much more relative power than the upper body during walking, however, for running, the difference between the power output on the upper and lower body is less significant. For walking, the same conclusion has been derived from the 2-DOF analysis, while the conclusion from 2-DOF analysis in running is different. The results of 2-DOF analysis show that for running, the elbow and wrist are able to generate more power than the lower body, but that the correlation of output power among participants is not as good as for the lower body.

The predominant frequencies that make a great contribution to the output power from 1-DOF generators have been identified during different activities. The results show that for walking the predominant frequency bands are all below 2.5 Hz at all locations, while for running, the higher frequency band of 2.5-3 Hz is introduced to provide high output power. The median of the predominant frequencies is between 0.875-1.75 Hz during walking; due to the strong impact between the ground and foot during running and both feet striking the ground, the median of the predominant frequencies on the upper body (2.61-2.66 Hz) is approximately twice that of the predominant frequencies on the lower body (1.31-1.34 Hz). The predominant frequency bands of 2-DOF generators are the same as 1-DOF generators.

Furthermore, a comparison between the 1-DOF and 2-DOF energy harvesters has been made in terms of the rotate ability τ. The rotate ability τ represents the ability to maintain 90% of the maximum power at rotation. The comparison results show that the rotate ability τ of 2-DOF generators is 5.7 times (average) greater than that of 1-DOF generators for relative power, and 5.2 times (average) greater for normalised power. This significant increase of the rotate ability τ

means that 2-DOF generators have a greater tolerance to rotation and a much greater potential to generate over 90% of the maximum power, compared to 1-DOF generators. In addition, caparison in terms of the output power and the angular tolerance α has been made. The results indicated that 2-DOF generators do not get significantly more power than 1-DOF generators if these two kinds of generators are both along the optimum orientations. During walking and running, 2-DOF generators produce 18% (average) more in the median of the relative power than 1-DOF generators along the optimum orientations, or just 6% for the normalised power. However, 2-DOF energy harvesters are able to significantly increase the tolerance to rotation. The average increase of the angular tolerance for the relative power is up to 73%, or 38% for the normalised power.

A complete table combining results of the analysis on 1-DOF and 2-DOF generators are shown in Table 4.9. It shows the optimum orientations, the relative and normalised power, the corresponding frequency, the angular tolerance α and the rotate ability τ. The values in the green and blue cells are the maximum power during walking and running, respectively.

In this chapter and previous chapter, the 1-DOF and 2-DOF inertial energy harvesters have been modelled and analysed. The analytical results show that 2-DOF generators' major contribution for harvesting energy from human motion is the angular tolerance, and they have greater angular tolerance compared to 1-DOF generators. To validate the results, a human-powered 2-DOF inertial energy harvester is designed and fabricated. This work is presented in the next chapter. In Chapter 6, the analytical results are validated experimentally.

Table 4.9 Complete results of analysis on 1-DOF and 2-DOF generators.

				β	$\emptyset$	θ	Power	α	τ	IQR	Band	f_x	IQR	f_y	IQR
Units:				[Degrees]			[% or W/kg]	[Degrees]	[%]	[% or W/kg]	[Hz]	[Hz]		[Hz]	
P_n [%]	ankle	walk	1-DOF	45	100	80	94	20	6.81	12	0.5-1	0.875	0.0625		
			2-DOF	85	320	10	96	20	40.5	6		0.844	0.0625	0.875	0.0859
		run	1-DOF	45	100	90	96	20	8.85	5	1-1.5	1.34	0.156		
			2-DOF	80	90	40	97	30	45.7	2		1.34	0.141	1.33	0.141
	knee	walk	1-DOF	65	190	120	94	10	5.74	8	0.5-1	0.875	0.0625		
			2-DOF	70	190	20	96	20	37.5	3		0.844	0.125	0.875	0.0625
		run	1-DOF	55	70	140	97	15	5.34	3	1-1.5	1.31	0.188		
			2-DOF	55	190	20	98	20	33.5	1		1.31	0.188	1.31	0.156
	waist	walk	1-DOF	80	110	30	84	15	9.82	25	1.5-2	1.75	0.0938		
			2-DOF	85	10	10	94	25	31.2	8		1.75	0.0938	1.75	0.188
		run	1-DOF	85	40	0	97	20	8.03	5	2-3	2.61	0.281		
			2-DOF	85	40	20	98	25	44.4	2		2.61	0.281	2.61	0.188
	elbow	walk	1-DOF	10	330	60	76	10	3.62	42	0.5-1	0.875	0.0859		
			2-DOF	0	140	20	92	10	8.41	10		0.875	0.0859	0.875	0.0859
		run	1-DOF	80	140	130	93	10	5.24	11	2-3	2.66	0.344		
			2-DOF	70	70	50	98	20	43.1	4		2.63	0.383	2.66	0.344
	wrist	walk	1-DOF	45	90	140	83	10	4.14	11	0.5-1	0.875	0.0625		
			2-DOF	0	50	60	92	10	9.73	8		0.875	0.0625	0.875	0.0781
		run	1-DOF	60	80	120	96	20	6.32	7	2-3	2.64	0.359		
			2-DOF	75	150	50	98	20	42.6	5		2.59	0.359	2.64	0.359
P_r [W/kg]	ankle	walk	1-DOF	60	290	80	0.229	10	6.65	0.27	0.5-1	0.875	0.0625		
			2-DOF	75	80	30	0.257	30	34.2	0.276		0.844	0.0547	0.875	0.0625
		run	1-DOF	80	160	90	2.60	15	10.6	3.01	1-1.5	1.34	0.156		
			2-DOF	35	100	0	2.88	20	43.0	3.20		1.31	0.109	1.34	0.156
	knee	walk	1-DOF	45	60	120	0.339	10	6.76	0.249	0.5-1	0.875	0.0625		
			2-DOF	55	230	40	0.345	20	40.8	0.241		0.844	0.0625	0.875	0.0625
		run	1-DOF	30	210	110	1.60	10	5.63	1.94	1-1.5	1.31	0.188		
			2-DOF	10	220	20	1.67	20	43.1	2.00		1.31	0.156	1.31	0.188
	waist	walk	1-DOF	60	110	70	0.0249	10	3.44	0.0196	1.5-2	1.75	0.188		
			2-DOF	75	200	50	0.0379	15	23.1	0.0498		1.75	0.0938	1.75	0.0938
		run	1-DOF	55	10	0	1.08	10	7.33	1.16	2-3	2.61	0.281		
			2-DOF	80	150	20	1.14	20	43.3	1.16		2.61	0.281	2.61	0.188
	elbow	walk	1-DOF	45	270	20	0.0359	10	4.56	0.0526	0.5-1	0.875	0.0859		
			2-DOF	10	340	10	0.0533	15	9.67	0.0786		0.875	0.0859	0.875	0.141
		run	1-DOF	70	70	140	2.10	10	3.53	1.67	2-3	2.66	0.344		
			2-DOF	65	80	50	2.25	10	33.6	1.90		2.63	0.383	2.66	0.344
	wrist	walk	1-DOF	45	180	110	0.0894	10	2.77	0.131	0.5-1	0.875	0.0781		
			2-DOF	10	230	20	0.113	10	7.31	0.132		0.875	0.0938	0.875	0.0625
		run	1-DOF	75	130	110	2.20	10	6.00	1.52	2-3	2.63	0.359		
			2-DOF	30	250	50	2.34	20	40.4	1.29		2.64	0.344	2.63	0.328

Chapter 5
A Novel 2-DOF Inertial Generator for Human-Powered Energy Harvesting

The analytical results in Chapter 4 show that if a 1-DOF and 2-DOF inertial energy harvester are along their optimum orientations and attached to the same location during the same activity, the 2-DOF inertial energy harvester is, while not generating significantly more power, able to significantly increase the tolerance to rotation, compared to the 1-DOF harvester. To validate these results rather than to design the best generator, a real human-powered inertial energy harvester is designed. In this chapter, mechanical-spring and magnetic-spring electromagnetic energy harvesters are considered for that purpose, two designs presenting different benefits. Both are easy to construct. Mechanical springs have the benefit of constant spring stiffness, and magnetic springs have the benefit of low mechanical fatigue.

In Section 5.1, the design requirements of the human-powered inertial energy harvesters are outlined, followed by the discussion of the design and analysis of a mechanical-spring resonator and a magnetic-spring resonator. Section 5.4 presents the coil design relating to the two resonator designs for constructing electromagnetic generators. Section 5.5 discusses the MATLAB models that are used to predict the voltage output of the designed generators under sinusoidal vibrations.

5.1 Design Requirements

To validate the benefit of 2-DOF energy harvesters in terms of tolerance to rotation, both a 1-DOF and a 2-DOF inertial energy harvester must be deployed at the same location during the same activity. The generators are rotated on the location to change the orientation, and the output power is measured to evaluate their angular tolerance.

To be consistent with the data analysis methods in Chapter 3, the 2-DOF inertial energy harvester that is used in the validation should comprise two orthogonal 1-DOF inertial energy harvesters. Similar to the comparison between 1-DOF and 2-DOF inertial energy harvesters in Section 4.3, the two orthogonal 1-DOF inertial energy harvesters should have the same resonant frequencies for comparison. Therefore, for simplicity, a 1-DOF inertial energy harvester is designed and two prototypes are fabricated to make up a 2-DOF inertial energy harvester.

As a comprehensive experimental validation for all the evaluated orientations (the five locations and the two activities) cannot be finished within the limited time available for PhD research, the configuration of the knee during running has been selected for the validation. The analytical results in the previous chapter show that the running activity is able to generate more power than the walking activity. During running, the lower body can generate relatively more output power than the upper body. The knee in particular permits a larger potential design volume for generators than the ankle does. It is according to these conditions that the knee and running are selected for the validation (Figure 5.1). A number of design requirements of human-powered inertial energy harvesters are next identified to ensure the energy harvesters are suitable for the validation.

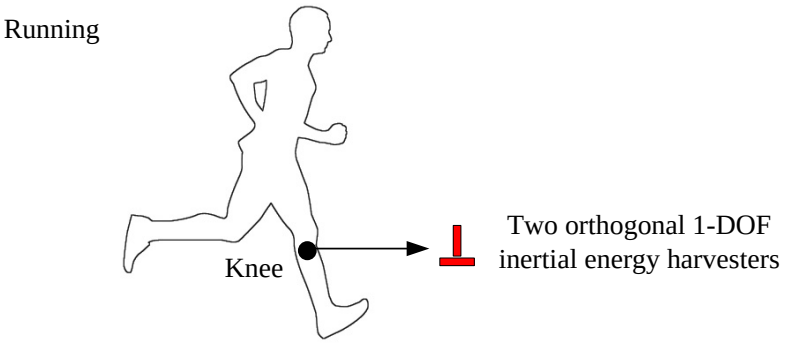

Figure 5.1 Illustration of the test location on the body and the test activity. The bars represent the two orthogonal 1-DOF inertial energy harvesters.

1) Size and Weight

Because the 2-DOF inertial energy harvester is just used to validate the results, it does not need to be as non-intrusive as commercial products would be. However, it does need to be light and small enough to be suitable to be worn on the knee, and must not affect the way people run. For example, the knee-mounted commercial leg cuff of the NESS L300™ foot drop system [92], a medical device used to stimulate the muscle in order to help people walk more naturally, is $135 \times 100 \times 15$ mm^3 and weighs approximately 150 g. The physical size and weight of some existing knee-worn energy harvesters have been reviewed in Sections 2.2 and 2.3. The human-powered generator proposed by Büren *et al.* [17], which can be worn on the knee, is $24 \times 38 \times 34$ mm^3 and approximately 43 g in weight. The ring-shaped knee-joint piezoelectric generator proposed by Pozzi *et al.* [79], shown in Figure 2.20, is of 60 mm radius, 21 mm in height and weighs approximately 235g. In that study, the participants did not report that the generator significantly affected the way they walked. Therefore, the test 2-DOF generator should be smaller than $120 \times 120 \times 20$ mm^3 and below 230 g in weight without interfering with the way people run.

2) Resonant Frequency

To maximise the generated output power from human-powered energy harvesters, the resonant frequency should match the predominant frequency of human motion. The analytical results (Table 4.1 and Table 4.4) show that the predominant frequencies at the knee during running for 1-DOF and 2-DOF energy harvesters are 1.3 Hz. To identify the resonant frequency of the test energy harvester, the output power from a 1-DOF energy harvester along the optimum orientation at different frequencies of human motion has been found, as illustrated in Figure 5.2. In the previous data analysis (Section 3.2.1), the maximum relative power within a 0.5 Hz frequency band is considered as the output relative power, and damping ratios are not considered in the analysis. To be consistent with that data analysis, in Figure 5.2, a window of 0.5 Hz is sliding from 0 Hz to 10 Hz, and then the maximum relative power in the window is considered as the obtainable power at the center frequency of the window. It is found that the first three harmonics of 1.3 Hz, 2.6 Hz and 3.9 Hz provide high output power.

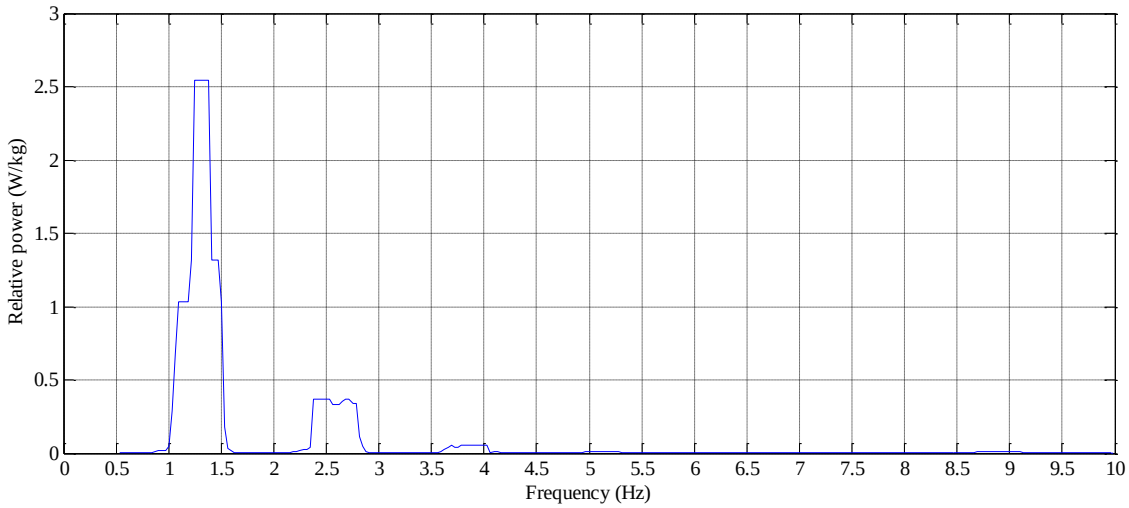

Figure 5.2 Relative output power from a 1-DOF energy harvester along the optimum orientation at different frequencies of human motion on the knee during running.

Inertial energy harvesters can be modelled as a second-order spring-mass system. From Equation (2.9), decreasing the resonant frequency results in an increase of the quiescent position of proof mass in a spring-mass system. The larger the quiescent position, the larger the physical size of the generator. Therefore, the quiescent position of the proof mass limits the design of the inertial energy harvester. Based on Equation (2.9), the quiescent position with respect to the resonant frequency is illustrated in Figure 5.3. At 1.3 Hz, the quiescent position is 147 mm, which is too large for a knee-worn inertial generator; however, at 3.9 Hz, the quiescent position is 16 mm, which makes the generator design much more feasible. At 3.9 Hz, the output power is

3% of the maximum power at 1.3 Hz, while the quiescent position is better than that at 1.3 Hz. Therefore, 3.9 Hz is chosen as the resonant frequency of the test 1-DOF inertial energy harvester.

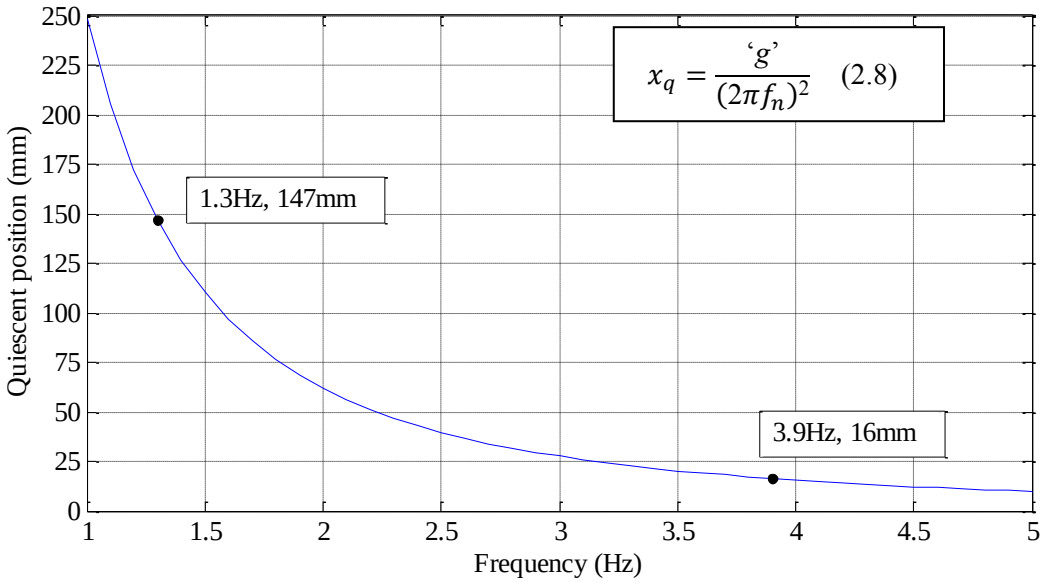

Figure 5.3 The quiescent position with respect to the resonant frequency.

To validate the results, the generators will be tested in different orientations. Due to the effect of gravity, the quiescent position of the seismic mass of the generator will change with rotation, and it is essential that the generators behave in the same way along different orientations. Therefore, the resonant frequency of the inertial energy harvester should be constant with rotation. For a given seismic mass of the generator, the resonant frequency only depends on the spring stiffness (Equation (2.6)). Hence, the spring stiffness has to be independent of the quiescent position to ensure a constant resonant frequency under rotation.

3) Test Generators

In the study done by Büren [17], it was found that piezoelectric and electromagnetic generators achieve higher power density than electrostatic generators, when generators are mounted on the lower body with a maximum displacement of proof mass over 800 μm. Piezoelectric and electromagnetic generators are therefore considered for this validation.

In the design of a 1-DOF inertial piezoelectric generator, a piezoelectric cantilever is one option [73, 93-95]. In this approach, one end of the cantilever is fixed and the other end is attached with an end load (Figure 2.21). In the previous data analysis, the proof mass is assumed to only move along the direction of vibrations. Hence, in the case of a cantilever, the cantilever beam

should be straight and perpendicular to the direction of vibrations, as shown in Figure 2.21. However, if the cantilever has a resonant frequency of 3.9 Hz and is perpendicular to the direction of gravity, the free end will deflect by 16 mm due to the effect of gravity, as shown in Figure 5.4. Therefore, the direction of vibrations is no longer perpendicular to the cantilever, which is not consistent with the previous data analysis. Further, the movement of the cantilever is not displaced along one axis but along two axes under the excitation of vibrations, and thus a potentially larger physical volume of the generator is required. Therefore, the cantilever structure is not suitable for the validation.

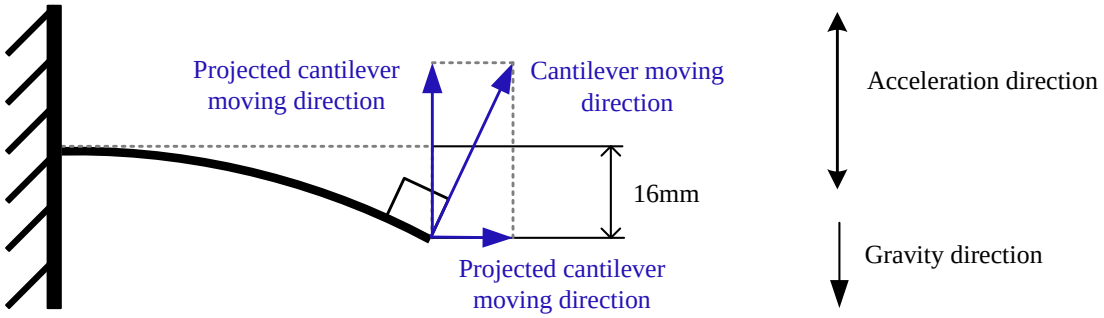

Figure 5.4 A cantilever deflected by 16 mm due to the gravity.

For a 1-DOF inertial electromagnetic generator, mechanical- and magnetic-spring electromagnetic generators are good choices. They are both easy to construct. The benefit of mechanical-spring electromagnetic generators [17, 63] is that the spring stiffness of a mechanical spring is constant within elastic limits and not affected by rotation. The benefit of magnetic-spring electromagnetic generators [86, 96] is the low level of mechanical fatigue. Magnetic springs exploit the magnetic repelling force between two magnets with the same poles facing each other (Figure 2.23). There is no physical contact between the suspended magnet and the two end magnets, thus the magnetic spring exhibits low mechanical fatigue. Unlike mechanical springs, magnetic springs have a nonlinear force-displacement relationship, and hence a variable stiffness, which leads to variable resonant frequencies. Therefore, the magnetic spring should be linearised in this research to meet the requirement of constant spring stiffness.

5.2 Mechanical-Spring Resonator

Section 5.2.1 presents the design and fabrication of a mechanical-spring resonator; the measurement of the spring stiffness of the fabricated spring is then presented in Section 5.2.2.

5.2.1 Design

No commercial springs were available that met the requirements of a low spring constant (for a 3.9 Hz resonant frequency) within the required physical size. Therefore, particular attention has to be paid to the design and specifications of a manufactured linear mechanical spring.

The spring constant of a coil spring is defined as [97]:

$$k = \frac{Gd^4}{8N_aD^3} \tag{5.1}$$

where G [Pa] is the modulus of rigidity of the wire material, N_a is the number of active coils, D [m] is the mean outside diameter of the spring coil (mean value of the inside diameter and the outside diameter) and d [m] is the wire diameter. The active coils are the coils that are free to move or deflect under a load.

Substituting Equation (5.1) in Equation (2.6), the resonant frequency of a spring mass system is expressed as:

$$f_0 = \frac{1}{2\pi}\sqrt{\frac{Gd^4}{8N_aD^3m}} \tag{5.2}$$

Equation (5.2) shows that increasing the number of coils N_a, the mean coil diameter D, or decreasing the wire diameter d all reduces the resonant frequency. However, increasing the number of coils N_a will increase the total length of the spring and then extend the dimension of the energy harvester. Furthermore, considering that the predominant direction of human motion is variable in daily life, a long, soft spring with a small value of G is easily deflected by an external force that is not along the central axis of the spring. In that case, the spring cannot be used to validate the results, because springs are considered to vibrate only along a single axis in the data analysis in Chapter 3, and the validation should be consistent with this analysis.

For manufacturing, the wire diameter d cannot be arbitrarily small and the mean outside diameter D cannot be arbitrarily large. Spring index I_s is defined as the ratio of the mean coil diameter D to the wire diameter d (Equation (5.3)), which is an important indicator for manufacturing ease and cost control. Typically, the spring index of a commercial spring is between 3 and 20 [98]. Springs designed outside this range increase cost and require more tolerance on the coil diameter, wire diameter and spring length, and hence the spring stiffness.

$$I_s = \frac{D}{d} \tag{5.3}$$

As discussed above, the test 1-DOF inertial energy harvester is required to be within $120 \times 120 \times 20$ mm^3 and below 230 g, and the specified resonant frequency is 3.9 Hz. The spring stiffness of the mechanical spring is designed to be as small as possible within the limitations of physical size. Through communicating with spring manufacturers and considering the manufacturing ease and cost, a spring with spring stiffness of 27 N/m and a free length of 45 mm is designed. The free length of a spring is the overall length of a spring in the unloaded position. Table 5.1 shows the specifications of the cylindrical compression spring with round wire. The values of the tolerances are provided by the spring manufacturer. In this research, 302 Stainless Steel is selected to fabricate the spring. It is a material commonly used in spring manufacture because of its corrosion-resistance and other physical properties. Considering the spring will be attached to a moving mass, closed and ground spring ends [99] were chosen in the design to provide a flat plane. The parameters d, D and N_a are designed to make the spring stiffness k and the spring index I_s small. However, the spring index I_s of the designed spring is 29, which is outside the typical range of spring indices; as a result, the manufacturing tolerances of the spring stiffness are increased. The fabricated springs therefore need to be tested to verify the spring stiffness.

Table 5.1 Design specifications of the cylindrical compression spring with round wire.

Parameters	Dimensions
Wire diameter (d)	0.380 ± 0.0102 mm
Free length	45 ± 4.09 mm
The mean coil diameter (D)	11.2 ± 0.529 mm
The number of active coils (N_a)	4.71
Total number of coils	6.71
End type	Closed and ground
Material of spring	302 Stainless Steel (G=69 Gpa)
Spring rate	21-35 N/m (27 N/m desired)

Figure 5.5 shows the structure of the mechanical-spring resonator. This resonator is a component of the electromagnetic generator, and consists of a tube, two end caps, a spring, two tungsten masses, and a cylindrical magnet. The two tungsten masses and the magnet are glued together so that they move as a single object. Both ends of the spring are glued to an end cap and tungsten mass separately. Experimental prototypes of the mechanical-spring resonator are fabricated, and its specifications of the mechanical-spring resonator are shown in Table 5.2.

Table 5.2 Specifications of the mechanical-spring resonator.

Parameters	Dimensions [mm]	Weight [g]	Material
Magnetic cylinder	Diameter=11.5 Height=12	9.30	NdFeB N33SH (B_r=1.15 T)
Tungsten masses	Diameter=11.6 Height=9.35	18.8	Tungsten
Tube	Outer diameter=15 Inner diameter=12 Height=120	43.4	Tufset Polyurethane
Moving mass	Two tungsten masses plus a magnetic cylinder	46.9	

Tufset Polyurethane is selected as a suitable material for the tube in order to minimise the dry friction between the moving mass and the inner face of the tube. One end cap that is not connected to the spring is made of rubber to reduce the mechanical damping in case of an end-stop collision between the moving mass and the end cap. The other end cap is made of plastic to ensure the cap is stiff enough to not affect the spring stiffness of the device. The spring between the plastic cap and the tungsten mass prevents the direct end-stop collision between them. The material used for the permanent magnet is NdFeB N33SH, with a remanent flux density B_r of 1.15 T. Tungsten is chosen as material for the mass because of its hardness and high density of 19,250 kg m^{-3}. The maximum allowed displacement of the magnet is 25 mm if the spring-mass generator stands up in the direction of gravity (as in Figure 5.5). Given the designed 27 N/m spring stiffness and the required 3.9 Hz resonant frequency, a 44.9 g moving mass is needed. Due to manufacturing issue, the fabricated moving mass is 2 g heavier than the design. Therefore, if the spring stiffness is 27N/m, the resonant frequency is 3.82 Hz.

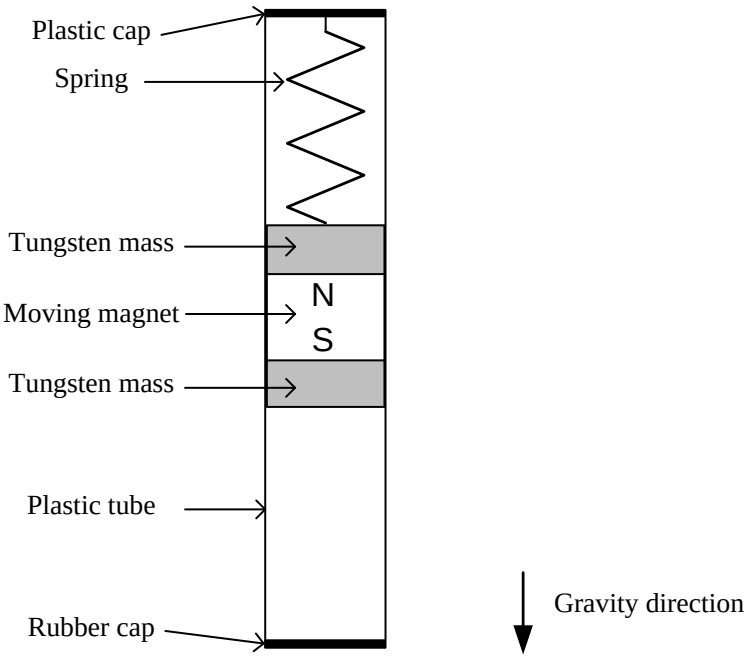

Figure 5.5 Structure of the mechanical-spring resonator.

5.2.2 Spring Stiffness Measurement

Hooke's law states that the force F_s [N] needed to extend or compress a spring by some distance X_s [m] is proportional to that distance, defined as:

$$F_s = kX_s \tag{5.4}$$

Therefore, the spring stiffness k is the ratio of the force to the displacement of the spring. To evaluate the spring stiffness of a fabricated spring, the relationship between displacement of the spring and applied force is investigated. Figure 5.6 shows the measurement setup used to evaluate the spring stiffness of the fabricated spring. The spring prototype is connected between a stationary board and a digital force meter (SPC Technology; SLD 5FGN) through two plastic caps using superglue. The force meter has a measurement range of ±50 N at a resolution of 10 mN, and it is pulled in line with the central axis of the spring over a measurement range of 0-25 mm in steps of 1 mm using 18AWG wire (1.02 mm diameter). 18AWG wire is chosen because it is stiff enough to not affect the spring stiffness measurement. A fixed ruler with a measurement range of 15 cm at a resolution of 1 mm is used to measure the displacement of the spring. A stationary aluminium plate is set under the force meter to reduce the dry friction. In the measurement, the force should be aligned with the central axis of the spring; therefore, two aluminium bars were used to shape a channel to ensure that the force meter was moving along the central axis of the spring, as shown in Figure 5.7.

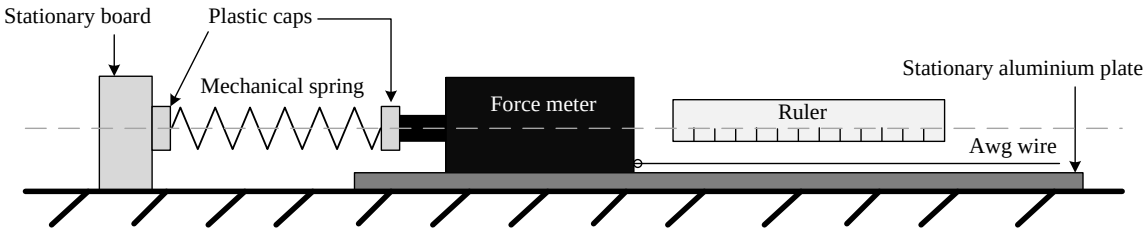

Figure 5.6 The measurement setup to evaluate the spring stiffness of the mechanical spring.

Figure 5.7 Measurement setup showing the two aluminium bars used to shape a channel to ensure the force meter moves along the central axis of the spring.

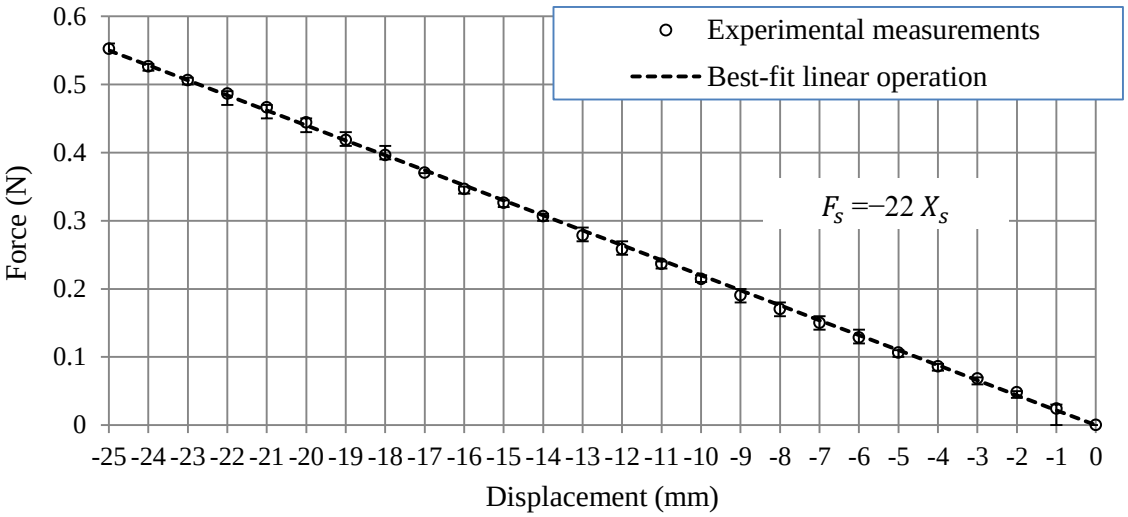

Figure 5.8 Force vs. displacement for the mechanical spring. The average force is represented by circles. The error bars show the minimum and maximum of the measurement results. The dashed line shows the best-fit linear operation based on the measurement results.

Figure 5.8 shows the applied force versus displacement. In Figure 5.6, if the spring is compressed from the original position, the displacement is presented as positive displacement. In contrast, if the spring is extended from the original position, the displacement is presented as negative displacement. Measurements were repeated five times. In Figure 5.8, the average force

is represented by circles. The error bars show the minimum and maximum of the measurement results. The dashed line shows the best-fit linear operation to the measurement results.

The best-fitting straight line is used to identify the spring stiffness of the spring, and is determined by minimising the deviations that are defined as the vertical distances between the measured data and a regression line in Figure 5.8. The independent linearity δ [%] of the applied force versus the displacement is investigated, defined by:

$$\delta = \frac{\sigma_{max}}{y_{pp}} \tag{5.5}$$

where σ_{max} [m] is the maximum deviation between the actual data and the best-fitting straight line and y_{pp} [m] is the full-scale region (displacement from -25 mm to +25 mm) of the best-fitting straight line. In Figure 5.8, σ_{max} is 0.008 N at 13 mm and 9 mm, and y_{pp} is 1.10N; thus the independent linearity δ is 0.727%, which means the graph of force versus displacement only deviates from the best-fitting straight line by a maximum of 0.727%. Therefore, the best-fitting straight line is able to adequately represent the relationship between force and displacement, and the spring stiffness of the best-fitting straight line is considered as the spring stiffness of the fabricated spring.

Based on Hooke's law, the best-fit linear operation has a spring stiffness of 22 N/m, which is smaller than expected. Therefore, the resonant frequency of the mechanical-spring electromagnetic generator with a 46.9 g moving mass is 3.45 Hz. The reason for the difference in the spring stiffness between the measurement and simulation results is probably due to the manufacturing processes. Because of the tolerances of the wire diameter and coil diameter in the manufacturing processes, the spring stiffness is in the range of 21-35 N/m. The other reason might be the change of the active coil number. By gluing the spring ends to the stationary board and the force meter, the active coil number might change, hence the difference in the spring stiffness. From Figure 5.2, if a generator is resonant at 3.45 Hz with bandwidth of 0.5 Hz, the relative output power is very small. Hence, in this study, a bandwidth of 1 Hz is required to harvest energy from 3.9 Hz and hence generate more energy from human motion.

5.3 Linearised Magnetic-Spring Resonator

Section 5.3.1 presents simulation of existing work on linearizing magnetic springs [86, 96] to help develop linearised magnetic springs for human-powered energy harvesting. In Section 5.3.2, a novel design of a linearised magnetic spring is proposed. The design is compared to

existing devices through Finite Element Analysis (FEA) modelling and simulation. The measurement of the spring stiffness of the fabricated springs is presented in Section 5.3.3.

5.3.1 Simulation of Existing Work on Linearizing Magnetic Springs

As shown in the literature review (Section 2.3.2), a magnetic spring for human-powered energy harvesting has been designed by Saha *et al*. [86]. The magnetic spring (shown in Figure 5.9) was formed from two identical cylindrical magnets (diameter: 10 mm, length: 1 mm) fixed at both ends of a Teflon tube. Suspended between these were two cylindrical magnets (diameter: 15 mm, length 8 mm) separated by a soft magnetic pole piece (diameter: 15 mm, length 3 mm), glued together so that they moved as a single object. The aim of Saha's design was to increase the flux density to produce an increased output voltage. The separation between the middle object and either end magnet was 16 mm, and the length of the tube was 55 mm. The authors report that the relationship between the force and the displacement of the central mass from the centre is considered 'almost linear' over the displacement range of -8 to +8 mm from the quiescent position.

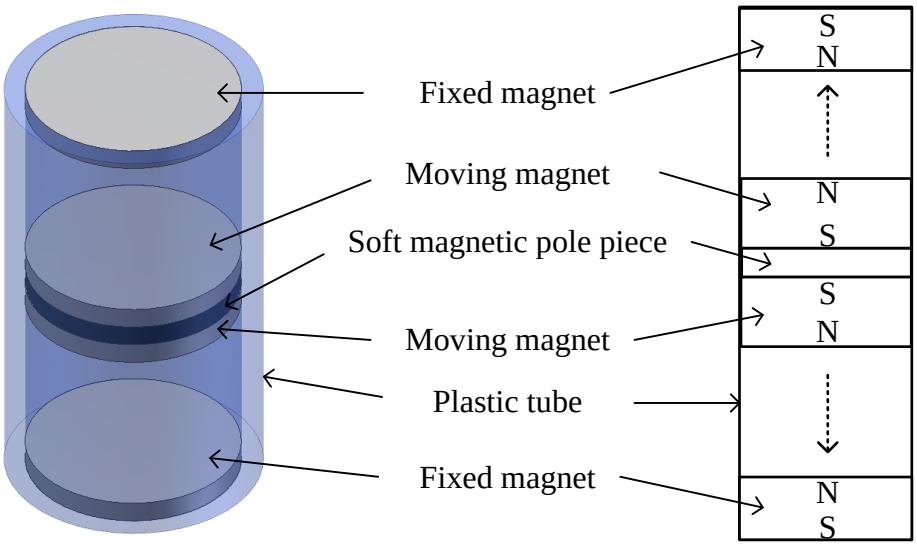

Figure 5.9 Structure of the magnetic spring reported by Saha *et al*. [86].

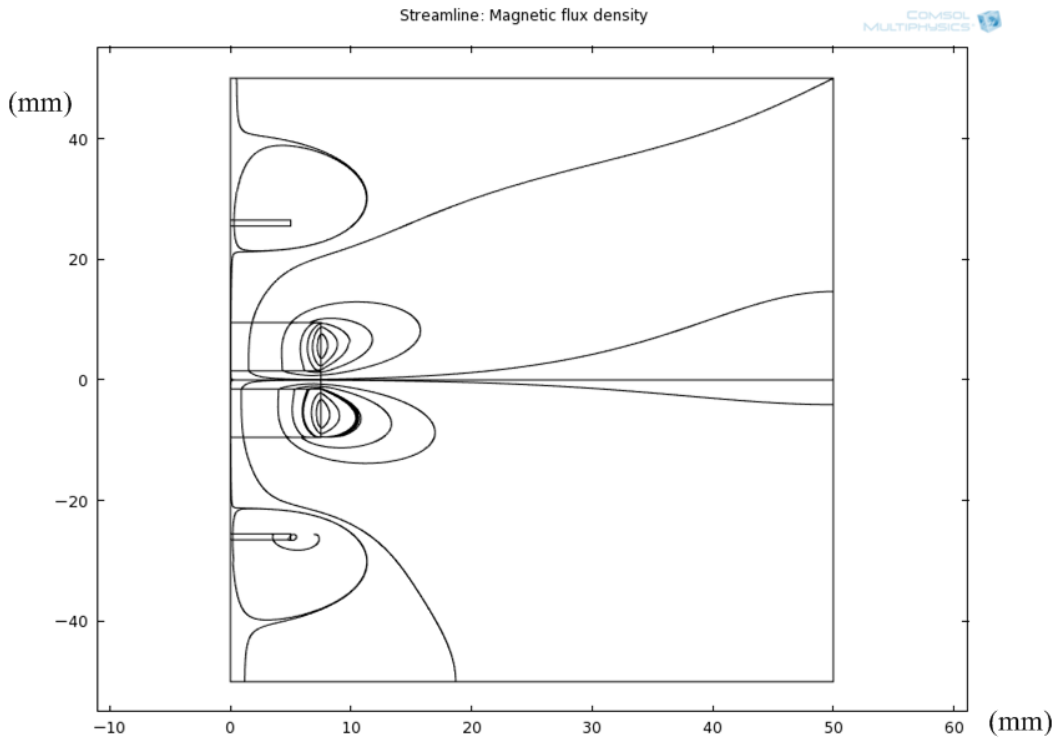

Figure 5.10 Finite element simulation showing the magnetic flux density streamline of an axis-symmetrical finite element simulation of the magnetic spring reported by Saha *et al.* [86].

Using the dimensions reported by Saha *et al.* [86], the reported device was modelled and analysed using FEA, and the simulation results were compared with the results shown in the paper (see Figure 5.11). Figure 5.10 illustrates the magnetic flux density streamline of an axis-symmetrical finite element simulation of the structure in Figure 5.9. In Figure 5.11, the solid line shows the simulation results of displacement against the force applied to the magnetic spring, and shows good correlation with the results reported in the paper (shown by the crosses). The root mean square (rms) of the deviation between the simulation results and the results reported in the paper is only 0.00876 N. In Figure 5.9, if the central magnet is moving from the middle position to the bottom, the displacement is presented as negative displacement. In contrast, if the spring is moving from the middle position to the top, the displacement is presented as positive displacement. The independent linearity of the simulation results (the dashed line in Figure 5.11, with a spring stiffness of 45.8 N/m) is 6.3%. The deviation between the measurement results and the best-fit linear operation means the spring stiffness is nonlinear with displacement and the resonant frequency changes with displacement if the moving mass is constant.

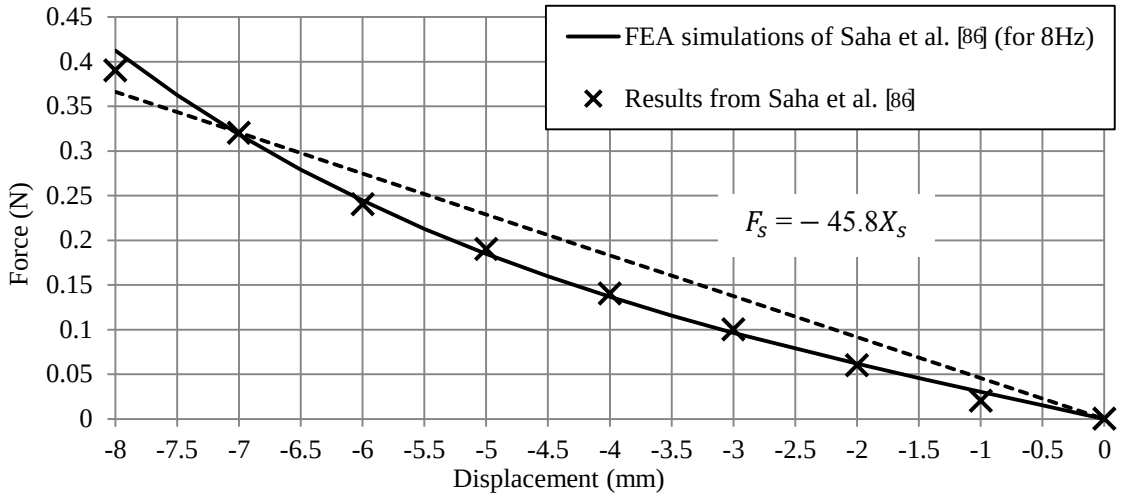

Figure 5.11 Force vs. displacement for the magnetic spring reported by Saha *et al.* [86]. The solid line shows the results of FEA simulation, the crosses are the results from the original paper, and the dashed line shows the desired linear operation.

To meet the requirement of a resonant frequency of 3.9 Hz, the quiescent position of the central magnet, when mounted vertically, is 16 mm from the centre of the device due to gravity. Thus, the region over which the spring behaves linearly will be greater than 16 mm. The existing device in Figure 5.9 was adapted in simulation to give it a resonant frequency of 3.9 Hz, increasing the separation between end magnets to 33 mm. This achieves a displacement of 25 mm with a force of 0.4 N, considering the moving central mass of 27 g in the existing device.

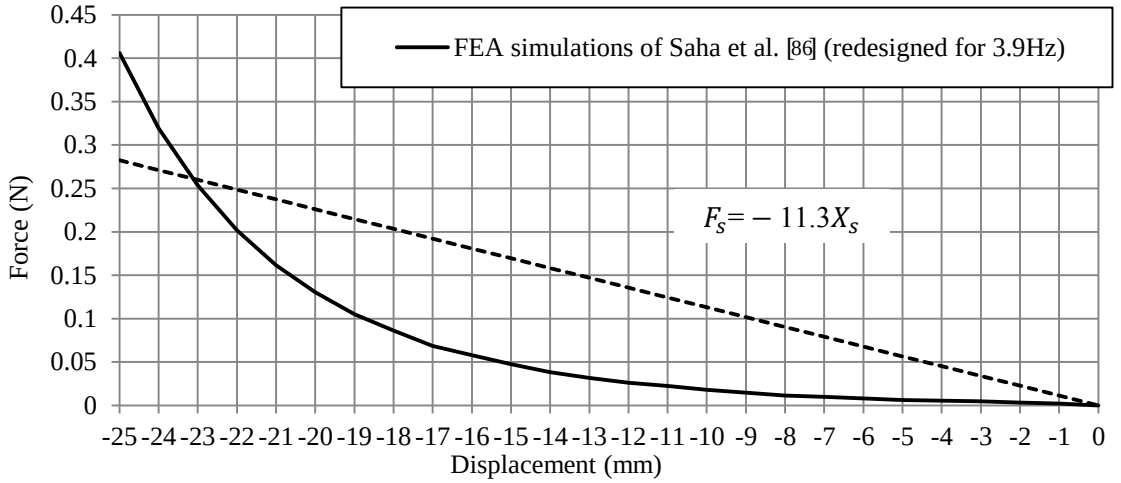

Figure 5.12 Force vs. displacement for the structure proposed by Saha *et al.* [86], redesigned for 3.9 Hz. The solid line shows the results of FEA simulation, and the dashed line shows the desired linear operation.

As can be seen from the simulation results (Figure 5.12), however, the independent linearity of the redesigned 3.9 Hz magnetic spring is 21.9%; clearly more linear operation is desired. In the

validation, the test generator is operated along different orientations by rotation. Hence the quiescent position of the moving mass is in the range of 0-16 mm. To ensure a constant resonant frequency in that range, the required magnetic spring should have a linear displacement range over 16 mm. In Saha *et al.* [86], the magnetic spring is linearised with 6.3% linearity. In this study, a magnetic spring with linearity below 5% is required, which means the variable spring stiffness deviates from a constant value by, at most, 5%. To linearise the operation, different magnet arrangements were investigated, which would allow 'shaping' of the magnetic field. One such solution was based upon that reported by Patt [96], the structure of which is shown in Figure 5.13. The coaxial magnetic spring is designed with an integral linear motor to oscillate a component in a cryogenic refrigerator. In Figure 5.13, the spring is formed from two radially poled ring magnets fixed at both ends of a tube. Suspended between these is a single object formed from two magnetic rings. A structure based around this design was modelled and analysed using FEA simulation. Figure 5.14 illustrates the magnetic flux density streamline of an axis-symmetrical finite element simulation of the structure in Figure 5.13. In this simulation, the moving magnet ring is 11 mm (outer diameter) × 4 mm (inner diameter) × 7 mm (height), the fixed magnet ring magnet is 19 mm (outer diameter) × 12 mm (inner diameter) × 7 mm (height) and the separation between the two moving magnet rings is 72 mm.

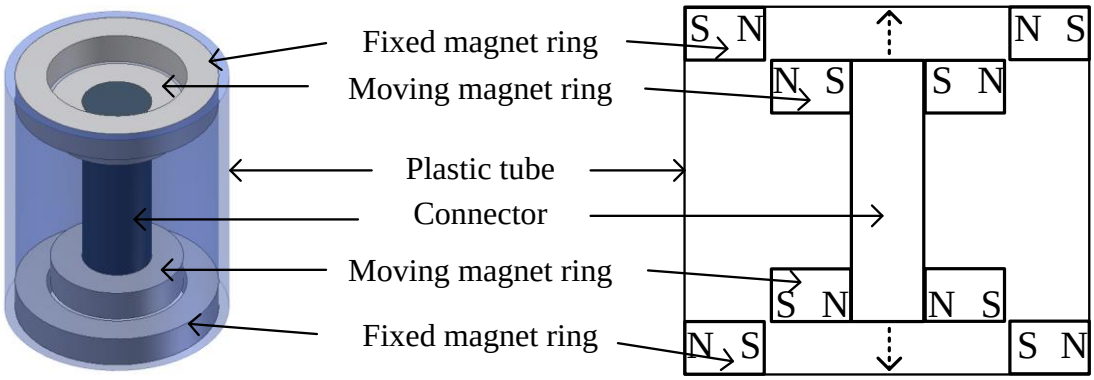

Figure 5.13 Structure of the magnetic spring reported by Patt [96].

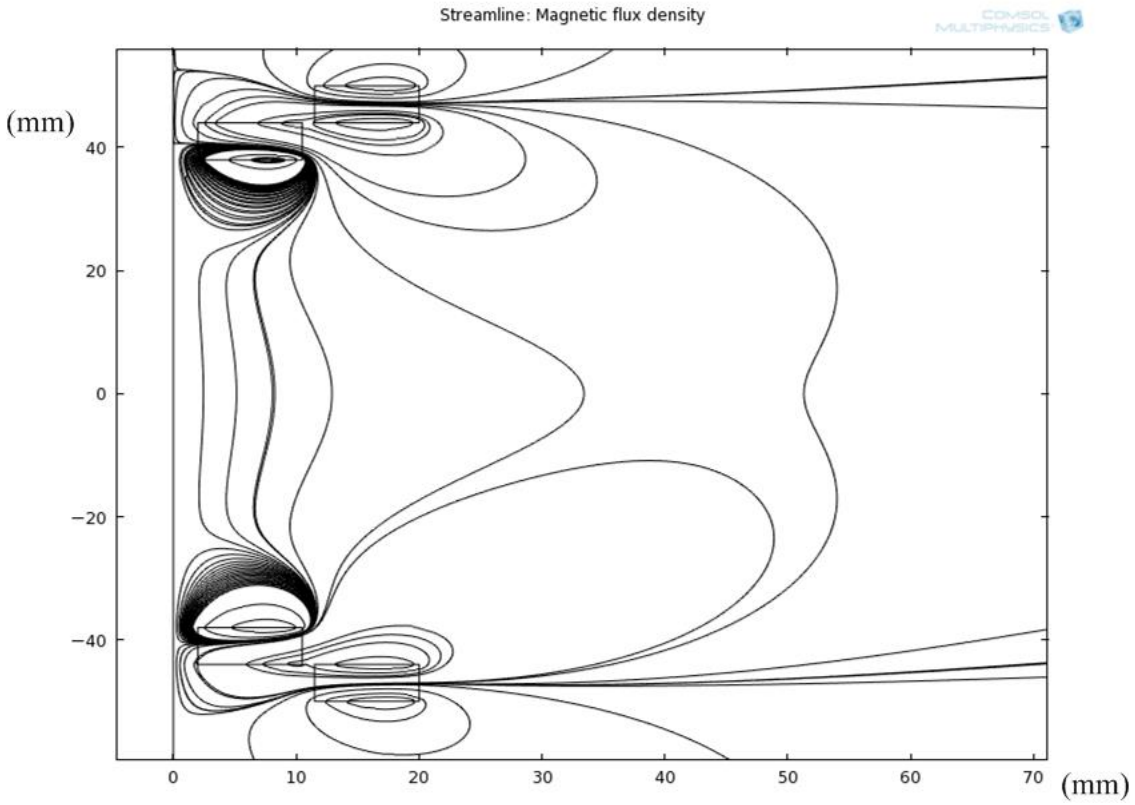

Figure 5.14 Finite element simulation showing the magnetic flux density streamline of an axis-symmetrical finite element simulation of the magnetic spring reported by Patt [96].

The force versus displacement of a simple magnet pair (one moving magnet ring and one fixed magnet ring) of the device was tested in Patt [96]. In the measurement, only one moving magnet ring is moving across the fixed magnet ring on the same side from -3 to +3 mm. The simulation results in Figure 5.15 show good correlation with the results reported in the paper (shown by the crosses). The rms of the deviation between the simulation results and the results reported in the paper is only 2.21 N. Therefore, the simulation model is shown to simulate the magnetic spring adequately. Then, the situation where the two moving magnet rings are moving across one of the two fixed magnet rings is simulated. The results of the force versus displacement are shown in Figure 5.16. While this device is much stiffer and requires more than 50 N magnetic force to displace the central magnet by 3 mm, it appears to be a promising solution to linearise the operation of the magnetic spring.

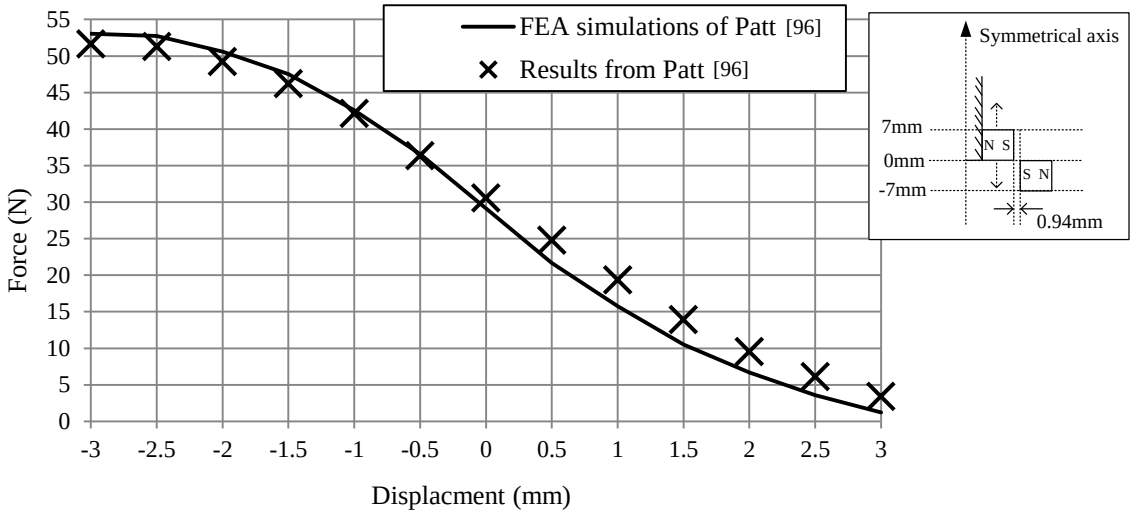

Figure 5.15 Force vs. displacement when only one moving magnet ring is moving across the fixed magnet ring on the same side for the magnetic spring reported by Patt [96]. The solid line shows the results of simulation and the crosses are the results from the original paper.

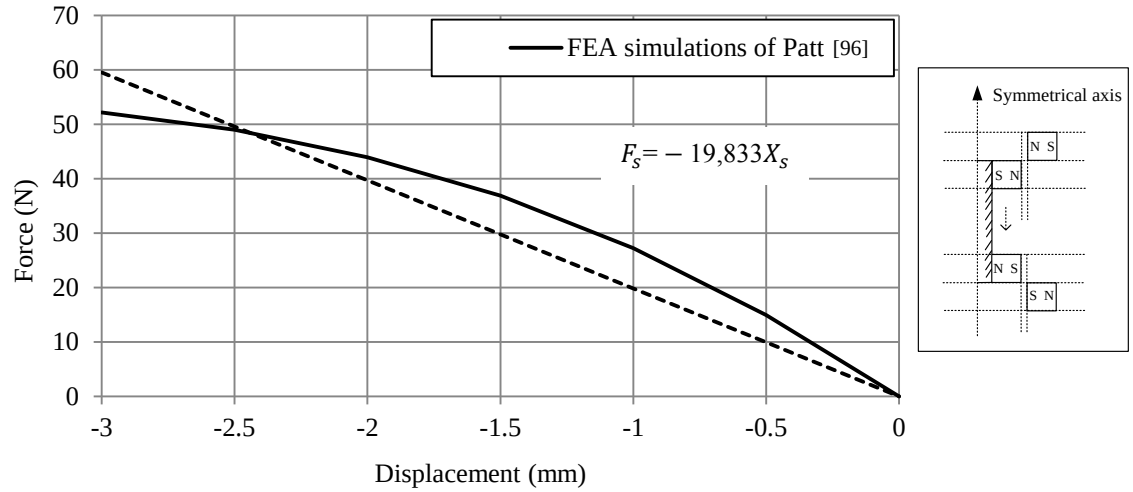

Figure 5.16 Force vs. displacement when two moving magnet rings are moving across one of the two fixed magnet rings for the magnetic spring reported by Patt [96]. The solid line shows the results of simulation, and the dashed line shows linear operation.

5.3.2 Design

A magnetic spring that merges the concepts reported by Saha *et al.* [86] and Patt [96] was designed, which utilises a cylindrical centre magnet and ring-shaped end magnets (as shown in Figure 5.17). The double center magnet in Saha *et al.*'s design was not adopted, as the increased flux density that this would have offered necessitates a longer tube to operate at 3.9 Hz. Axially poled magnet rings were used instead of radially poled ring magnets to significantly reduce the

tooling cost. A permanent magnet was placed inside a low-friction plastic tube, and two ring magnets fixed at either end. The center magnet is free to move but suspended due to the repelling forces. Two tungsten masses are glued on both sides of the moving magnet to increase the seismic mass.

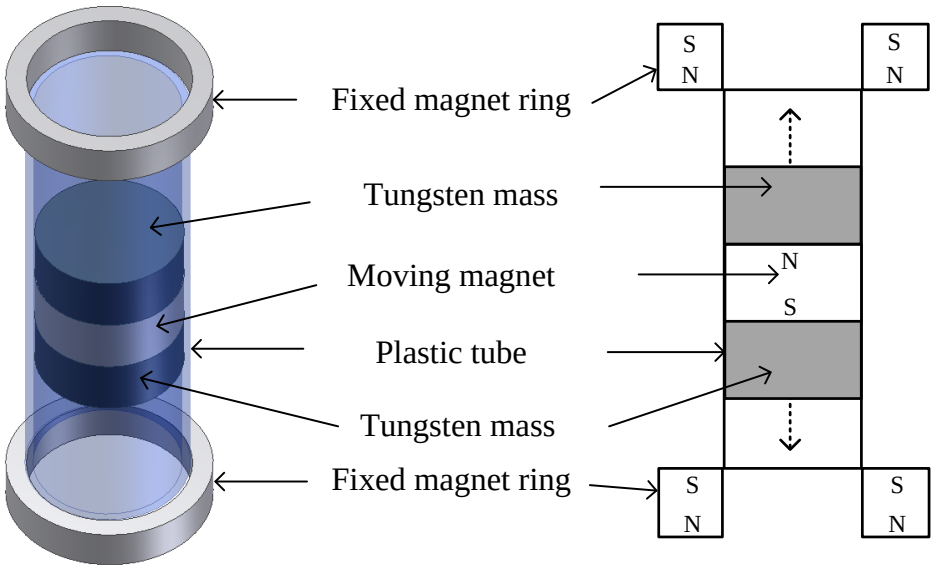

Figure 5.17 Structure of the proposed magnetic spring.

The linearised magnetic spring was designed and optimised using FEA and the force-displacement relationship of the central magnet was investigated. To understand the flux linkage inside the tube, Figure 5.18 illustrates the magnetic flux density streamline of an axis-symmetrical finite element simulation of the structure in Figure 5.17. In this simulation, the middle moving magnet is 22 mm (diameter) × 8 mm (height) and the two fixed end magnets are 40 mm (outer diameter) × 23 mm (inner diameter) × 6 mm (height). The overall specifications are given in Table 5.3. The solid line in Figure 5.19 shows how the displacement of the central mass varies with force between -25 mm and 0 mm. The negative displacement means the central magnet is moving from the middle position to the bottom, as shown in Figure 5.17. The independent linearity of the simulation results (the dashed line in Figure 5.19, with a spring stiffness of 134 N/m) is 1.9%. This represents a significant improvement on previously reported work. Based on Hooke's law, the best-fit linear operation has a spring stiffness of 134 N/m. Hence, the resonant frequency is 4.25 Hz with a moving mass of 188 g.

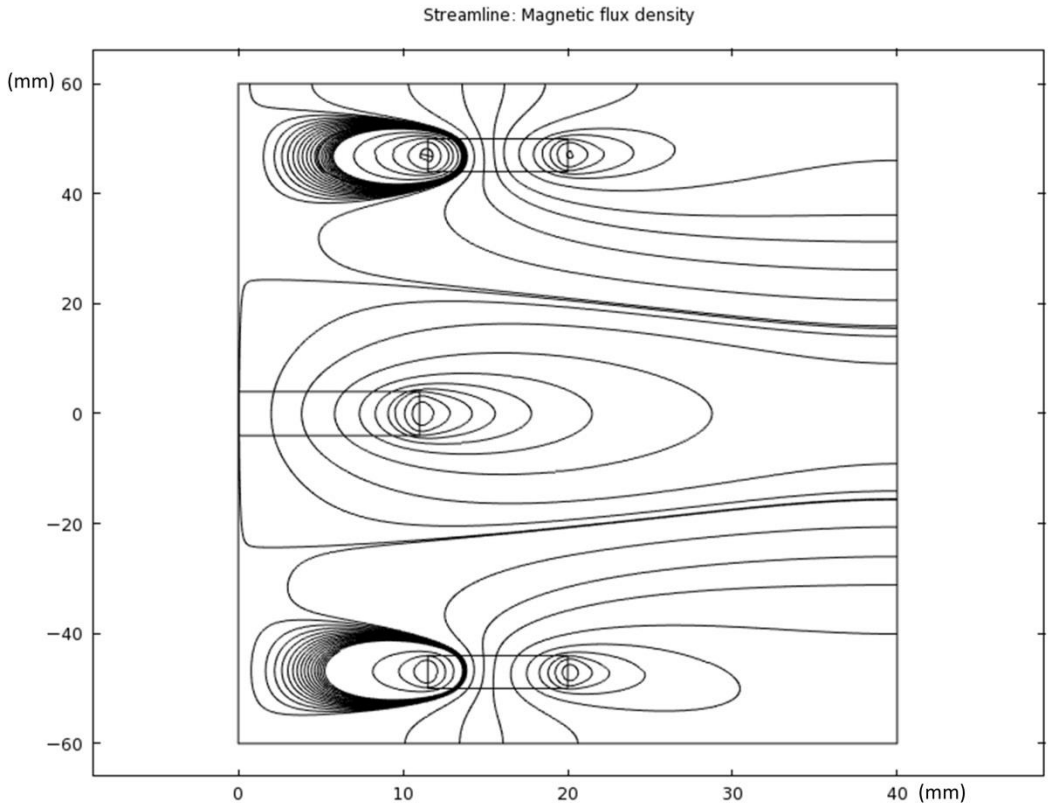

Figure 5.18 Finite element simulation showing the magnetic flux density streamline of an axis-symmetrical finite element simulation of the magnetic spring consisting of two fixed magnet rings and a middle moving magnet cylinder.

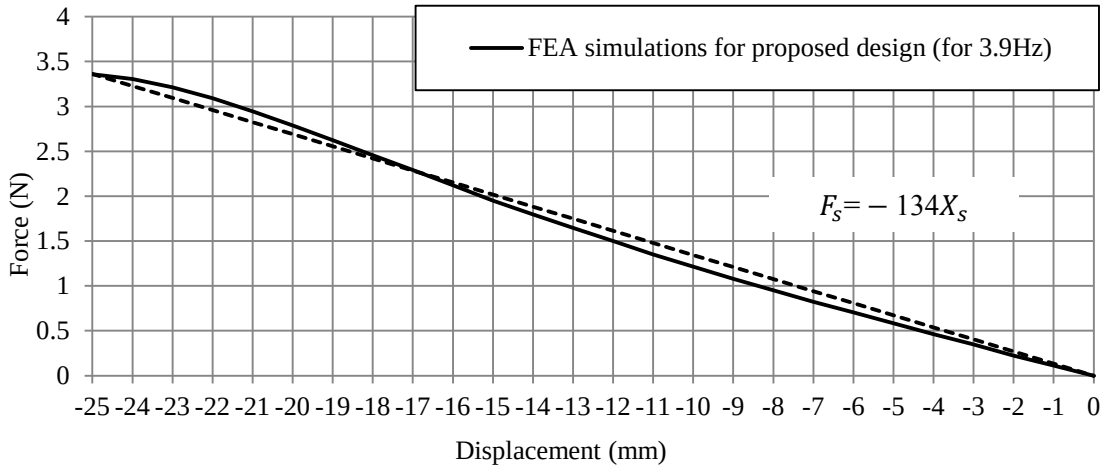

Figure 5.19 Force vs. displacement for the proposed magnetic spring (designed for 3.9 Hz operation) from -25 mm to 0 mm. The solid line shows the results of FEA simulation, and the dashed line shows the desired linear operation.

The above results show that the magnetic spring has been linearized well through using the proposed structure. The linearized magnetic spring has wider linear displacement and lower

linearity than the device reported by Saha *et al.* [86]. To illustrate the benefit of the proposed structure in linearizing magnetic springs, a comparison between the device reported by Saha *et al.* [86] and the proposed device in this study (Figure 5.17) is made. The proposed device was modified to tune the spring stiffness to a suitable level for a resonant frequency of 8 Hz since the resonant frequency of Saha *et al.*'s generator is at approximately 8 Hz. The fixed magnet rings (inner diameter: 15 mm, outer diameter: 23 mm, length: 3 mm) and central magnet (diameter: 14 mm, length 4 mm) were chosen. The total length of the device is 56 mm, which is close to the length of the device reported in the literature. The dashed and solid lines in Figure 5.20 show simulation results based on the reported and the proposed designs respectively. The linearity of our proposed structure is 1.2% compared to that reported in the literature (6.3%). Therefore, the proposed structure provides a more efficient way to linearize magnetic springs over the existing method.

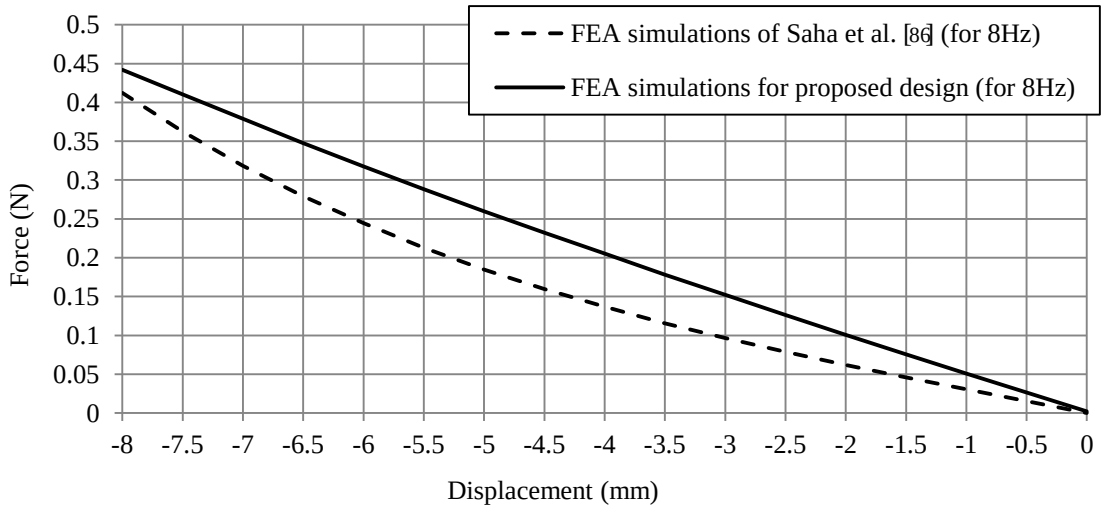

Figure 5.20 Force vs. displacement for the magnetic spring (dashed line) reported by Saha *et al.* [86] and our proposed 8 Hz structure (solid line).

Two prototypes of the linearized magnetic spring were fabricated, because two 1-DOF generators are needed to make up a 2-DOF generator. Permanent magnets made of NdFeB N42, with a remanent flux density B_r of 1.28 T, were inserted into the hollow plastic tubes made of Tufset polyurethane, while two permanent magnet rings made of NdFeB N38M, with a remanent flux density B_r of 1.23 T, were glued to both ends of each tube with opposing polarity. The separation between the middle and either end magnet was 40 mm. Two plastic holders were designed to hold the end magnet rings; the holders were made of Tufset in one version of the prototype, and Delrin in the other. Two end caps made of rubber are used to seal the generator and also to reduce the mechanical damping in case of end-stop collision. The complete specifications of the magnetic springs are given in Table 5.3, and Figure 5.21 shows the photo

of one prototype.

Table 5.3 Specifications of the magnetic-spring resonator.

Part	Dimensions [mm]	Weight [g]	Material
End magnet rings	Outer diameter: 40 Inner diameter: 23 Height: 6	37.6	NdFeB N38M (B_r=1.23 T)
Central magnet	Diameter: 22 Height: 8	22.8	NdFeB N42 (B_r=1.28 T)
Tungsten mass	Diameter: 22 Height: 11.7	82.7	Tungsten
Moving mass	One central magnet and two Tungsten masses	188	
Tubes	Outer diameter: 24.4 Inner diameter: 22.4 Height: 88	27.5 (Delrin holders) 24.3 (Tufset holders)	Tufset Polyurethane

Figure 5.21 Photograph of the prototype of the magnetic spring alongside an AA battery.

5.3.3 Spring Stiffness Measurement

To evaluate the linearity of the fabricated linearised magnetic spring, the displacement of the central magnet with applied force was tested. Figure 5.22 shows the measurement setup to evaluate the spring stiffness of one experimental prototype of the magnetic spring. The measurement technique for the magnetic spring is the same as that used for the mechanical spring except for the type of connection between the spring and the force meter. The magnetic-spring resonator is securely glued to a surface. The central magnet is connected to the force meter through a Tufset tube using superglue, and the force meter is pulled in line with the central axis of the tube over a measurement range of 0-25 mm in steps of 1 mm. During measurement, to ensure that the force meter is moving along the central axis of the tube, a non-

magnetic stationary aluminium plate (thickness: 8.2 mm) was designed to hold the force meter. Figure 5.23 show the photos of the measurement setup.

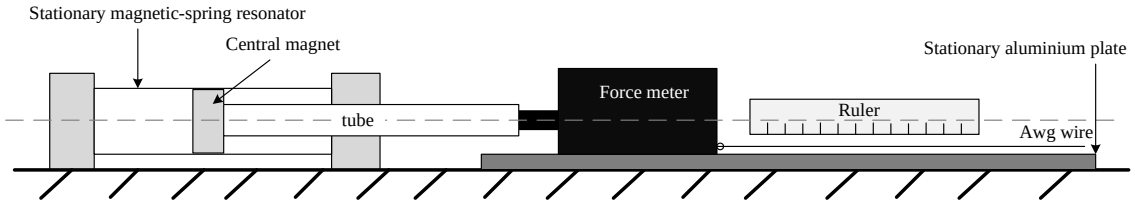

Figure 5.22 The measurement setup to evaluate the spring stiffness of the magnetic spring.

Figure 5.23 Photo of the measurement setup to evaluate the spring stiffness of the magnetic spring.

Measurements were repeated five times for each of the two prototypes and the simulation results and the experimental measurement results are shown in Figure 5.24. Negative displacement means the moving magnet is extended from the original position in Figure 5.22. The average force of the five-group measurement is represented by circles and crosses for different devices. The error bars show the minimum and maximum values in the five-group measurement results. The results from the first prototype (Tufset end holders) exhibit a linearity of 2.0%, while the second prototype (Delrin end holders) exhibits a linearity of 1.7%. The rms of the deviation between the simulation results and the measurement results is only 0.106 N and 0.162 N for devices 1 and 2, respectively. Comparing these results with the simulation results shows good correlation, and highlights the ability of our magnetic spring to operate with good linearity over a displacement of -25 mm to +25 mm.

It can be observed from Figure 5.24 that there is some discrepancy between the experimental results and the simulations. This difference is due to a number of factors, including measurement error and difficulty in aligning the magnets so they are exactly parallel with each other. For example, a ruler was used to measure displacement. The measured force read form the force meter is equal to the sum of the real spring force and the unavoidable friction between the moving mass and the inner face of the tube. Hence, the measured force is greater than the

real spring force, and the derived spring stiffness from the measurement results is greater than the real spring stiffness. Considering this, lubricant was spread on the inner face of the tube, and Tufset Polyurethane is selected to make the tube in order to minimise the friction.

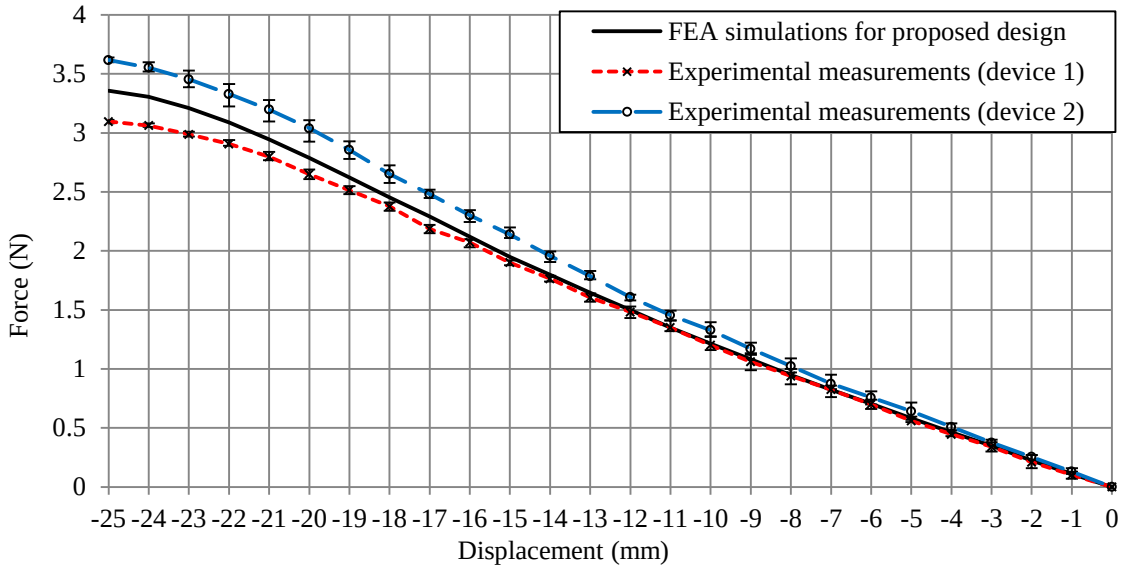

Figure 5.24 Measurements of force vs. displacement from the two prototype devices. The average force is represented by crosses (device 1) and circles (device 2). The error bars show the minimum and maximum values of the measurement results. The dashed line shows the measurement results from device 1 (red dashed line) and device 2 (blue dashed line).

The spring stiffness values for the two prototypes are 128 N/m (device 1) and 145 N/m (device 2). Therefore, the corresponding resonant frequencies for the two prototypes are 4.15 Hz (device 1) and 4.42 Hz (device 2), with the moving mass of 188 g. From Figure 5.2, if a generator resonates at 4.15 Hz or 4.42 Hz with a bandwidth of 0.5 Hz, the relative output power is very low. Hence, in this study, a bandwidth of 1 Hz is required to harvest energy from 3.9 Hz and hence generate more energy from human motion.

5.4 Coil Design

The quiescent position of the moving magnet changes with the rotation of the electromagnetic generator, and thus the coil should be designed to cover as much as possible of the whole travel length of the moving magnet. Moreover, based on Faraday's law of induction and Lenz's law, the emf across a coil is equal to the negative rate of flux change (Equation (2.25)). To maximise the magnetic flux cut by the coil and thus maximise the induced voltage, the axial height of the coil is equal to the height of the moving magnet. Therefore, to cover as much of the travel length as possible, five coils (each 12 mm in height) are used in the mechanical-spring

electromagnetic generator to cover the 60 mm length in the centre of the tube, considering the 12 mm magnet length and the 25 mm maximum displacement. Seven coils (each 8 mm in height) are used in the magnetic spring electromagnetic generator to cover 56 mm length in the centre of the tube, considering the 8 mm magnet length and the 25 mm maximum displacement. The adjacent coils are wound in different directions and connected in series. The specifications of the coils are shown in Table 5.4. Figure 5.25 illustrates the series connection of three coils of an electromagnetic generator. The measured resistance of the fabricated coils and the total weight of the generator prototypes are shown in Table 5.5.

Table 5.4 Design specifications of the coils.

	Mechanical-spring generator	Magnetic-spring generator
Number of coils	5	7
Inner diameter	15.5 mm	24.6 mm
Outer diameter	20.6 mm	32.6 mm
Height	12 mm	8 mm
Number of turns per coil	2000	2000
Enamel cooper wire	42SWG a	42SWG

[a] 42SWG enamel cooper wires have 0.102 mm diameter.

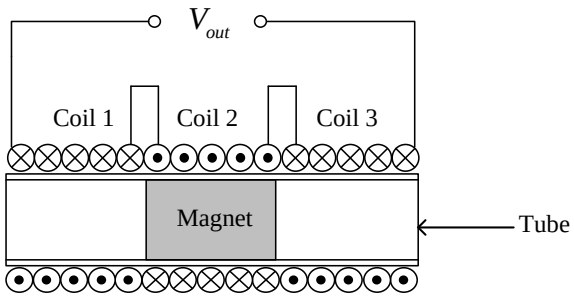

Figure 5.25 A cross-sectional view of three series-connected coils of an electromagnetic generator.

Table 5.5 The measured resistance of the coils and the weight of the generator prototypes.

	Mechanical-spring generator	Magnetic-spring generator [a]
Resistance of a coil	258 Ω	404 Ω
Total resistance of coils	1.29 kΩ	2.84 kΩ
Total weight of the prototype	115 g	422 g

[a] Prototype with Delrin end holders. (device 2)

When a load resistance R_L is placed across the terminals of an electromagnetic generator (Figure 2.5), the power P_L dissipated in the load is expressed as (without considering the influence of the overall damping ratio of the generator):

$$P_L = \left(\frac{\text{emf}}{R_L + R_c}\right)^2 R_L \tag{5.6}$$

The value R_L for which Equation (5.6) is a maximum can be calculated by differentiating it. Hence, to obtain the maximum power output on the load, the load resistance is equal to the coil resistance, i.e. $R_L = R_c$. Therefore, the optimum loads for the maximum power output from the mechanical- and magnetic-spring generator are 1.29 kΩ and 2.84 kΩ, respectively.

Figure 5.26 shows the prototype of the mechanical-spring electromagnetic generator. Figure 5.27 shows the prototype of the magnetic-spring electromagnetic generator alongside a cell phone. Considering that the same two designs of 1-DOF inertial energy harvesters are used in the on-body experimental validation, the total weight of the test 2-DOF magnetic-spring inertial energy harvester is 844 g. If the vibration along the direction of gravity on the knee is 1‘g’ [m s^{-2}] due to the running activity, the force required to hold the generator steady is as high as 16.6 N. Therefore, the mechanical-spring generator with the much lighter weight (27% of the weight of the magnetic-spring generator) is more wearable than the magnetic-spring generator.

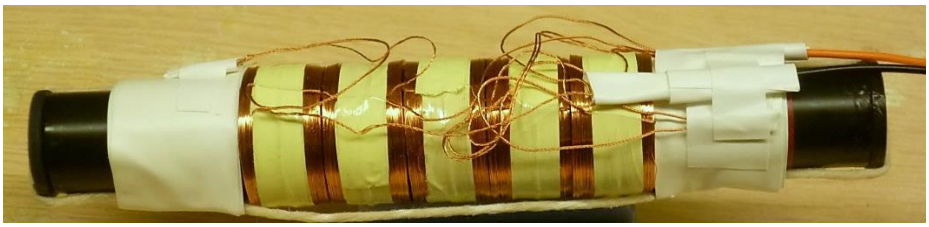

Figure 5.26 Prototype of the mechanical-spring electromagnetic generator.

Figure 5.27 Prototype of the magnetic-spring electromagnetic generator alongside a cell phone with a height of 119 mm and a width of 60 mm.

5.5 Simulation of the Designed Electromagnetic Generators

To ensure that the resonant frequencies of the two designs of electromagnetic generators are constant with rotation, the frequency response at different rotation angles is investigated. MATLAB models are created for this purpose to predict the open-circuit voltage. In the simulation scenario, both the generators and external vibration are initially orientated in the direction of gravity, as shown in Figure 5.28. The generators are rotated from 0 ° to 80 ° in steps of 10 ° with respect to the direction of gravity. The MATLAB models simulate the situation where the generators are excited by a controlled vibration source, such as a shaker, generating a sinusoidal input signal.

In Section 5.5.1, the effect of the resistance and inductance of the coils of the designed generators is discussed. Section 5.5.2 presents the simulation models for voltage generation by a magnet moving through five or seven coils. In Section 5.5.3, frequency response when the generators are rotated at different angles is investigated. The effect of coil connection on the voltage produced by the designed generators is discussed in Section 5.5.4.

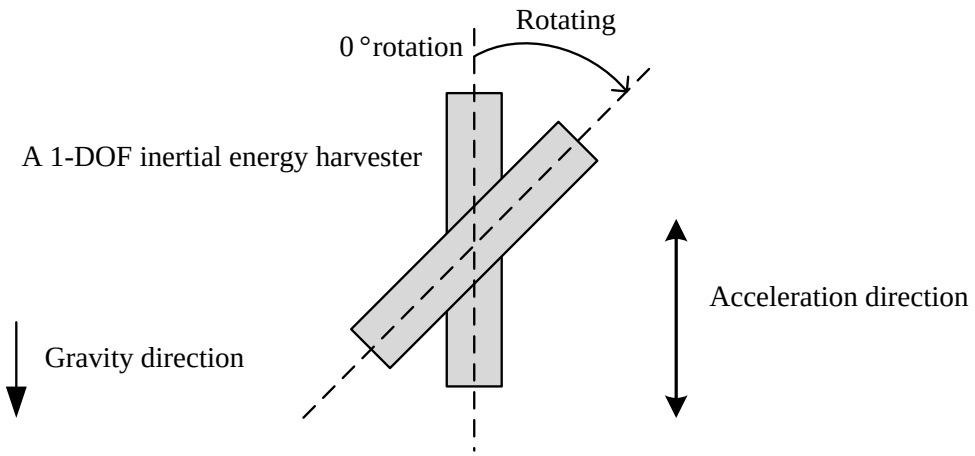

Figure 5.28 Illustration of the simulation scenario where a generator is aligned with the direction of gravity, and an external sinusoidal vibration is applied in the same direction. The generator is rotated from 0 ° to 80 ° with respect to the direction of gravity.

5.5.1 Coil Inductance and Resistance

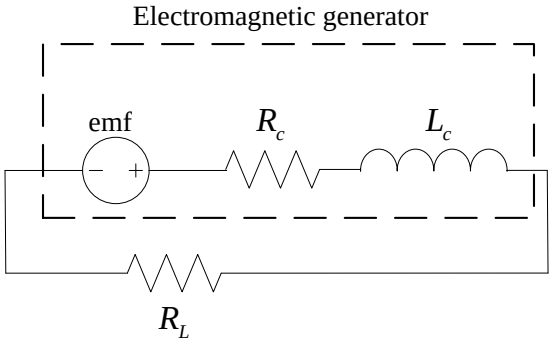

Figure 2.5 Circuit representation of an electromagnetic generator with a resistive load. (Reproduced from [50])

The circuit representation of an electromagnetic generator consists of a voltage source, the resistance of the coil and the inductance of the coil (Figure 2.5). If

$$R_c \gg X_L \tag{5.7}$$

where f_c [Hz] is the frequency of the emf across the coil and X_L ($X_L = 2\pi f_c L_c$) [Ω] is the inductive reactance of the coil, then the effects of the coil inductance are negligible compared to those of the coil resistance [100]. For the mechanical-spring electromagnetic generator, if f_c=3.9 Hz (which is the designed resonant frequency of the generators), X_L=4 Ω (L_c=175 mH) and R_c (R_c=1.29 kΩ) $\gg X_L$; for the magnetic-spring electromagnetic generator, if f_c=3.9 Hz, X_L=24 Ω (L_c=965 mH) and R_c (R_c=2.84 kΩ) $\gg X_L$. Hence, in the subsequent analysis, the effects of the coil inductance are considered negligible and the resistance effects are assumed to dominate the electromagnetic generators.

5.5.2 Simulation Models for Voltage Generation

According to Faraday's law, the open-circuit voltage, emf, induced across *N* turns of a coil is the negative integral of the rate of change of magnetic flux Φ over the cross-sectional area of the coil A_c [m^2]. The direction of the emf is given by Lenz's law. The open-circuit voltage induced across the coil is expressed as:

$$\text{emf} = -N \int \frac{d\Phi}{dt} dA_c \tag{5.8}$$

Using Equation (5.8), Aparna [100] proposed a MATLAB model to calculate the voltage generated by relative movement of a magnet and a coil. In the model, the coil is fixed and external sinusoidal vibrations are directly applied on the moving magnet. Based on this model,

two further MATLAB models are developed to calculate the voltage generated by a magnet moving through five and seven coils. Figure 5.29 illustrates the cross-sectional view of the mechanical-spring electromagnetic generator. Friction between the moving magnet and the inner face of the tube is not considered in the models. There are three differences between Aparna's model [100] and the proposed models used in this thesis. The differences are:

1) The relative movement of the coils and the magnet results from an inertial force. External simulated vibrations $y(t)$ are applied on the tube of the generators. The relative displacement $x(t)$ between the coils and the magnet is given by Equation (2.3).

$$x(t) = \frac{\omega^2}{\sqrt{\left(\frac{k}{m} - \omega^2\right)^2 + \left(\frac{b\omega}{m}\right)^2}} Y sin(\omega t) \tag{2.3}$$

2) For the designed electromagnetic generators, the emf is generated from series-connected coils. For example, the total emf across the five coils of the mechanical-spring electromagnetic generator is calculated as:

$$\text{emf}_{total} = \text{emf}_1 - \text{emf}_2 + \text{emf}_3 - \text{emf}_4 + \text{emf}_5 \tag{5.9}$$

where emf_i is the emf across coil i.

3) The electromagnetic generators are not always positioned along the direction of external vibrations. These are rotated as discussed above.

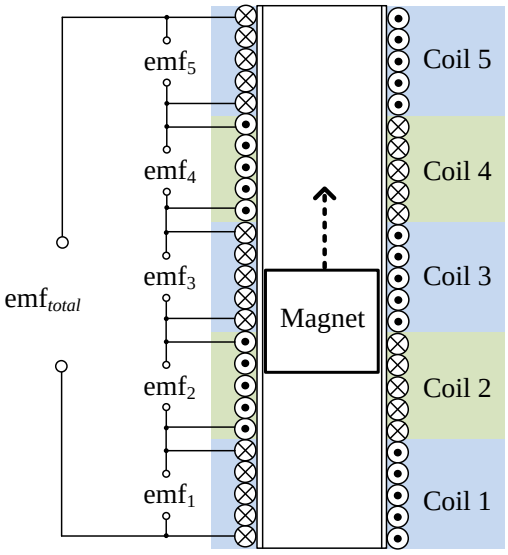

Figure 5.29 A cross-sectional view of the mechanical-spring electromagnetic generator simulated in the MATLAB model.

The parameters of the designed electromagnetic generators, including the physical size, spring stiffness, remanent flux density of the magnet material, and weight of the moving mass, are fed into the MATLAB simulation. In addition to these parameters, the Q-factor of the generators and the vibration source are required to predict the output voltage. The Q-factor values are defined from the measurement results of the fabricated generators (detailed in Section 6.1). The vibration source is set to be the same as that in the experimental validation on a controlled vibration source (detailed in Section 6.1). The values for the Q-factor and the vibration source used in the simulation are shown in Table 5.6.

Table 5.6 The values for the Q-factor and the vibration source used in the simulation of the voltage generation from the designed electromagnetic generators.

Peak amplitude of external vibration	0.3‘g’ (rms) [m s^{-2}]
Frequency of external vibration	1-7 Hz
Q-factor of the mechanical-spring electromagnetic generator	3.5
Q-factor of the magnetic-spring electromagnetic generator	3.8

5.5.3 Frequency Response at Different Rotation Angles

The simulation results in Figure 5.30 and Figure 5.31 show the frequency responses of the mechanical- and magnetic-spring electromagnetic generator, respectively. It is found that for both of the generators, the resonant frequency remains constant over different rotation angles.

Moreover, for both generators, the peak emf is decreased as the rotation angle increases. This is because the smaller the vibration, the slower the coils cut the magnetic flux, and hence the lower the induced voltage. Furthermore, the vibration along the generator is a component of the external vibration. If the rotation angle is θ, the peak amplitude of the vibration along the generator, A_{out} [m s^{-2}], is given by:

$$A_{out} = A_{in} \cdot cos\theta \tag{5.10}$$

where A_{in} [m s^{-2}] is the peak amplitude of the external vibration, i.e. 0.3‘g’ (rms) [m s^{-2}]. Therefore, when the generator is rotated by a bigger rotation angle, the peak amplitude of the vibration along the generator is smaller, and hence the induced voltage is lower.

In addition, it is noted that the magnetic-spring energy harvester is able to generate a greater voltage than the mechanical-spring energy harvester. This is because the magnetic-spring generator has two more coils, and the magnetic material used in the magnetic-spring generator has a higher remanent flux density B_r and hence more magnetic flux is cut by coils. For example, at 0 ° rotation, the peak amplitude of generated voltage from the magnetic-spring

generator (14.2 V) is 4.09 times greater than that from the mechanical-spring generator (3.47 V); if the generators are connected to the corresponding optimum loads, the magnetic- and mechanical-spring generators are able to generate 17.7 mW (power normalised for mass: 41.9 mW/kg) and 2.30 mW (power normalised for mass: 20.0 mW/kg) on the optimum loads, respectively. Therefore, under the same vibration, the magnetic-spring electromagnetic generator performs better than the mechanical-spring electromagnetic generator in terms of power output on the optimum load.

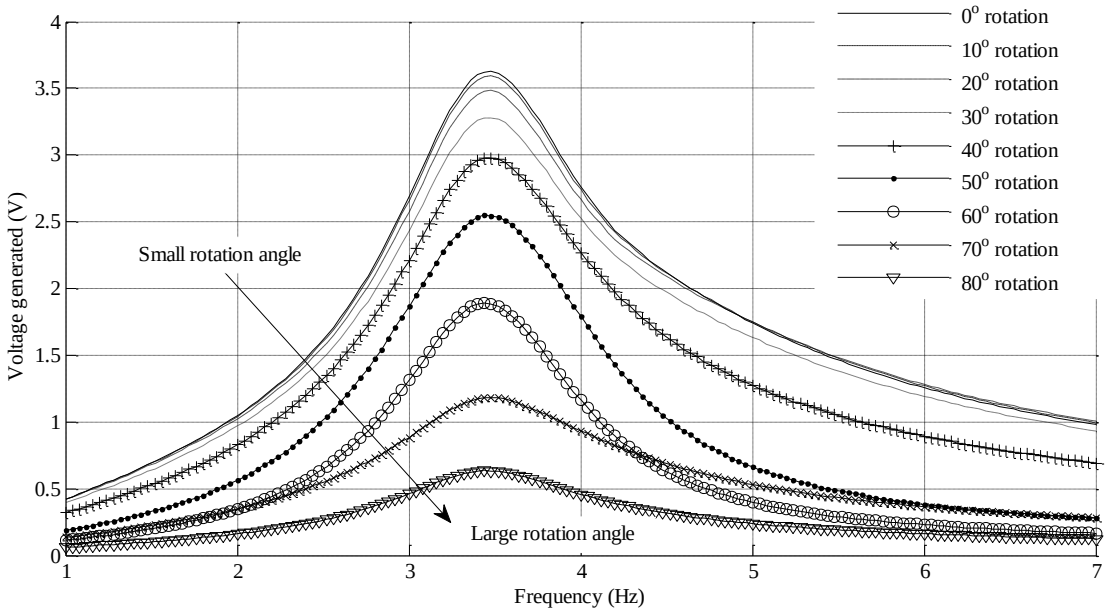

Figure 5.30 The frequency response when the mechanical-spring electromagnetic generator rotates from 0 °to 80 °.

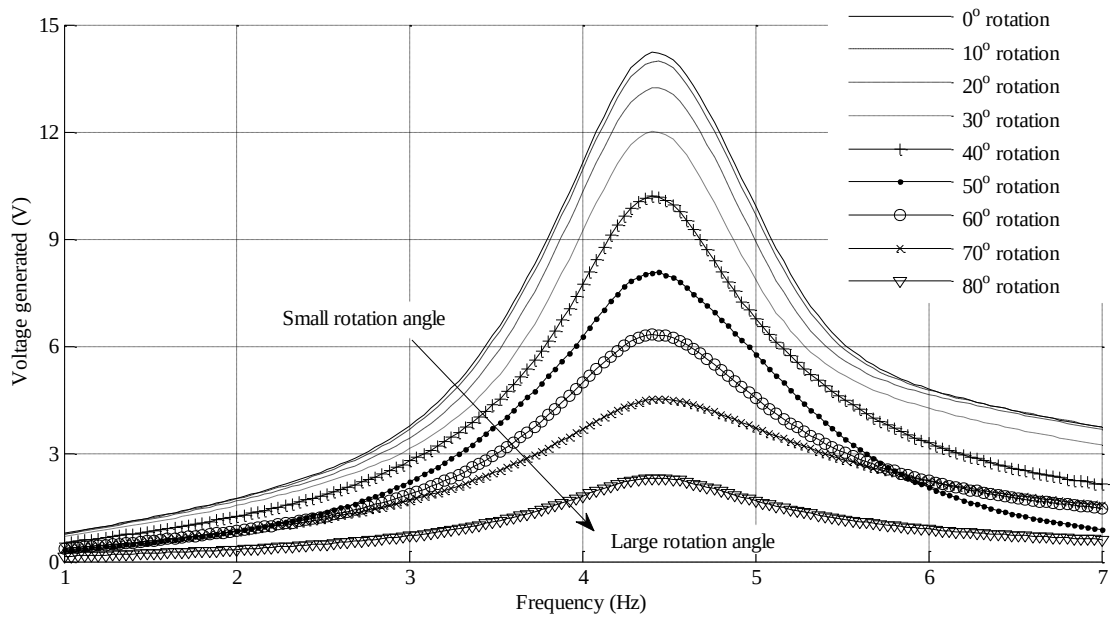

Figure 5.31 The frequency response when the magnetic-spring electromagnetic generator rotates from 0 °to 80 °.

5.5.4 Effect of Coil Connection on Voltage Generation

As discussed in Section 5.4, five and seven coils have been designed for the mechanical- and magnetic-spring electromagnetic generators, respectively, to cover as much of the travel length of the moving magnet as possible. The adjacent coils are wound in different directions and

connected in series. The benefit of this type of connection is that if a magnet is moving inside two adjacent coils, the voltage induced from the two coils has the same phase. However, if the magnet is moving outside the two coils, the induced voltage is out of phase and they cancel each other out. To illustrate this, Figure 5.29 shows a magnet moving out from coil 2 to coil 3 inside the mechanical-spring electromagnetic generator. The $-\text{emf}_2$ and emf_3 are in the same phase and thus add up. On the contrary, the emf_3 and $-\text{emf}_4$ are out of phase and thus cancel one another out.

To investigate the effect of the type of the coil connection used in this thesis (Figure 5.29) on the induced voltage, Figure 5.32 shows the frequency responses with different coil connections when the mechanical-spring electromagnetic generator is positioned along the direction of gravity without rotation. It is found that the resonant frequency remains constant over different coil connections. In addition, the frequency response when four and five coils are connected in series is almost the same. Due to the resonant frequency of 3.45 Hz, the quiescent position of the moving magnet is within coil 1. When coils 1 and 2 are connected in series, the induced voltage at resonance is highest. The induced voltage at resonance from five coils is 87% of that from coils 1 and 2, which clearly demonstrates the effect of voltage cancellation among the five coils. Therefore, some generated energy is wasted in the coils, and the type of the coil connection, which is designed to validate the analytical results, is not an optimum method to maximise the efficiency of conversion from vibration energy to electrical energy.

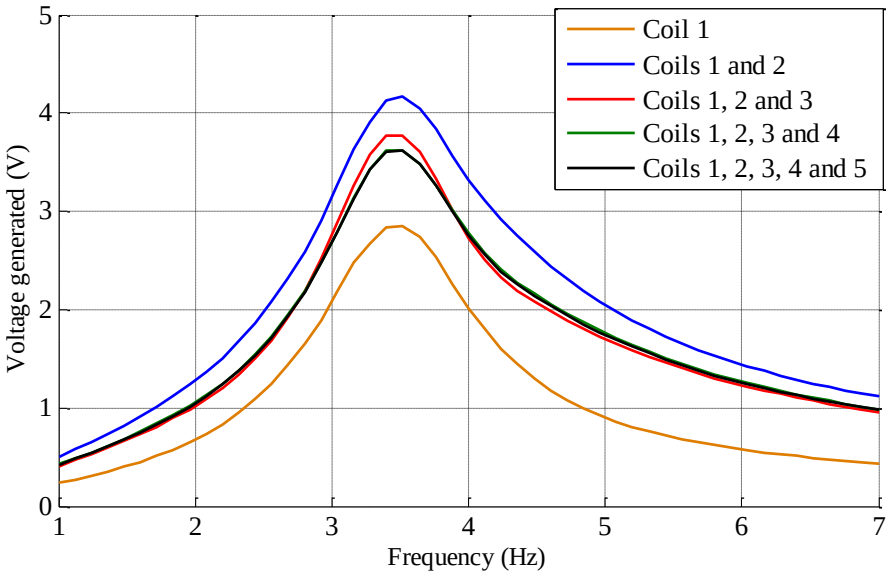

Figure 5.32 The frequency response with different coil connections when the mechanical-spring electromagnetic generator is along the direction of gravity without rotation.

5.6 Conclusions

To validate the analytical results reported in the previous chapter, 1-DOF inertial energy harvesters with resonant frequency of 3.9 Hz are required, and the test location and activity are identified as the knee and running. This chapter describes the design of mechanical-spring and linearised magnetic-spring electromagnetic energy harvesters for low-frequency operation. A cantilever with a low resonant frequency is not suitable for this study due to the large quiescent position variation resulting from the effect of gravity. Instead, a linear mechanical spring with a low spring constant of 27 N/m has been designed. The spring stiffness of the fabricated spring has been measured experimentally. The measured spring stiffness is 22 N/m with a linearity of 0.727%. Considering the fabricated moving mass of 46.9 g, the resonant frequency is 3.45 Hz, which is lower than expected. Hence, in this study, a bandwidth of 1 Hz is required to harvest energy over 3.9 Hz.

In addition to the mechanical spring, a linearised magnetic spring for the low-frequency operation is presented. FEA simulations show that the proposed design has a linearity of 1.9% over a displacement range of 50 mm, representing a significant improvement over reported devices. The designed spring stiffness is 134 N/m. Two prototypes have been fabricated to validate the design, and the relationships between applied force and displacement are measured. The results from the first prototype (Tufset end holders) exhibit a linearity of 2.0%, while the second prototype (Delrin end holders) exhibits a linearity of 1.7%. The results show good correlation with FEA simulations. The spring stiffness values for the two prototypes are 128 N/m (device 1) and 145 N/m (device 2). Therefore, the corresponding resonant frequencies for the two prototypes are 4.15 Hz (device 1) and 4.42 Hz (device 2), for a moving mass of 188 g. Hence, the resonant frequencies are higher than expected, and thus a bandwidth of 1 Hz is necessary to harvest energy at around 3.9 Hz.

The coils for the mechanical- and magnetic-spring electromagnetic generators have been designed and fabricated. Based on the fabricated coils, the estimated optimum loads of the mechanical- and magnetic-spring electromagnetic generators are 11.29 kΩ and 2.84 kΩ.

MATLAB models have been created to predict the open-circuit voltage generated from the designed electromagnetic generators. The measurement results show that the effect of the coil inductance is much smaller than the effect of the coil resistance; therefore, the simulation assumes that the resistance effects dominate the electromagnetic system. The simulation results show that for both of the generators, the resonant frequencies are constant with rotation. If the generators are connected to the optimum loads, the magnetic- and mechanical-spring generators

are able to generate 17.7 mW and 2.30 mW on the optimum loads at resonance, respectively.

In this chapter, two electromagnetic generator designs have been presented. To validate the analytical results on the human body, one of the designed electromagnetic generators needs to be selected. The total weight of the fabricated mechanical-spring generator is only 27% of the weight of the magnetic-spring generator, and hence it is more wearable than the magnetic-spring generator. However, the better generator for the validation is also dependent on the performances in other aspects, such as the frequency response when the generators are rotated to different orientations, and the change in resonant frequency with rotation, which is evaluated in the next chapter. In the next chapter, the designed electromagnetic generators are tested and characterized on a controlled vibration source. Through comparing the performances of the two electromagnetic generators, one design of electromagnetic generators is chosen to validate the analytical results on the human body. With the selected electromagnetic generator, an experimental validation on the human body is made.

Chapter 6
Validating the Effect of Orientation on Harvested Power

The analytical results in Chapter 4 show that during the process of harvesting energy from human motion, 2-DOF inertial energy harvesters have a greater tolerance to rotation compared to 1-DOF harvesters. To validate the results, mechanical- and magnetic-spring electromagnetic harvesters have been designed and fabricated, as presented in Chapter 5. In this chapter, the fabricated harvesters are tested and characterised with a controlled vibration source in order to determine the optimum loads, the resonant frequencies at different rotation angles, and the bandwidths; these results are shown in Section 6.1. To validate the analytical results derived from the previous on-body acceleration measurement (Section 3.1), the validation scenario should be consistent with the previous measurement. Therefore, an experimental validation on the human body was carried out using the fabricated inertial energy harvesters. This work is presented in Section 6.2.

6.1 Experimental Validation on a Controlled Vibration Source

In Chapter 5, the resonant frequencies of the fabricated energy harvesters have been calculated, and the simulation results show that the resonant frequencies are constant with rotation. in the next section, to validate the results and characterise the generators, measurements for the generators were carried out on a controlled vibration source. The fabricated prototypes of the mechanical-spring generator and the magnetic-spring generator (the one with Delrin end holders) were tested. Section 6.1.1 presents the measurement setup. The optimum resistive loads, the frequency response of open-circuit voltage with rotation, and the bandwidth of the generators were measured. The measurement results are presented and analysed in Section 6.1.2.

6.1.1 Measurement Setup

A schematic drawing of the measurement setup is shown in Figure 6.1, while a photographic image can be seen in Figure 6.2. In the setup, the generator is driven by a controlled vibration source (model Derritron VP180 LS shaker). A flat aluminium plate is securely mounted on the top of the vibration source to allow the plate to be vertically displaced, and the generator is mounted on the plate. The amplitude and the frequency of driving vibrations are controlled by

an oscillator. An oscilloscope (model TDS 2002) is used to monitor and record the voltage from the test generator. A single axis accelerometer (model EGCS-D0-10) is taped on to the aluminium plate to measure the output vibration on the plate. The accelerometer, signal conditioner and digital multimeter (model 1906 DVM) make up the acceleration calibration devices to ensure the driving vibration is constant in the study.

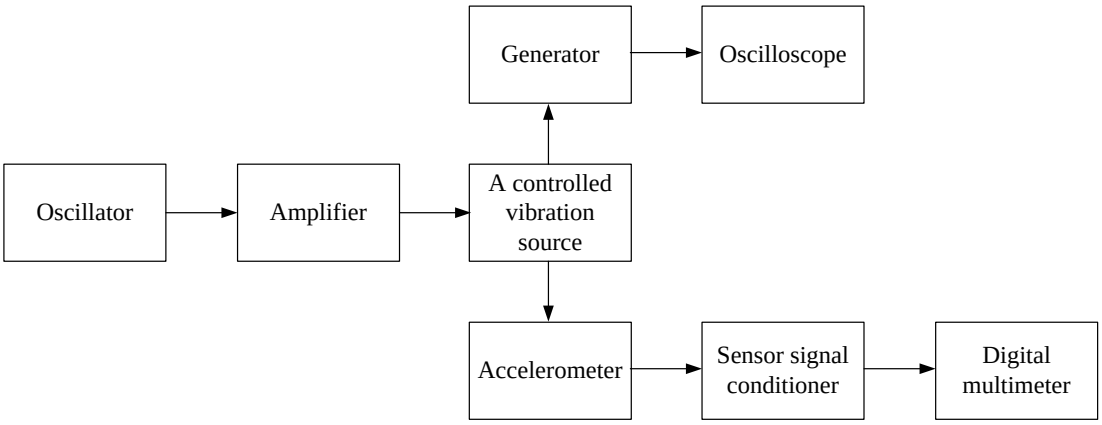

Figure 6.1 Schematic drawing of measurement setup on a controlled vibration source.

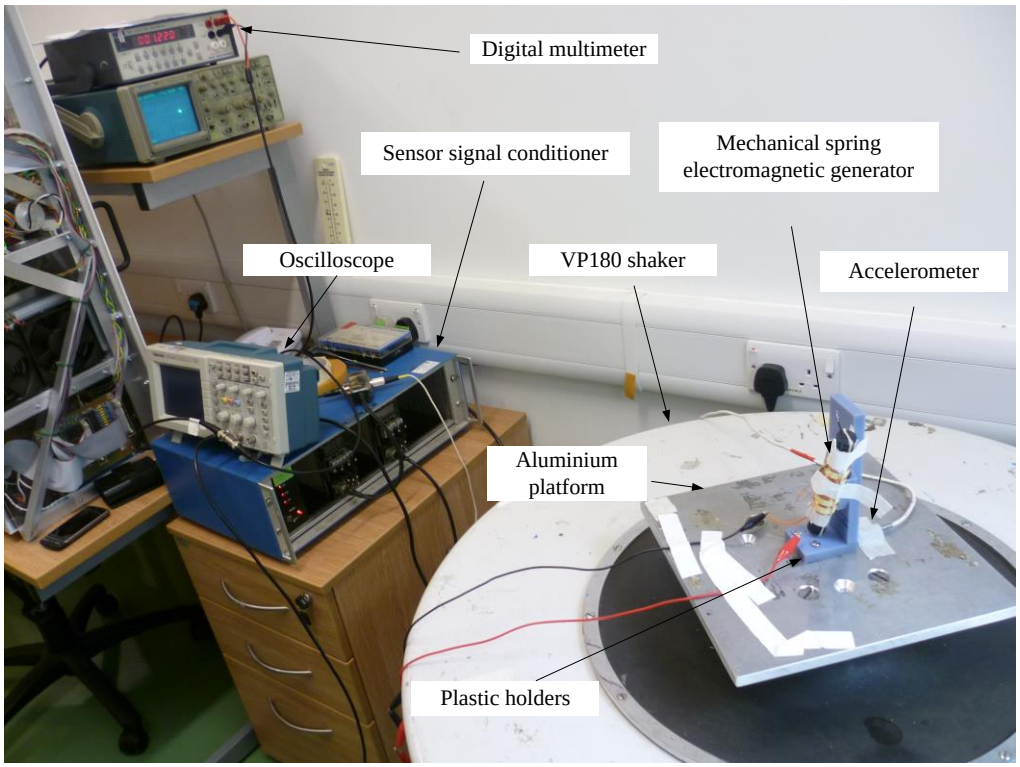

Figure 6.2 Picture of measurement setup on a controlled vibration source.

Two holders were made to secure the generator to the vibration source, and also to hold it in the correct orientation and allow it to be rotated from 0 ° to 180 ° in steps of 10 °. The design of the holders is shown in Figure 6.3. One holder has a concave design for attachment to the side of

the generator (Figure 6.3c). The indentation design (Figure 6.3a) and the convex design (Figure 6.3b) allow the generator to be rotated in steps of 10 °.


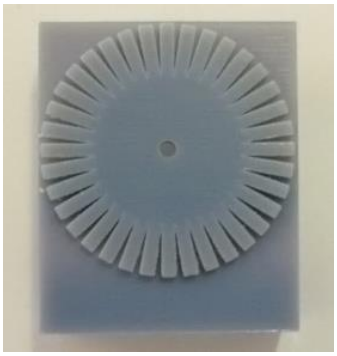


(a) (b) (c)

Figure 6.3 (a) One holder with indentation. Three bolts help mount the holder on the aluminium plate. (b) The other holder with a convex design on one side and (c) a concave design on the other side.

6.1.2 Measurement Results

In the measurement, some distortion of the output vibration from the vibration source was observed, which is discussed in Section 6.1.2.1. The effect of coil connection on the induced voltage is experimentally validated in Section 6.1.2.2. To maximise the load power from the generators, the optimum resistive loads were considered, as discussed in Section 6.1.2.3. To validate the resonant frequencies and explore whether or not the resonant frequencies change with rotation, the frequency response of the open-circuit voltage from the generators was measured. This work is presented in Section 6.1.2.4. The measurement results of the total damping ratio, the Q-factor and the bandwidth of the generators are presented and analysed in Section 6.1.2.5.

6.1.2.1 Distortion during Low-Frequency Vibrations

The controlled vibration source has a maximum displacement of 25 mm, a peak acceleration of 300 m s^{-2} (i.e. 30.6‘g’ [m s^{-2}]), and a frequency range from 1 to 200 Hz. It should perform uniaxial, stable and distortion-free vibration movement at any desired frequency and amplitude within the allowed range without generating additional sources of uncertainty. However, these ideal specifications are not met in practice. To illustrate this, Figure 6.4 shows the output vibration on the aluminium plate at an input vibration of 0.3‘g’ (rms) [m s^{-2}] at 3 Hz. The sinusoidal vibration signal appears distorted. As discussed in existing studies [101, 102],

distortion of the output vibration from a controlled vibration source is commonly displayed in low-frequency operation (<10 Hz) because of the mechanical constraints of the moving mass-suspension system used in the vibration source.

The vibration along the oscillation axis of the generator decreases with rotation (Equation (5.10)); hence, the driving vibration should be adequate such that the induced voltage from the generator after rotating is measureable under the effect of distortion. Therefore, in the measurement of the frequency response, the driving vibration was set to be 0.3‘g’ (rms) [m s^{-2}] and the frequency was increased from 3 to 10 Hz. The driving vibration below 3 Hz was not tested, because displacement close to the displacement limit causes vibration distortions [101]. With a given acceleration, the displacement is inversely proportional to the frequency (Equation (6.1)); at 0.3‘g’ (rms) [m s^{-2}], i.e. $A = 0.3‘g’ \times \sqrt{2} = 4.16$ m s^{-2}, the frequency f_0 should be at least 2 Hz below the limit of the maximum displacement of the vibration source ($Y = 25$ mm).

$$A = (2\pi f_0)^2 Y \tag{6.1}$$

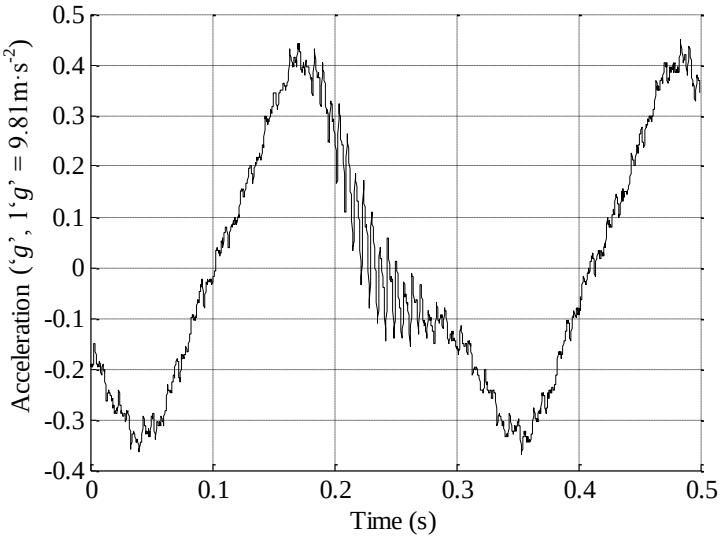

Figure 6.4 The output vibration on the aluminium plate at an input vibration of 0.3‘g’ (rms) [m s^{-2}] at 3 Hz.

6.1.2.2 Validation of the effect of Coil Connection on Voltage Generation

The simulation results in Section 5.5.4 show that some generated energy is wasted in the coils, and that, in the mechanical-spring generator, the induced voltage from coils 1 and 2 is greater than that from the five coils (Figure 5.32). To validate this, the open-circuit voltage induced by the coils 1 and 2 and that by the five coils was measured. The generator was driven by a

vibration of 0.3‘*g*’ (rms) [m s^{-2}] in 7-11 Hz, and was oriented upright. The results are shown in Figure 6.5 showing that the measured emf from the two coils is greater than that from the five coils combined at the five test frequencies, strongly agreeing with the simulation results.

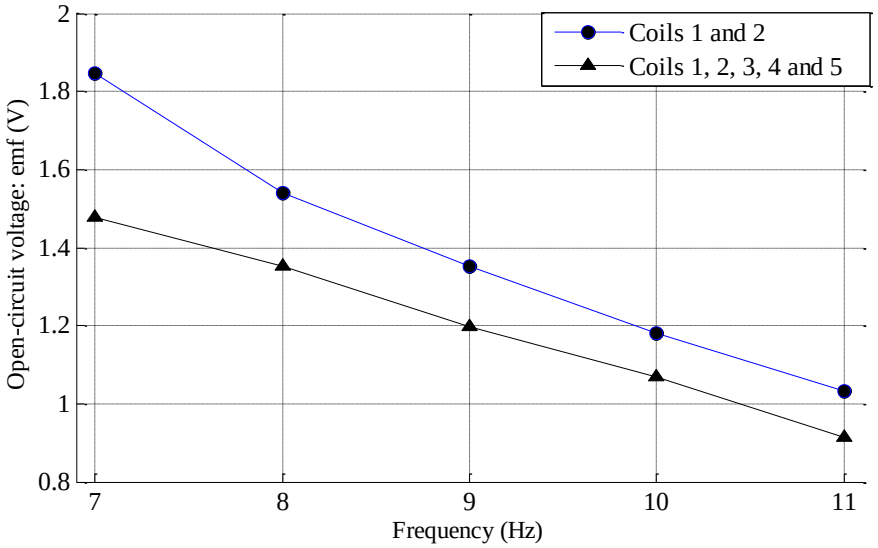

Figure 6.5 Induced voltage with different coil connections when the mechanical-spring electromagnetic generator is driven by a vibration of 0.3‘*g*’ (rms) [m s^{-2}] in 7-11 Hz and is oriented upright.

6.1.2.3 Optimum Loads

The theoretical optimum resistive loads for maximising the load power generated from the mechanical- and magnetic-spring electromagnetic generators have been calculated as 1.29 kΩ and 2.84 kΩ, respectively, in Section 5.4. To validate the results, the generated voltage across different resistive loads was measured and the corresponding load power was then calculated. In the measurements, the generators were along the direction of gravity, being placed upright. A programmable resistance (model IET PRS series) located away from the vibration source was connected to the generators as a resistive load. The input vibration was set to 0.1‘*g*’ (rms) [m s^{-2}] at 30 Hz, at which settings the output vibration on the aluminium plate appeared undistorted.

Figure 6.6 and Figure 6.7 show the load power against the variable resistive load for the mechanical- and magnetic-spring electromagnetic generators, respectively. The maximum power is available at load resistance of 1.27 kΩ and 2.88 kΩ for the mechanical- and magnetic-spring electromagnetic generators, respectively. The measured optimum loads differ from the theoretical results by 2% and 1% for the mechanical- and magnetic-spring electromagnetic generators, respectively, showing good correlation.

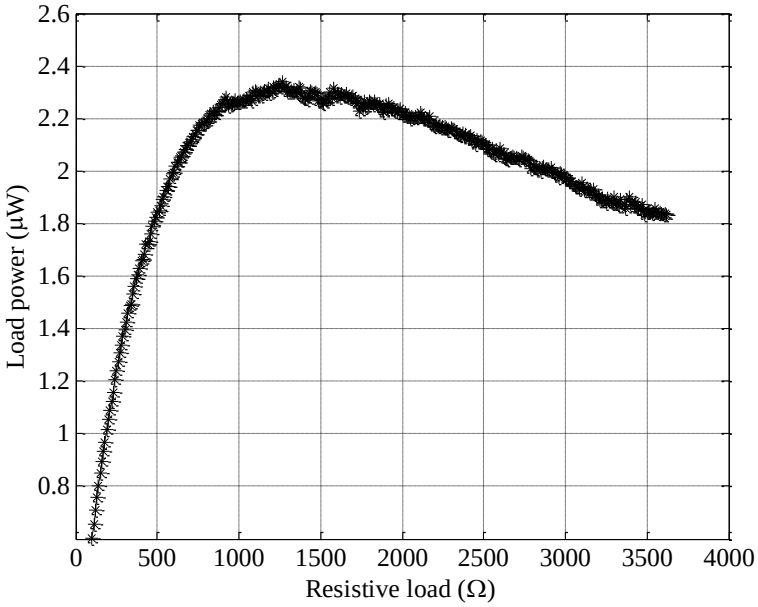

Figure 6.6 Load power vs. resistive load at an input vibration of 0.1'g' (rms) [m s^{-2}] at 30 Hz for the mechanical-spring electromagnetic generator.

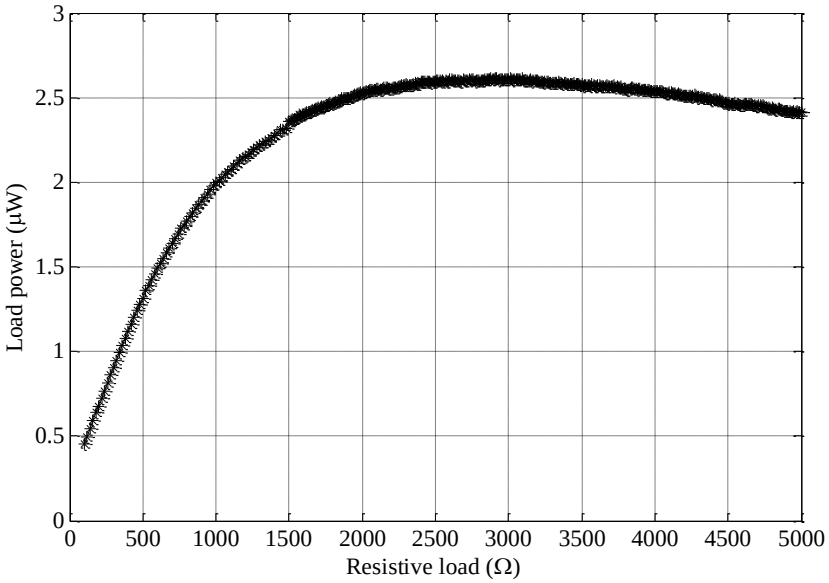

Figure 6.7 Load power vs. resistive load at an input vibration of 0.1'g' (rms) [m s^{-2}] at 30 Hz for the magnetic-spring electromagnetic generator.

6.1.2.4 Frequency Response at Different Rotation Angles

In Chapter 5, the resonant frequencies of the mechanical- and magnetic-spring electromagnetic generators were calculated as 3.45 Hz and 4.42 Hz, respectively. Also, the simulation results show that the resonant frequencies are constant with rotation. To validate the results, the

frequency response of open-circuit voltage when the generators are rotated along different orientations was measured. In the measurement, the generators were rotated from 0 °to 60 °with respect to the direction of gravity. A comprehensive experimental validation from 0 °to 80 °was not made, because at 70 °and 80 °, the open-circuit voltage could not be adequately measured due to the low acceleration along the tube, particularly under the effect of distortion. Figure 6.8 illustrates the generators, which are mounted on the holder and rotated by 30 °.

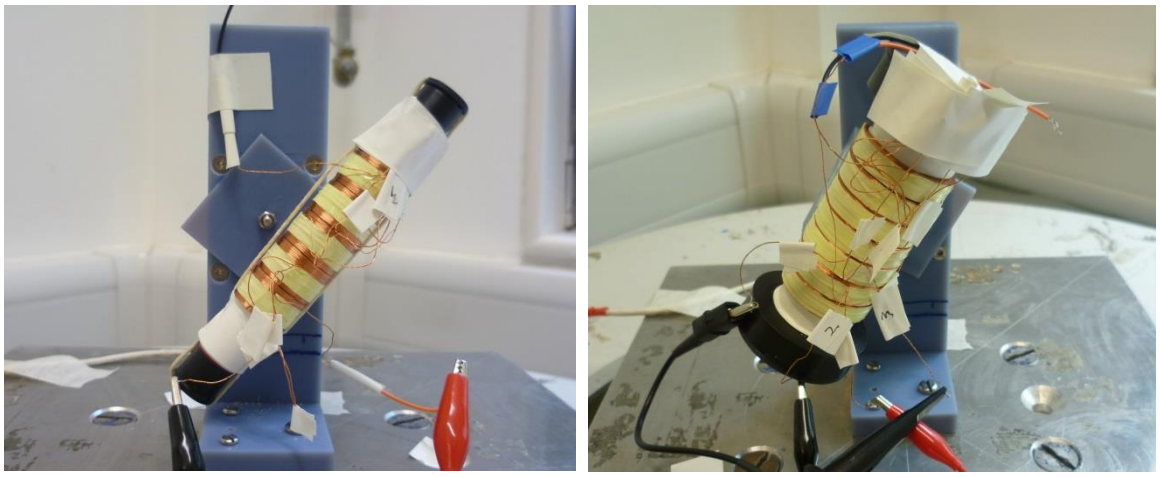

(a) (b)

Figure 6.8 (a) Mechanical-spring electromagnetic generator and (b) magnetic-spring electromagnetic generator, mounted on the holder at 30 °rotation angle.

In the study, the induced voltage from the generators with five or seven coils connected in series could not be adequately measured, because some generated energy is wasted in the series-connected coils, as discussed in Section 5.5.4, particularly under the effect of distortion from the vibration source. Therefore, in the measurement, the number of test coils was reduced to ensure the induced voltage is measurable.

If the generator is rotated by θ, the quiescent position of the moving mass, $x_q{}'$, under the effect of gravity is expressed as:

$$x_q{}' = \frac{`g' \cdot cos\theta}{(2\pi f_0)^2} \tag{6.2}$$

Then, if the generators are rotated from 0 °to 60 °, the quiescent position for the mechanical-spring generator is decreased from 21 mm to 10 mm (f_0=3.45 Hz), or from 13 mm to 6 mm (f_0=4.42 Hz) for the magnetic-spring generators. Therefore, the quiescent position is within coils 1 and 2 for the mechanical-spring generator (Figure 6.9a), and within coils 2 and 3 for the magnetic-spring generator (Figure 6.9b). The simulation results in Section 5.5.4 show that the

resonant frequency remains constant over different coil connections. Taking that into consideration, the frequency response of the open-circuit voltage from the mechanical-spring generator with series-connected coils 1 and 2 was measured, as shown in Figure 6.10, and the frequency response of the open-circuit voltage from the magnetic-spring generator was measured with coil 2, as shown in Figure 6.11.

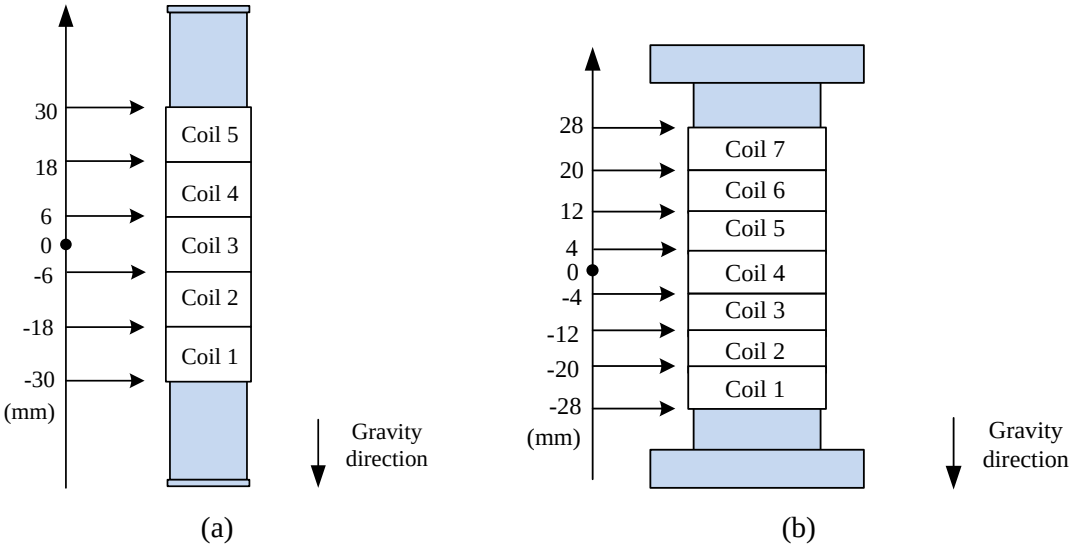

Figure 6.9 Schematic of (a) the mechanical-spring electromagnetic generator and (b) the magnetic-spring electromagnetic generator oriented to the direction of gravity without rotation.

In Figure 6.10 and Figure 6.11, the frequency response appears distorted, and it is difficult to exactly identify the resonant frequencies at different rotation angles. Instead, taking that into consideration, the frequencies with the emf greater than $\sqrt{1/2}$ of the maximum emf are found and the 3dB bandwidths are then identified, as shown in Table 6.1. The results show that due to the distortion, the bandwidths of the generators cannot be identified adequately from Table 6.1. To identify the bandwidths, the total damping ratios of the generators were measured, as detailed in the next section. In addition, at all test angles for the mechanical-spring electromagnetic generator, the resonant frequencies are in the range of 3.3-4.4 Hz, where the calculation resonant frequency of 3.45 Hz also lies; for the magnetic-spring electromagnetic generator, the resonant frequencies are in the range of 3.0-8.0 Hz, which covers the calculated 4.42 Hz resonant frequency. The simulation results show that the resonant frequencies are constant with rotation. However, due to the distortion of the measurement results on the frequency response, that simulation result cannot be validated. Except the distortion of the output vibration from the controlled vibration source, another reason for the distortion in Figure 6.10 and Figure 6.11 is the Coulomb friction between the moving mass and the inner face of the tube. Coulomb friction resists relative lateral motion of two solid surfaces in contact. It acts in a

direction opposite to the direction of velocity. The friction F_f [N] is given by [103]:

$$F_f = \mu F_n \tag{6.3}$$

where F_n [N] is the normal force and μ is the coefficient of kinetic friction. The value of the coefficient of friction depends on the materials in contact and the condition of the surfaces in contact. Hence, Coulomb friction is independent of the displacement and velocity. It depends only on the normal force between the sliding surfaces. When the generator is rotated along different orientations, the force of gravity that is perpendicular to the inner face of the tube varies. The Coulomb friction between the moving mass and the inner face of the tube increases with the increase of the rotation angle. Due to Coulomb friction, Coulomb damping is independent of the displacement and velocity. When the generator is tested on the controlled vibration source, the Coulomb friction reduces the amplitude of the vibration of the moving mass, and energy is dissipated due to Coulomb damping. In addition, Coulomb damping introduces non-linearity to the resonant system, but the natural frequency of the resonant system is unaltered with the addition of Coulomb damping.

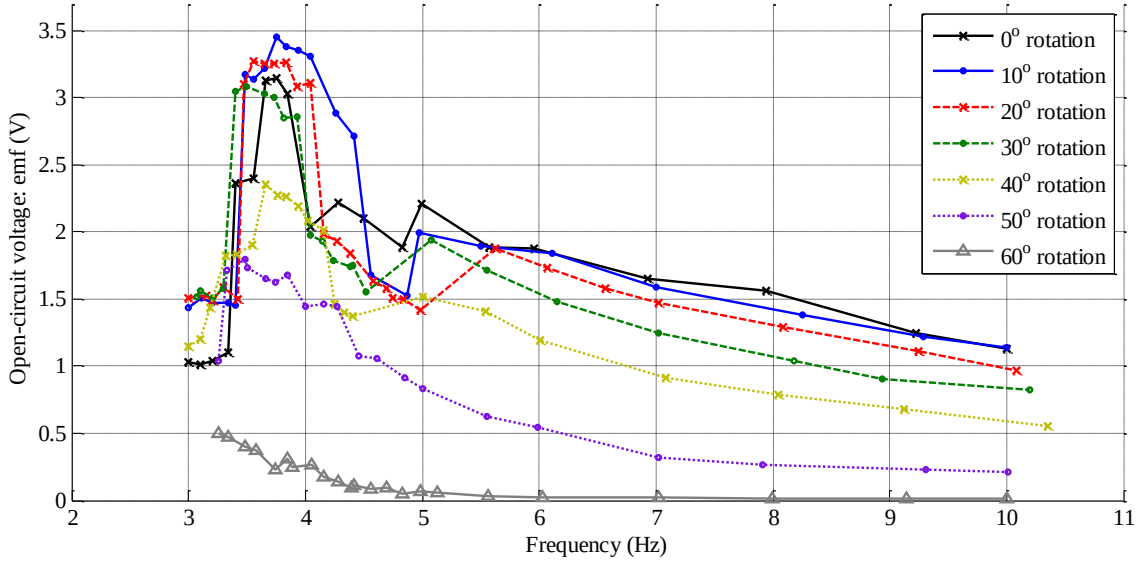

Figure 6.10 Frequency response of the open-circuit voltage from the mechanical-spring electromagnetic generator with coils 1 and 2 connected in series.

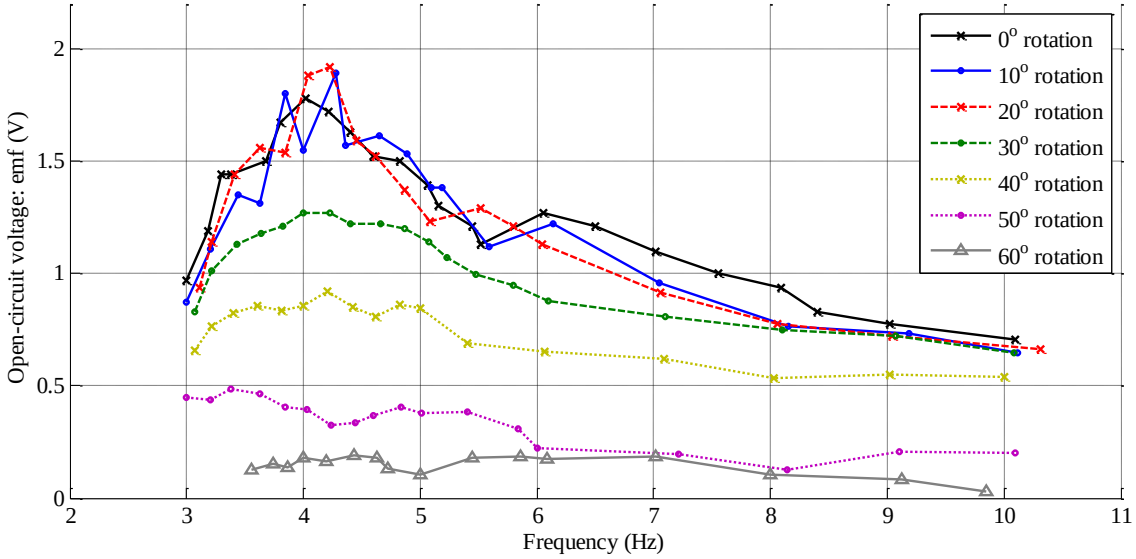

Figure 6.11 Frequency response of the open-circuit voltage from the magnetic-spring electromagnetic generator with coil 2.

Table 6.1 Frequencies with the emf greater than $\sqrt{1/2}$ of the maximum emf and the bandwidths when the generators are rotated at different angles.

Mechanical-spring electromagnetic generator							
Rotation angles	0 °	10 °	20 °	30 °	40 °	50 °	60 °
Frequency range [Hz]	3.4-4.3	3.5-4.4	3.5-4.0	3.4-3.9	3.3-4.2	3.3-4.3	3.3-3.6
Bandwidth [Hz]	0.9	0.9	0.5	0.5	0.8	0.9	0.3
Magnetic-spring electromagnetic generator							
Rotation angles	0 °	10 °	20 °	30 °	40 °	50 °	60 °
Frequency range [Hz]	3.3-5.0	3.4-5.2	3.4-4.6	3.2-5.8	3.1-7.1	3.0-5.8	3.6-8.0
Bandwidth [Hz]	1.7	1.8	1.2	2.6	4.0	2.8	4.4

6.1.2.5 Bandwidth of the Energy Harvesters

The resonant frequencies of the mechanical- and magnetic-spring electromagnetic generators were calculated as 3.45 Hz and 4.42 Hz, respectively. A bandwidth of 1 Hz is desirable to harvest energy from 3.9 Hz and hence generate more energy from human motion. To evaluate the bandwidth of the generators, the total damping ratios of the generators are measured and the Q-factors are then identified by Equation (2.15).

$$Q = \frac{1}{2\xi_T} \tag{2.15}$$

Based on the values of the resonant frequencies and the Q-factors, the bandwidths of the generators are evaluated by Equation (2.16).

$$\Delta f = \frac{f_0}{\mathrm{Q}} \tag{2.16}$$

In the measurement of the total damping ratio, the generator was connected with the identified optimum load resistance, and oriented to the direction of gravity. The ratio was then measured by delivering a stable driving vibration and then shutting down the vibration source suddenly. The total damping ratio was evaluated through observing the voltage under damping over time. An example of the voltage output under damping is show in Figure 6.12, where the input vibration is set to be 0.3'g' (rms) [m s^{-2}] at 10 Hz. The magnitude of the voltage output under damping was measured at two separate points, n periods apart. The damping ratio can then be calculated as [104]:

$$\xi_T = \frac{\ln\left(\frac{V(t_1)}{V(t_1+nT)}\right)}{2\pi n} \tag{6.4}$$

where $V(t_1)$ [V] is the magnitude at one point of the voltage under damping at time t_1, and $V(t_1 + nT)$ is the magnitude at another point after n periods time.

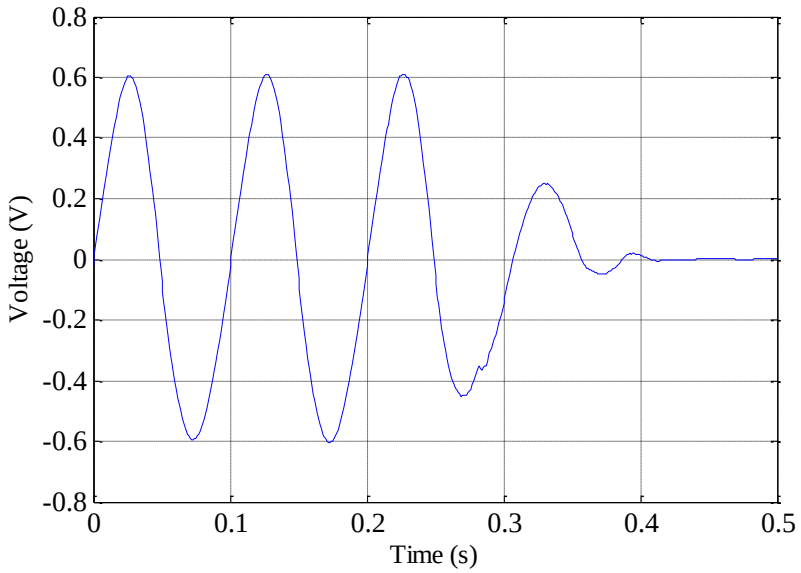

Figure 6.12 Voltage output under damping from the mechanical-spring electromagnetic generator.

Measurements of the total damping ratio were repeated five times. The total damping ratio of the mechanical-spring generator with five series-connected coils was measured as 0.14 ± 0.026 (mean ± STD). The Q-factor is 3.5 ± 0.64. Due to the distortion from the vibration source, the total damping ratio of the magnetic-spring generator with seven series-connected coils could not be adequately measured. Hence, instead, the mechanical damping ratio of the magnetic-spring

generator with coil 2 was measured as 0.13 ± 0.017. The Q-factor corresponding to this mechanical damping ratio is 3.8 ± 0.46. The mechanical damping ratio was measured without the optimum load, and the measurement followed the same procedure as for the total damping ratio. More coils increase the coil resistance and then more energy is wasted across the coils; hence the damping ratio is increased. As a result, the total damping ratio of the magnetic-spring generator with seven series-connected coils is over 0.13 and then the Q-factor is below 3.8.

Based on the measurement results of resonant frequencies and the Q-factors, the bandwidths of the generators are calculated. The bandwidth of the mechanical-spring electromagnetic generator is 1.0 Hz, and higher than 1.2 Hz for the magnetic-spring electromagnetic generator. Therefore, the kinetic energy from human motion at 3.9 Hz can be harvested by the two electromagnetic generators.

6.1.3 Summary

In Section 6.1, the experimental validation on a controlled vibration source has been presented. Distortion of output vibrations from the controlled vibration source at low frequencies (<10 Hz) has been found. The measurements show that the induced voltage from coils 1 and 2 is greater than that from five coils in the mechanical-spring electromagnetic generator, which validates the simulation results, showing that some generated energy is wasted in the five series-connected coils.

The optimum load resistances for maximising the load power have been measured as 1.27 kΩ and 2.88 kΩ for the mechanical-and magnetic-spring electromagnetic generators, respectively. To validate the calculated resonant frequencies of the generators, and explore whether or not the resonant frequencies change with rotation, the frequency response of the generators rotated to different angles has been measured. In the measurement, the generators were rotated from 0 °to 60 °through 10 °steps with respect to the direction of gravity. However, the frequency response was distorted and it was difficult to exactly identify the resonant frequencies at different angles. Therefore, instead, the frequencies with an emf greater than $\sqrt{1/2}$ of the maximum emf were found. The results showed that the resonant frequencies are in the range of 3.3-4.4 Hz for the mechanical-spring electromagnetic generator, or 3.0-8.0 Hz for the magnetic-spring electromagnetic generator. The calculated resonant frequencies (the mechanical-spring generator: f_0 =3.45 Hz, and the magnetic-spring generator: f_0 =4.42 Hz) are within the corresponding measured frequency ranges. The simulation results in the previous chapter show that the resonant frequencies are constant with rotation. However, due to the distortion of the measurement results on the frequency response, this simulation result cannot be validated.

The total damping ratio of the mechanical-spring electromagnetic generator was measured, and the Q-factor and the bandwidth were then calculated. The measurement results are summarised in Table 6.2. A range for the total damping ratio of the magnetic-spring electromagnetic generator is given instead of a specific value. This is because the total damping ratio of the magnetic-spring electromagnetic generator with seven series-connected coils could not be measured under the effect of the distortion from the vibration source. Instead, the mechanical damping ratio of the generator with coil 2 was measured, after which a range for the total damping ratio of the generator with seven series-connected coils was deduced.

From Table 6.2, it is found that the mechanical-spring electromagnetic generator with 3.45 Hz resonant frequency has 1.0 Hz bandwidth, and the magnetic-spring electromagnetic generator with 4.42 Hz resonant frequency has over 1.2 Hz bandwidth. Therefore, the kinetic energy from human motion at 3.9 Hz can be harvested by the two electromagnetic generators, but, as discussed in Section 5.6, the mechanical-spring generator is more wearable than the magnetic-spring generator due to its lighter weight. Accordingly, the mechanical-spring generator is used in the on-body test to validate the benefit of 2-DOF energy harvesters in terms of the tolerance to rotation. This validation on the human body is presented in the next section.

Table 6.2 Measurement results of the damping ratios, Q-factors and bandwidths.

Mechanical-spring electromagnetic generator			
	ξ_T	Q-factor	Bandwidth
Mean ± STD	0.14 ± 0.026	3.5 ± 0.64	1.0 Hz
Magnetic-spring electromagnetic generator			
	ξ_T	Q-factor	Bandwidth
Mean ± STD	> (0.13 ± 0.017)	< (3.8 ± 0.46)	> 1.2 Hz

6.2 Experimental Validation on the Human Body

The analytical results in Chapter 4 show that when harvesting energy from human motion, 2-DOF inertial energy harvesters have greater tolerance to rotation than 1-DOF harvesters. To validate the results, an experimental validation on the human body was carried out. A 2-DOF energy harvester that consists of two orthogonal 1-DOF energy harvesters was mounted on the human body, and the output power generated from the energy harvester at different rotations was evaluated when participants were doing a specified activity. Subsequently, the benefit of 2-DOF energy harvesters in terms of the angular tolerance was validated. The mechanical-spring electromagnetic generator has been chosen (as discussed in Section 6.1) for use in the validation on the human body. Section 6.2.1 presents the measurement setup. The measurement results of

the output power and the angular tolerance from the test generators are shown and analysed in Section 6.2.2.

6.2.1 Measurement Setup

As discussed in Section 5.1, the knee position and running activity have been selected for the validation due to the high output power and the large acceptable volume for generators. To be consistent with the previous acceleration measurements, participants were asked to run on a treadmill in the study. Ethical approval for the study was obtained from the University's FPAS Faculty Ethics Committee with RGO reference 3421.

To evaluate the tolerance to rotation, the 2-DOF generator needs to be tested along different orientations. As a comprehensive experimental validation for all the evaluated orientations on the knee (as analysed in Chapter 3) cannot be finished within the time allowed to complete a doctoral thesis, a subset of orientations was selected for the study. Bearing in mind that body-worn generators would shift away from the expected location or the expected orientation due to human motion, three locations around the knee and four different orientations at each location were chosen. In total, 12 different positionings of the 2-DOF generator on the knee were measured.

The test locations are shown in Figure 6.13. One test location is on the knee where the G-link was attached in the previous on-body acceleration measurements (as shown in Section 3.1). This location is termed the 'middle of the knee'. Another location is found by rotating the location at the middle of the knee around the tibia to the back by 20°. This location is termed the 'back of the knee'. Another location is reached by rotating the location at the middle of the knee around the tibia to the front by 20 °. This location is termed the 'front of the knee'. At each location, the 2-DOF generator was rotated by 0 °, 20 °, 40 ° and 60 ° with respect to the direction of gravity. To illustrate this, Figure 6.14 shows the four test orientations at the middle of the knee.

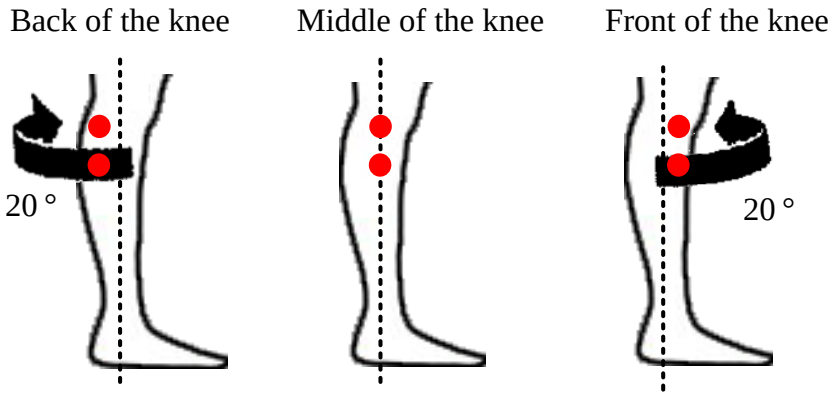

Figure 6.13 Three test locations on the knee. The red solid circles represent the 1-DOF generators.

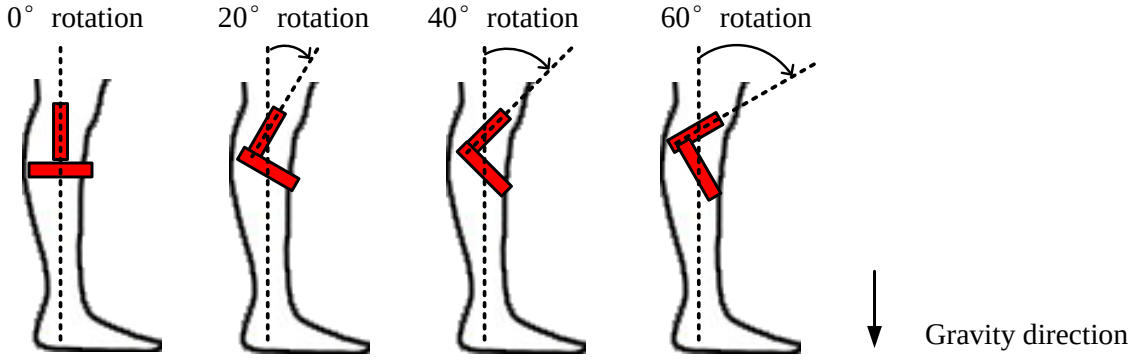

Figure 6.14 Four test orientations at the middle of the knee. The red bars represent the 1-DOF generators.

A schematic drawing of the measurement setup is shown in Figure 6.15, while a photographic image can be seen in Figure 6.16. Two experimental prototypes of the 1-DOF mechanical-spring electromagnetic generators were fabricated and orthogonally oriented to form a 2-DOF electromagnetic generator. A triple axis accelerometer (G-link) is used to monitor the motions on the knee. In the study, participants reported that the 2-DOF generator and the accelerometers did not significantly affect the way they ran. The two 1-DOF generators are connected with optimum resistive loads. When participants were running on the treadmill, the real-time voltages across the optimum loads were sampled at 1k Hz and saved on a computer through a data acquisition device (model NI USB-6008), and the acceleration data, sampled at 128 Hz, were saved locally in the G-link memory. When the participant finished all exercises, the data were wirelessly downloaded from the G-link and saved on a computer with the aid of a G-link USB base station.

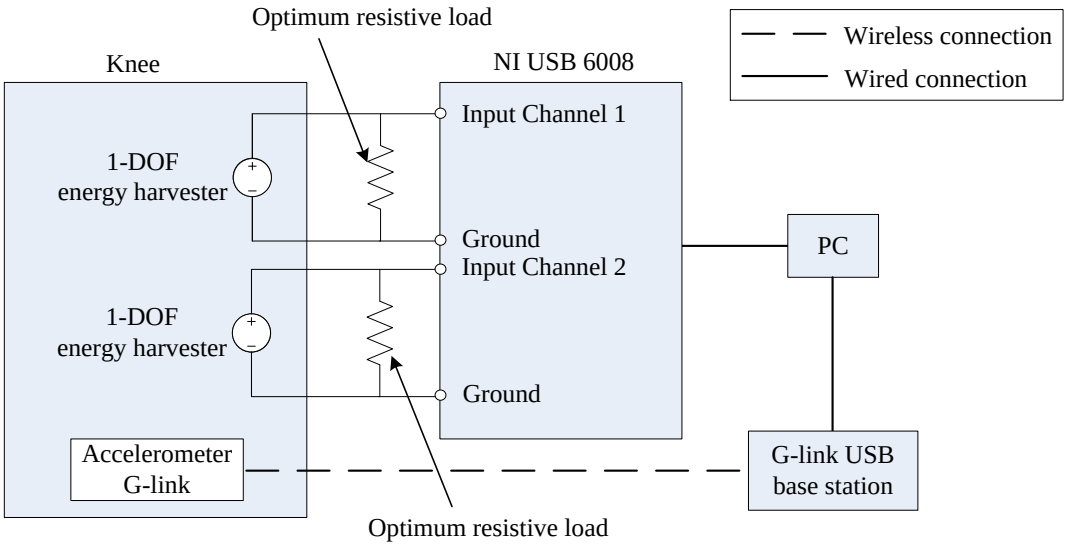

Figure 6.15 Schematic drawing of measurement setup on the human body.

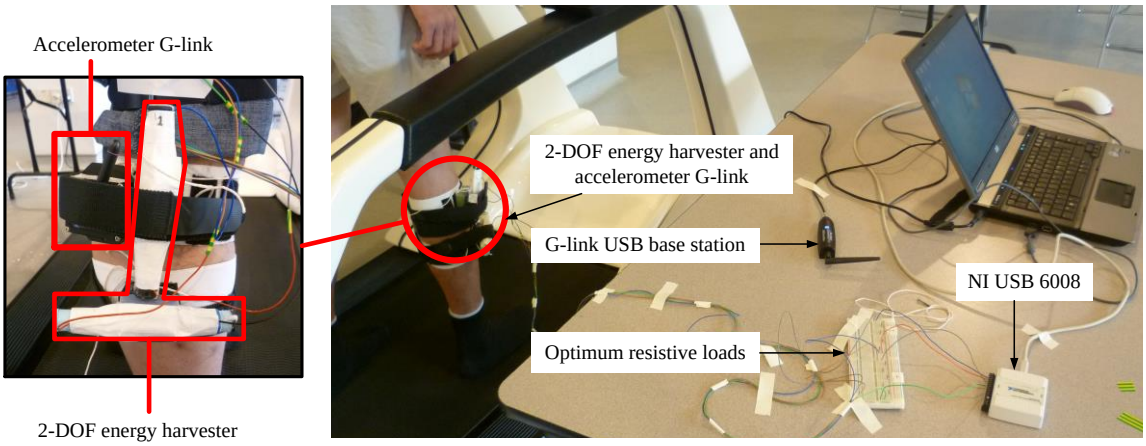

Figure 6.16 Picture of measurement setup on the human body.

Two holders were constructed to mount one generator on the human body, and to hold it in the correct orientation and allow it to rotate from 0 ° to 180 ° in steps of 10 °. One holder is the same as that used in the validation on a controlled vibration source; it has a concave design on one side to hold the generator (Figure 6.3c) and a convex design on the other side for rotation (Figure 6.3b). The other holder is shown in Figure 6.17. The indentation design allows the generator to rotate through steps of 10 °.

In the test, participants were asked to wear two 'instrumented bands', each of which comprises a band of elastic with two combined holders secured by Velcro. One 1-DOF generator was glued firmly onto the combined holders. In addition, the accelerometer was glued firmly onto a holder. The elastic bands were tightly fastened to the knee using Velcro ends to ensure that the generators and the accelerometer closely follow the motions of the body.

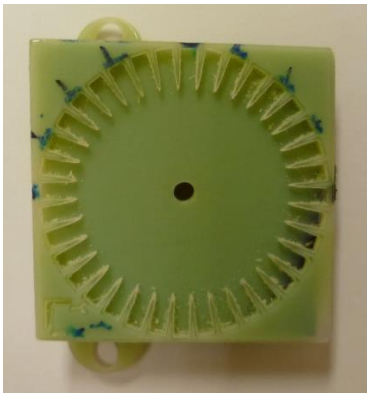

Figure 6.17 A holder with an indentation design allowing generators to rotate through 10 °steps.

Figure 6.18 A participant standing on a treadmill, with the 2-DOF energy harvester and the accelerometer mounted on the middle of the knee with 0 °rotation.

Data were collected from 13 participants (10 male and three female, age: 27 ± 2.5 years, height: 174 ± 10.0 cm, running speed: 6.5 ± 1.27 km/h, step frequency: 2.5 ± 0.12 Hz (mean ± STD)) wearing the accelerometer and the 2-DOF generator (Figure 6.18). As with the acceleration measurement, participants were wearing socks without shoes during the measurements. At first, each participant set the treadmill to run at a speed he/she felt comfortable running at, and this speed was recorded. After that, the participant was asked to maintain this speed during the test with the aid of a metronome. For each test, participants were asked to run for 30 seconds.

6.2.2 Measurement Results

The generated power P_{opt} [W] over the 30 seconds' measurement from the 1-DOF generators on the optimum load resistance was derived by Equation (6.5).

$$P_{opt} = \frac{1}{t_2\text{-}t_1} \cdot \sum_{t_1=10}^{t_2=40} \frac{V_t^2}{R_{opt} \cdot f_s} \tag{6.5}$$

where f_s [Hz] is the sampling frequency, V_t [V] is the measured voltage across the optimum load resistance, t is the time interval and R_{opt} [Ω] is the optimum load resistance. The power from the 2-DOF generator was calculated by adding the power generated from two orthogonal 1-DOF generators. To validate the analytical results, the measured acceleration data were fed into the data-processing methods (as presented in Section 3.2) for evaluating power availability from the 1-DOF and 2-DOF generators. The measurement results and the analytical results of the power output from 1-DOF and 2-DOF generators at the three test locations are shown in Figure 6.19. The results shown in Figure 6.19 are analysed in terms of the power output and the angular tolerance, as shown in the following sections.

6.2.2.1 Power Output

To compare the measurement results of the power at the three locations around the knee, the average of the median of the power at each location is calculated and the results are shown in Table 6.3. It is found that the back of the knee generates the most power for both the 1-DOF and 2-DOF generators, and the front of the knee provides the least power, which closely agrees with the analytical results. The difference of the output power at the three locations is because of the different magnitudes of the vibrations resulting from the running activity. The measurement results show that the average accelerations are 1.24‘g’, 1.12‘g’ and 1.02‘g’ [m s^{-2}] at the back, middle and front of the knee, respectively.

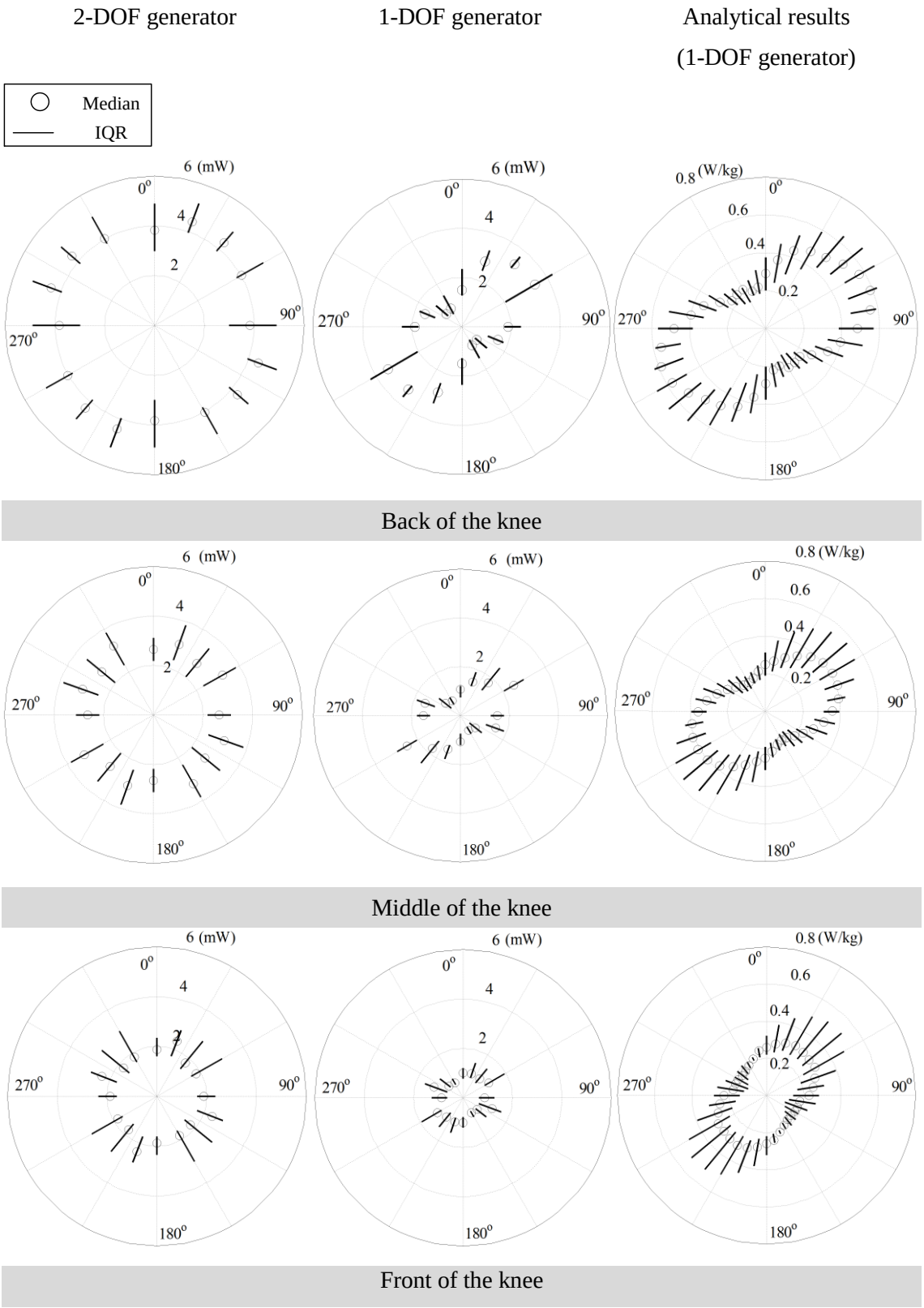

Figure 6.19 Median and IQR of the measurement results and the analytical results of the power output from 1-DOF and 2-DOF generators at the three test locations.

Table 6.3 Average of the median of the power from the 1-DOF and 2-DOF generators at the three locations.

	Back of the knee	Middle of the knee	Front of the knee
1-DOF generator	2.03 mW	1.41 mW	0.980 mW
2-DOF generator	4.16 mW	2.90 mW	1.96 mW
Analytical results (1-DOF generator)	0.387 W/kg	0.294 W/kg	0.241 W/kg
Analytical results (2-DOF generator)	0.773 W/kg	0.588 W/kg	0.481 W/kg

Comparing the measurement results of the power from the 2-DOF and 1-DOF generators, it is found that if the 2-DOF generator and the 1-DOF generator were placed along the same orientation, the 2-DOF generator would be able to harvest more power than the 1-DOF generator. Along each orientation, the increase in the median of the power output is calculated. It is found that the median of the power from 2-DOF generators harvest is 2.04 times (average) greater than that from 1-DOF generators, and the analytical results show that this increase is 2.15 times. Therefore, the measurement results of this power increase differ from the expected by just 5%, showing good correlation.

6.2.2.2 Tolerance to Rotation

Based on the analytical methods in Section 3.2, the angular tolerance is calculated through the power distribution among the orientations, while the angular tolerance guarantees that the power will not decrease by over 10%. However, due to the small number of samples over different orientations, the angular tolerance of the test orientations could not be calculated. Therefore, normalised power is used to analyse the angular tolerance. At each location, the median of the power is normalised to the maximum of the median of the power that the 1-DOF or 2-DOF generators harvested.

At the back of the knee, if a 1-DOF generator is rotated from 0 ° to 360 °, the analytical results show that the normalised power is 36%-100%, while it is 90%-100% for a 2-DOF generator, showing a significant improvement over 1-DOF generators. Hence, 2-DOF generators perform better in terms of the angular tolerance and this is true for all three locations (Table 6.4). To validate these analytical results, the normalised power of the measurement results is calculated in practice. It is found that, at the back of the knee, if the 1-DOF generator is rotated from 0 ° to 360 °, the normalised power is 24%-100%, while it is 86%-100% for the 2-DOF generator, which confirms that the 2-DOF generator is more reliable in terms of output power and has greater tolerance to rotation. This improvement of the normalised power is found for the other

two locations (Table 6.4). 2-DOF generators can generate over 81% (average) of the maximum power in all orientations. For 1-DOF generators, it is only 35%. Therefore, the measurement results adequately validate the benefit of 2-DOF generators in terms of the angular tolerance.

In addition, at the back of the knee, the rotate ability τ of the 1-DOF generator is 25%, while it is 75% for the 2-DOF generator. This significant increase in the rotate ability τ means that 2-DOF generators have a greater tolerance to rotation and a much larger potential to generate over 90% of the maximum power, compared to 1-DOF generators. This increase of the rotate ability τ is also found for the middle of the knee.

Table 6.4 Normalised power from the 1-DOF and 2-DOF generators at the three locations.

	Back of the knee	Middle of the knee	Front of the knee
1-DOF generator	24%-100%	27%-100%	54%-100%
2-DOF generator	86%-100%	82%-100%	74%-100%
Analytical results (1-DOF generator)	36%-100%	54%-100%	43%-100%
Analytical results (2-DOF generator)	90%-100%	92%-100%	94%-100%

6.2.3 Summary

In Section 6.2, the experimental validation on the human body has been presented. The validation has been performed at three various locations around the knee while running, and four different orientations have been tested at each location. In the measurements, participants were asked to wear a 2-DOF electromagnetic generator that consists of two orthogonal 1-DOF mechanical-spring electromagnetic generators, and a triple axis accelerometer used to monitor body motion. The generated power from the 1-DOF and 2-DOF generators on the optimum load resistance has been evaluated. To validate the analytical results, the measured acceleration data have been fed into the data-processing methods presented in Section 3.2 for evaluating power availability. The measurement results of the power are shown in Table 6.5. The values in the blue and green cells are the maximum of the median of the power output from 1-DOF and 2-DOF generators, respectively. Table 6.6 shows the measurement results of the power density (output power normalised for mass).

The measurement results show that due to the different magnitudes of the vibrations at the three locations, the back of the knee generates the most power, and the front of the knee provides the least power for both the 1-DOF generator and the 2-DOF generator, which agrees with the analytical results. In addition, it is found that if the 2-DOF generator and the 1-DOF generator were placed along the same orientation, the 2-DOF generator would be able to harvest more

power than the 1-DOF generator. The median of the power from 2-DOF generators is 2.04 times greater than that from 1-DOF generators, and the analytical results show that this increase is 2.15 times, demonstrating good correlation.

Due to the small sample of the orientation, the angular tolerance of the test orientations could not be calculated. Therefore, normalised power was used to analyse the tolerance to rotation. At each location, the median of the power was normalised to the maximum of the median of the power that the 1-DOF or 2-DOF generators harvested. Significant improvement of the normalised power was found for all three locations from the 2-DOF generator over the 1-DOF generator, which shows that the 2-DOF generator is more reliable in terms of output power and has greater tolerance to rotation, which in turn shows strong agreement with the analytical results. At the back and middle of the knee, a significant increase of the rotate ability τ has been found from the 2-DOF generator over the 1-DOF generator, which demonstrates that 2-DOF generators have a much larger potential to generate over 90% of the maximum power. Therefore, the measurement results have adequately validated the benefit of 2-DOF generators in terms of the tolerance to rotation.

Table 6.5 The measurement results of the power on the optimum loads generated from the 1-DOF and 2-DOF generators on the knee while running.

	Rotation Angle [Degrees]	P_{opt} [mW]					
		Back of the knee		Middle of the knee		Front of the knee	
		Median	IQR	Median	IQR	Median	IQR
1-DOF generator	0	1.48	1.09	1.07	0.467	1.01	0.444
	20	2.83	0.867	1.47	0.605	1.02	0.643
	40	3.32	0.610	1.77	1.16	1.03	0.753
	60	**3.44**	2.20	**2.50**	0.944	1.20	0.960
	90	1.89	0.685	1.50	0.547	0.866	0.633
	110	1.58	0.680	1.52	0.798	**1.26**	0.971
	130	0.816	0.618	0.772	0.647	0.735	0.565
	150	0.866	0.884	0.681	0.315	0.684	0.268
2-DOF generator	0/90	3.83	1.93	2.64	0.943	1.87	0.746
	20/110	**4.44**	1.25	3.02	1.51	**2.37**	1.11
	40/130	4.35	1.02	2.71	1.51	1.76	1.43
	60//150	4.02	1.23	**3.21**	1.51	1.84	1.42

Table 6.6 The measurement results of the power density on the optimum loads generated from the 1-DOF and 2-DOF generators on the knee while running.

	Rotation Angle [Degrees]	Power density (power normalised for mass) [mW/kg]		
		Back of the knee	Middle of the knee	Front of the knee
1-DOF generator	0	12.9	9.30	8.78
	20	24.6	12.8	8.87
	40	28.9	15.4	8.96
	60	**29.9**	**21.7**	10.4
	90	16.4	13.0	7.53
	110	13.7	13.2	**11.0**
	130	7.10	6.71	6.39
	150	7.53	5.92	5.95
2-DOF generator	0/90	16.7	11.5	8.13
	20/110	**19.3**	13.1	**10.3**
	40/130	18.9	11.8	7.65
	60//150	17.5	**14.0**	8.00

Chapter 7
Conclusions and Future Work

7.1 Conclusions

Human-powered inertial energy harvesting, which can convert the kinetic energy from human motion into electric energy, is considered as a practical alternative to electric power supplied by batteries. A literature review of on-body human-powered initial energy harvesting has been presented. The literature review has shown that all of the reported on-body energy harvesters are 1-DOF, efficient only along one axis and not able to harvest the full amount of the kinetic energy from human motion. Based on the literature around existing 2-DOF energy harvesters for other applications, it has been found that 2-DOF energy harvesters have the potential to generate more power and have a greater tolerance to rotation compared to 1-DOF energy harvesters. However, none of the existing 2-DOF energy harvesters have been designed for harvesting energy from human motion. The benefits in terms of output power and tolerance to rotation have not been investigated for 2-DOF energy harvesters being used to harvest energy from human motion. In this thesis, a 2-DOF energy harvester consisting of two orthogonal 1-DOF energy harvesters has been studied. The effects of orientation, location and activity on the obtainable power from 2-DOF human-powered inertial energy harvesters have been theoretically and experimentally investigated.

To understand the important properties of human motion, and to evaluate power availability from motion, acceleration measurements on the human body have been taken from 23 participants during walking and running on a treadmill. Triple axis acceleration data were measured from five locations on the body (the ankle, knee, waist, elbow and wrist). The methods for analysing the acceleration data for evaluating power output from 1-DOF and 2-DOF inertial energy harvesters have been presented. Based on the evaluated output power from 1-DOF and 2-DOF energy harvesters, the effects of orientation, location and activity on the output power have been investigated. The results show that the output power is affected by the orientation of both 1-DOF and 2-DOF energy harvesters. A rotation of 20° from the optimum direction reduces the available output power from 1-DOF generators by at least 10%. For 2-DOF generators, this tolerance is increased to 30°. As for the effect of location and activity on output power, the results of 1-DOF generators show that the lower body can generate much more power than the upper body during walking; however, for running, the difference between the power output on the upper and lower body is less significant. For walking, the same

conclusion has been derived from the 2-DOF analysis, while the conclusion from 2-DOF analysis of running is different. The results of 2-DOF analysis show that for running, the elbow and wrist are able to generate more power than the lower body, but that the correlation of output power among participants is not as good as it is for the lower body. Furthermore, the normalised and relative power have been considered in conjunction to identify the optimum locations to place 1-DOF and 2-DOF generators. The optimum placement of generators should provide a high relative power and a high normalised power simultaneously. It has been found that for 1-DOF generators, the knee and the ankle are the optimum locations for walking and running, respectively, while in the case of 2-DOF generators, the optimum locations are the ankle and the wrist.

The predominant frequencies that make a great contribution to the output power from 1-DOF and 2-DOF generators have been identified during different activities. The results show that, for walking, the predominant frequency bands are all below 2.5 Hz at all locations, while for running, the higher frequency band of 2.5-3 Hz is introduced which provides high output power. The median of the predominant frequencies is between 0.875-1.75 Hz during walking; due to the strong impact between the ground and the foot during running and both feet striking the ground, the median of the predominant frequencies on the upper body (2.61-2.66 Hz) is approximately twice that of the predominant frequencies on the lower body (1.31-1.34 Hz).

Furthermore, a comparison between the 1-DOF and 2-DOF energy harvesters has been made in terms of the rotate ability τ. The rotate ability τ represents the ability to maintain 90% of the maximum power at rotation. The comparison results show that the rotate ability τ of 2-DOF generators is 5.7 times (average) greater than that of 1-DOF generators for relative power, and 5.2 times (average) greater for normalised power. This significant increase of the rotate ability τ means that 2-DOF generators have a greater tolerance to rotation and a much larger potential to generate over 90% of the maximum power, compared to 1-DOF generators. In addition, caparison in terms of the output power and the angular tolerance α has been made. If a 2-DOF and a 1-DOF generator are placed along the same orientation, the 2-DOF generator is able to harvest more power than the 1-DOF generator. The relative power from 2-DOF generators harvest is 2.10-2.67 times greater than that of 1-DOF generators, while the optimum orientations of 1-DOF and 2-DOF generators are not the same for the same location and activity. If a 2-DOF and 1-DOF generator are both along their optimum orientations, the 2-DOF generator does not receive significantly more power than the 1-DOF generator. During walking and running, 2-DOF generators produce 18% (average) more in terms of the median of the relative power than 1-DOF generators along the optimum orientations, or just 6% for the

normalised power. However, 2-DOF energy harvesters are able to significantly increase the tolerance to rotation. The average increase of the angular tolerance for the relative power is up to 73%, or 38% for the normalised power.

To validate the analytical result that 2-DOF generators have greater tolerance to rotation compared to 1-DOF generators, a real human-powered inertial energy harvester is required. The knee during running has been selected for the validation and the test energy harvester is designed to be resonant at 3.9 Hz. Considering the existing knee-mounted devices, and attempting not to interfere with the way people run, the test 2-DOF generator should be smaller than $120 \times 120 \times 20$ mm^3 and below 230 g in weight. In this thesis, mechanical-spring and magnetic-spring electromagnetic energy harvesters have been considered for the purpose, each of which has different benefits. Mechanical springs have the benefit of constant spring stiffness, and magnetic springs have the benefit of low mechanical fatigue. No commercial springs were available that met the requirements of a low spring constant (necessary for a 3.9 Hz resonant frequency) within the required physical size. Therefore, particular attention had to be paid to the design and specification of a manufactured linear mechanical spring. A linear mechanical spring with a low spring constant of 27 N/m has been designed in this work. The spring stiffness of the fabricated spring has been experimentally measured as 22 N/m with a linearity of 0.727%. Given the fabricated moving mass has a weight of 46.9 g, the resonant frequency is 3.45 Hz. In addition to the mechanical spring, a linearised magnetic spring for low-frequency operation has been presented. FEA simulations show that the proposed design has a linearity of 1.9% over a displacement range of 50 mm, representing a significant improvement over past reported devices. The spring stiffness of a prototype has been experimentally measured as 145 N/m with a linearity of 1.7%, showing good correlation with FEA simulations. Given the 188 g moving mass, the resonant frequency is 4.42 Hz. The coils for the mechanical- and magnetic-spring electromagnetic generators have been designed and fabricated. The specifications of the prototypes of both generators are summarised in Table 7.1. The resonant frequencies of the two generators differ from the expected value of 3.9 Hz; hence, in this study, a bandwidth of 1 Hz was desired to harvest energy over 3.9 Hz. MATLAB models have been created to predict the open-circuit voltage generated from the designed electromagnetic generators. The simulation results showed that for both of the generators, the resonant frequencies are constant with rotation.

Table 7.1 Specifications of the prototypes of the mechanical- and magnetic-spring electromagnetic generators

	Mechanical-spring generator	Magnetic-spring generator [a]
Spring stiffness	22 N/m	145 N/m
Spring linearity	0.7%	1.7%
Resonant frequency	3.45 Hz	4.42 Hz
Volume	20.6 mm (diameter) ×120 mm (height)	32.6 mm (diameter) ×88 mm (height)
Total weight	115 g	422 g

[a] Generator with Delrin end holders.

To validate the resonant frequencies of the generators and explore whether or not the resonant frequencies change with rotation, the frequency response of the generators at different angles has been measured on a controlled vibration source. In the measurement, the generators were rotated from $0°$ to $60°$ through $10°$ steps with respect to the direction of gravity. Due to the distortion from the vibration source on the frequency response, the resonant frequencies at different rotation angles could not be exactly identified. Instead, the frequencies with an emf greater than $\sqrt{1/2}$ of the maximum emf were found. The results showed that the resonant frequencies are in the range of 3.3-4.4 Hz for the mechanical-spring electromagnetic generator, or 3.0-8.0 Hz for the magnetic-spring electromagnetic generator. The calculated resonant frequencies (the mechanical-spring generator: f_0=3.45 Hz and the magnetic-spring generator: f_0=4.42 Hz) are within the corresponding frequency ranges. In addition, the optimum resistive loads for maximising the load power generated from the mechanical- and magnetic-spring electromagnetic generators have been measured as 1.27 kΩ and 2.88 kΩ, respectively. Moreover, the total damping ratios, Q-factors and bandwidths of the fabricated generators have been characterised. The measurement results showed that the mechanical-spring generator with 3.45 Hz resonant frequency has 1.0 Hz bandwidth, and the magnetic-spring generator with 4.42 Hz resonant frequency has over 1.2 Hz bandwidth. Therefore, the kinetic energy from human motion at 3.9 Hz can be harvested by the two generators.

To validate the benefit of a 2-DOF generator in terms of angular tolerance, an experimental validation on the human body was carried out on 13 participants. The mechanical-spring generator has been chosen for the validation because the total weight of the fabricated mechanical-spring generator is only 27% of the weight of the magnetic-spring generator, and it is hence more wearable. The validation has been performed at three various locations around the knee while running, and four different orientations have been tested at each location. In the measurements, participants were asked to wear a 2-DOF generator that consists of two orthogonal 1-DOF mechanical-spring generators, with a triple axis accelerometer used to monitor body motion. The generated power from the 1-DOF and 2-DOF generators on the

optimum load resistance has been evaluated. To validate the analytical results, the measured acceleration data have been fed into the data-processing methods to estimate the power output from the generators. The measurement results show that due to the different magnitudes of the vibrations at the three locations, the back of the knee generates the most power, and the front of the knee provides the least power for either the 1-DOF generator or the 2-DOF generator, which adequately agrees with the analytical results. In addition, it was found that if the 2-DOF generator and the 1-DOF generator were placed along the same orientation, the 2-DOF generator would be able to harvest more power than the 1-DOF generator. The median of the power from 2-DOF generators harvest is 2.04 times greater than that of 1-DOF generators, and the analytical results show an increase of 2.15 times, showing good correlation.

Due to the small sample size of the orientation measurements, the angular tolerance of the test orientations could not be calculated. Instead, normalised power was used to analyse the angular tolerance. At each location, the median of the power was normalised to the maximum of the median of the power that the 1-DOF or 2-DOF generators harvested. It was found that at the back of the knee, if the 1-DOF generator is rotated from $0\,°$ to $360\,°$, the normalised power is 24%-100%, while it is 86%-100% for the 2-DOF generator, which shows that the 2-DOF generator is more reliable in terms of output power and has greater tolerance to rotation. This improvement of the normalised power was found for the other two locations. In addition, at the back of the knee, the rotate ability τ of the 1-DOF generator is 25%, while it is 75% for the 2-DOF generator. This significant increase of the rotate ability τ means that 2-DOF generators have a greater tolerance to rotation and a much larger potential to generate over 90% of the maximum power, compared to 1-DOF generators. This increase of the rotate ability τ is found for the middle of the knee. Therefore, the measurement results adequately validate the benefit of 2-DOF generators in terms of the tolerance to rotation.

7.2 Recommendations for Future Work

The research that has been undertaken for this thesis has successfully met the research aims proposed in Section 1.2. There are, however, still additional investigations that could be carried out in the research area of the effect of orientation, location and activity on power output from human-powered inertial energy harvesters. Some of these areas of future work are presented in the following paragraphs.

In this thesis, five locations on the body and two activities have been investigated to understand human motion as it relates to on-body energy harvesting. To further this research, more

locations on the body and more activities of daily living could be investigated. The on-body acceleration data could be collected from other locations, such as the head, chest, back and hip, and from other activities, such as jumping, cycling and rowing. To achieve a more comprehensive experimental validation than that shown in this thesis, more locations and more activities could be tested in the experimental validation on the human body. In this thesis, three locations around the knee and four orientations at each location have been tested. Due to the small sample data sets, the angular tolerance of the test orientations could not be verified. Hence, in the future, more locations around the knee and more orientations at each location could be tested in order to evaluate the angular tolerance.

In this thesis, the magnetic-spring electromagnetic generator has shown good performance in terms of linearity, but it is less wearable on the knee than the mechanical-spring electromagnetic generator. In the future, the magnetic-spring electromagnetic generator could be optimised by reducing the weight and the size through using different magnetic material or structures, and then it could be used in the on-body validation. In addition, the 2-DOF generator used in this thesis consists of two orthogonal 1-DOF generators. The limitation of this 2-DOF generator design is that two seismic masses are needed which would double the 1-DOF generator's physical size and weight. To make the 2-DOF generator lighter and smaller, in the future, the 2-DOF generator could be optimised to have one seismic mass which would make it more wearable on the body. The seismic mass could be moving along two different axes.

In this study, wired measurement has been used to measure the output voltage from the test generators on the human body. Participants reported that the wired measurement did not significantly affect the way they ran. However, for other activities, such as cycling and rowing, it could affect the way participants perform the activities and hence affect the measurement. Therefore, in those cases, wireless measurement is a better choice, and then wireless communication could be developed for the on-body measurement in the future. The output voltage from the generators could be measured and wireless-transferred to a computer through wireless transceivers.

Bibliography

[1] O. Aziz, B. Lo, A. Darzi, and G. Yang, "Introduction," in *Body Sensor Networks*, G.-Z. Yang, Ed., ed: Springer, pp. 1-40, 2006.

[2] T. Gao, C. Pesto, L. Selavo, Y. Chen, J. Ko, J. Lim, A. Terzis, A. Watt, J. Jeng, B.-r. Chen, K. Lorincz, and M. Welsh, "Wireless medical sensor networks in emergency response: implementation and pilot results," in *Proc. IEEE Int. Conf. Technologies for Homeland Security*, Waltham, MA, pp. 187-192, 2008.

[3] V. Shnayder, B.-r. Chen, K. Lorincz, T. R. F. Fulford-Jones, and M. Welsh, "Sensor networks for medical care," in *Harvard University Technical Report TR-08-05*, 2005.

[4] O. Ojetola, E. I. Gaura, and J. Brusey, "Fall detection with wearable sensors-SAFE (SmArt Fall dEtection)," in *Proc. 7th Int. Conf. on Intelligent Environments*, Nottingham, UK, pp. 318-321, 2011.

[5] S. Abbate, M. Avvenuti, P. Corsini, A. Vecchio, and J. Light, "Monitoring of human movements for fall detection and activities recognition in elderly care using wireless sensor network: a survey," in *Wireless Sensor Networks: Application-Centric Design*, G. V. Merret and Y. K. Tan, Eds., ed: InTech, pp. 147-166, 2010.

[6] R. C. King, D. G. McLlwraith, B. Lo, J. Pansiot, A. H. McGregor, and G. Yang, "Body sensor networks for monitoring rowing technique," in *Proc. 6th Int. Workshop on Wearable and Implantable Body Sensor Networks*, Berkeley, CA, pp. 251-255, 2009.

[7] L. Mateu and F. Moll, "Review of energy harvesting techniques and applications for microelectronics," *VLSI Circuits and Systems II (Sevilla) Proc. SPIE*, vol. 5837, pp. 359-373, 2005.

[8] P. D. Mitcheson, "Energy harvesting for human wearable and implantable bio-sensors," in *Proc. Int. Conf. IEEE Engineering in Medicine and Biology Society*, Buenos Aires, Argentina, pp. 3432-3436, 2010.

[9] R. Riemer and A. Shapiro, "Biomechanical energy harvesting from human motion: theory, state of the art, design guidelines, and future directions," *Journal of NeuroEngineering and Rehabilitation*, vol. 8, 2011.

[10] S. E. Jo, M. K. Kim, M. S. Kim, and Y. J. Kim, "Flexible thermoelectric generator for human body heat energy harvesting," *Electronics Letters*, vol. 48, pp. 1013-1015, 2012.

[11] Q. Li, V. Naing, and J. M. Donelan, "Development of a biomechanical energy harvester," *Journal of NeuroEngineering and Rehabilitation*, vol. 6, 2009.

[12] J. Granstrom, J. Feenstra, H. A. Sodano, and K. Farinholt, "Energy harvesting from a backpack instrumented with piezoelectric shoulder straps," *Smart Materials and Structures*, vol. 16, pp. 1810-1820, 2007.

[13] N. S. Shenck and J. A. Paradiso, "Energy scavenging with shoe-mounted piezoelectrics," *IEEE Micro*, vol. 21, pp. 30-42, 2001.

[14] S. Beeby and N. White, "Kinetic energy-harvesting applications," in *Energy Harvesting for Autonomous Systems*, S. Beeby and N. White, Eds., ed: Artech House, pp. 92-95,

2010.

[15] J. A. Paradiso and T. Starner, "Energy scavenging for mobile and wireless electronics," *IEEE Pervasive Computing*, vol. 4, pp. 18-27, 2005.

[16] L. C. Rome, L. Flynn, E. M. Goldman, and T. D. Yoo, "Generating electricity while walking with loads," *Science*, vol. 309, pp. 1725-1728, 2005.

[17] T. V. Büren, "Body-worn inertial electromagnetic micro-generators," Ph.D. dissertation, Swiss Federal Institute of Technology, ETH Zurich, 2006.

[18] "EH network data repository." [Online]. Available: http://eh-network.org/data/ Last accessed December 2012.

[19] V. Bedekar, J. Oliver, and S. Priya, "Pen harvester for powering a pulse rate sensor," *Journal of Physics D: Applied Physics*, vol. 42, pp. 105105-105113, 2009.

[20] A. Olivares, G. Olivares, P. Gloesekoetter, J. M. Górriz, and J. Ramírez, "A study of vibration-based energy harvesting in activities of daily living," in *Proc. 4th Int. Conf. Pervasive Computing Technologies for Healthcare (PervasiveHealth)*, Munich, Germany, pp. 1-4, 2010.

[21] G. V. Merrett, A. S. Weddell, and N. R. Harris, "Energy requirements of autonomous devices," in *Energy Harvesting for Autonomous Systems*, S. Beeby and N. White, Eds., ed: Artch House, pp. 9-19, 2010.

[22] G. Sebald, E. Lefeuvre, and D. Guyomar, "Pyroelectric energy conversion: optimization principles," *IEEE Transactions on Ultrasonics, Ferroelectrics, and Frequency control*, vol. 55, pp. 538-551, 2008.

[23] J. Yun, S. N. Patel, M. S. Reynolds, and G. D. Abowd, "Design and performance of an optimal inertial power harvester for human-powered devices," *IEEE Transactions on Mobile Computing*, vol. 10, pp. 669-683, 2011.

[24] J. Yun, S. Patel, M. Reynolds, and G. Abowd, "A quantitative investigation of inertial power harvesting for human-powered devices," in *Proc. 10th Int. Conf. Ubiquitous Computing*, Seoul, Korea, pp. 74-83, 2008.

[25] T. V. Büren, P. D. Mitcheson, T. C. Green, E. M. Yeatman, A. S. Holmes, and G. Troster, "Optimization of inertial micropower generators for human walking motion," *IEEE Sensors*, vol. 6, pp. 28-38, 2006.

[26] S. Beeby, M. Tudor, and N. White, "Energy harvesting vibration sources for microsystems applications," *Measurement Science and Technology*, vol. 17, pp. R175-R195, 2006.

[27] P. D. Mitcheson, T. C. Green, E. M. Yeatman, and A. S. Holmes, "Architectures for vibration-driven micropower generators," *Microelectromechanical Systems*, vol. 13, pp. 429-440, 2004.

[28] S. Roundy, P. K. Wright, and J. Rabaey, "A study of low level vibrations as a power source for wireless sensor nodes," *Computer Communications*, vol. 26, pp. 1131-1144, 2003.

[29] C. B. Williams and R. B. Yates, "Analysis of a micro-electric generator for microsystems," in *Proc. 8th Int. Conf. Solid-State Sensors and Actuators Eurosensors IX*, Stockholm, Sweden, pp. 369-372, 1995.

[30] J. M. Gilbert and F. Balouchi, "Comparison of energy harvesting systems for wireless sensor networks," *Int. Journal of Automation and Computing*, vol. 5, pp. 334-347, 2008.

[31] W. T. Thomson, "Harmonically excited vibration," in *Theory of Vibration With Applications*, W. T. Thomson, Ed., 4th ed: Stanley Thornes, pp. 51-91, 1993.

[32] N. G. Stephen, "On energy harvesting from ambient vibration," *Sound and Vibration*, vol. 293, pp. 409-425, 2006.

[33] S. S. Rao, "Fundamentals of vibration - classification of vibration," in *Mechanical Vibrations*, 4th ed: Pearson Educatioin International, pp. 16-17, 2004.

[34] R. Sood, Y. B. Jeon, J.-h. Jeong, and S. G. Kim, "Piezoelectric micro power generator for energy harvesting," in *Proc. Tech. Dig. of the 2004 Solid-State Sensor and Actuator Workshop*, Hilton Head, SC, 2004.

[35] S. R. Anton and H. A. Sodano, "A review of power harvesting using piezoelectric materials (2003-2006)," *Smart Materials and Structures*, vol. 16, pp. R1-R21, 2007.

[36] D. Fourie, "Shoe mounted PVDF piezoelectric transducer for energy harvesting," *MIT Undergraduate Research Journal*, vol. 19, pp. 66-70, 2010.

[37] S. Priya, "Advances in energy harvesting using low profile piezoelectric transducers," *Journal of Electroceramics*, vol. 19, pp. 167-184, 2007.

[38] J. L. Gonzalez, A. Rubio, and F. Moll, "A prospect on the use of piezoelectric effect to supply power to wearable electronic devices," in *Proc. 4th Int. Conf. Materials Engineering for Resources*, Akita, Japan, pp. 202-207, 2001.

[39] Y. B. Jeon, R. Sood, J. h. Jeong, and S. G. Kim, "MEMS power generator with transverse mode thin film PZT," *Sensors and Actuators A: Physical*, vol. 122, pp. 16-22, 2005.

[40] S.-J. Jeong, M.-S. Kim, J.-S. Song, and H.-k. Lee, "Two-layered piezoelectric bender device for micro-power generator," *Sensors and Actuators A: Physical*, vol. 148, pp. 158-167, 2008.

[41] S. L. Kok, N. M. White, and N. R. Harris, "A novel piezoelectric thick-film free-standing cantilever energy harvester," in *Proc. Eurosensors XXII*, Dresden, Germany, pp. 395-399, 2008.

[42] D. N. Shen, J. H. Park, J. H. Noh, S. Y. Choe, S. H. Kim, H. C. Wikle, and D. J. Kim, "Micromachined PZT cantilever based on SOI structure for low frequency vibration energy harvesting," *Sensors and Actuators A: Physical*, vol. 154, pp. 103-108, 2009.

[43] D. F. Berdy, P. Srisungsitthisunti, J. Byunghoo, X. Xianfan, J. F. Rhoads, and D. Peroulis, "Low-frequency meandering piezoelectric vibration energy harvester," *IEEE Trans Ultrason Ferroelectr Freq Control*, vol. 59, pp. 846-858, 2012.

[44] S. Roundy, P. K. Wright, and K. S. J.Pister, "Micro-electrostatic vibration-to-electricity converters," in *Proc. 2002 ASME Int. Mechanical Engineering Congress and Exposition*, New Orleans, LA, 2002.

[45] F. Peano and T. Tambosso, "Design and optimization of a MEMS electret-based capacitive energy scavenger," *Journal of Microelectromechanical Systems*, vol. 14, pp. 429-435, 2005.

[46] L. Hsi-wen and T. Yu-Chong, "Parylene-based electret power generators," *Journal of Micromechanics and Microengineering*, vol. 18, pp. 104006-1040014, 2008.

[47] H. Daniel, F. Bernd, and M. Yiannos, "Fabrication, characterization and modelling of electrostatic micro-generators," *Journal of Micromechanics and Microengineering*, vol. 19, pp. 1-11, 2009.

[48] Y. Suzuki, D. Miki, M. Edamoto, and M. Honzumi, "A MEMS electret generator with electrostatic levitation for vibration-driven energy-harvesting applications," *Journal of Micromechanics and Microengineering*, vol. 20, pp. 104002-1040010, 2010.

[49] R. Guilllemet, P. Basset, D. Galayko, F. Cottone, F. Marty, and T. Bourouina, "Wideband MEMS electrostatic vibration energy harvesters based on gap-closing interdigited combs with a trapezoidal cross section," in *Proc. 26th IEEE Int. Conf. Micro Electro Mechanical Systems (MEMS)*, Taipei, pp. 817-820, 2013.

[50] D. Zhu, "Methods of frequency tuning vibration based micro-generator," Ph.D. Thesis, Electronics and Computer Science, University of Southampton, 2009.

[51] S. P. Beeby, R. N. Torah, M. J. Tudor, P. Glynne-Jones, T. O'Donnell, C. R. Saha, and S. Roy, "A micro electromagnetic generator for vibration energy harvesting," *Micromechanics and Microengineering*, vol. 17, pp. 1257-1265, 2007.

[52] I. Sari, T. Balkan, and H. Kulah, "A wideband electromagnetic micro power generator for wireless microsystems," in *Proc. Int. Conf. Solid-State Sensors, Actuators and Microsystems*, Lyon, France, pp. 275-278, 2007.

[53] B. Yang, C. Lee, W. F. Xiang, J. Xie, J. H. He, R. K. Kotlanka, S. P. Low, and H. H. Feng, "Electromagnetic energy harvesting from vibrations of multiple frequencies," *Journal of Micromechanics and Microengineering*, vol. 19, pp. 035001-035009, 2009.

[54] O. Zorlu, S. Turkyilmaz, A. Muhtaroglu, and H. Kulah, "An electromagnetic energy harvester for low frequency and low-g vibrations with a modified frequency up conversion method," in *Proc. 26th IEEE Int. Conf. Micro Electro Mechanical Systems (MEMS)*, Taipei, pp. 805-808, 2013.

[55] Q. Zhang and E. S. Kim, "Energy harvesters with high electromagnetic conversion efficiency through magnet and coil arrays," in *Proc. 26th IEEE Int. Conf. Micro Electro Mechanical Systems (MEMS)*, Taipei, pp. 110-113, 2013.

[56] B. S. Lee, S. C. Lin, W. J. Wu, X. Y. Wang, P. Z. Chang, and C. K. Lee, "Piezoelectric MEMS generators fabricated with an aerosol deposition PZT thin film," *Journal of Micromechanics and Microengineering*, vol. 19, pp. 065014-065021, 2009.

[57] P. D. Mitcheson, P. Miao, B. H. Stark, E. M. Yeatman, A. S. Holmes, and T. C. Green,

"MEMS electrostatic micropower generator for low frequency operation," *Sensors and Actuators A: Physical*, vol. 115, pp. 523-529, 2004.

[58] P. Miao, P. D. Mitcheson, A. S. Holmes, E. M. Yeatman, T. C. Green, and B. H. Stark, "MEMS inertial power generators for biomedical applications," *Microsystem Technologies-Micro-and Nanosystems-Information Storage and Processing Systems*, vol. 12, pp. 1079-1083, 2006.

[59] R. Torah, P. Glynne-Jones, J. Tudor, T. O'Donnell, S. Roy, and S. Beeby, "Self-powered autonomous wireless sensor node using vibration energy harvesting," *Measurement Science and Technology*, vol. 19, pp. 125202-125209, 2008.

[60] S. P. Beeby, M. J. Tudor, R. N. Torah, S. Roberts, T. O'Donnell, and S. Roy, "Experimental comparison of macro and micro scale electromagnetic vibration powered generators," *Microsystem Technologies*, vol. 13, pp. 1647-1653, 2007.

[61] A. Jansen and S. Van Leeuwen, "Design of a fuel cell powered radio, a feasibility study into alternative power sources for portable products," in *Proc. IEEE Int. Symposium on Electronics and the Environment*, San Francisco, CA, pp. 155-160, 2000.

[62] S. P. Wyche and L. L. Murphy, "Powering the cellphone revolution: findings from mobile phone charging trials in off-grid Kenya," in *Proc. SIGCHI Conf. on Human Factors in Computing Systems*, Paris, France, pp. 1959-1968, 2013.

[63] R. Amirtharajah and A. P. Chandrakasan, "Self-powered signal processing using vibration-based power generation," *IEEE Journal of Solid-State Circuits*, vol. 33, pp. 687-695, 1998.

[64] T. Starner and J. A. Paradiso, "Human generated power for mobile electronics," in *Low Power Electronics Design*, C. Piguet, Ed., ed Boca Raton, FL: CRC Press, pp. 1-35, 2004.

[65] Y. Naruse, N. Matsubara, K. Mabuchi, M. Izumi, and S. Suzuki, "Electrostatic micro power generation from low-frequency vibration such as human motion," *Journal of Micromechanics and Microengineering*, vol. 19, pp. 115025-115036, 2009.

[66] M. Renaud, P. Fiorini, R. Schaijk, and C. Hoof, "Harvesting energy from the motion of human limbs: the design and analysis of an impact-based piezoelectric generator," *Smart Materials and Structures*, pp. 035001-035016, 2009.

[67] R. Morais, N. Silva, P. Santos, C. Frias, J. Ferreira, A. Ramos, J. Simões, J. Baptista, and M. Reis, "Permanent magnet vibration power generator as an embedded mechanism for smart hip prosthesis," in *Proc. Eurosensors XXIV*, Linz, Austria, pp. 766-769, 2010.

[68] A. D. Kuo, "Harvesting Energy by Improving the Economy of Human Walking," *Science*, vol. 309, pp. 1686-1687, 2005.

[69] "Soldier's load and combat readiness." [Online]. Available: http://www.globalsecurity.org/military/library/report/call/call_01-15_ch11.htm Last accessed July 2011.

[70] M. Pozzi, M. S. H. Aung, M. Zhu, R. K. Jones, and J. Y. Goulermas, "The pizzicato knee-joint energy harvester: characterization with biomechanical data and the effect of

backpack load," *Smart Materials and Structures,* vol. 21, pp. 075023-075030, 2012.

[71] J. M. Donelan, Q. Li, V. Naing, J. A. Hoffer, D. J. Weber, and A. D. Kuo, "Biomechanical energy harvesting: generating electricity during walking with minimal user effort," *Science,* vol. 319, pp. 807-810, 2008.

[72] I.-H. Kim, H.-J. Jung, B. M. Lee, and S.-J. Jang, "Broadband energy-harvesting using a two degree-of-freedom vibrating body," *Applied Physics Letters,* vol. 98, p. 3, 2011.

[73] H. Wu, L. Tang, Y. Yang, and C. K. Soh, "A compact 2 degree-of-freedom energy harvester with cut-out cantilever beam," *Japanese Journal of Applied Physics,* vol. 51, p. 3, 2012.

[74] U. Bartsch, J. Gaspar, and O. Paul, "Low-frequency two-dimensional resonators for vibrational micro energy harvesting," *Micromechanics and Microengineering,* vol. 20, 2010.

[75] Y. Zhu, S. O. R. Moheimani, and M. R. Yuce, "A 2-DOF MEMS ultrasonic energy harvester," *IEEE Sensors,* vol. 11, pp. 155-161, 2011.

[76] B. Andò, S. Baglio, F. Maiorca, and C. Trigona, "Two dimensional bistable vibration energy harvester," in *Proc. 26th European Conf. Solid-State Transducers Eurosensors XXVI*, Kraków, Poland, pp. 1061-1064, 2012.

[77] K. Ashraf, M. H. M. Khir, and J. O. Dennis, "Energy harvesting in a low frequency environment," in *Proc. National Postgraduate Conference*, Kuala Lumpur, Malaysia, pp. 1-5, 2011.

[78] I. Sari, T. Balkan, and H. Kulah, "An electromagnetic micro power generator for low-frequency environmental vibrations based on the frequency upconversion technique," *Journal of Microelectromechanical Systems,* vol. 19, pp. 14-27, 2010.

[79] M. Pozzi and M. Zhu, "Plucked piezoelectric bimorphs for knee-joint energy harvesting: modelling and experimental validation," *Smart Materials and Structures,* vol. 20, pp. 055007-055016, 2011.

[80] O. Zorlu, E. T. Topal, and H. Kulah, "A mechanical frequency up-conversion mechanism for vibration based energy harvesters," in *Proc. Tech. Dig. IEEE Sensors,* Christchurch, New Zealand, pp. 1366-1369, 2009.

[81] L. Gu and C. Livermore, "Impact-driven, frequency up-converting coupled vibration energy harvesting device for low frequency operation," *Smart Materials and Structures,* vol. 20, pp. 045004-045013, 2011.

[82] S. S. Rao, "Fundamentals of vibration - spring elements," in *Mechanical Vibrations*, 4th ed: Pearson Educatioin International, pp. 20-30, 2004.

[83] W. J. Choi, Y. Jeon, J. H. Jeong, R. Sood, and S. G. Kim, "Energy harvesting MEMS device based on thin film piezoelectric cantilevers," *Journal of Electroceramics,* vol. 17, pp. 543-548, 2006.

[84] H. Hu, H. Xue, and Y. Hu, "A spiral-shaped harvester with an improved harvesting element and an adaptive storage circuit," *IEEE Transactions on Ultrasonics,*

Ferroelectrics and Frequency Control, vol. 54, pp. 1177-87, 2007.

[85] Q. F. Niu, L. Wang, T. Dong, and H. J. Yang, "Application of a MEMS-based energy harvester for artificial heart wireless energy transmission," in *Proc. ISECS Int. Colloquium on Computing, Communication, Control, and Management*, pp. 38-41, 2009.

[86] C. R. Saha, T. O'Donnell, N. Wang, and P. McCloskey, "Electromagnetic generator for harvesting energy from human motion," *Sensors and Actuators A: Physical*, vol. 147, pp. 248-253, 2008.

[87] E. Romero, M. R. Neuman, and R. O. Warrington, "Rotational energy harvester for body motion," in *Proc. 24th IEEE Int. Conf. Micro Electro Mechanical Systems (MEMS)*, Cancun, Mexico, pp. 1325-1328, 2011.

[88] C. K. Yew and J. M. Gilbert, "Energy harvesting and human movement," presented at the Energy Harvesting Dissemination Event, IET London, Savoy Place,London, UK, 2011.

[89] N. Yarkony, K. Sayrafian-Pour, and A. Possolo, "Statistical modeling of harvestable kinetic energy for wearable medical sensors," in *Proc. 11th Annu. IEEE Int. Symposium on a World of Wireless, Mobile and Multimedia Networks*, Montrreal, QC, Canada, pp. 1-5, 2010.

[90] M. Gorlatova, J. Sarik, M. Cong, I. Kymissis, and G. Zussman, "Movers and shakers: kinetic energy harvesting for the Internet of things," in *Technical Report*, 2013.

[91] "G-Link wireless accelerometer node." [Online]. Available: http://files.microstrain.com/G-LINK_LXRS_Datasheet_Rev_1.02e.pdf Last accessed April 2013.

[92] "NESS L300 Foot Drop System technical specifications." [Online]. Available: http://www.gigapixelcreative.com/portfolio/bioness/bioness_foot_technical.php Last accessed May 2013.

[93] H. Kim and S. Priya, "Piezoelectric microgenerator - current status, challenges, and applications," in *Proc. 17th IEEE Int. Symposium on the Applications of Ferroelectrics*, Santa Fe, NM, pp. 1-2, 2008.

[94] K. Hyun-Uk, L. Woo-Ho, H. V. R. Dias, and S. Priya, "Piezoelectric microgenerators-current status and challenges," *IEEE Transactions on Ultrasonics, Ferroelectrics and Frequency Control*, vol. 56, pp. 1555-1568, 2009.

[95] S. Roundy and P. K. Wright, "A piezoelectric vibration based generator for wireless electronics," *Smart Materials and Structures*, vol. 13, pp. 1131-1142, 2004.

[96] P. Patt, "Design and testing of a coaxial linear magnetic spring with integral linear motor," *IEEE Transactions on Magnetics*, vol. 21, pp. 1759-1761, 1985.

[97] J. Arora, "Optimum design problem formulation," in *Introduction to Optimum Design*, J. Arora, Ed., 2nd ed: Academic Press, pp. 36-38, 2004.

[98] "Sping and metal form technical article: spring index." [Online]. Available:

http://www.newcombspring.com/article_spring_index.html Last accessed May 2013.

[99] "Compression spring: end types." [Online]. Available: http://springipedia.com/compression-end-types.asp Last accessed May 2013.

[100] A. S. Jonnalagadda, "Magnetic Induction Systems to Harvest Energy from Mechanical Vibrations," Master thesis, Dept. of Mechanical Engineering, Massachusetts Institute of Technology, 2007.

[101] G. P. Ripper, R. S. Dias, and G. A. Garcia, "Primary accelerometer calibration problems due to vibration exciters," *Measurement*, vol. 42, pp. 1363-1369, 2009.

[102] Z. Wei and F. Phillips, "Analysis of vibrator performance at low frequencies," *First break*, vol. 29, pp. 55-61, 2011.

[103] S. S. Rao, "Free vibration of single-degree-of-freedom systems - free vibration with Coulomb damping," in *Mechanical Vibrations*, 5th ed: Pearson Educatioin South Asia, pp. 185-192, 2011.

[104] M. L. James, G. M. Smith, J. C. Wolford, and P. W. Whaley, *Vibration of Mechanical and Structural Systems: With Microcomputer Applications*, 2nd ed., New York: Harpercollins College Div, 1994.